Numerical modelling of radiative heat transfer and tabulated chemical kinetics in multiphase reactive processes

Jurić, Filip

FACULTY OF MECHANICAL ENGINEERING AND NAVAL ARCHITECTURE

FILIP JURIĆ

NUMERICAL MODELLING OF RADIATIVE HEAT TRANSFER AND TABULATED CHEMICAL KINETICS IN MULTIPHASE REACTIVE PROCESSES

DOCTORAL THESIS

Zagreb, 2022

Sveučilište u Zagrebu

FAKULTET STROJARSTVA I BRODOGRADNJE

FILIP JURIĆ

NUMERIČKO MODELIRANJE PRIJENOSA TOPLINE ZRAČENJEM I TABELIRANE KEMIJSKE KINETIKE U VIŠEFAZNIM REAKTIVNIM PROCESIMA

DOKTORSKI RAD

Zagreb, 2022.

FACULTY OF MECHANICAL ENGINEERING AND NAVAL ARCHITECTURE

FILIP JURIĆ

NUMERICAL MODELLING OF RADIATIVE HEAT TRANSFER AND TABULATED CHEMICAL KINETICS IN MULTIPHASE REACTIVE PROCESSES

DOCTORAL THESIS

SUPERVISOR:

Prof.dr.sc. NEVEN DUIĆ

Zagreb, 2022

FAKULTET STROJARSTVA I BRODOGRADNJE

FILIP JURIĆ

NUMERIČKO MODELIRANJE PRIJENOSA TOPLINE ZRAČENJEM I TABELIRANE KEMIJSKE KINETIKE U VIŠEFAZNIM REAKTIVNIM PROCESIMA

DOKTORSKI RAD

Mentor:

Prof.dr.sc. Neven Duić

Zagreb, 2022.

BIBLIOGRAPHY DATA

TABLE OF CONTENTS

ACKNOWLEDGEMENT

Many thanks to the other colleagues from PowerLab. With them, the time in the office was more enjoyable and fun.

I would like to express my deepest gratitude to my girlfriend Ana for her support in finishing PhD, and her patience and understanding, which she always had even when it was the hardest.

In the end, I dedicate this thesis to my parents, Sanda and Tadija, who have always been my source of love, support, and encouragement. Their sacrifices and unwavering belief in me and my abilities have been a constant source of motivation and inspiration.

SPECIAL ACKNOWLEDGEMENT

SUMMARY

Radiative heat transfer plays a significant role in total heat transfer in industrial systems that operate at high temperatures. Therefore, this research aims to implement a spectral-line weighted-grey-gas model based on single grey gas and transparent window (SLW-1) to calculate the radiative absorption coefficient. The finite volume method for control volumes is applied to solve the radiative transfer equation. The SLW-1 model is validated using analytical results for simple geometries and experimental data from Sandia Flame D and internal combustion engines. Additionally, an automated procedure for efficiently calculating laminar flame velocity and the autoignition of an air-fuel mixture. The developed procedure for creating laminar flame speed and autoignition lookup databases employs the correlation functions for linking the existing data from a stable tabulation regime. The procedure is developed and implemented as a pre-processing tool of the computational fluid dynamic software based on the lognormal distribution for laminar flame speed in equivalence ratio direction and exponential functions for pressure, temperature, and exhaust gas recirculation directions. The implemented radiative absorption coefficient model and developed automated procedure provide more accurate and industrially feasible calculations of multiphase reactive processes.

SAŽETAK

Prijenos topline zračenjem ima značajnu udio u ukupnom prijenosu topline u industrijskim sustavima koji rade na visokim temperaturama. Stoga, ovo istraživanje ima za cilj implementirati model za proračun koeficijenta apsorpcije zračenja unutar metode kontrolnih volumena, uzimajući u obzir spektralna svojstva medija pomoću jednog sivog plina i jednog transparentnog plina (SLW-1) u medijima koji sudjeluju u prijenosu topline zračenjem. Metoda kontrolnih volumena primjenjuje se za rješavanje jednadžbe prijenosa topline zračenja. Model SLW-1 validiran je s analitičkim rezultatima za jednostavne geometrije i eksperimentalnim podacima predmiješanog plamena Sandia Flame D i motora s unutarnjim izgaranjem. Nadalje, razvijen je i automatizirani postupak za učinkovito izračunavanje laminarne brzine plamena i samozapaljenja mješavine zraka i goriva. Razvijeni postupak za izradu baza podataka za pretraživanje brzine laminarnog plamena i samozapaljenja koristi korelacijske funkcije za povezivanje postojećih podataka iz stabilnog režima. Postupak je razvijen i implementiran kao alat za predtabliranje laminarne brizne plamena i zapaljenja mješavine goriva i zraka u softveru računalne dinamike fluida koji se temelji na lognormalnoj distribuciji za laminaranu brzinu plamena sastava smjese i eksponencijalnim funkcijama za tlak, temperaturu i udio recirkulacije ispušnih plinova. Implementirani model koeficijenta apsorpcije zračenja i razvijena automatizirana procedura služit će za točnije i industrijski prihvatljive proračune višefaznih reaktivnih procesa.

PROŠIRENI SAŽETAK

Ključne riječi: prijenos topline zračenjem, koeficijent apsorpcije zračenja, laminarna brzina plamena, samozapaljenje, emi*sije, motor s unutrašnjim izgaranjem*

Razvoj i poboljšanje sustava za izgaranja velik je izazov koji se pokušava riješiti dugi niz godina. Poznato je da proces izgaranja fosilnih goriva kao egzotermni višefazni reaktivni proces negativno utječe na okoliš. Nedavna istraživanja ukazuju da je za postizanje održivog ekosustava potrebno smanjiti štetne emisije iz sustava za izgaranje. Plinske turbine, motori s unutarnjim izgaranjem, industrijske peći i kotlovi predstavljaju značajan izvor štetnih emisija, a njihovo smanjenje je od presudne važnosti za smanjenje atmosferskog onečišćenja u skoroj budućnosti. Moderni pristup za optimizaciju i smanjenje emisija iz sustava za izgaranje je uporaba eksperimentalnih istraživanja u kombinaciji s numeričkim istraživanjima. Numeričko modeliranje procesa izgaranja znanstveno je područje koje pokriva složene pojave poput interakcija između gibanja fluida, prijenosa topline, turbulencije, kinetike kemijskih reakcija i termodinamike izgaranja. Računalna Dinamika Fluida (RDF) kao numerički alat nudi potpuni uvid u integrirani utjecaj svih tih pojava na proces izgaranja.

Pri visokim temperaturama tijekom procesa izgaranja, prijenos topline zračenjem postaje sve izraženiji. Produkti izgaranja ugljikov dioksid, vodena para i čađa participiraju u prijenosu topline zračenjem i utječu na temperaturne profile, a samim tim i na procese formiranja emisija unutar komore za izgaranje. Zbog toga više nije dovoljno zanemariti utjecaj prijenosa topline zračenjem na proces stvaranja emisija radi njihovog uspješnog predviđanja [1]. Plinoviti medij sudjeluje u prijenosu topline zračenjem pomoću tri fenomena: apsorpcija, emisija i refleksija. Ako se uzme u obzir sudjelovanje medija u prijenosu topline zračenjem, potrebno je riješiti transportnu jednadžbu zračenja (TJZ). Za rješavanje takve integralne diferencijalne jednadžbe potrebno je aproksimirati jednadžbu numeričkim modelima [2]. U numeričkim simulacijama motora s unutarnjim izgaranjem uobičajeno se ne uzima prijenos topline zračenjem u obzir zbog malih geometrija i dodatne računalne zahtjevnosti [3]. Među mnogim istraživanjima na temu utjecaja prijenosa topline zračenjem u motorima s unutarnjim izgaranjem, samo je nekoliko istraživanja rješavalo TJZ [4]. Sva istraživanja koja su uključivala prijenos topline zračenjem u motorima su uglavnom koristila metodu diskretnih ordinata (DOM) za rješavanje TJZ i model sume ponderiranih sivih plinova (WSGG) za računanje apsorpcije plinovitog medija i čađe [5]. Utjecaj zračenja na prijenos topline, stvaranja čađe i emisije dušikovih oksida, prvi je put istražen u radu [6], gdje su postignute visoke vrijednosti koeficijenta apsorpcije unutar komore

za izgaranje motora zbog visokih koncentracija čađe i visokog radnog tlaka u motoru. Iako je utjecaj zračenja na cijeli prijenos topline u motoru mali, zbog malih geometrija, još uvijek se ne može zanemariti utjecaj na procese formiranja emisija [6]. Procijenjeno je da kemijski procesi stvaranje čađe ovisi više o prijenosu topline zračenja u motorima s unutarnjim izgaranjem nego procesa stvaranja NO_x [7]. Numerička ispitivanja prijenosa topline zračenjem u motorima s unutarnjim izgaranjem koja su koristila DOM za rješavanje TJZ pokazala su da zračenje utječe na predviđanja čađe do 50% [8]. U [9] autori su procijenili da količina izgubljene energije zbog utjecaja čađe na izmjenu topline zračenjem iznosi od 0.5% do 10%. Zbog toga su autori u [10] razvili novi jednodimenzionalni model izračunavanja interakcije čađe i zračenja u dizelskim plamenima, gdje su konstante modela dobivene iz eksperimentalnog istraživanja.

Od svih postojećih modela, DOM i njegova konzervativna modifikacija za kontrolne volumene najviše su korišteni u simulacijama motora s unutarnjim izgaranjem [11]. Apsorpcijska i emisijska svojstva plinova i čađe uobičajeno se računaju modelom ponderiranih sivih plinova (WSGG) na osnovi ne izotermnih i ne homogenih korelacija za smjese H2O i CO2 [12]. Dok se koeficijent apsorpcije čađe uobičajeno modelira korelacijom za sivi plin iz literature [13]. Fenomen raspršivanja (refleksije) može se zanemariti za simulacije motora s unutarnjim izgaranjem, budući da je zanemaren u svim do sad provedenim istraživanjima motora s unutarnjim izgaranjem, jer se čestica čađe koje su pre sitne da bi reflektirale zračenje izvrsno opisuju modelom sivog plina [14].

Dodatna točnost modela zračenja topline može se postići izračunavanjem koeficijenta apsorpcije u TJZ za ne-sive medije. Ako se uzmu u obzir spektralne karakteristike plinova koji sudjeluju u zračenju, koeficijent apsorpcije rješava se modelom spektralnog ponderiranog zbroja sivih plinova (SLW) [15]. Funkcija spektralne raspodjele za apsorpciju CO_2 i H_2O određuje se iz izraza u literaturi [16]. Ako se SLW model za rješavanje koeficijenta apsorpcije primijeni na konvencionalne modele zračenja poput DOM ili njegovog konzervativnog oblika za kontrolne volumene, koeficijent apsorpcije dijeli se na spektre za koje je potrebno riješiti dodatne transportne jednadžbe [17]. U [18], autori su usporedili rezultate s tradicionalnim WSGG modelom i SLW modelom za proračun predviđanja plamena izgaranja, gdje je postignuto značajno poboljšanje i slaganje s eksperimentalnim podacima, za oko deset puta duže vrijeme kalkulacije zračenja sa SLW modelom. Autori [19] su predstavili formulaciju modela SLW koristeći samo jedan sivi plin i jedan transparentni plin, koji se naziva SLW-1 model. SLW-1 model rješava isti broj transportni jednadžbi kao i konvencionalni WSGG model

i pokazuje bolje podudaranje s validacijskim podacima zbog razmatranja spektralnih svojstava plinova [20]. Prema dostupnoj literaturi, model SLW-1 nikada nije implementiran u kod RDF-a te simulacije nikada nisu provodile na složenim trodimenzionalnim pokretnim mrežama, koje se koriste za simulacije motora s unutarnjim izgaranjem. Očekivani rezultati implementiranog SLW-1 modela su bolje podudaranje s eksperimentalnim podacima u približno istom vremenu računanja kao s WSGG modelom.

Nadalje, proces izgaranja definira temperaturne profile i temperaturne fluktuacije unutar komore za izgaranje, koje se koriste kao ulazni podaci za izračun prijenosa topline zračenjem [21]. Za modeliranje izgaranja unutar komore motora s unutarnjim izgaranjem, poboljšani koherentni model plamenova (ECFM-3Z) u tri zone pokazao se kao stabilan i dovoljno precizan model [22]. ECFM-3Z model izgaranja pretpostavlja beskonačno tanak i glatki segment turbulentnih plamena za područje svježe smjese [23]. Potrebna turbulentna brzina plamena se računa iz interakcije između kemijske kinetike i parametara turbulencije, gdje je brzina laminarnog plamena izračunata u pred procesiranju za slobodne predmiješane plamenove. Glavna mana takvog pristupa je osjetljivost predmiješanih slobodnih plamena na visokim temperaturama, što često dovodi do divergencije rezultata. Stoga se vrijednosti brzine plamena na visokim temperaturama moraju metodom interpolacije ili korelacijskim funkcijama povezati s postojećim podacima iz stabilnog režima tabeliranja, u potpuno automatiziranoj i stabilno proceduri. Za izračun procesa samozapaljenja mješavine goriva i zraka, automatizirani postupak će izračune vršiti na temelju gradijenata profila brzine laminarnim plamena.

CILJ I HIPOTEZA

Ciljevi ovog rada su:

1. Poboljšati točnost izračuna koeficijenta apsorpcije zračenja unutar metode kontrolnih volumena, koristeći spektralna svojstva čađe i plinovitih medija u odnosu na konvencionalni WSGG pristup, bez značajnog povećanja potrebe za računalnim resursima.
2. Automatizirati proceduru za učinkoviti izračun brzine laminarnog plamena i samozapaljenje smjese goriva i zraka primjenom tabelirane kemijske kinetike, koja će poboljšati proračune procesa izgaranja i stvaranja onečišćujućih tvari u industrijskim sustavima za izgaranje.

Hipoteza ovog istraživanja je da će modeliranje koeficijenta apsorpcije zračenja pomoću spektralnih svojstava plinova i čađe koristeći formulaciju za samo jedan sivi i jedan transparentni plin u kombinaciji s tabeliranom kemijskom kinetikom brzine laminarnog plamena i samozapaljenje smjese goriva i zraka poboljšati točnost izračuna temperaturnih profila i procesa stvaranja onečišćujućih tvari u industrijskim sustavima za izgaranje, bez značajnog povećanja potrebe za računalnim resursima.

ZNANSTVENI DOPRINOS

Rezultati ovog istraživanja su sljedeći:

1. Razvijen i implementiran numerički model za proračun koeficijenta apsorpcije zračenja unutar metode kontrolnih volumena, uzimajući u obzir spektralna svojstva medija pomoću jednog sivog plina i jednog transparentnog plina u medijima koji sudjeluju u prijenosu topline zračenjem;
2. Razvijeni automatizirani postupak za računanje brzine laminarnog plamena i tabeliranog procesa samozapaljenja mješavine zraka i goriva koji koristi metodu interpolacije ili korelacijske funkcije za povezivanje s postojećim podacima iz stabilnog režima;
3. Integrirani pristup za učinkovitiju procjenu stvaranja onečišćujućih tvari u industrijskim višefaznim reaktivnim procesima koristeći razvijene modele zračenja i tabelirane kemijske kinetike.

METODE I POSTUPCI

Prvi dio teze je implementacija modela diskretnih ordinata, u konzervativnom obliku za kontrolne volumene, primjenom korisničkih funkcija u programskom jeziku FORTRAN u kod računalne dinamike fluida AVL FIRE™. Nadalje, implementirani model sadržavat će algoritam za prostornu diskretizaciju s proizvoljnim brojem kutova zenita i azimuta, pri čemu će se svaki definirani prostorni kut pripisati jednoj ordinati, odnosno jednom smjeru. Nakon provođenja prostorne diskretizacije, transportna jednadžba zračenja topline računa se s transportnim jednadžbama za incidentno zračenje u svakoj ordinati, a njegov doprinos dodaje se kao izraz izvora energije u jednadžbi očuvanja energije. Simetrični, periodični i difuzni neprozirni granični uvjeti implementirani su za opisivanje zračenja u svim smjerovima na rubovima

domene. Validacija implementiranog modela provela se na jednostavnim geometrijama za koje su analitička rješenja dostupna u literaturi, poput temperaturnog profila između paralelnih ploča i toplinskog toka kroz bazu cilindra. Nakon postizanja zadovoljavajućeg podudaranja s analitičkim rezultatima, model se nadogradio za paralelan rad na više računalnih jezgri i pokretnim mrežama u svrhu rada na simulacijama motora s unutarnjim izgaranjem.

Drugo, u okviru implementiranog rješavača transportne jednadžbe zračenja, istražili se se i implementirali dodatni modeli koeficijenata apsorpcije. Konvencionalni WSGG model se prvi implementirao u postojeći model diskretnih ordinata uz ažurirane korelacije s polinomima za izračun ponderirane sume sivi plinova. Ovo istraživanje je uključilo i napredne modele apsorpcije topline zračenja u medijima koji sudjeluju u prijenosu topline zračenjem: SLW i SLW-1. SLW model poboljšava konvencionalni model WSGG uzimajući u obzir spektralnu linijsku apsorpciju i emisiju medija, dok je SLW-1 formulacija SLW modela koja koristi samo jedan sivi i jedan transparentni plin te time značajno smanjuje potrebu za računalnim resursima. SLW i SLW-1 modela su implementirani i prilagođeni za paralelan rad na više računalnih jezgri i pokretnim mrežama, kako bi se omogućila verifikacija i validacija modela na eksperimentalnim rezultatima u motoru s unutarnjim izgaranjem. Specifični cilj istraživanja i primarni znanstveni doprinos ove teze je razvoj i implementacija SLW-1 modela za učinkovito predviđanje apsorpcije i emisije zračenja topline plinova i čestica čađe pri visokim temperaturama u kod RDF. Implementirani SLW-1 prvo je validiran na jednostavnim geometrijama za koje postoje analitički rezultati dostupni u literaturi, a potom na plamenicima u kojima je prisutan proces izgaranja. Ovo će se istraživanje dodatno usredotočiti na modeliranje zračenja topline u kombinaciji s postupkom izgaranja u motorima s unutarnjim izgaranjem.

Treće, nakon uspješne implementacije i validacije modela SLW-1, provedeno je istraživanje i procjena utjecaja prijenosa topline zračenjem na proces stvaranja emisija unutar komore za izgaranje. Naglasak je bio na utjecaju zračenja na procesa stvaranja čađe i NOx, gdje je snažniji utjecaj zračenja biti vidljiv u radnim točkama motora s većim sadržajem čestica čađe i udjelom recirkulacije ispušnih plinova. Utjecaj prijenosa topline zračenjem na formiranje emisija čađe i NO_x-a proveden je na primjeru motora s unutarnjim izgaranjem, gdje se ispitao utjecaj faktora emisije površina komore i broj ordinata s ciljem dobivanja analize osjetljivosti numeričkih simulacija.

Četvrti dio donosi implementaciju interakcije između turbulencije i zračenja (TRI) unutar konzervativnog modela diskretnih ordinata. Metoda interakcije između turbulencije i zračenja uzima u obzir srednje fluktuacije temperature koje su rezultat turbulentnog protoka fluida. Kombinacija diskretnih ordinata u konzervativnom obliku za kontrolne volumene, model SLW-1 i TRI predstavljaju vremenski učinkovito rješenje za proračun prijenosa topline zračenjem, koji sadrže detaljnije opisane fizikalne pojave od konvencionalnih modela.

Za modeliranje izgaranja korišten je model izgaranja trodimenzionalni poboljšani koherentni model plamenova (ECFM-3Z), detaljna kemijska kinetika i reducirana kemijska kinetika. ECFM-3Z model se temelji na predtabeliranim podacima laminarne brzine plamena i podacima samozapaljenja mješavine goriva i zraka, za čije generiranje su primijenjene dodatne tehnike tabelacije u ovoj tezi. Nadalje, razvio se novi postupak za automatsku i stabilnu generaciju tablica brzine plamena i vremena samozapaljenja. Novim postupkom povezali su se rezultati neuspješnih kalkulacija predmiješanih plamena, uzrokovani nedostacima kemijskog mehanizma i rješavača brzine plamena, na temelju susjednih točaka temperature, tlaka, ekvivalentnog omjera i omjera recirkulirajućih plinova. Osim toga, razvio se novi način tabelacije rezultata samozapaljenja smjese goriva i zraka u ECFM-3Z modelu. Nakon poboljšanja modela izgaranja, provela se detaljna verifikacija i validacija pristupa u modeliranju izgaranja na motor s unutarnjim izgaranjem.

Razvijeni i implementirani modeli su validirani s dostupnim eksperimentalnim podacima, a simulacije su izračunate i na pojednostavljenim slučajevima i složenim geometrijama za stvarne industrijske primjene. Na kraju, na temelju dobivenih rezultata, predložio se najprikladniji automatiziran pristup za baze podataka izračuna samozapaljenja i laminarne brzine plamena za izračun procesa izgaranja, čađe i formacije dušikovih oksida zajedno sa smjernicama za daljnje korake u istraživanju.

Ciljevi ovog doktorskog rada su obrađivani u šest objavljenih znanstvenih radova i jednom radu u postupku objavljivanja te prikazani rezultati kronološki prate spomenute radove. Kroz objavljene radove je potvrđena postavljena hipoteza te su postignuti prethodno navedeni ciljevi.

LITERATURA

[1] Bohlooli Arkhazloo N, Bouissa Y, Bazdidi-Tehrani F, Jadidi M, Morin J-B, Jahazi M. Experimental and unsteady CFD analyses of the heating process of large size forgings in a gas-fired furnace. Case Studies in Thermal Engineering 2019;14:100428. https://doi.org/10.1016/j.csite.2019.100428.

[2] Modest MF, Haworth DC. Radiative heat transfer in high-pressure combustion systems. SpringerBriefs in Applied Sciences and Technology, Springer Verlag; 2016, p. 137–48. https://doi.org/10.1007/978-3-319-27291-7_7.

[3] Benajes J, Martin J, Garcia A, Villalta D, Warey A, Domenech V, et al. An Investigation of Radiation Heat Transfer in a Light-Duty Diesel Engine. SAE Int J Engines 2015;8. https://doi.org/10.4271/2015-24-2443.

[4] Paul C, Ferreyro Fernandez S, Haworth DC, Roy S, Modest MF. A detailed modeling study of radiative heat transfer in a heavy-duty diesel engine. Combust Flame 2019;200:325–41. https://doi.org/10.1016/j.combustflame.2018.11.032.

[5] Coelho PJ. Advances in the discrete ordinates and finite volume methods for the solution of radiative heat transfer problems in participating media. J Quant Spectrosc Radiat Transf 2014;145:121–46. https://doi.org/10.1016/j.jqsrt.2014.04.021.

[6] Fernandez SF, Paul C, Sircar A, Imren A, Haworth DC, Roy S, et al. Soot and spectral radiation modeling for high-pressure turbulent spray flames. Combust Flame 2018;190:402–15. https://doi.org/10.1016/j.combustflame.2017.12.016.

[7] Skeen S, Manin J, Pickett L, Dalen K, Ivarsson A. Quantitative spatially resolved measurements of total radiation in high-pressure spray flames. SAE Technical Papers 2014;1. https://doi.org/10.4271/2014-01-1252.

[8] Yue Z, Reitz RD. Numerical investigation of radiative heat transfer in internal combustion engines. Appl Energy 2019;235:147–63. https://doi.org/10.1016/j.apenergy.2018.10.098.

[9] Benajes J, Martín J, García A, Villalta D, Warey A. In-cylinder soot radiation heat transfer in direct-injection diesel engines. Energy Convers Manag 2015;106:414–27. https://doi.org/10.1016/j.enconman.2015.09.059.

[10] López JJ, García-Oliver JM, García A, Villalta D. Development of a soot radiation model for diesel flames. Appl Therm Eng 2019. https://doi.org/10.1016/j.applthermaleng.2019.04.120.

[11] Coelho PJ. Radiative Transfer in Combustion Systems. Handbook of Thermal Science and Engineering, Cham: Springer International Publishing; 2018, p. 1173–99. https://doi.org/10.1007/978-3-319-26695-4_61.

[12] Dorigon LJ, Duciak G, Brittes R, Cassol F, Galarça M, França FHR. WSGG correlations based on HITEMP2010 for computation of thermal radiation in non-isothermal, non-homogeneous H_2O/CO_2 mixtures. Int J Heat Mass Transf 2013;64:863–73. https://doi.org/10.1016/j.ijheatmasstransfer.2013.05.010.

[13] Cassol F, Brittes R, Centeno FR, da Silva CV, França FHR. Evaluation of the gray gas model to compute radiative transfer in non-isothermal, non-homogeneous participating medium containing CO_2, H_2O and soot. Journal of the Brazilian Society of Mechanical Sciences and Engineering 2015;37:163–72. https://doi.org/10.1007/s40430-014-0168-5.

[14] Granate P, Coelho PJ, Roger M. Radiative heat transfer in strongly forward scattering media using the discrete ordinates method. J Quant Spectrosc Radiat Transf 2016;172:110–20. https://doi.org/10.1016/j.jqsrt.2015.12.011.

[15] Ozen G, Selçuk N. SLW model for computational fluid dynamics modeling of combustion systems: Implementation and validation. Numerical Heat Transfer, Part B: Fundamentals 2016;70:47–55. https://doi.org/10.1080/10407790.2016.1173499.

[16] Pearson JT, Webb BW, Solovjov VP, Ma J. Efficient representation of the absorption line blackbody distribution function for H_2O, CO_2, and CO at variable temperature, mole fraction, and total pressure. J Quant Spectrosc Radiat Transf 2014;138:82–96. https://doi.org/10.1016/j.jqsrt.2014.01.019.

[17] Garten B, Hunger F, Messig D, Stelzner B, Trimis D, Hasse C. Detailed radiation modeling of a partial-oxidation flame. International Journal of Thermal Sciences 2015;87:68–84. https://doi.org/10.1016/j.ijthermalsci.2014.07.022.

[18] Webb BW, Ma J, Pearson JT, Solovjov VP. SLW modeling of radiation transfer in comprehensive combustion predictions. Combustion Science and Technology 2018;190:1392–408. https://doi.org/10.1080/00102202.2018.1452123.

[19] Solovjov VP, Andre F, Lemonnier D, Webb BW. The Generalized SLW Model. J Phys Conf Ser 2016;676. https://doi.org/10.1088/1742-6596/676/1/012022.

[20] Ozen G, Ates C, Selçuk N, Kulah G. Assessment of SLW-1 model in the presence of gray and non-gray particles. International Journal of Thermal Sciences 2019;136:420–32. https://doi.org/10.1016/j.ijthermalsci.2018.10.038.

[21] Wang Z, Liu H, Reitz RD. Knocking combustion in spark-ignition engines. Prog Energy Combust Sci 2017;61:78–112. https://doi.org/10.1016/j.pecs.2017.03.004.

[22] Bougrine S, Richard S, Michel JB, Veynante D. Simulation of CO and NO emissions in a SI engine using a 0D coherent flame model coupled with a tabulated chemistry approach. Appl Energy 2014;113:1199–215. https://doi.org/10.1016/j.apenergy.2013.08.038.

[23] Sjerić M, Kozarac D, Schuemie H, Tatschl R. A new quasi-dimensional flame tracking combustion model for spark ignition engines. Energy Convers Manag 2018;165:263–75. https://doi.org/10.1016/j.enconman.2018.03.008.

KEYWORDS

Radiative heat transfer

Radiative absorption coefficient

Laminar flame speed

Autoignition

Emission

Internal combustion engine

KLJUČNE RIJEČI

Prijenos topline zračenjem

Koeficijent apsorpcije zračenja

Laminarna brzina plamena

Samozapaljenje

Emisije

Motor s unutarnjim i izgaranjem

LIST OF ABBREVIATIONS

ALBDF   Absorption-line blackbody distribution function

CFD   Computational Fluid Dynamics

CPU   Central Processing Unit

DOM   Discrete Ordinates Method

DTRM   Discrete Transfer Radiative Method

ECFM   Extended Coherent Flame Model

ECFM-3Z   Three-zone Extended Coherent Flame Model

EGR   Exhaust Gas Recirculation

FVM   Finite Volume Method

ICE   Internal Combustion Engines

RANS   Reynolds-averaged Navier–Stokes

RoHR   Rate of Heat Release

RTE   Radiative Transfer Equation

SLW   Spectral Line Weighted-sum-of-gray-gases

SLW-1   Spectral Line Weighted-sum-of-grey-gases consisting of a single gray gas and a transparent window

TDC   Top Dead Centre

TRI   Turbulence Radiation Interaction

WSGG   Weighted-Sum-of-Grey Gases

3D   Three dimensional

NOMENCLATURE

Latin	Description	Unit
a	Weight ratio of grey gas	
A	Surface	m^2
b	Weighted factor	
c	Progress variable	
C_j	Gas absorption cross-section	
C_1	WAVE breakup model constant 1	
C_2	WAVE breakup model constant 2	
C_{rite}	Convergence criteria	
d	Droplet diameter	m
D	Effective diffusion coefficient	$m^2\,s^{-1}$
D_{ci}	Term that describes the orientation between the face wall and the control angle	
$E_{b\eta}$	Planck black body emissive power	W
f	Mixture fraction	
F	Absorption-line blackbody distribution function	
g	Residual gas mass fraction	
G	Incident radiation	$W\,m^{-2}$
h	Enthalpy	$kJ\,kg^{-1}$
H	Total enthalpy interfacial exchange term	$kJ\,kg^{-1}$
I	Intensity of incident radiation	$W\,m^{-3}srad^{-1}$
k	Turbulent kinetic energy	$m^2\,s^{-2}$
m	Mass	kg
$\dot{m}$	Mass flow	$kg\,s^{-1}$
M	Molecular weight	$kg\,kmol^{-1}$
n_r	Refractive index	
n_w	Normal wall vector	
N	Molar density	$mol\,m^{-3}$
N	Integer number	
p	Pressure	Pa
P	Probability density function	

XIX

P$_{1,2,3}$	Flame property	
r	Droplet radius	m
R	Ideal gas constant	J mol^{-1} K^{-1}
q	Heat flux	W m^{-2}
s	Ordinate direction	m
S	Source term	
Sc	Schmidt number	
t	Time	s
T	Temperature	K
u,v	Velocity	m s^{-1}
V	Volume	m^3
W$_k$	Molecular weight of species k	kg kmol^{-1}
x$_i$	Cartesian coordinates	m
y$_i$	Mass fraction of species i	
Z	Mixture fraction	

Greek	Description	Unit
α	Weight factor	
β	ECFM-3Z+ model constant/	
ε	Dissipation rate	m^2 s^{-3}
ε	Emissivity	
ϵ_w	Wall emissivity	
η	Spectral wavenumber	m
ζ	Velocity scale ratio	
Γ	Diffusion coefficient	
κ	Absorption coefficient	m^{-1}
λ_w	Wavelength	m
μ	Dynamic viscosity	Pa s
μ_t	Turbulent viscosity	Pa s
ρ	Density	kg m^{-3}
σ	Stefan-Boltzmann constant	W m^{-2} K^{-4}
σ_s	Scattering cefficient	m^{-1}
Σ	Turbulent flame surface density	m^{-1}

φ	Extensive property of general conservation equation	
Φ	Scattring phase function	
ϕ	Polar angle	rad
χ	Scalar dissipation rate	s^{-3}
τ	Time	s
θ	Azimuthal angle	rad
ω_i	Chemical source of species i	kg m^{-3} s^{-1}
Ω	Wave growth rate	s

LIST OF FIGURES

XXIII

LIST OF TABLES

1 INTRODUCTION

The Introduction section provides the motivation and general overview of the topic for this thesis. This is followed by the literature review, divided into two parts. Firstly, a literature review of radiative heat transfer modelling in computational fluid dynamics (CFD) with an emphasis on absorption coefficient modelling in radiative transfer equation (RTE) is presented. The second part is a literature review of combustion modelling with pre-process generated laminar flame speed and autoignition data bases. In the end, hypotheses and scientific contributions are presented.

1.1   Motivation and general overview

With the current increased fuel prices and disorder with the fuel supply, the focus on the energy transition is even more significant, for which two solutions are imposed: electrification of the transport sector and development of new carbon-neutral fuels. Electrification requires additional investment and mainly aims for passenger transport, while the development of new fuels aims for heavy-duty transport and faster transition due to the possibility of being implemented on the current infrastructure. The carbon neutral fuels are still not thoroughly investigated, and how can their implementation in the existing transportation system be carried out [1].

Nevertheless, the combustion of fossil fuels is still the dominant energy source. As a non-renewable source, fossil fuel combustion directly harms the ecosystem with its products. An approach for solving such a challenge in the current energy transition is increasing energy efficiency and reducing harmful emissions from multiphase reactive systems. Multiphase reactive flow systems, such as gas turbines, jet engines, internal combustion engines (ICEs), industrial furnaces, and boilers, represent a significant source of pollution. Thus, developing and improving multiphase reactive processes to increase energy efficiency and reduce pollutant emissions are objectives that still need to be solved. The most thriving approach for increasing energy efficiency and reducing pollutant emissions of multiphase reactive systems is the simultaneous use of experimental and numerical research. Numerical research of the combustion process gives insight into phenomena such as interactions between fluid motion, heat transfer, turbulence, chemical reactions, and thermodynamics of combustion. Numerical

analysis of CFD is commonly applied for investigating the combustion phenomena of biofuels, carbo-neutral fuels, and pollutant formation processes. CFD is currently the most dominant numerical tool for calculating the integrated influence of all phenomena on the multiphase reactive process.

1.2   Radiative heat transfer

During the combustion process, high temperatures occur, and radiative heat transfer becomes increasingly pronounced. The gaseous phase participates in heat transfer and affects the temperature profiles and, consequently, the emission formation processes inside the combustion chamber. That is why it is not sufficient to exclude the influence of radiative heat transfer on the emission formation process to calculate the emissions concentrations precisely [2]. Gaseous media participate in radiative heat transfer with three mechanisms shown in Figure 1: absorption, emitting, and scattering.
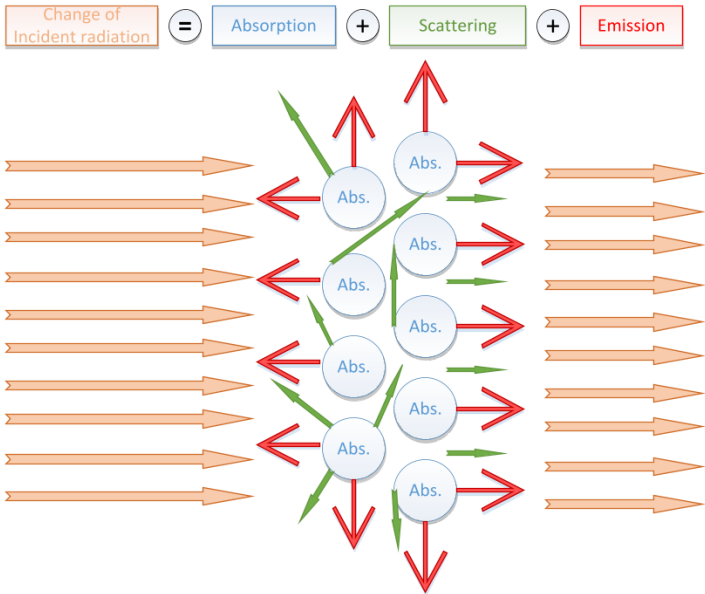
Figure 1   Radiative heat transfer in participating media

If the participation of a medium in the radiative heat transfer is considered, the RTE is required to be solved. Approximation with the numerical models must be employed to resolve such an integrodifferential equation [3]. The radiative heat transfer in the numerical simulations of ICE is commonly not considered due to its small geometries and additional computational complexity [4]. Among the many types of research on the topic of radiative heat transfer in ICE, just a few were carried out by solving the RTE [5]. In the literature, all types of calculations

2

were conducted with a discrete ordinate method (DOM) radiative solver and the wide-band spectral model for calculating the absorption of the gas medium, including soot [6]. The impact of radiative heat transfer and soot and nitrogen oxides (NO_x) formation process was investigated for the first time in the paper [7], where the high values of absorption coefficient inside the combustion chamber of the ICE were achieved due to the high soot concentrations and high-pressure. Although the impact of radiation on the whole heat transfer is small due to their small geometries, the effect on the emission formation processes cannot still be ignored [8]. It was evaluated that the soot process formation depends greater on the radiation heat transfer in ICEs than the NO_x formation process [9]. A numerical investigation of radiative heat transfer in internal combustion engines employing DOM showed that radiation influences soot predictions by as much as 50% [10]. In [11], the authors evaluated that the amount of energy lost to soot radiation varies from 0.5 to 10%. Due to that, the authors of [12] developed a new one-dimensional model for calculating soot and radiation interaction in diesel flames, where the model constants were obtained by validation against experimental data.

Of all the existing models, DOM and finite volume method (FVM), are the most employed in ICE simulations [13]. Additionally, models that feature raytracing, such as the discrete transfer radiation method (DTRM) and Monte Carlo, are adequate for solving RTE since the cylinder motion would require recalculation of raytracing before each time step, which would result in inefficient computational simulation.

The absorptivity and emissivity are modelled with a weighted-sum-of-grey-gases model (WSGG) based on non-isothermal and non-homogeneous correlations for H_2O and CO_2 mixtures [14]. In contrast, the soot absorption coefficient is commonly modelled by the correlation presented in the [15]. The scattering phenomena can be neglected for the ICE simulation since it was neglected in all conducted ICE calculations due to the size of soot particles and grey gas behaviour [16].

Additional accuracy of the radiative heat transfer models can be achieved with the calculation of the absorption coefficient in RTE for non-grey media. If the spectral line characteristics of gasses that participate in radiation are considered, the absorption coefficient is solved by the spectral-line weighted-sum-of-grey-gases model (SLW) [17]. Where the absorption line blackbody distribution function for CO_2 and H_2O is addressed from terms in literature [18]. If SLW model is applied to conventional RTE solvers such as DOM or FVM, the spectral absorption coefficient is approximated with an arbitrary number of grey gases and transparent gas for which additional transport equations must be solved [19]. In [20], the authors compared results with the traditional WSGG model and SLW model for calculation of

combustion flame prediction, where the significant improvement and agreement with experimental data was achieved at the expense of additional computational time, which was around ten times longer with the SLW model. Authors of [21] introduced SLW model formulation using only a single grey gas and one clear gas, which is termed SLW-1 model. Such a model solves the same number of transport equations as a conventional WSGG model and shows better agreement with the validation data due to consideration of spectral line properties of gasses [22]. According to available literature, the SLW-1 model has never been implemented into the CFD code, and the simulations have never been conducted on complex three-dimensional moving mesh with a rezoning procedure, like in ICEs. The results obtained with the SLW-1 model are expected to show better agreement with the experimental data for the insignificant increase in computation demand.

A recent publication [5] stated that considering radiative heat transfer in CFD simulation could improve the temperature field distribution and pollutant formation process inside internal combustion engines. Calculating the radiative transport equation (RTE) gives an additional layer of complexity to the numerical simulations, increasing the accuracy of the calculated temperature and computational demand [23]. As far as the pollutant emissions from ICE are concerned, the two most often observed are nitrogen oxides (NO_x) which are most affected by temperature, and soot, which has the most significant effect on heat transfer by radiation [24].

The influence of radiation on diesel engine combustion was first investigated by [25], where the authors showed that the influence of radiative heat transfer on NO_x and soot emissions is not significant, with about a 3% difference in NO_x. For the soot emission, the different injection pressure was investigated, where an augmented radiative heat transfer was achieved for low-pressure injections and the lower needle lift-offs [26]. For the spray injection under ICE conditions in a pressurized combustion chamber, the carbon dioxide (CO_2) and water (H_2O) vapour have proven to be the primary generator of total radiative absorption and emission of media compared to the soot [27]. On the experimental diesel engine in Sandia Laboratory, the same result was achieved, where the participating media was mainly determined by gaseous radiative, which has overcome radiation from the soot [10]. The influence of differential approximation based on one spherical harmonic (P1) was observed for hydrocarbon air mixtures at elevated pressures [28]. The results showed that diverse ICE operating conditions modelled with grey gas absorption models achieved decreased accuracy with around 60% overestimation. The influence of the NO_x and soot formation inside large geometry marine engines was investigated detailly employing the DOM and P1 radiative transfer solver [29].

4

Except for increasing the accuracy of the simulation by applying high-order schemes [30], additional accuracy for the ICE conditions can be achieved with the absorption coefficient model. DOM with the weighted sum of grey gas (WSGG) model was applied to an industrial engine in the work of Mukut and Roy [31]. They achieved around 20% lower NO_x emissions and increased soot emissions compared to the simulation without considering radiation. An increased accuracy was obtained at the expense of an additional computational time of around 50%. WSGG, in combination with other RTE solvers in the CFD framework, also showed a reasonable correlation with the benchmark cases, where an insignificant increase in NO_x concentrations is achieved, while for the soot concentrations, the considerably larger size of soot particles is achieved [32]. A more detailed absorption coefficient model, the spectral line weighted-sum-of-grey-gas model (SLW), which divides RTE into the spectrum intervals described with the arbitrary number of grey gases, was applied on ICE for a one-cylinder engine [33]. SLW model scheme is shown in Figure 2. From the spectral line properties of participating gas, the gas absorption cross section is reconstructed with different an arbitrary number of grey gases [34]. The absorption-line blackbody distribution function (ALBDF) is then used to determine the grey gas weights based on the limits of the absorption cross-sections.
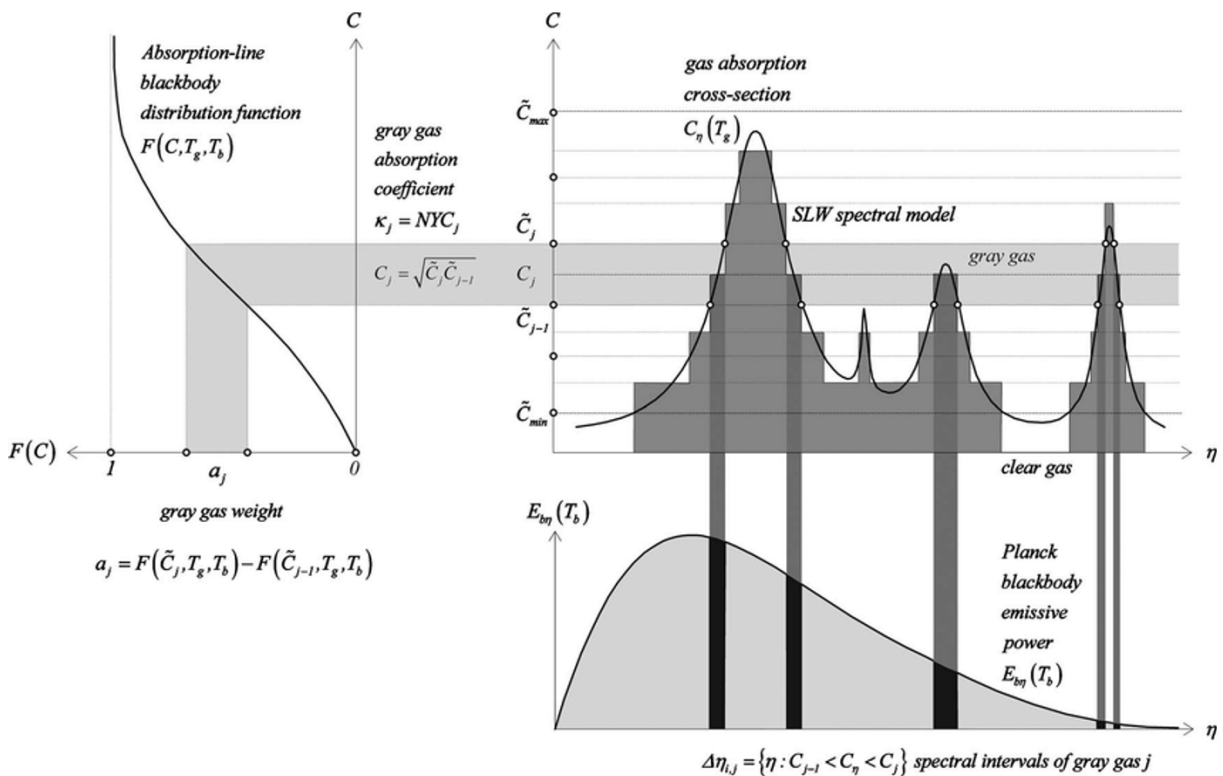
Figure 2   Spectral Line Weighted-sum-of-grey-gases (SLW) [34]

SLW model is widely applicable to high-temperature regions of combustion systems, such as rocket exhaust [35]. The authors showed around 6% of the total heat loss was generated from H_2O and CO_2 gasses, with approximately twice an increase in the computational duration. SLW model is already well known to be implemented for different industrial applications such as for fluidized med combustors [36] and industrial glass furnaces [37].

A simplified version of SLW model, which accounts for spectral line properties for a single grey gas and transparent gas, was developed by [38] and is called SLW-1. In SLW-1, the same number of transport equations as a conventional WSGG model achieves better agreement with the validation data due to consideration of spectral line properties of gasses [39]. In Figure 3, SLW-1 model scheme is shown. Like SLW model, ALBDF is used for calculating grey gas weight, which is now defined with a single grey gas. SLW-1 model achieves lower accuracy than SLW model due to the integration of the absorption cross-section curve, which is described with a single grey gas that is represented with grey rectangles under the curve.
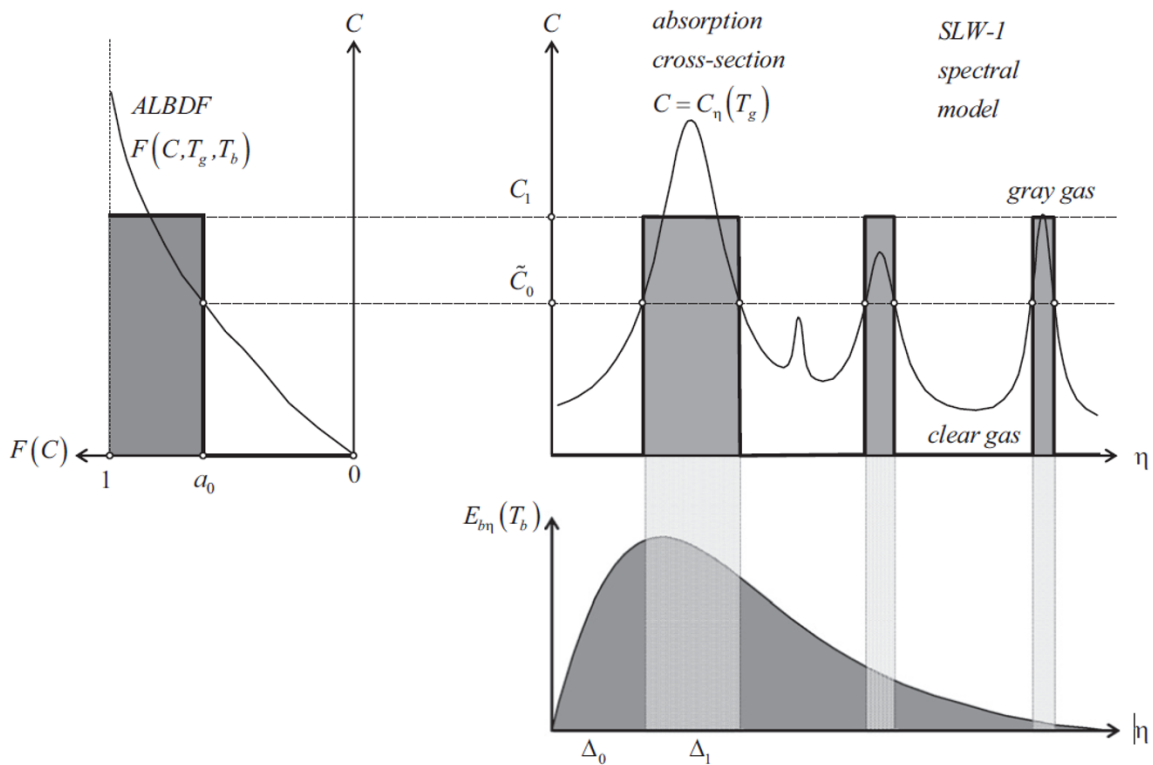
Figure 3   Spectral Line Weighted-sum-of-grey-gases minimal formulation consisting of a single grey gas and a clear one [38]

SLW and SLW-1 models employ rectangular integration over wavelengths, while absorption line black body distribution is commonly applied for the cumulative spectral properties of H_2O and CO_2 mixtures[40]. For the three-dimensional (3D) case that features combustion in a

fluidized bed, SLW-1 model was applied for absorption coefficient calculation and compared with the grey gas approximation [22]. Although SLW-1 model performed an increased accuracy in combination with lower computational demand, its inaccuracy is shown in the presence of non-grey particles. The first 3D implementation of SLW-1 for non-grey gas surrounded by non-grey walls was performed by [41]. The authors showed that the computational demand is lower by around 20 times than with SLW model while achieving accuracy for a different type of participating media.

Additional improvement of RTE in CFD simulations is possible by including turbulence-radiation interaction (TRI), which is especially important in the case of Reynolds-averaged Navier–Stokes (RANS) equations. The TRI arises from the non-linearity of temperature fluctuations that influence the overall radiation intensity fluctuations [42]. In most radiative models, TRI is not considered, and the average quantities are used for the calculation of the RTE, which in the case of intensive turbulent combustion, can lead to an error in the range of 10% to 100% [43]. TRI influence on pollutant formation was investigated by [44], which proved that for diesel spray conditions, TRI influences radiative heat transfer for around 10% of net radiative heat transfer. For the increased pressure values, such as in ICE, the results of considering TRI showed decreased influence [5].

According to available literature, the SLW-1 featuring TRI model has never been implemented in the CFD. Additionally, in recent publications, the radiative heat transfer models still lack validation on the complex 3D moving mesh with rezoning procedures, such as in ICE. The results of such validation could give insight into additional phenomena and increase the accuracy of CFD simulations for an insignificant increase in calculation time.

1.3   Laminar flame speed and Autoignition calculation

In order to apply radiative heat transfer calculations for ICE, the combustion modelling inside the ICE chamber is of great importance. Currently, compression ignition engines represent the majority of truck engines, heavy-duty and marine engines, which are producers of a significant amount of harmful pollutants [45]. The more stringent regulations that enforce the reduction of pollutant emissions led to an extensive study of the combustion characteristics in internal combustion engines [46]. However, the numerical modelling of combustion systems is also challenging since the interaction of the fluid flow, turbulence, heat transfer, and chemical

7

reactions need to be solved simultaneously [47]. That is applicable not only to internal combustion engines but also to combustion systems such as jet engines [48].

Potential for emission reduction is observed in controlling fuel injection influence on combustion characteristics with the application of the injection system and rail pressure [49]. In [50], the author experimentally and numerically studied the multiple-injection strategy on the emission formation and combustion processes at underload conditions, where the rate of heat release (RoHR) results show a good agreement with the multiple injection strategies. The pre-injection timing in such multiple injection strategies can dominantly influence the combustion and emission characteristics, from which the NO_x are influenced the most, owing to the different temperature changes over time [51]. Another parameter that has the potential for lowering the emission is the piston bowl design, which can be easily assessed with the employment of the CFD simulations [52,53].

In order to accurately describe a combustion process, specific mechanisms for each fuel are necessary [1]. With the development of numerous new alternative fuels, new mechanisms are required in order to describe their combustion process numerically [54]. Such modern fuels are commonly biodiesel fuels made from vegetable oils [55], animal oil [56] or waste [57]. The number of chemical species and elementary reactions included in the detailed chemical mechanisms is generally quite large [58]. As an illustration, a detailed reaction mechanism of diesel fuel can consist of 2900 chemical species and 15000 elementary reactions [59]. Such large mechanisms require significant computational resources for the simulation of industrial combustion systems to calculate all interactions between elementary reactions that govern the combustion process [60]. This computational demand arises from the number of transport equations that need to be solved for each chemical species and the number of mesh elements [61].

One way to reduce the required number of equations that have to be solved is assuming that the chemical time and length scale in most flames are small-scale [62]. Chemical reduction techniques and laminar flamelet models represent two main approaches based on modelling the detailed dynamics and structure of chemically reacting flow [63]. Laminar flamelet methods assume that the flame structures are considerably thinner compared to other scales of the distortions in the flow [64]. Furthermore, this implies that the chemical reactions are faster than all other time scales [65]. All flamelet models assume that the chemical reaction occurs within relatively thin layers that separate the fresh unburned gas from the full bunt gas. The internal structure of the flame is approximately frozen while it moves around in the flow. The dynamic of the thin flame front is predicted by computing a kinematic equation for the propagation of

the flame front, a mixture fraction equation for the mixing, and a CFD solver for the fluid flow [66]. One of the several laminar flamelet models, which has proven an ability to accurately describe the combustion process in internal combustion engines, is the extended coherent flame model (ECFM) developed by Colin et al. [67]. The ECFM belongs to the flame surface density type of approach, which was first proposed in the context of diffusion flames in the work of Marble and Broadwell [68]. More recently, this approach has been extended by considering a generalised flame surface density, including all possible values of the mixture fraction. In contrast, a library of transient diffusion flames provides reaction rates per unit of flame surface[69]. Based on the ECFM model, the unified diesel/petrol three-zones extended coherent flame model (ECFM-3Z) was briefly presented in [70]. In the ECFM-3Z, the description of unburned/burned gas is inherited from ECFM. The model is based on the flame surface density equation and can be employed to describe premixed and diffusion flames. In order to account for diffusion flame and mixing processes, each computational cell is split into three mixing zones: unmixed fuel zone, unmixed air plus possible residual gases (EGR) zone, and completely mixed fuel-air mixture zone. This model is formulated and later validated by various researchers for partially-premixed and highly stratified combustion cases, such as gasoline direct injection [71] and combustion cases with a high amount of exhaust gas recirculation [72].

The tabulation of chemistry properties for determining flamelet speed, autoignition, and enthalpy sources has recently attracted the attention of the combustion scientific society to the significantly reduced computational time during simulation processing and retention of all the effects of detailed chemistry [73]. Figure 4 shows the main challenge for determining the required laminar flame speed data in ICE simulations. Black dots are temperature-pressure traces during ICE operating cycle, which exceed experimentally available measure data (green dots). An additional complication is that for each new fuel, it is necessary to obtain the value of the laminar flame speed.
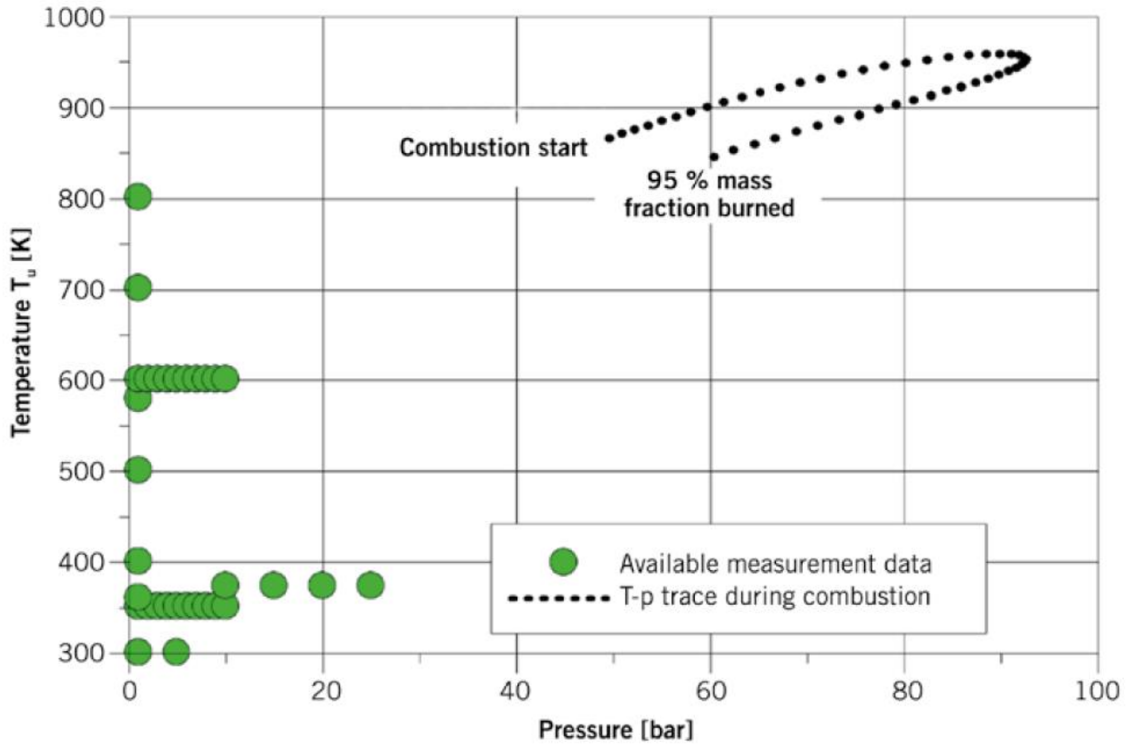
Figure 4   Laminar flame speed measurement data against the temperature-pressure operating points in ICE [74]

An approach for calculating the combustion process based on large eddy simulations and an exponential equation for turbulent flame speed was developed by [75]. In their work, the tabulation of Cantera premixed reactors for laminar flame speed was tuned with additional constants in the exponential equation to obtain turbulent flame speed. The flamelet-generated manifold approach for tabulating all general gas phase chemistry in lookup tables is commonly applied to solve the combustion process [76]. Source terms are obtained from lookup tables based on transport values such as progress variable, mixture fraction, temperature, and pressure during the combustion process. Such models require long-term preprocessing that is specific to each operating case. The combustion process inside combustion chambers dictates the temperature profiles and fluctuations inside the combustion chamber, which are used as input for the calculation of the radiative heat transfer [77].

For the combustion modelling inside the ICE chamber, three-zone enhanced coherent flame model (ECFM-3Z) model has proved to be a robust and sufficiently precise model [78]. The ECFM-3Z combustion model features an infinitely thin and smooth flame segment that entrains the fresh mixture by the turbulent flame speed [79].

10

The ECFM-3Z is a precise flame model that uses case-independent databases pre-tabulated for arbitrary fuel [80]. The required turbulent flame speed is calculated from an interaction between laminar chemical kinetics and turbulence parameters, where the laminar flame speed is calculated as a database in preprocessing on premixed freely propagating flame reactors [81]. The main disadvantage of such an approach is the sensitivity of the premixed freely propagating flame reactors at high-temperature conditions, which often leads to unsuccessful calculations [82]. Therefore, the laminar flame speed values at high temperatures must be extrapolated from successful reactors to have a fast, fully automated, and reliable procedure. For the tabulation of laminar flame speed and autoignition for the ECFM-3Z model, the method developed by Colin et al. [83] was used in the thesis. Figure 5 shows three zones of ECFM-3Z model, which are shown in the mixture fraction and progress variable direction.
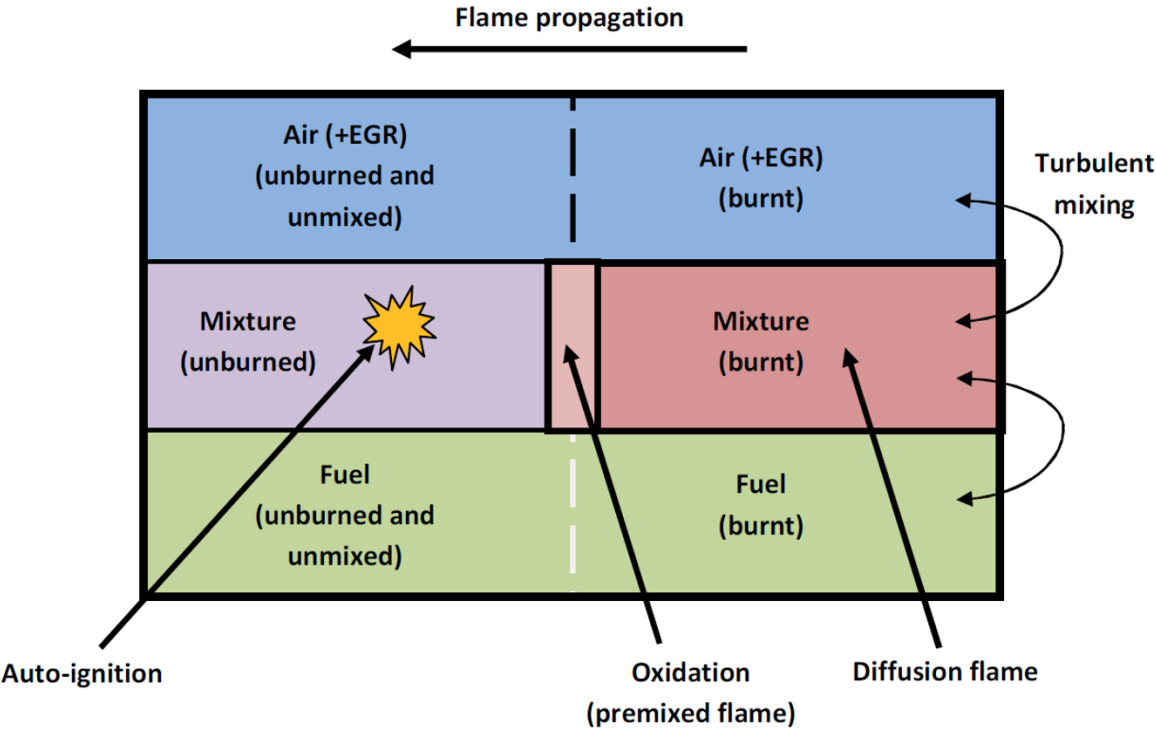
Figure 5   Scheme of cell division in three zones of Extended coherent flame model [68]

The required turbulent flame speed is calculated from an interaction between laminar chemical kinetics and turbulence parameters, where the laminar flame speed is calculated as a database in pre-processing on premixed freely propagating flame reactors. The main disadvantage of such an approach is the sensitivity of the premixed freely propagating flame reactors at high-temperature conditions, which often leads to unsuccessful calculations. Therefore, the laminar flame speed values at high temperatures need to be extrapolated or interpolated from successful reactors in order to have a fast, fully automated, and reliable

procedure. An automated procedure for calculating ignition time can be developed from profiles of laminar flame velocity.

Van Oijen and de Goey introduced a reduction method that can be interpreted as combining the flamelet and the manifold approaches, namely the flamelet-generated manifold (FGM) technique [84]. An overview of the general FGM technique can be found in [85]. Successful application of the FGM combustion model, used in this PAPER 4, for diesel engine was reported in [86]. A correct prediction of the combustion process in a diesel engine case using FGM as well as the emission processes based on a large number of chemical reactions, is presented in the work of Priesching et al.[87]. Figure 6 shows chemical species lookup tables generated for different temperatures, progress variables and mixture fraction values.
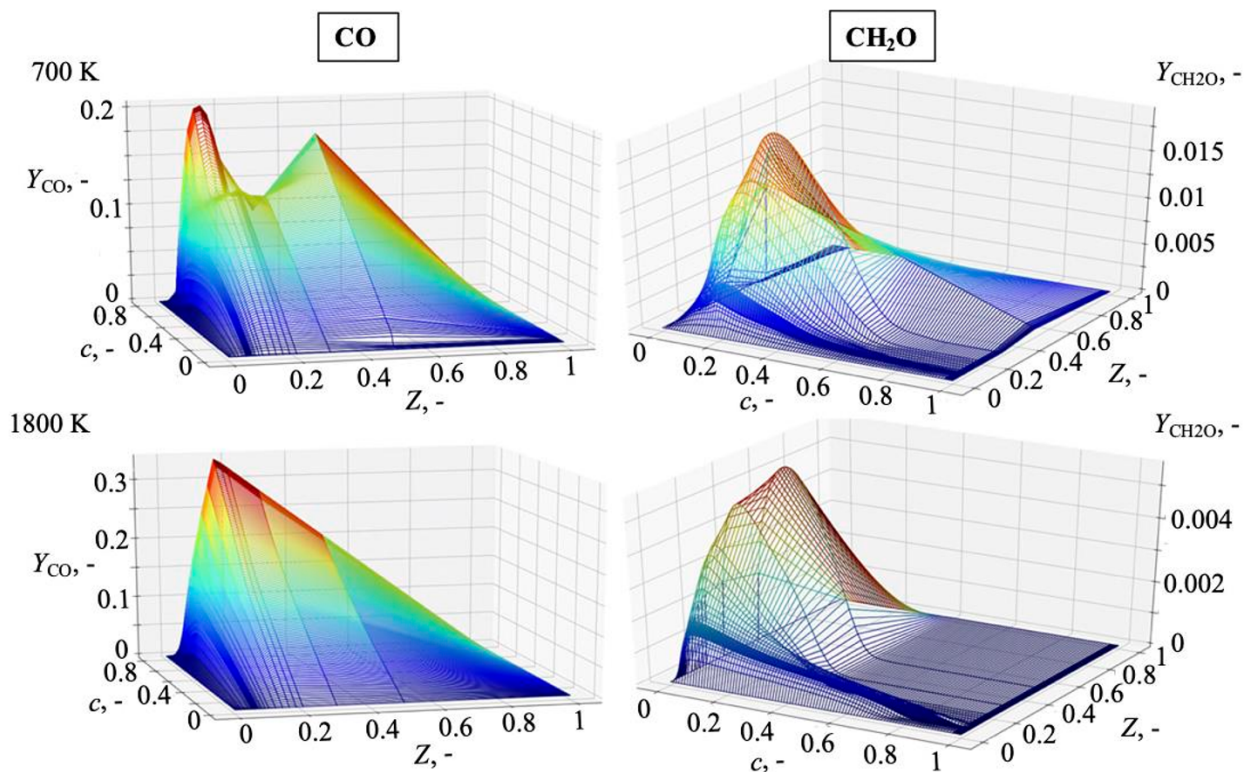
Figure 6   Visualisation of generated chemistry look-up data at temperatures 700 K and 1800 K for progress variable and mixture fraction values

The chemical kinetics is often too computationally demanding for numerical simulations, leading to the frequent use of combustion models, such as coherent flame models [68]. In coherent flame models, ignition delay and laminar flame velocities for different operating conditions must be precalculated in the form of a database or correlation formula [88]. The standard correlations for new biofuels and e-fuels are not accurate enough to validate their combustion process, primarily the low-temperature auto-ignition phenomenon [89]. In [90], the

correlation functions between autoignition timing and flame speed propagation were developed based on the temperature gradients measured from the rapid compression.

Correlation functions for the autoignition of biodiesel fuels that feature ignition of fuel-air mixtures at high temperatures, and their validation with the chemistry kinetic mechanisms were presented by the authors in [91], where significant agreement between the previously published mechanism was achieved. The dependency of autoignition timing and pollutant emissions results was demonstrated in [92], where the convenient diesel fuels with some percentages of biodiesel were observed at high-temperature conditions. The investigation results are that the rise in the ambient temperature lowers the ignition delay for all diesel fuel, which was expected. Recent publications have also investigated the investigation of biodiesel fuels produced by different sources [93]. For example, the autoignition delay of microalgae biodiesel blends was investigated numerically to determine combustion efficiency and pollutant emissions [94]. Additionally, an experimental autoignition investigation of biodiesel produced from the plant oil and its impact on the combustion process inside a compression ignition engine was observed [95]. The results showed that the biodiesel blend at 20% of the content exhibited better combustion performance and emission characteristics than other blend proportions.

In [96], the authors performed an experimental optical study of biodiesel ignition delay, where the correlation between autoignition timing and combustion process was demonstrated. The authors examined a similar approach for determining the influence of pollutant concentrations of nitrogen oxides and carbon monoxide on autoignition timing under different exhaust gas recirculation (EGR) mass fractions [97], where diesel fuel with a small share of biodiesel was used. A numerical method named spherically expanded flames was used for the internal combustion engine operating conditions to determine the autoignition and laminar flame speed propagation for a different share of e-fuel (dimethyl-ether), air, and helium [98]. The simulation results adequately captured the physics of unsteady flame propagation, autoignition, and the controlling reactions, but not at the early ignition stages.

Lately, the penetration of machine learning techniques has accelerated enormously in all science areas, so in this area too. Rahnama et al. [99] proposed the machine learning neural network for fuel consumption reduction in internal combustion engines, where the start of injection and its influence on autoignition timing was observed. Deep neural networks for internal combustion engines were also employed to determine emissions from the biodiesel combustion process [100]. In [101], the authors published the results of dual-fuel autoignition, which were predicted by the machine learning technique. The sensitivity analysis showed that the fuel ratio between the primary and secondary fuels has the most significant effect on dual-

fuel ignition. Furthermore, an exciting approach, similar to the developed procedure in this thesis, was published by the authors of [102], where the calculation of the autoignition and laminar flame speed was modelled by ignition to propagation reduced scheme, which was upgraded to additionally calculate the autoignition timing. Another approach that aims to obtain laminar flame speed with general formula is presented in [103]. The authors introduced a term that depends on polynomial, exponential factors, with an additional constant defined from the precomputed database. Additionally, the same procedure was applied for obtaining ethanol/gasoline blend databases, where high accuracy in correlation is achieved [104]. Other researchers tend to determine laminar flame speed correlations for a single fuel. In [105], the authors proposed correlation functions for surrogate gasoline fuels as an exponential function in temperature and pressure direction. An exceptional scientific contribution was conducted to developing correlation functions of hydrogen fuel for spark ignition operating conditions [106]. Furthermore, additional research has been undertaken to develop correlation functions capable of describing hydrogen mixture with gasoline [107] and methanol [108] for combustion inside spark-ignition engines.

The tabulation procedure is developed and implemented into CFD software based on the lognormal distribution for laminar flame speed in equivalence ratio direction and exponential functions for pressure, temperature, and exhaust gas recirculation directions. Three parameters are used to determine the dependence of the laminar flame speed or autoignition results on pressure and equivalence ratio directions. Additionally, the method is also applicable to dual-fuel combustion. The ignition delay and laminar flame speed values of fuel blends are described with the additional parameter of the fuel composition.

1.4 Objective and hypotheses of the research

The objectives of this thesis are:

1. Improved accuracy of radiative absorption coefficient calculations in the finite volume method procedure using the spectral-line formulation of soot and gaseous media to enhance calculations compared to the conventional WSGG, but also reduce the computational demand compared to full-spectrum models.
2. Automated procedure for efficient computational assessment of laminar flame speed and autoignition employing tabulated chemistry kinetics that will enhance calculations of the combustion process and pollutant formation in industrial combustion systems.

3. The research hypothesis is that modelling of radiative absorption coefficient considering the spectral-line formulation using only a single grey gas and one transparent gas in combination with tabulated chemical kinetics of laminar flame speed, and autoignition will improve the accuracy of calculated temperature profiles and pollutant formation processes in industrial combustion systems, for not a significant increase in computational demand.

1.5 Scientific contribution

The scientific contribution of this research is:

1. An implemented numerical model for the finite volume method calculation of the radiative absorption coefficient considering the spectral-line formulation using only a single grey gas and one transparent gas in radiative heat transfer participating media;
2. A newly developed automated procedure for computation of the laminar flame velocities and autoignition databases employing the interpolation procedures or correlation functions for linking the existing data from a stable tabulation regime;
3. An integrated simulation approach for more efficient estimation of pollutant formation in industrial multiphase reactive applications employing the developed radiation models and tabulation of chemical kinetics.

2 A BRIEF OVERVIEW OF METHODS

2.1 Radiative heat transfer modelling

The radiation in participating media is modelled by implementing RTE solvers: FVM and DOM. Radiative heat transfer consists of three phenomena: absorption, emission and scattering. Figure 1 shows the scheme of the radiation heat balance, where the media absorb the incoming radiation through participating media, enhanced by the emission of the media and scattered in different directions. Such phenomena are specified by the RTE, which in its full form can be written as:

$$\frac{1}{c_{sl}}\frac{dI_\eta(\vec{r},\vec{s})}{dt} + \frac{dI_\eta(\vec{r},\vec{s})}{ds} =$$

$$= \kappa_\eta(\vec{r})I_b(\vec{r}) - \left(\kappa_\eta + \sigma_s\right)(\vec{r})I_\eta(\vec{r},\vec{s}) + \frac{\sigma_s(\vec{r})}{4\pi}\int_{4\pi} I_\eta(\vec{r},\vec{s}')\Phi(\vec{r},\vec{s},\vec{s}')d\Omega'$$

(1)

The speed of light c_{sl} is so large compared to local time and length scales that the transient term in the equation can be neglected for the vast majority of engineering applications [109]. The following expression is obtained when DOM model assumptions are applied to Equation (1) for the calculation intensity of radiation in an ordinate direction s_l:

$$\frac{\partial I_l}{\partial s_l} = -(\kappa + \sigma_s)I_l + \kappa\left(n_r{}^2\frac{\sigma T^4}{\pi}\right) + \frac{\sigma_s}{4\pi}\sum_{l=1}^{N_{ord}} I_l w_l \Phi^l$$

(2)

If FVM is applied on Equation (1), the following expression for the spatial angle discretisation:

$$\frac{\partial I_l}{\partial s_l} = -(\kappa + \sigma_s)I_l + \kappa\left(n_r{}^2\frac{\sigma T^4}{\pi}\right) + \frac{\sigma_s}{4\pi}\sum_{l=1}^{N_\Omega} I_l \Phi_l \Delta\Omega_l$$

(3)

In Equation (2) and (3) I_l in the is the radiative intensity in the l direction, κ is the absorption coefficient, σ_s is scattering coefficient, n_r is refractive index, Φ is scattering phase function. In DOM, w_l is the quadrature weight of the ordinate l. In FVM, s_l is a normal vector of control angle with its spatial angle $\Delta\Omega_l$, and N_Ω is the total number of control angles. Although, DOM and FVM are very similar methods, due to the disadvantages of DOM in the conservation of radiative energy, the following work will be focus on developing models in the FVM framework. The spatial angle discretisation is shown in Figure 7, where the control angle normal s^l is oriented perpendicular to its spatial angle.
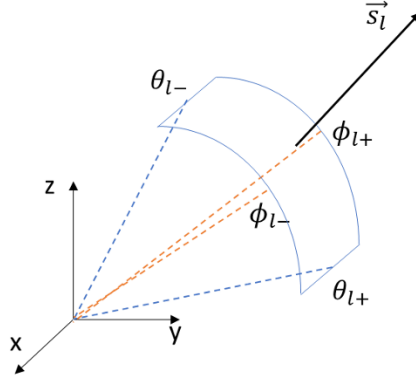
Figure 7   Spatial angle discretisation

Equation (3) has to be solved for each discretised spatial angle [109]. When the intensity of incident radiation in each control angle is obtained, the incident radiation is calculated as:

$$G = \sum_{l=1}^{N_\Omega} I_l \, \Delta\Omega_l \tag{4}$$

where n is the total number of control angles (spatial angle discretisation). The interaction between the radiation heat transfer and the energy conservation equation for each cell in the computational domain is then modelled as the radiative heat source term in the energy conservation equation. The radiative source term is defined as:

$$S_{rad} = \kappa(G - 4\sigma T^4) \tag{5}$$

which then is considered as an input in the source term of the energy conservation equation. If Equation (9) is applied to the computational domain with three-dimensional discretised cells, the following equation is obtained:

$$\sum_{i=1}^{N_{\Delta A_i}} \Delta A_i I_l \int_0^{\Delta\Omega_l} \left(s_{l,i}\, n_{\mathrm{w}i}\right) d\Omega_l =$$
$$= \left[-(\kappa + \sigma_\mathrm{s})I_l + \kappa\left(\frac{\sigma T^4}{\pi}\right) + \frac{\sigma_\mathrm{s}}{4\pi} \sum_{l=1}^{N_\Omega} I_l \Phi_l \Delta\Omega_l \right] \Delta\Omega_l \Delta V \tag{6}$$

The term on the left-hand side in Equation (6) presents the divergence of the radiation intensity, which can be affected by the three above-mentioned phenomena. Equation (6) is calculated iteratively during the fluid flow iterations together with the fluid flow calculation. The

17

symmetry and diffusive opaque boundary conditions are implemented in FVM for the description of radiation intensity at the domain boundaries. The boundary condition for the diffusive walls is calculated only for the directions that are oriented into the computational domain and are calculated as [110]:

$$I_{l,\text{w}} = \epsilon_\text{w} \frac{n_r{}^2 \sigma T^4}{\pi} + \frac{1 - \epsilon_\text{w}}{\pi} \sum_{\substack{(n_\text{w} s_l) < 0}}^{N_\Omega} I_l \, |n_\text{w} s_l| \, \Delta\Omega_l \tag{7}$$

where ϵ_w is the wall emissivity, and n_r is a refractive index which is for all surfaces in this thesis assumed one. The intensity of radiation for diffusive walls consists of the emission and reflection term. Diffusive reflection is assumed for the wall boundary conditions, where the radiation intensity from the wall is of the same value in all control angles that are oriented into a domain.

The implemented algorithm for calculating spatial angle boundaries and directions is based on the upwind differencing scheme, and it is shown in Figure 3. Figure 3 shows how the intensities of incident radiation propagate in the computational domain with the global coordinate system.
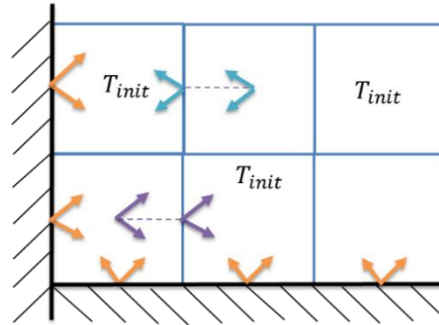
Figure 8   Algorithm for calculation of incident radiation.

Convergence criterium, C$_{\text{rite}}$ of Equation (11) is modelled with the following equation:

$$\frac{I_{\text{new}}^l - I_{\text{old}}^l}{I_{\text{new}}^l} < C_{\text{rite}} \tag{8}$$

2.1.1   Weighted-sum-of-grey-gas model

The absorption coefficient in this thesis is modelled by implemented WSGG for grey gases, which is based on the CO_2 and H_2O correlations in the literature [14]. The correlations in [13] model the soot absorption coefficient, added to the gas absorption coefficient based on the

superposition rule of RTE. The following equation, where the calculate the total absorption coefficient κ_s presents the soot absorption coefficient:

$$\kappa = -\frac{\ln(1-\varepsilon)}{s} + \kappa_s \qquad (9)$$

The s in Equation (16) presents the thickness of absorption media, which is calculated by the following equation:

$$s = 3.6\frac{\Delta V}{A_{\text{tot}}} \qquad (10)$$

where ΔV presents the cell volume and A_{tot} is the sum of all cell's faces. Emissivity ε in Equation (17) is calculated with the following equation of WSGG:

$$\varepsilon = \sum_{i=0}^{2} \alpha_i\left(1 - e^{-a_i ps}\right) \qquad (11)$$

where α_i is the weight factor for the ith grey gas and is dependent only on temperature. The absorption coefficient a_i the ith grey gas is determined by partial pressure p of the water vapour and carbon dioxide, which absorbs the incident radiation. For $i = 0$ the gas absorption coefficient has a value α_o to resolve transparent windows in the spectrum between spectral regions of high absorption. For the transparent windows, the weight factor is calculated as:

$$\alpha_o = 1 - \sum_{i=0}^{2} \alpha_i \qquad (12)$$

The other weighting factors are given by a polynomial of third order in the following form, where $b_{i,j}$ is the polynomial coefficient:

$$\alpha_i = \sum_{j=0}^{3} b_{i,j}\, T^j \qquad (13)$$

The soot absorption coefficient κ_s is considered to be independent of the wavenumber and can be determined by an emission-based average along the spectrum [111]:

$$\kappa_s = b f_v(c_0 + c_1 T + c_2 T) \qquad (14)$$

In the previous equation, f_v is the dimensionless volumetric fraction of the soot agglomerate, and b is a dimensionless constant that depends on the fuel. In this work, b was 4.1 for methane combustion and 6.3 for diesel combustion based on research by [111]. In the brackets is a polynomial approximation based on the constant coefficient published by [111].

2.1.2 SLW model

For the calculations with the SLW model, several grey gases are utilized as the replacement for non-grey gas, where each contribution is symbolized with the supplemental absorption cross-section $\overline{C}_{abs,j}$ and correlate the weight of grey gas a_j. The absorption cross-section ranges between $3 \cdot 10^{-5}$ and 60 m²mol⁻¹ for water vapour, while for CO_2, the range is between $3 \cdot 10^{-5}$ and 120 m²mol⁻¹ [112]. These limits of the absorption cross-sections, $C_{\min}$ and $C_{\max}$ are used for the calculation of a supplemental absorption cross-section $\overline{C}_{abs,j}$ of each grey gas:

$$\overline{C}_{abs,j} = C_{\min} \left(\frac{C_{\max}}{C_{\min}} \right)^{\frac{j}{J}} \tag{15}$$

The absorption cross-section domain is divided into intervals equally spaced on a logarithmic scale, and the range between two consecutive supplemental absorption cross-sections, $\overline{C}_{abs,j}$ and $\overline{C}_{abs,j+1}$, treated as an independent grey gas, whose absorption cross-section $C_{abs,j}$, is defined as follows:

$$C_{abs,j} = \sqrt{\overline{C}_{abs,j}\, \overline{C}_{abs,j+1}} \tag{16}$$

The grey gas weights, a_j can be obtained from the absorption-line blackbody distribution functions F, which are determined by the high-resolution HITEMP2010 database that accounts for the radiative participation of CO_2 and H_2O [113]. The distribution function F is defined as:

$$F(C_{abs,j}) = \frac{\pi}{\sigma T^4} \int\limits_{\{\eta: C_{\eta,j} < C_{abs,j}\}} I_{b\eta}(T)\,d\eta \tag{17}$$

where the integral is calculated over the spectral wavenumber η. The weight of the jth grey gas can be calculated as the difference distribution function F at the supplemental cross-section interval limits:

$$a_j = F(\overline{C}_{abs,j+1}) - F(\overline{C}_{abs,j}) \tag{18}$$

The combined absorption coefficient of CO_2 and H_2O, $\kappa_{CO2+H2O}$ is defined as the sum of the contributions of the two species [19]:

$$\kappa_{CO2+H2O} = N_{H_2O}\, C_{abs,k,CO_2} + N_{H_2O}\, C_{abs,k,CO_2} \tag{19}$$

where N is the molar density of the gas, which is determined from the local cell temperature and the species mass fraction. In this thesis, twenty grey gases were used to compute non-gey radiative properties used in the SLW model. The soot absorption coefficient is calculated from Equation (14).

20

2.1.3 SLW-1 model

In this thesis, the SLW-1 model is implemented by means of user function routines in the AVL FIREm™ CFD software. The results were compared with the grey gas WSGG and SLW models that were previously implemented in AVL FIREm™ CFD software [33,114]. WSGG coefficients are based on HITEMP2010 correlations by Dorigon et al. (2013), and SLW model spectroscopic properties are calculated by HITEMP2010 correlation for absorption line blackbody distribution function (ALBDF) [113]. The SLW-1 model is a simplified formulation of the SLW model, where only one grey gas and a transparent window are considered. When the SLW-1 model is applied to the RTE, the two following equations are obtained, where the first one is for the transparent window, and the second one is for the single participating grey gas [38]:

$$\frac{d\bar{I}_{l,0}}{ds_l} = 0 \tag{20}$$

$$\frac{d\bar{I}_{l,1}}{ds_l} = \overline{a_1 \kappa_1 I_b} - \overline{\kappa_1}\bar{I}_{l,1} \tag{21}$$

The parameters of the clear gas in SLW-1 are determined as follows:

$$a_0 = 1 - a_1 \tag{22}$$

$$\kappa_0 = 0 \tag{23}$$

The parameters of the single participating grey gas a_1 and κ_1 are unknown. To solve them, firstly, the double integration procedure from SLW model also is employed for SLW-1 model and is applied to CO_2 and H_2O mixture as a single gas with the following equations for two emissivities in the arbitrary band of the spectrum.

$$\varepsilon_{mix,j,L_2} = \sum_{i=0}^{N_{CO2}} \sum_{j=0}^{N_{H2O}} a_{w,i} a_{c,j} \left(1 - e^{-N(Y_w C_{w,i} + Y_c C_{c,j})L_1}\right) \tag{24}$$

$$\varepsilon_{mix,j,L_1} = \sum_{i=0}^{N_{CO2}} \sum_{j=0}^{N_{H2O}} a_{w,i} a_{c,j} \left(1 - e^{-N(Y_w C_{w,i} + Y_c C_{c,j})L_2}\right) \tag{25}$$

Where grey gas weights $a_{w,i}$ and $a_{c,j}$ are calculated using ALBDF:

$$a_{w,i} = F_w\left(\widetilde{C}_l, T_g, Y_w\right) - F_w\left(\widetilde{C}_l, T_g, Y_w\right) \tag{26}$$

$$a_{c,j} = F_c\left(\widetilde{C}_j, T_g, Y_c\right) - F_w\left(\widetilde{C}_j, T_g, Y_c\right) \tag{27}$$

Solovjov et al., (2011a) proposed several implementation methods for single-participating grey gas a_1 and κ_1 with the uncertainty analysis, from which $\varepsilon_1 - \varepsilon_2$ method is applied in this thesis,

which fits the total emissivity calculated for two different pathlengths L_1, and L_2. Total emissivities are calculated by SLW model.

$$\varepsilon_{mix,1} = a_1(1 - e^{-\kappa_1 L_1}) \tag{28}$$

$$\varepsilon_{mix,2} = a_1(1 - e^{-\kappa_1 L_2}) \tag{29}$$

From algebraic Equations (28) and (29), a_1 and κ_1 are obtained for $L_1 = 2L_2$. Furthermore, the clear gas spectral parameter a_0 is obtained from Equation (22), and the cross section C₀ is obtained from ALBDF multiplication approach of the mixture by bisection approach:

$$a_0 = F_{mix}(C_0, T, Y_c, Y_w) \tag{30}$$

Finally, the reference grey gas absorption cross-section is calculated from the following term:

$$C_1 = \frac{\kappa_1}{N} \tag{31}$$

The in-cell grey gas absorption coefficient is then defined as:

$$\kappa_{loc} = \kappa_1 + \kappa_s \tag{32}$$

where κ_s is grey gas absorption soot coefficient. The soot absorption coefficient was calculated from Equation (14).

2.1.4   Turbulence radiation interaction

In this thesis, FVM radiative transport model is used for the solution of RTE, where only absorption and emission are considered. For the control angle discretization, polar and azimuthal discretization of the spherical coordinate system was used to divide RTE in the transport equation for each control angle [116]. When TRI is applied to RTE with optically thin fluctuation approximation the transport equation has the following form:

$$\frac{d\bar{I}_{l,j}}{ds_l} = \overline{a_j \kappa_j I_b} - \bar{\kappa}_j \bar{I}_{l,j} \tag{33}$$

where $\bar{I}_{l,j}$ is mean radiation intensity of control angle l and grey gas j. s_l is control angle normal vector, κ_j is absorption coefficient, a_j is the weighted ratio of grey gas, and I_b is radiation intensity of the black body. The transient term of radiation intensity is neglected due to the instantaneous propagation of radiation, which results in several order lower magnitude. The transient term in RTE is neglected since the scale of radiation intensity change with time is negligible. The mean absorption coefficient is calculated based on the PDF in NO turbulence fluctuation model:

$$\overline{\kappa_j} = \int_0^1 \kappa_j(T) \, P(T) dT \tag{34}$$

The emission term in Equation (33) is calculated as well from the PDF:

$$\overline{a_j \kappa_j I_b} = \int_0^1 a_j(T) \kappa_j(T) I_b(T) \, P(T) dT \tag{35}$$

The wall boundary conditions of radiation intensity is defined for grey non-transparent walls:

$$\bar{I}_{\mathrm{w},l,j} = \epsilon_{\mathrm{w}} a_j \frac{\sigma T_{\mathrm{w}}{}^4}{\pi} + (1 - \epsilon_{\mathrm{w}}) \frac{\sum_{(s_l \cdot n_{\mathrm{w}}) > 0} I_{l,j} \, |n_{\mathrm{w}i} D_{ci}|}{\sum_{(s_l \cdot n_{\mathrm{w}}) < 0} n_{\mathrm{w}i} D_{ci}} \tag{36}$$

Where ϵ_{w} is wall emissivity, n_{w} is the normal vector of a boundary face, D_{ci} is auxiliary term that calculates the orientation between the face wall and the control angle. Additionally, for ICE cases where the only slice of the cylinder includes the volume of spray region from a single nozzle hole, a new periodic inlet/outlet boundary condition is required to be implemented. The first thing to set periodic boundary conditions is to have mirrored boundary faces with the same distribution, number, and mutual position of boundary faces, which is called boundary connection. Figure 9 shows how the boundary connection was implemented for defining incident radiation values at boundary faces. All values that were oriented outside of the one boundary connection face are set as the wall values on the other boundary connection face with the orientation toward the domain. From Figure 9, it is shown, that the incident radiation with a green vector on the left-hand side of the domain is translated to its opposite direction $\bar{I}_{\mathrm{w},l}{}''(x_i'')$ as purple vector on the right hand side, while the orange components of incident radiation are preserved. Additionally, Equation (37) describes the procedure, where $''$ in $\bar{I}_{\mathrm{w},l}{}''(x_i'')$ denotes boundary connection wall values.
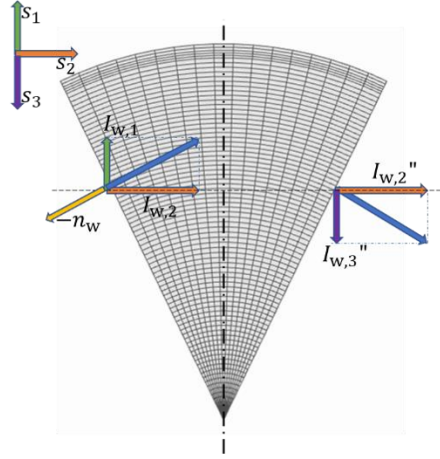
Figure 9   Boundary connection for periodic inlet/outlet boundary condition

$$\bar{I}_{\mathrm{w},l}(x_i) = \begin{cases} \bar{I}_{\mathrm{w},l}''(x_i'') & (s_l \cdot n_{\mathrm{w}}) \geq 0 \\ \bar{I}_{\mathrm{w},l}(x_i) & (s_l \cdot n_{\mathrm{w}}) < 0 \end{cases} \tag{37}$$

The radiative intensity is computed from the summation of the number of gases and the number of control volumes:

$$G = \sum_{l=1}^{N_\Omega} \left[\left(\sum_{j=0}^{N_g} I_{l,j} \right) \cdot \Delta\Omega_l \right] \tag{38}$$

The total enthalpy radiation source term is defined as the sum of grey gas contributions in the radiative participating media, calculated by the following equation [117]:

$$\nabla q = \sum_{j=0}^{N_g} \left(4\pi \overline{a_j \kappa_j I_b} - \bar{\kappa}_j \sum_{l=1}^{N_\Omega} \overline{I_{l,j}} \Delta\Omega_l \right) \tag{39}$$

2.2   Combustion modelling

The flamelet model ECFM-3Z was employed for combustion process modelling inside ICE, which has decoupled treatment of chemistry and turbulence. ECFM-3Z is based on an equation for flame surface density that incorporates the impact of turbulent eddies on the wrinkling of the flame front surface. In the ECFM-3Z model, all computational cells are split into three regions to describe non-premixed combustion: unmixed fuel zone, mixed zone, and unmixed initial air zone [118]. The overall state influences each zone within the computational cell. If the fuel is introduced into the system and observed in a representative computational cell, initially only consisting of unburned and unmixed air, the fuel occupies a finite amount of

24

cell space after evaporation. During this stage, it remains unmixed with the existing air, thereby creating two zones (unmixed and unburned air and unmixed and unburned fuel). Subsequently, the fuel and air begin to mix within the intermediate zone, giving rise to the third zone, which is mixed and unburned. At this point, the mixed zone is prepared for monitoring the ignition criterion. Once the ignition criterion is met, combustion initiates and propagates through the mixed zone, dividing it into two sub-zones: the burnt and unburned mixed zone. The representation of gas state determines the fundamental transport equations in the ECFM3Z model through two properties: progress variable c and the mixture fraction Z. Additionally, transport equations for the following species are also solved [83]: oxygen (O_2), nitrogen (N_2), nitrogen monoxide (NO), CO_2, carbon monoxide (CO), hydrogen (H_2), H_2O, hydrogen (H) and nitrogen (N) cation, oxygen (O), hydroxide (OH) anions.

$$\frac{\partial \bar{\rho}\tilde{Y}_X}{\partial t} + \frac{\partial \bar{\rho}\tilde{u}_i\tilde{Y}_X}{\partial x_i} = \frac{\partial}{\partial x_i}\left(\left(\frac{\mu}{Sc} + \frac{\mu_t}{Sc_t}\right)\frac{\partial \tilde{Y}_X}{\partial x_i}\right) + \bar{\rho}\tilde{S}_X \tag{40}$$

t is the time variable, x_i is the space coordinate, μ is dynamic viscosity. Sc is Schmidt number, and t index indicates turbulent values. The turbulent Schmidt number is defined similarly, incorporating both the turbulent momentum transfer (eddy viscosity) and the turbulent mass transfer. $\tilde{S}_X$ is the mass-specified source term of chemical species X and $\tilde{Y}_X$ is its average mass fraction, which is defined as:

$$\tilde{Y}_X = \frac{\overline{m_x}}{\bar{m}} \tag{41}$$

where $\overline{m_x}$ is the average mass of species X, and $\bar{m}$ is the total mass inside a cell. The previously defined general transport equation is divided to account for the burned and unburned subzones of the computational cell when considering the fuel species.

$$\frac{\partial \bar{\rho}\tilde{Y}_{uF}}{\partial t} + \frac{\partial \bar{\rho}\tilde{u}_i\tilde{Y}_{uF}}{\partial x_i} = \frac{\partial}{\partial x_i}\left(\left(\frac{\mu}{Sc} + \frac{\mu_t}{Sc_t}\right)\frac{\partial \tilde{Y}_{uF}}{\partial x_i}\right) + \bar{\rho}\tilde{S}_F\, c + \overline{\dot{\omega}_{uF}} - \overline{\dot{\omega}_{u\to b}} \tag{42}$$

$$\frac{\partial \bar{\rho}\tilde{Y}_{bF}}{\partial t} + \frac{\partial \bar{\rho}\tilde{u}_i\tilde{Y}_{bF}}{\partial x_i} = \frac{\partial}{\partial x_i}\left(\left(\frac{\mu}{Sc} + \frac{\mu_t}{Sc_t}\right)\frac{\partial \tilde{Y}_{bF}}{\partial x_i}\right) + \bar{\rho}\tilde{S}_F\, (1-c) + \overline{\dot{\omega}_{bF}} + \overline{\dot{\omega}_{u\to b}} \tag{43}$$

This partition of the fuel species into the unburned $\tilde{Y}_{uF}$, and burned $\tilde{Y}_{bF}$ is necessary to enable the influence of both propagating and diffusion flames. The rate of gaseous fuel production, resulting from phenomena such as the evaporation of liquid fuel droplets, is represented by the symbol $\tilde{S}_F$. This production rate is distributed between the burned and

unburned sub-zones based on the progress variable $\tilde{c}$. The progress variable is calculated based on the assumption that the flame is an interface of infinitesimal thickness that separates the fresh gases from the burned gases and is given in Equation (44), where $\overline{\tilde{Y}_{\text{TuF}}}$ is the fuel mass fraction before the start of the combustion.

$$c = 1 - \frac{\overline{\tilde{Y}_{\text{uF}}}}{\tilde{Y}_{\text{TuF}}} \tag{44}$$

The reaction rate at which the unburned fuel is consumed in propagating flame is represented by the variable $\overline{\dot{\omega}_{\text{uF}}}$, and the rate on the opposite side represents the burned fuel oxidation in diffusive flame. The rates of fuel consumption are influenced by the local flame surface density and laminar flame velocity, and their calculations are outlined in the following section. In situations where the local equivalence ratio is rich, the unburned sub-zone lacks sufficient oxygen to completely consume all the unburned fuel. As a result, a portion of the unburned fuel represented with the term $\overline{\dot{\omega}_{\text{u} \rightarrow \text{b}}}$ is transferred into the burned sub-zone through the source term. $\overline{\dot{\omega}_{\text{u} \rightarrow \text{b}}}$ is the source term due to the mixing process, which is defined as the turbulent properties and partial fuel density.

$$\overline{\dot{\omega}_{\text{u} \rightarrow \text{b}}} = \frac{\varepsilon}{k} \frac{\tilde{Y}_{Fu}}{\rho_{Fu}} \left(1 - \tilde{Y}_{Fu} \right) \tag{45}$$

where k is turbulent kinetic energy and ε is the rate of turbulent energy dissipation from the turbulence model. Through the mixing turbulent time scale, turbulence interacts with the development of the combustion process.

In ECFM-3Z, the fuel combustion rate per unit volume is defined as the product of flame surface density and the local fluid velocity of the fuel/oxidizer mixture. The transport equation of flame surface density, Σ is defined as [119]:

$$\frac{\partial \Sigma}{\partial t} + \frac{\partial \tilde{u}_i \Sigma}{\partial x_i} = \frac{\partial}{\partial x_i} \left(\frac{1}{\bar{\rho}} \left(\frac{\mu}{Sc} + \frac{\mu_t}{Sc_t} \right) \frac{\partial \Sigma}{\partial x_i} \right) + (P_1 + P_2 + P_3) \Sigma - D \tag{46}$$

In the above equation, besides already defined convection, diffusion and unsteady terms, on the right side of the equation, the following source terms are introduced.

$$P_1 = 1.6 \, K_t \tag{47}$$

This property is flame surface production by turbulent stretch being net flame stretched, K_t. The second of the sink terms represents the flame surface production by mean flow dilatation and is modelled as:

$$P_2 = \frac{2}{3}\frac{\partial \tilde{u}_i}{\partial x_i} \tag{48}$$

The last term in the section appearing next to the flame surface density, P₃ describes the effects of the flame expansion and curvature in the following manner:

$$P_3 = \frac{2}{3}S_{\mathrm{L}}\frac{1-c}{c}\Sigma \tag{49}$$

The sink term in the equation is the destruction term due to fresh gas consumption defined by the equation:

$$D = S_{\mathrm{L}}\frac{\Sigma^2}{1-c} \tag{50}$$

where $\tilde{S}_{mix}$ is the source term due to the mixing process, which is defined as the turbulent properties and partial fuel density.

$$\tilde{S}_{mix} = -\frac{\varepsilon_t}{k_t}\frac{\tilde{Y}_{Fu}}{\rho_{Fu}}\left(1 - \tilde{Y}_{Fu}\right) \tag{51}$$

where k is turbulent kinetic energy, and ε is the rate of turbulent energy dissipation from the turbulence model. Through the mixing turbulent time scale, turbulence interacts with the development of the combustion process.

$$\overline{\dot{\omega}_{\mathrm{uF}}} = \bar{\rho}\tilde{Y}_{\mathrm{uF}}\Sigma S_L \tag{52}$$

Within the ECFM-3Z combustion model, a straightforward methodology for ignition tracking is employed, drawing inspiration from the approach commonly utilized for predicting knocking in gasoline engines. This involves introducing a tracking intermediate species, denoted as I, which is entirely hypothetical and solely serves to determine the initiation time of ignition accurately. Initially, it was utilised exclusively to track the primary ignition. However, as da Cruz (2004) suggested, this principle can also be extended to account for low-temperature ignition, thereby incorporating the simulation of cool flame phenomena [120]. In the combustion model, the intermediate species undergo temporal evolution based on the following equation [121]:

$$\frac{\partial \bar{\rho}\tilde{Y}_I}{\partial t} = \tilde{Y}_F \frac{\sqrt{\tau_d{}^2 + 4(1-\tau_d)\dfrac{\tilde{Y}_I}{\tilde{Y}_F}}}{\tau_d} \tag{53}$$

2.2.1 Laminar flame speed database

For the definition of the correlation function of the laminar flame speed points, firstly, the calculation on chemistry solvers was performed. The chemistry solver calculations were defined with the four-dimensional grid: temperature, pressure, equivalence ratio, and EGR. The calculations were performed on premixed freely propagating reactors, where each combination of four previously mentioned parameters was calculated as a separated reactor. The raw calculated data were sorted in the five-dimensional matrix on which the correlation function is performed. Figure 10 shows the procedure of the developed method for generating a laminar flame speed database for the coherent flame models.
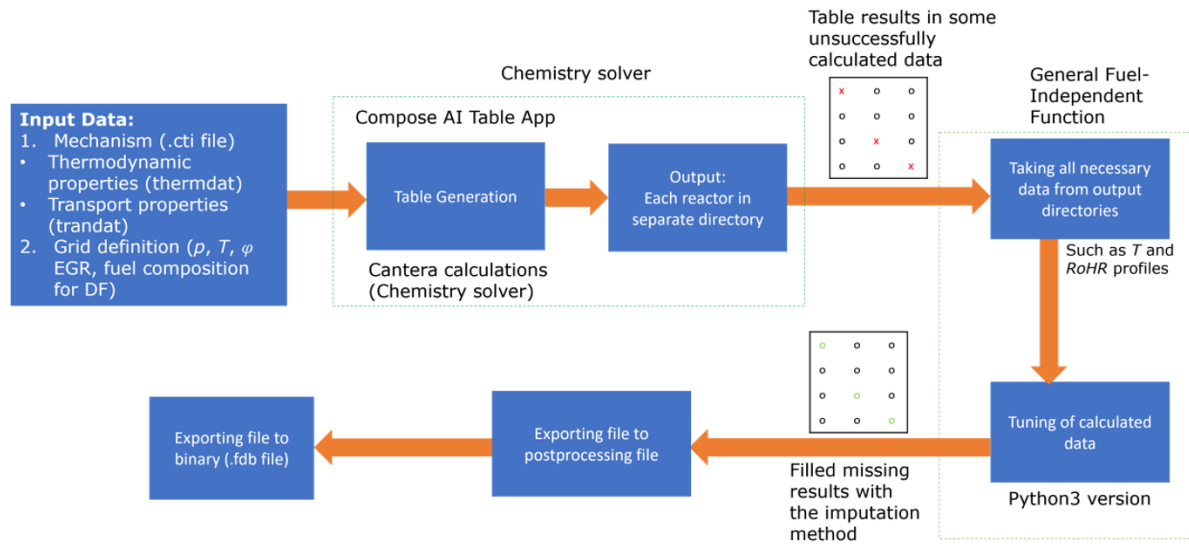
Figure 10   Flowchart of the developed procedure for generation of laminar flame speed and autoignition databases

The correlation function was tuned for calculated data, which was defined as the lognormal distribution for equivalence ratio (φ) and as the exponential function for the pressure (p) direction. The tuning equation has the following form:

$$S_{\mathrm{L}}(p,\varphi) = S_{\mathrm{L,ref}} \left[\frac{1}{\varphi \sigma \sqrt{2\pi}} \exp\left(-\frac{(\ln\varphi - \mu)^2}{2\sigma^2} \right) \right] \left(\frac{p}{p_{ref}} \right)^{\beta} \qquad (54)$$

where μ and σ are two tuning parameters that are calculated for each combination of the temperature and EGR. The nonlinear least-squares method was employed with the Levenberg-Marquardt algorithm for the calculation of μ and σ parameters that have the lowest disagreement with the raw computed data. p_{ref} is reference pressure of 0.1 MPa, while $S_{L,ref}$ is referent laminar

flame speed at the selected calculated point, which was in this case, at equivalence ratio 1, and pressure 0.1 MPa. The algorithm was based on SciPy open-source package and its function scipy.optimize.least_squares that accounts for the optimized parameters of the general function for each temperature point. In order to obtain the optimized parameters, the objective function is defined as:

$$f_{S_{\mathrm{L}}} = \min \sum_{i=1}^{N_{p,\varphi}} \left[S_{\mathrm{L}i} - S_{\mathrm{L}}(p_i, \varphi_i) \right]^2 \tag{55}$$

where $S_{\mathrm{L}i}$ is the calculated laminar flame speed from the chemistry solver, and $N_{p,\varphi}$ is the number of points used for obtaining the formula of laminar flame speed. The objective function is approximated by the linearization in each iteration step. The φ is changed with the estimation $\varphi + \delta$, and to determine δ the following term has to be calculated:

$$f_{S_{\mathrm{L}}} \approx S_{\mathrm{L}}(p_i, \varphi_i + \delta) + \frac{\partial S_{\mathrm{L}}(p_i, \varphi_i)}{\partial \varphi} \delta \tag{56}$$

2.2.2 Autoignition timing database

For the definition of the correlation function of the autoignition points, firstly, the calculation on chemistry solvers was performed. The chemistry solver calculations were also defined with the four-dimensional grid, where the parameters were temperature, pressure, equivalence ratio, and EGR, the same as in the laminar flame speed calculations. The calculations were performed on nondimensional, perfectly stirred reactors, where each combination of the four previously mentioned parameters was calculated as a separated reactor. The raw calculated data were sorted in the eight-dimensional matrix, where the four additional output parameters were autoignition timing, cold flame autoignition timing, released heat, and heat released by cold flame. The procedure of the developed method for generating the autoignition (τ) database is similar to the laminar flame speed database for the coherent flame models.

$$\tau(p, \varphi) = \tau_{\mathrm{ref}} \left(\frac{p}{p_{\mathrm{ref}}} \right)^{\alpha} (\varphi)^{\beta} \tag{57}$$

where α and β are two tuning parameters calculated for each combination of the temperature and EGR. The nonlinear least-squares method was employed with the Levenberg-Marquardt algorithm for the calculation of α and β parameters that have the lowest disagreement with the raw calculated data. The objective function is defined as

$$f_\tau = \min \sum_{i=1}^{N_{p,\varphi}} [\tau_i - \tau(p_i, \varphi_i)]^2 \tag{58}$$

Where the objective function is approximated by the linearization in each iteration step. The φ is changed with the estimation $\varphi + \delta$, and to determine δ the following term has to be calculated:

$$f_\tau \approx \tau(p_i, \varphi_i + \delta) + \frac{\partial \tau(p_i, \varphi_i)}{\partial \varphi} \delta \tag{59}$$

As in the case of the laminar flame speed algorithm was set to bisquare robust regression.

2.3 Spray modelling

CFD simulations were performed by using the Euler Lagrangian (EL) modelling approach, considering processes such as fuel atomization, droplet evaporation, and vapour combustion [122]. The definition of the EL spray approach is that the two-phase flow is described for a gas phase and a liquid fuel in a different manner. The gas phase is treated as a continuum, while the liquid fuel is treated as discrete parcels. The continuum assumption is based on the conservation equations for the finite control volume approach, where the fluid flow is divided into a selected number of control volumes [123]. The discrete parcels are tracked through the flow field by using the Lagrangian mechanics. In this research, authors considered only the drag force occurring due to the high relative velocities between the interacting phases. The parcel trajectories are described as:

$$F_{Di} = m_p \frac{du_{pi}}{dt} \tag{60}$$

where the drag force, F_{Di}, is calculated by employing the Schiller-Neumann drag law [124]:

$$0.5\pi \, r^2 \rho C_D u_i{}^2 = m_p \frac{du_{pi}}{dt} \tag{61}$$

where the drag coefficient C_D is calculated from Schiller Neuman correlation formulation for a single sphere, based on Reynolds number (Re):

$$C_D = \begin{cases} \dfrac{24}{ReC_p}(1 + 0.15Re^{0.687}) & Re < 10^3 \\[4mm] \dfrac{0.44}{C_p} & Re \geq 10^3 \end{cases} \tag{62}$$

Reynolds number is defined as the combination of inertial forces for injected fuel parcels and viscous forces for the fluid viscosity.

$$Re = \frac{|\overline{u_p}|D_p}{v_g}$$

(63)

Cunningham correction factor C_p is based on Knudsen number [125]:

$$C_\mathrm{p} = 1 + Kn\left(2.492 + 0.84e^{\frac{-1.74}{Kn}}\right)$$

(64)

Knudsen number was defined as the ratio between the free path length of the gas phase and parcel diameter Dp.

$$Kn = \frac{1}{D_\mathrm{p}} \frac{k_b T_\mathrm{g}}{d_\mathrm{g}\sqrt{2}\,\pi p_\mathrm{g}}$$

(65)

Where the mean molecule diameter in the gas phase, d_g=2.8·10^{-10} m. WAVE break-up model was employed for the growth of an initial perturbation on a liquid surface, where the radius reduction ratio of the parcels is defined as [126]:

$$\frac{dr}{dt} = -\frac{\Lambda\Omega(r - C_1 * \Lambda)}{3.726C_2 r}$$

(66)

The constant C2 is used for tuning the break-up time equation to account for injector geometry. The droplet radius of parcels is defined with C_1 constant and the highest wave wavelength value on the surface of the parcel, where Λ is the wavelength, and Ω is the growth rate of a wave, which depends on the fluid properties in the cell. The size of droplet diameters ranges from 0.005 to 0.1 mm, and the radius of disintegrated droplets in each subsequent step is defined from C1 constant that was set to model a default value of 0.61 [127]. Different Weber number correlations were used for the droplet interaction with the wall based on the work of Jiro et al. (1994).

Abramzon model was employed for spray droplet evaporation, which accounts for transient heat and mass transfer of spherical droplets [129]. In addition to the presence of liquid ligaments and the break-up of droplets, the evaporation process occurs simultaneously in the spray region. It occurs as a result of the reduction in droplet diameters as they travel through the surrounding gas due to evaporation. This approach is based on the classical film theory, where the resistances to heat and mass transfer are represented by fictitious gas films of constant thickness, denoted as δ_T and δ_m. However, in the case of evaporating droplets, these film thickness values need to

be adjusted using correction factors F_T and F_M. The evaporation of droplets is described by empirical Nusselt and Sherwood laws, which are derived from experiments conducted on single droplets under specific conditions. In Equation (67), the evaporation rate of droplets is defined [130].

$$\dot{m} = \pi \overline{\rho_g} D_d Sh \ln(1 + B_M) \tag{67}$$

$$\dot{m} = \pi \frac{\overline{k_g}}{\overline{c_{pF}}} D_d Nu \cdot \ln(1 + B_T) \tag{68}$$

where D_d is the droplet diameter, and $\overline{\rho_g}$, is average density, $\overline{\beta_g}$ is binary diffusion coefficient, and $\overline{k_g}$ is thermal conductivity of the gas mixture at reference conditions, $\overline{c_{pF}}$ is the average specific heat capacity of the vapour. The dimensionless quantity Nusselt and Sherwood numbers are calculated from unidimensional number non-evaporating droplet Sh_0 and Nu_0, and the corresponding correction factors for the film thickness F_M and F_T.

$$Sh = 2 + \frac{Sh_0 - 2}{F_M} \tag{69}$$

$$Sh_0 = 2 + 0.552 \, Re^{\frac{1}{2}} \, Sc^{\frac{1}{3}} \tag{70}$$

$$Nu = 2 + \frac{Nu_0 - 2}{F_T} \tag{71}$$

$$Nu_0 = 2 + 0.552 \, Re^{\frac{1}{2}} \, Pr^{\frac{1}{3}} \tag{72}$$

The mass and heat transfer numbers, B_M and B_T are then derived from the following equation.

$$B_M = \frac{Y_{Fs} - Y_{\infty}}{1 - Y_{Fs}} \tag{73}$$

$$B_T = \frac{\overline{c_{pF}}(T_{\infty} - T_s)}{L(T_s) + \frac{Q_L}{\dot{m}}} \tag{74}$$

In Equations (73) and (74), Y_{Fs} represents the fuel mass fraction, and $L(T_s)$ represents the latent heat of vaporization at temperature T_s. The subscript s indicates the condition at the surface of the droplet, while the subscript ∞ represents the ambient condition. Q_L is the heat transferred to the droplet, and $\dot{m}$ is vaporisation rate.

2.4 NO$_x$ formation modelling

In general, the most significant NO source in ICE is thermal NO, while prompt NO and fuel NO are almost negligible. One of the most widely used models to describe NO formation at high temperatures is the extended Zeldovich mechanism:

$$N_2 + O \overset{k_1}{\leftrightarrow} N + NO \tag{75}$$

$$N + O_2 \overset{k_2}{\leftrightarrow} O + NO \tag{76}$$

$$N + OH \overset{k_3}{\leftrightarrow} H + NO \tag{77}$$

where k_1, k_2, k_3 are forward and backward reaction rates. For the extended Zeldovich mechanism, the additional impact of O2 and N$_2$ in the presence of hydrogen radicals is considered. It is worth noting that all three reactions exhibit a strong temperature dependency, where the change of NO concentration over time is given by:

$$\frac{dc_{NO}}{dt} = k_{1f}c_O c_{N_2} + k_{2f}c_N c_{O_2} + k_{3f}c_N c_{OH} - k_{1b}c_{NO}c_N - k_{2b}c_{NO}c_O \tag{78}$$
$$- k_{3b}c_{NO}c_H$$

where c denotes the concentration of indexed chemical species, while b and f denote backward and forward reactions.

2.4.1 Temperature fluctuation model

Combustion processes commonly occur in turbulent environments, necessitating special considerations for predicting NO (nitric oxide) concentrations. Significant discrepancies can arise in NO profiles when using mean values of temperature and density compared to incorporating the fluctuating values of these properties caused by turbulence. Therefore, it is crucial to account for the effects of turbulent fluctuations on the NO formation process. To address this, a presumed Probability Density Function (PDF) approach is employed to consider the impact of turbulent fluctuations on the kinetic rates of NO. The NO rate is integrated with respect to the fluctuation temperature like:

$$\bar{S}_{Y_{NO}} = \int_0^1 P(T)S_{Y_{NO}}(T)\, dT \tag{79}$$

where P(T) is PDF of the normalized temperature $\bar{T}$, and $S_{Y_{NO}}$ is instantaneous NO source. The PDF is assumed to be a second-moment beta function and is defined as:

33

$$P(T) = \frac{1}{B(\alpha,\beta)} T^{\alpha-1}(1-T)^{\beta-1} \tag{80}$$

$$B(\alpha,\beta) = \frac{\Gamma(\alpha)\Gamma(\beta)}{\Gamma(\alpha+\beta)} \tag{81}$$

where Γ is gamma function and α and β are parameters that depend on the mean temperature $\bar{T}$ value and its variance $\overline{T'^2}$.

$$\alpha = \frac{1}{B(\alpha,\beta)} T^{\alpha-1}(1-T)^{\beta-1} \tag{82}$$

$$B(\alpha,\beta) = \frac{\Gamma(\alpha)\Gamma(\beta)}{\Gamma(\alpha+\beta)} \tag{83}$$

$$\alpha = \bar{T}\left(\frac{\bar{T}(1-\bar{T})}{\overline{T'^2}} - 1\right) \tag{84}$$

$$\beta = (1-\bar{T})\left(\frac{\bar{T}(1-\bar{T})}{\overline{T'^2}} - 1\right) \tag{85}$$

The lower limit of $\overline{T'^2}$ is 0.002. The transport equation of the temperature variance is solved inside the ECFM-3Z model, and is given in Equation (86).

$$\frac{\partial \rho \overline{T'^2}}{\partial t} + \frac{\partial \rho u_i \overline{T'^2}}{\partial x_i} = \frac{\partial}{\partial x_i}\left(\frac{\mu_t}{\sigma_t}\frac{\partial \rho \overline{T'^2}}{\partial t}\right) + C_g \mu_t \left(\frac{\partial \bar{T}}{\partial x_i}\right) - C_d \frac{\varepsilon}{k}\rho \overline{T'^2} \tag{86}$$

σ_t, C_g and C_d are constants having the values 0.85, 2.86 and 2.0, respectively.

2.5   Soot formation modelling

The soot is modelled based on a detailed soot formation kinetic scheme [131], where the reduced kinetic soot formation model incorporates seven gas phase reactions in the combustion model, with only one additional species for the soot [132]. The used reduced mechanism is described with the following chemical reactions:
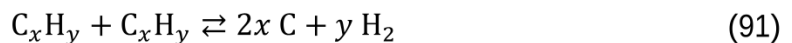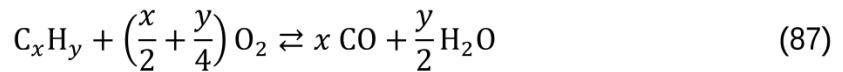
$$C_x H_y + \left(\frac{x}{2} + \frac{y}{4}\right) O_2 \rightleftarrows x\, CO + \frac{y}{2} H_2 O \tag{87}$$

$$2H_2 + O_2 \rightleftarrows 2H_2 O \tag{88}$$

$$2CO + O_2 \rightleftarrows 2CO_2 \tag{89}$$

$$CO + H_2 O \rightleftarrows CO_2 + H_2 \tag{90}$$

$$C_x H_y + C_x H_y \rightleftarrows 2x\, C + y\, H_2 \tag{91}$$

$$2C + O_2 \rightleftarrows 2CO \tag{92}$$

$$C + H_2O \rightleftarrows CO + H_2 \tag{93}$$

where the chemical species denoted by C represents the soot. In this work, C_xH_y is modelled for diesel fuel combustion as $C_{12}H_{26}$.

3 SELECTED RESULTS AND DISCUSSION

In this section, the results of the implemented radiative heat transfer model, DOM FVM is presented for the validation of simple geometry cases, furnace, and ICE. The furnace and ICE cases are shown for the absorption coefficient model, WSGG. The second part is the validation results of implemented SLW and SLW-1 absorption coefficient models. Subsequently, the validation and verification of laminar flame speed and autoignition data base generation tool are presented. Finally, the results when both procedures are considered are presented with a special focus on emission results.

3.1 Validation of Finite Volume Method Discrete Ordinates Method

Validation of the implemented model is conducted on simple geometry cases for which the analytical results exist, where good agreement with analytical results is obtained. The validation is first conducted on parallel plates for which analytic result is available in [133]. The case with the absorption coefficient 0.1 m^{-1}, and 1 m distance between two plates where the first plate is at 0 K and the second plate is at 2000 K is selected from the unidimensional solution. The numerical simulation is performed on 10x10x10 cells (1x1x1 m) cube mesh where the two opposing walls are set as black surface boundary conditions, where one plate does not emit any radiation due to its temperature 0 K. All remaining walls as symmetry boundary conditions, and the implemented FVM DOM was described with eight ordinates. Figure 11 shows the temperature field between two plates, where a good agreement with the implemented and the analytical result is achieved. The second validation case involved a cylinder with walls assumed to be black surfaces at 0 K, and the inside of the cylinder was at 500 K with an absorption coefficient of 1 m^{-1} [134]. The cylinder has all walls assumed as black surfaces at 0 K, so there is not any emittance from cylinder walls. Only the absorption and emissivity of media at 500 K with absorption factor 1 m^{-1} inside the cylinder is assumed. Figure 12 shows the result of the unidimensional wall heat flux at the cylinder base on cylinder hexahedron mesh with 20 cells in each direction. The good agreement with the analytical result is achieved. The more details about validation cases can be found in PAPER 2.
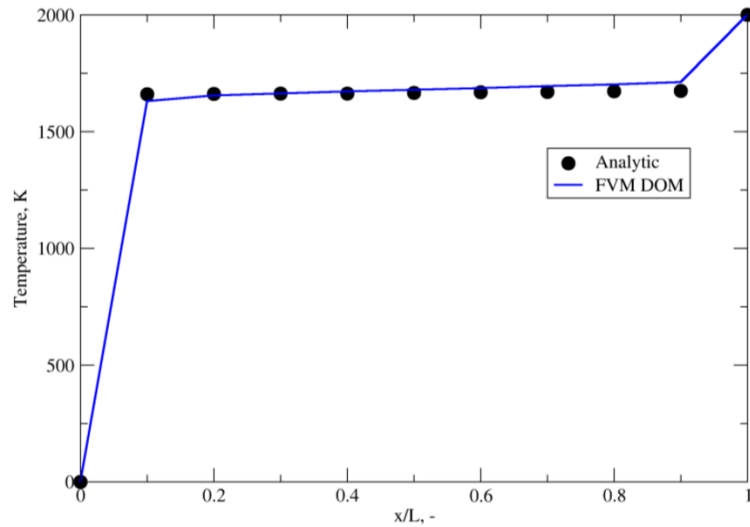
Figure 11   Validation results for the parallel plates with analytical results in [133]
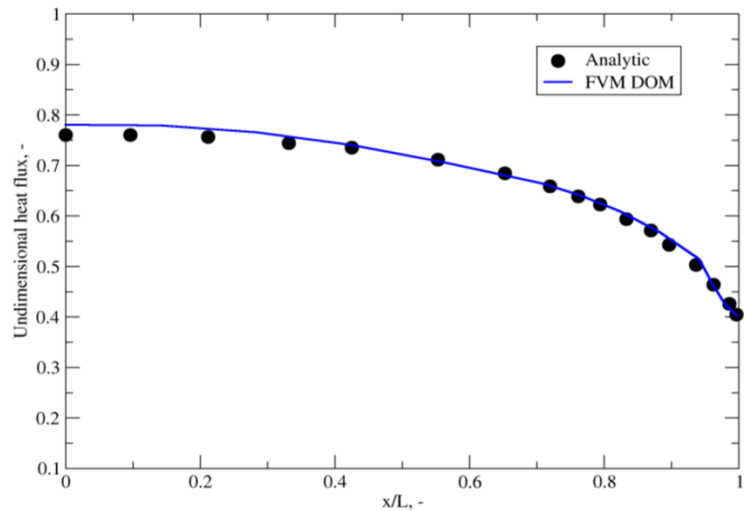
Figure 12 Validation results for cylinder case with analytical results in [134]

A comparison of the temperature profile inside an ICE cylinder is shown in Figure 13, with the orange curve representing the results without considering radiative heat transfer and the blue curve representing the results using the FVM radiation model. The rate of heat release (RoHR) results show that energy loss due to radiation is dominant for the highest RoHR values. The smaller discrepancy between the result without radiation and the result using the FVM can be attributed to the lower initial concentrations of CO_2 and H_2O and the higher oxidizing temperature of soot due to a better air-to-fuel ratio. The numerical setup for the ICE validation case can be found in PAPER 2.
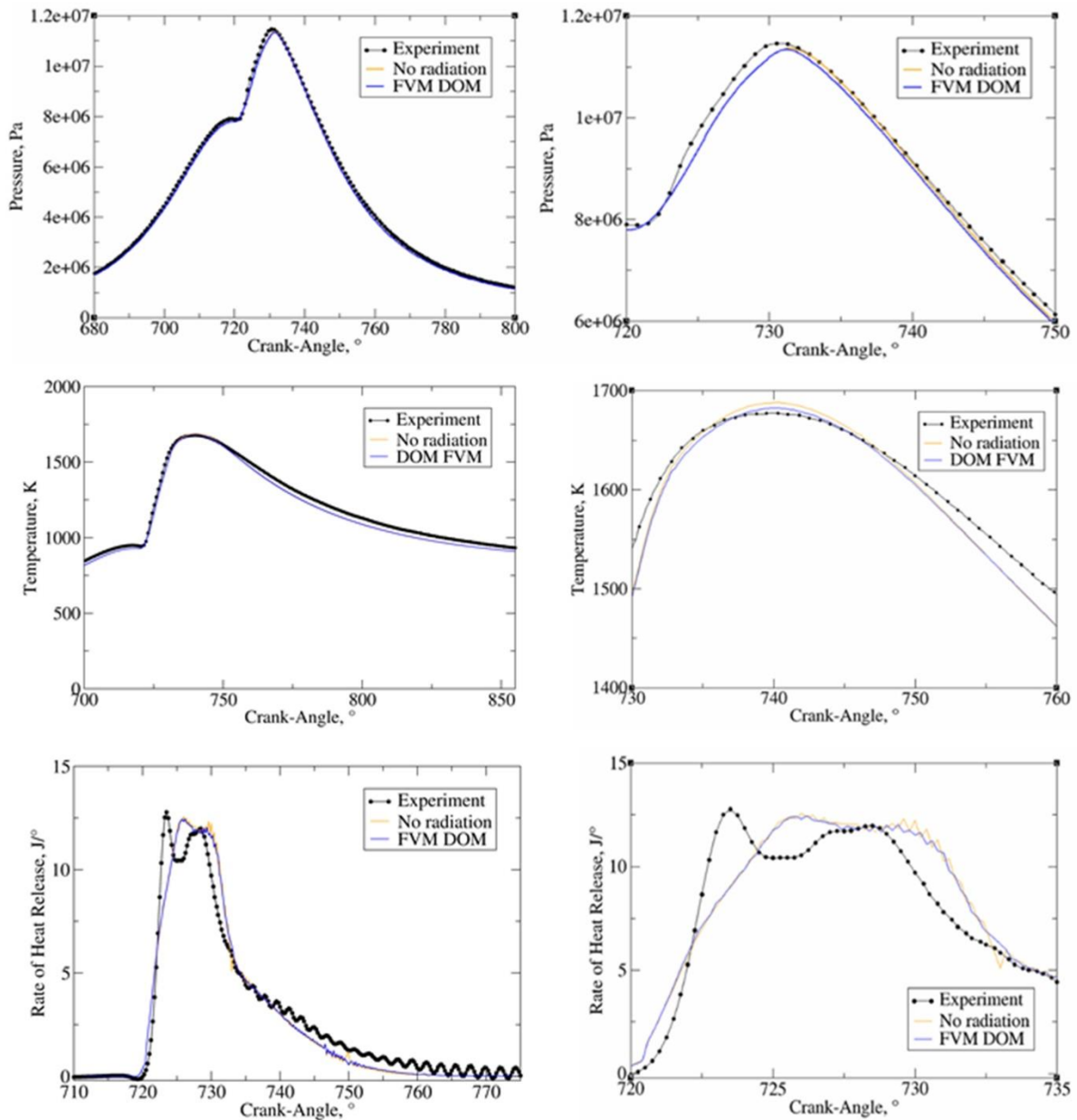
Figure 13   Mean pressure, temperature, and rate of heat release curves for the results without considering radiative heat transfer and with FVM DOM (zoomed diagrams on right)

Figure 14 shows 3D temperature profiles, with the temperature field at the maximum soot mass fraction (740 °C) on the left side of the diagram for the simulation without radiation, and on the right side for the simulation with included radiation. The highest difference in peak local temperature values between the simulation without radiation and the simulation with the FVM is around 15 K. Some discrepancy in the temperature profiles is noticeable at regions of high soot concentrations, which are also shown for 740 °C in Figure 15. In the middle of the high-temperature region shown in Figure 14, the discrepancy between the simulations is visible and

can be attributed to the absorption of H_2O and CO_2, as this region has low values of soot mass fraction and CO_2 and H_2O, products of the combustion process, are the most dominant in this region where the first ignition is expected to occur. Figure 15 shows the soot mass fraction profile inside an internal combustion engine, with the highest discrepancy between the simulation without radiation and the simulation with the FVM visible in the regions of the highest temperature gradients. The distribution of soot mass fraction in Figure 15 shows good agreement, with the regions of highest and lowest soot concentrations preserved in the calculations with and without radiative heat transfer. The total difference in soot mass fraction is approximately 20% higher in the calculations with the FVM than in the calculations without considering radiation.
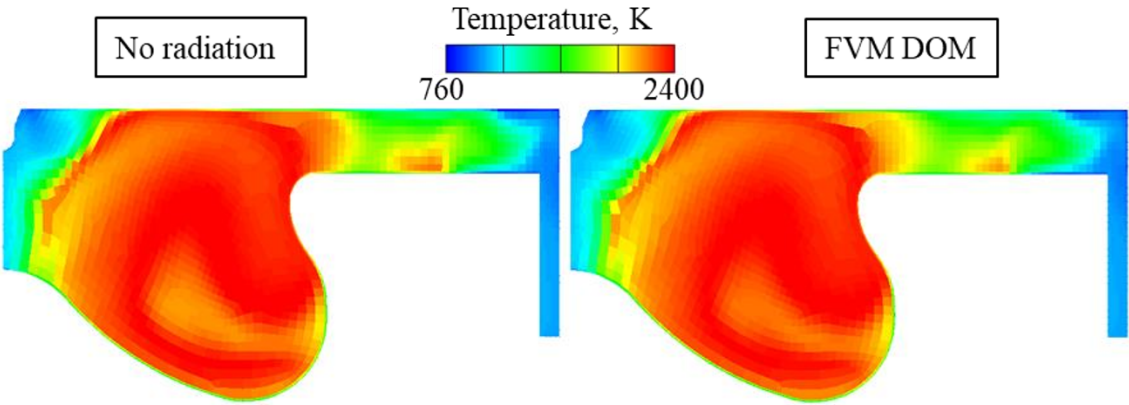
Figure 14   Temperature field for simulation without radiative heat transfer and with DOM FVM
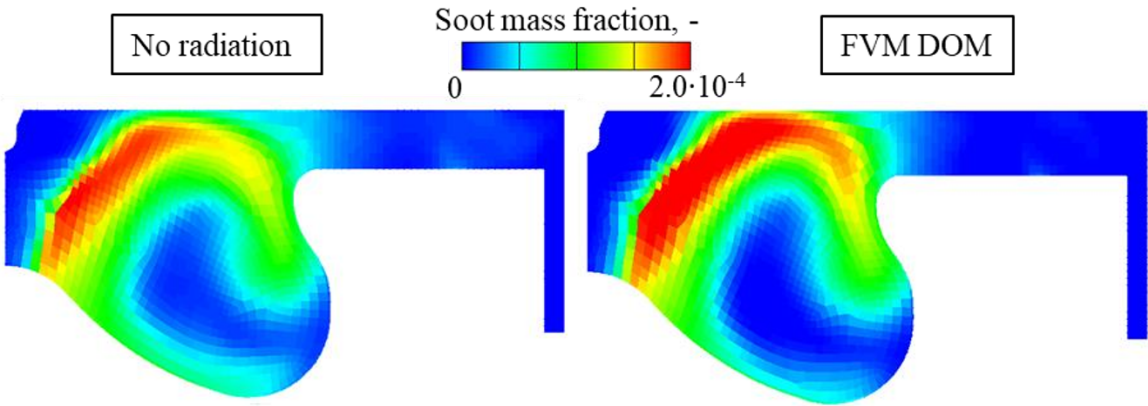
Figure 15   Soot mass fraction for simulation without radiative heat transfer and with FVM

Table I compares the calculation time between simulations with and without radiation, showing that simulations that include radiative heat transfer are approximately 50% more time-consuming.

Table I   Computational time for simulations with and without radiation performed on single and multiple CPUs

Number of CPUs	No radiation	With radiation
1	2 hours	3.5 hours
20	24 minutes	36 minutes

3.2   Validation of SLW absorption coefficient model

The absorption coefficient SLW model that has been implemented has been validated using one-dimensional cases with known analytical solutions. The authors selected two cases and provided the predefined temperature and mole fraction of CO_2 and H_2O for Table II [135]. They generated a hexahedral mesh of cubic cells 3 x 3 x 300 and used it to observe the profile of the enclosed cell layer along the mesh axis.

Table II   Specifications of the two validation cases [135]

	T, K	Y_{H2O}	Y_{CO2}	ϵ, -
1.	$1000 + 250 \cos(\tilde{x})$	0.1	0	1
2.	$1000 - 300 \cos(2\tilde{x})$	$0.5 - 0.5 \cos(\tilde{x})$	$0.5 + 0.5 \cos(\tilde{x})$	1

The nondimensional coordinate $\tilde{x}$ is defined as:

$$\tilde{x} = \frac{\pi x}{L} \tag{94}$$

where x is the position in the coordinate system, and L is the total length. Figure 16 shows a comparison of the SLW model against the analytical radiative source term for the first validation case in Table II, and a good agreement is observed for the trigonometric temperature profile. Figure 17 shows the validation for the second validation case in Table II, in which the molar ratio of CO_2 and H_2O is also described using a trigonometric profile. The results in Figure 17 show that the simulation results do not significantly change when more control angles are applied to the numerical simulations. Based on these validations, it can be concluded that the implemented SLW model is suitable for accurately describing the CO_2 and H_2O gas radiative properties.
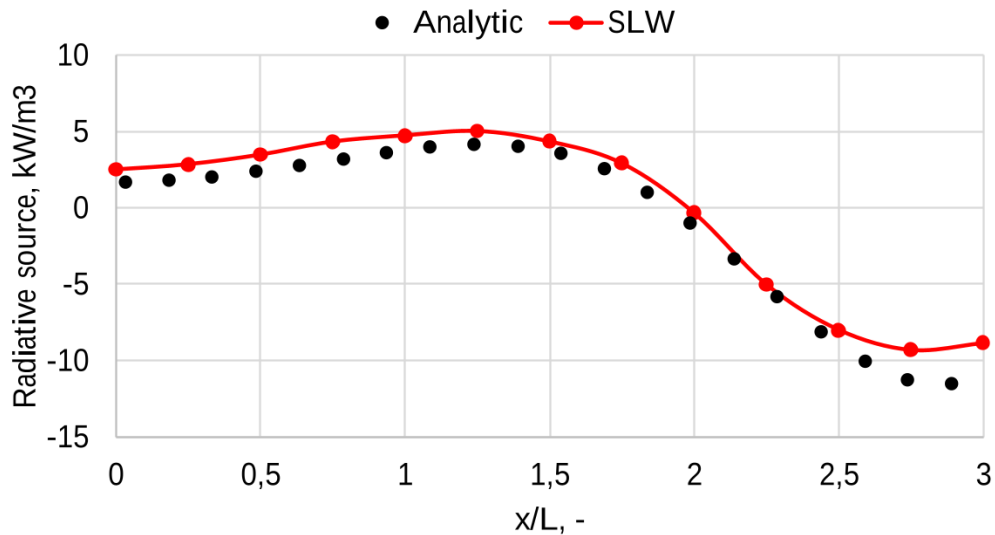
Figure 16   Radiative source profile results for the first validation case
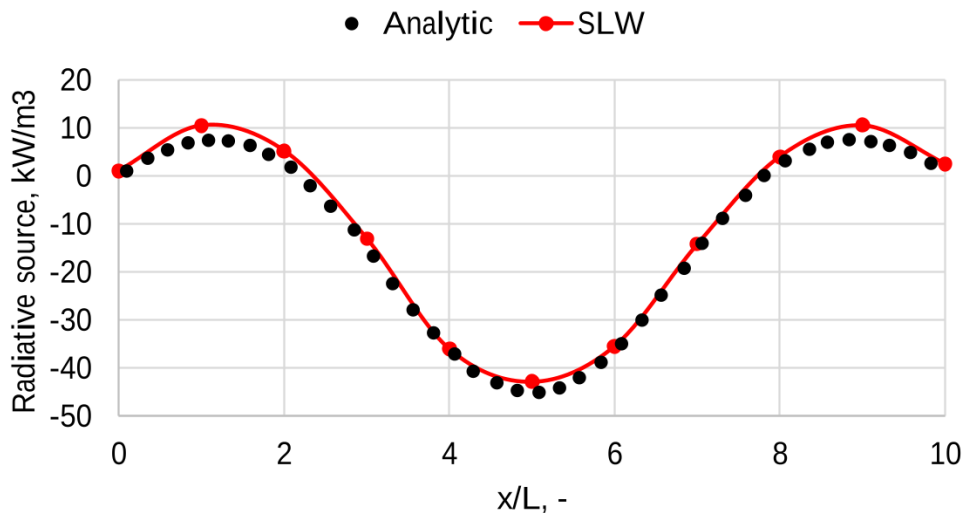
Figure 17   Radiative source profile results for the second validation case

In PAPER 6, the numerical setup for analyzing ICE results is presented. Figure 18compares the mean pressure, temperature, and RoHR for single injection (Case a) and multi-injection (Case b) using experimental data (black lines with dots), results without considering radiation heat transport (blue curves), and results from the implemented SLW model (orange curves). The RoHR results are based on a computational mesh representing an eighth of an engine combustion chamber. The difference in the ignition delay between the results with and without radiation is clearly visible in Figure 18, which can be attributed to the different values of the radiative absorption coefficient. The radiative absorption energy of CO_2 and H_2O is similar in both Case a and Case b due to their similar gas composition and thermodynamic conditions.

However, the difference between the calculated impact of radiation between the two cases is noticeable in Figure 18. This difference can be attributed mainly to the absorption of soot particles, which exhibit gray gas behavior. As expected, the radiative absorption of a large portion of the incident radiative flux is highest in regions of high temperature. Overall, the SLW model, which accounts for the additional spectral phenomenon of radiative heat transport, produces more accurate results and better agreement with experimental data.
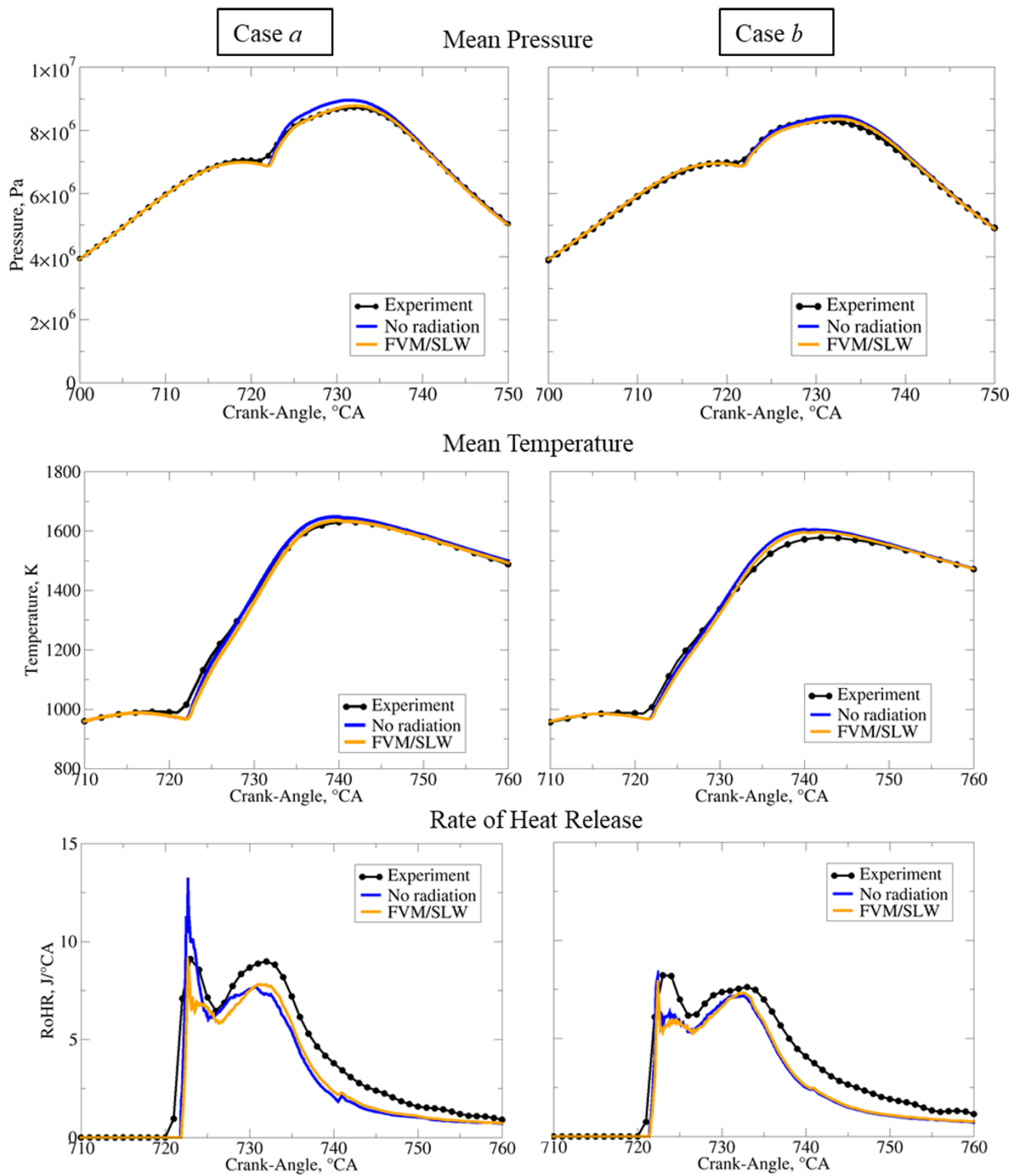
Figure 18   Mean in-cylinder pressure results, mean temperature, and RoHR results for Case a (left) and Case b (right) with SLW model and without radiation against experimental results

Calculations of heat loss profiles for various crank angle positions for Case b are shown in Figure 19. These heat losses are determined through the wall boundary layer, where approximately 9.5% of the total fuel energy is lost due to convective losses. In comparison, net

radiative loss, resulting from higher emission than absorption of CO_2 and H_2O gases, is approximately 7-8% of the convective heat loss.
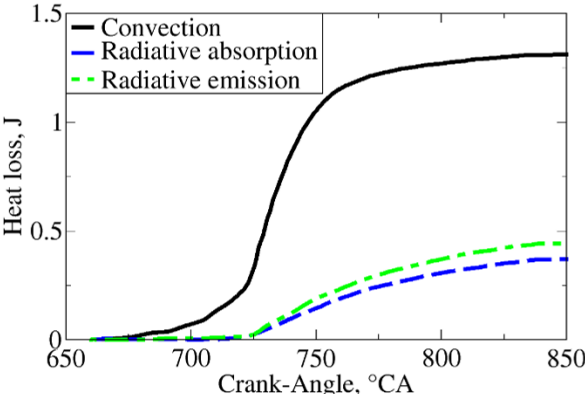
Figure 19   Convective, radiative absorption, and radiative emission heat losses for Case b

In Figure 20, the profiles of soot mass fraction for simulations with and without radiative heat transfer are presented. The following Figure 21 displays the temperature difference contour at the crank angle position with the highest soot concentration, 732°CA.
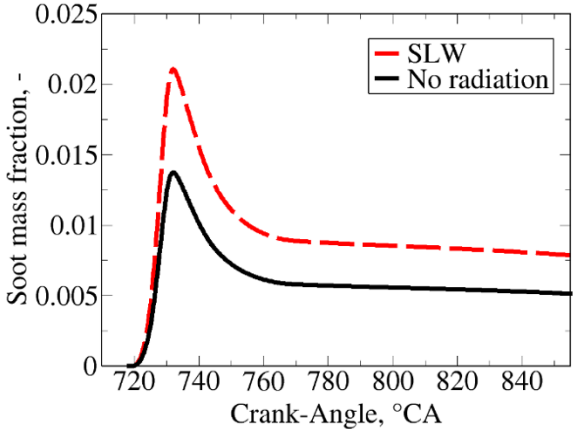
Figure 20   Soot mass fraction profile for Case b

The relationship between soot concentrations and radiative heat transfer is not as straightforward as the interaction between soot concentrations and NO formation. The results suggest that the soot formation is largely influenced by the regions of lower temperatures, as computed by SLW simulations, which are more dominant compared to the regions with higher temperatures, as shown in Figure 18. Higher temperature differences are correlated with fuel-rich regions in high-temperature regions. The area with the highest difference is around the

equivalence ratio values of 2-3, where the neighboring cells have already ignited and consumed their oxygen.
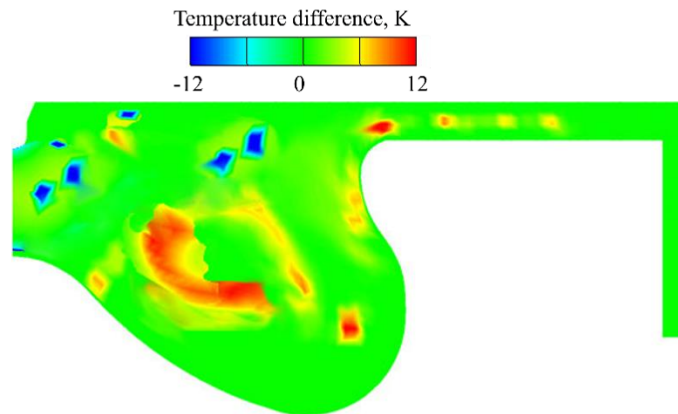
Figure 21   Temperature difference between results with SLW and without radiation at the crank-angle position with peak soot values (732°CA) for Case b

3.3   Validation and verification of SLW-1 model

The implemented radiative absorption coefficient model SLW-1 is validated on 1D cases with a benchmark solution. Two observed 1D cases have the predefined temperature, CO_2, and H_2O mole fraction profile [19]. Figure 9 shows the validation of SLW-1 model against the benchmark results of the radiative heat source for the first validation case in Table II. In Figure 22, from all absorption coefficient models, WSGG achieves the highest disagreement with the benchmark test case for the first period of the sinusoid function, while for the low temperature and low H_2O concentrations, it achieves overprediction of the radiative source term, that is contrary to the SLW and SLW-1 results. For all models, a good trend and symmetrical sinusoid curve are achieved. Although, for the SLW, additional transport equations for the incident radiation did not result in better agreement with the benchmark results for low temperature and water vapour mass fraction. Even though the SLW-1 model achieved a better agreement, it could be attributed to the bias of the SLW-1 model and not to the correctness of the model itself.

In Figure 23, the validation is shown for the second validation in Table II. Opposite to validation in the first validation case, CO_2 mass fraction is introduced, but as the constant along the line. In the second validation case, a higher discrepancy from the benchmark results is achieved for all models. The overprediction of SLW at the lower water vapour mass fraction is reached again, although the most significant discrepancy is at 3 m, where the emissivity is not so pronounced as in WSGG and SLW-1 model. For the second validation case, more correct

results are obtained with the SLW-1 model than with WSGG, which indicates that the included spectral line properties impact the accuracy of the results. From the conducted 1D validation, it can be stated that the implemented SLW-1 model is suitable for describing the radiative gas properties.
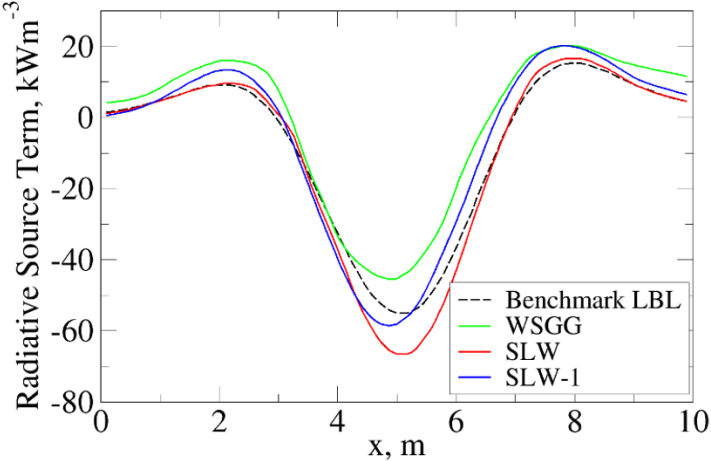
Figure 22   The 1D validation: radiative source term along the observed axis
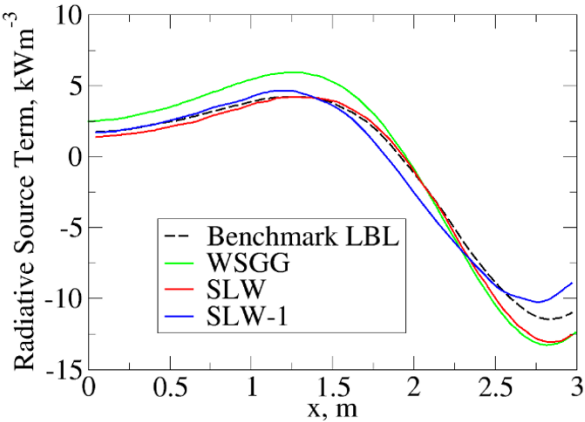
Figure 23   The 1D validation: radiative source term along the observed axis

Temperature profiles at the different axial locations (x=15D and x=30D) are compared in Figure 24 for the 2D validation case of Sandia flame D. WSGG, SLW and SLW-1 are calculated together with the FVM radiation model and ECFM-3Z combustion model. The same as in the 1D validation case, the total number of control angles was 64 for all absorption coefficient model calculations, and the number of grey gasses in SLW was 20. The best agreement between all radiative absorption coefficient models is achieved at the radial position of tube diameter D. A higher discrepancy is achieved at the axis for the position x=30D, in which the SLW model achieves more accurate results than the WSGG and SLW-1 models. Although the trend of

46

WSGG is well predicted at x=15D, it is significantly changed near the axis at x=15D compared to SLW and SLW-1 models. That indicates that the flame temperature could be better described within the SLW-1 model compared to the WSGG. The best agreement was achieved with the SLW model. The SLW-1 model achieves a similar trend to the SLW model. Temperature profiles of the SLW and SLW-1 model with TRI influence are shown in Figure 25.

Figure 24 Temperature profiles for two different axial positions of benchmark case Sandia flame D: x=15D, and x=30D
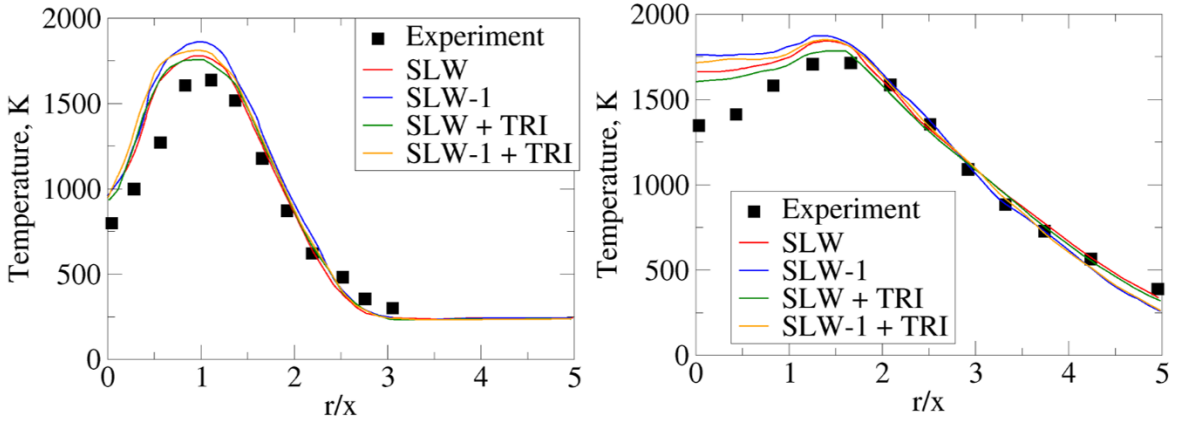
Figure 25 Temperature profiles with TRI for two different axial positions of benchmark case Sandia flame D: x=15D, and x=30D

3.4 Validation of tabulation method

For the validation of the calculated data from chemistry solvers, four mechanisms of e-fuel OME-3 were compared with the experimental data: Cai et al. [89], Ren et al. [136], Sun et al.

[137], and Lin et al. [138]. Figure 26 shows the calculated laminar flame results at a pressure of 0.1013 MPa and temperature of 408 K, and with four previously mentioned chemical mechanisms, where good agreement was achieved with all data.
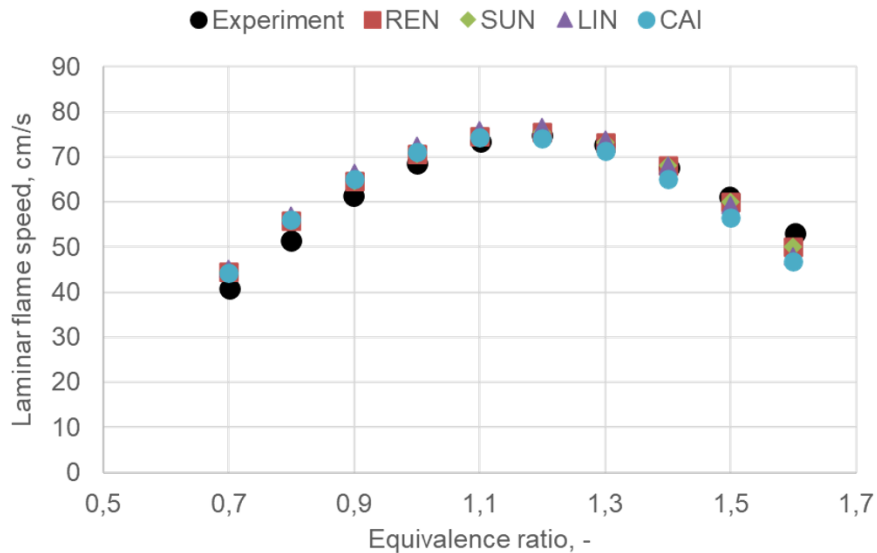
Figure 26   Comparison of calculated laminar flame speed with four chemical mechanisms and experimental data at 0.1013 MPa and 408 K

The validation of autoignition results is performed with the same mechanisms, where the best agreement with experimental data was achieved with the Lin et al. mechanism. The autoignition results were performed in Figure 27, where the results are shown at the pressure of 2 MPa for equivalence ratio values of 0.5, 1.0, and 2.0. The experimental autoignition results are taken from [89]. According to the performed validation, the Cai et al. chemical mechanism was selected to further investigate the correlation function since it features the highest number of chemical reactions and chemical species.
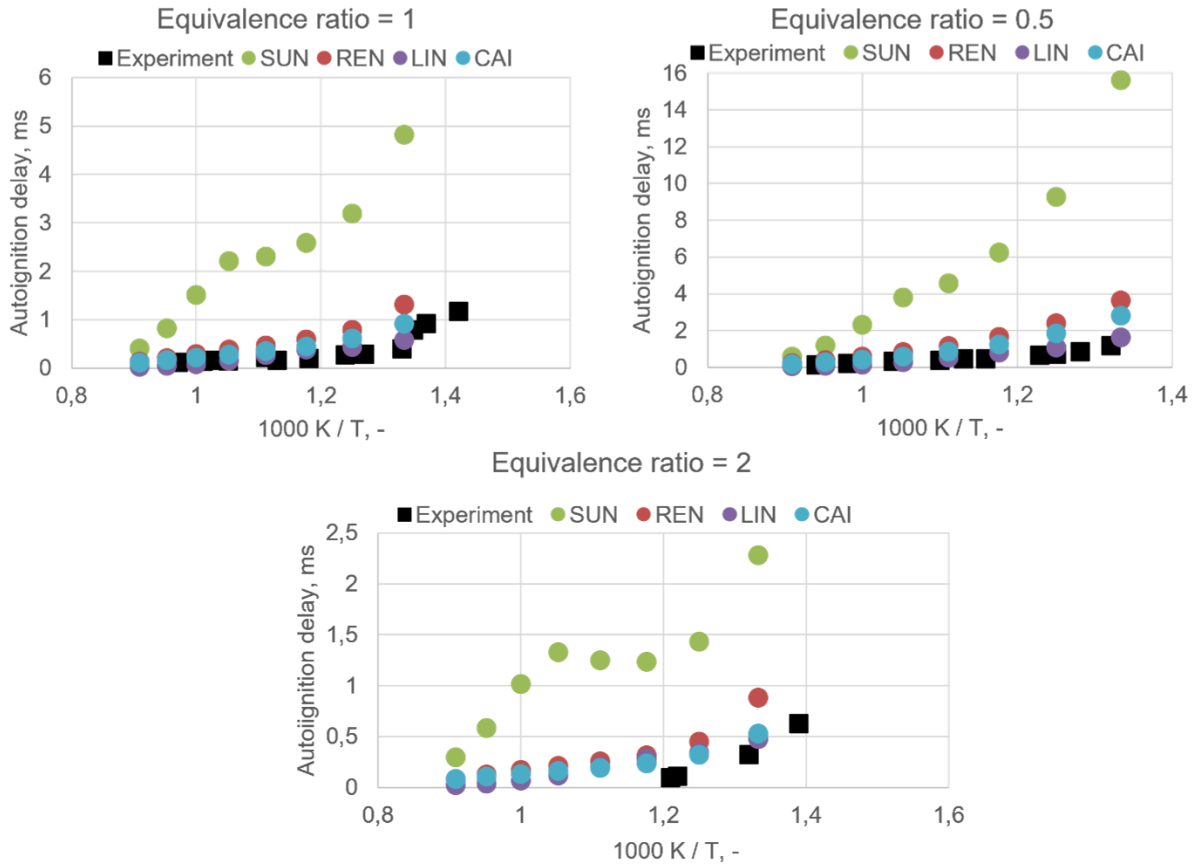
Figure 27   Comparison of calculated autoignition data with four chemical mechanisms and experimental data at 2 MPa for equivalence ratios: 0.5, 1.0 and 2.0

In this section, the results of the developed correlation functions and calculated data were compared on three-dimensional and two-dimensional diagrams. Figure 28 shows the calculated and tuned laminar flame speed results with the correlation function in Equation (54) at 1100 K with Cai et al. chemical mechanism. The a) diagram of Figure 28 shows the surface of raw data calculated from the chemistry solver, which is tuned with the correlation function, and where the results at the b) diagram of Figure 28 are obtained.
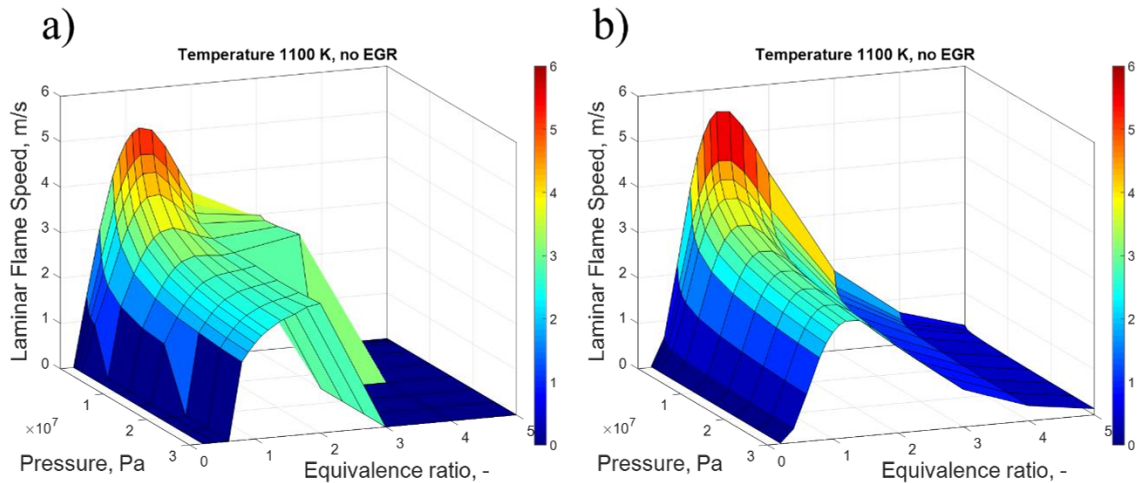
Figure 28   Calculated chemistry solver results (a) and laminar flame speed results with the correlation functions (b) at 1100K

Figure 29 shows the calculated results from the chemistry solver used as input to obtain the shape of laminar flame speed data and the shape obtained by the correlation function procedure on four parameters: temperature, equivalence ratio, pressure, and EGR mass fraction. The calculated laminar flame speed data is shown as black dots, while the surface shows the results with the correlation function in Equation (54). In Figure 29, a good trend is achieved between calculated results and the results obtained from the general function approach. For the highest temperature, 1250 K, only 6 points are obtained from chemistry solver reactions, compared to the lower temperatures where the chemistry solver is more stable. The general function approach shows a robust extrapolation solution for such cases since it only needs 3 points to determine the whole laminar flame speed shape in pressure and equivalence ratio directions. In Figure 30, the same results for different pressure values. It can be seen that the agreement between the general function approach and calculated data using the conventional Gülder approach for extrapolation [139] is better for the lean mixtures and around the stoichiometric equivalence ratio. At the same time, a more significant discrepancy was achieved for the fuel-rich region.
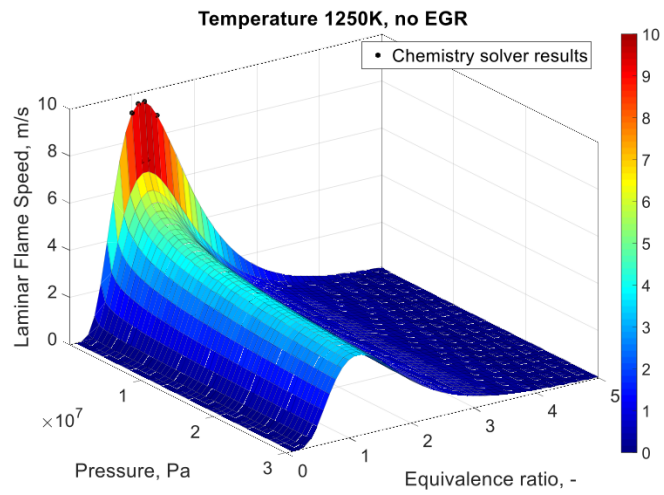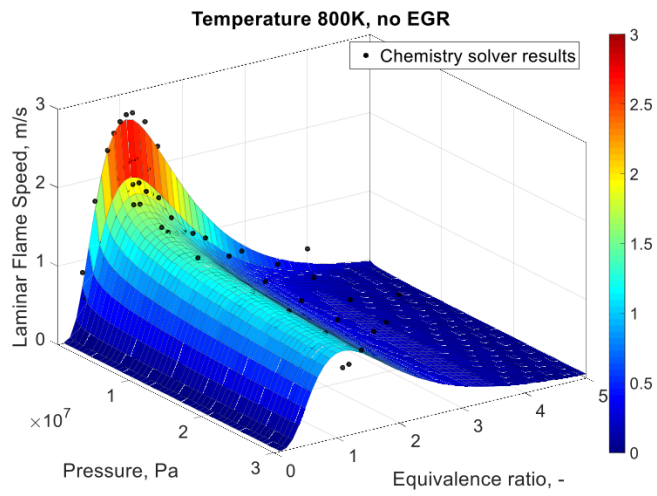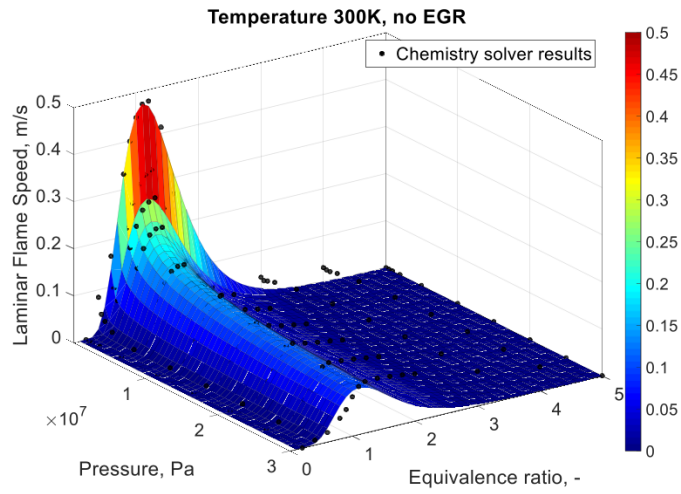
Figure 29   Laminar flame speed results with the correlation functions at 300, 800 and 1250 K and without EGR
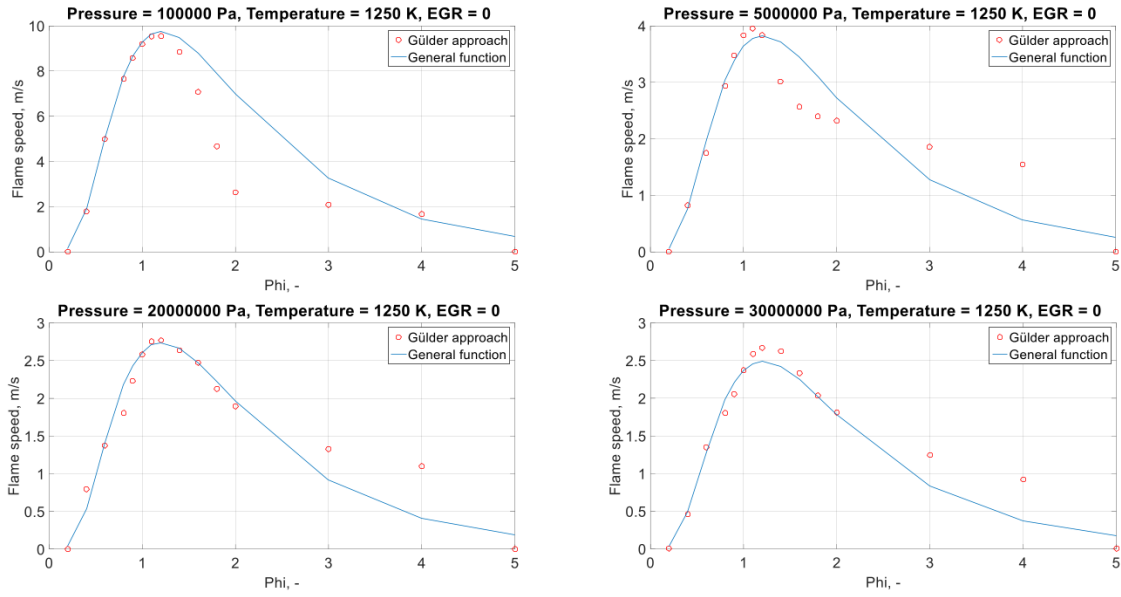
Figure 30   Calculated results with Gülder approach and laminar flame speed results with the
correlation function at 1250 K

Figure 31 shows the same results as in Figure 7 for the temperature of 800 K, at different pressure values. Additionally, the number of successfully calculated data from the chemistry solver (red circles) is reduced with pressure and equivalence ration increase. Nevertheless, as shown, the general function method shows good robustness with fewer obtained points. Additionally, the method was also validated against calculated laminar flame speeds at different EGR values in Figure 32. With increased EGR, a more significant discrepancy with chemistry solver data is obtained, which has unexpectedly high values in fuel-rich regions. Such high values can also be attributed to the drawback of a chemical mechanism not intended to calculate the laminar flame speed for such conditions or to chemistry solver converging deficiency.
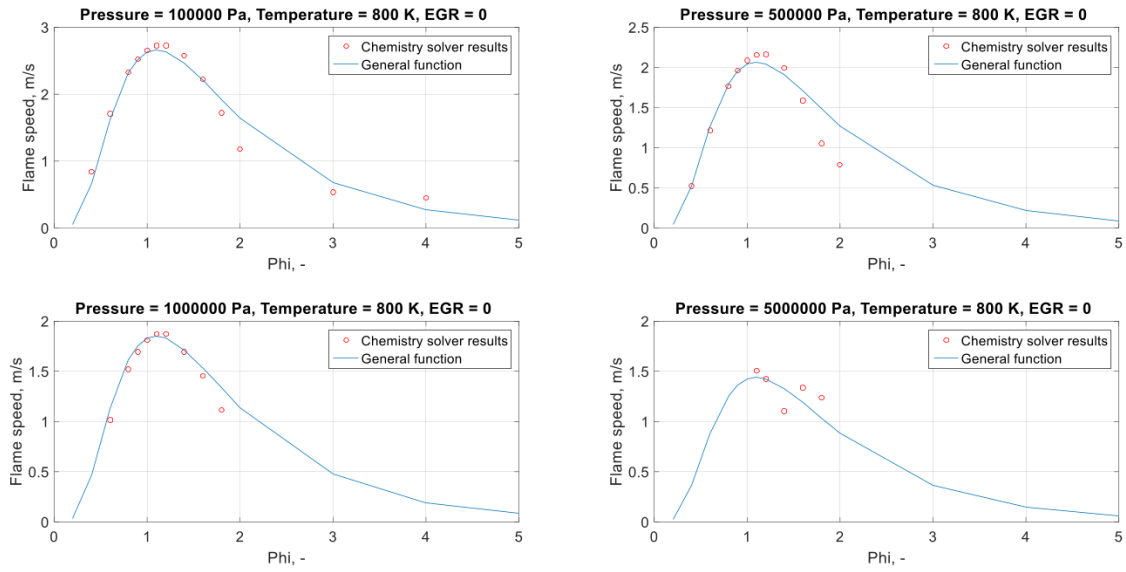
Figure 31   Chemistry solver results and laminar flame speed results with the correlation function at 800 K
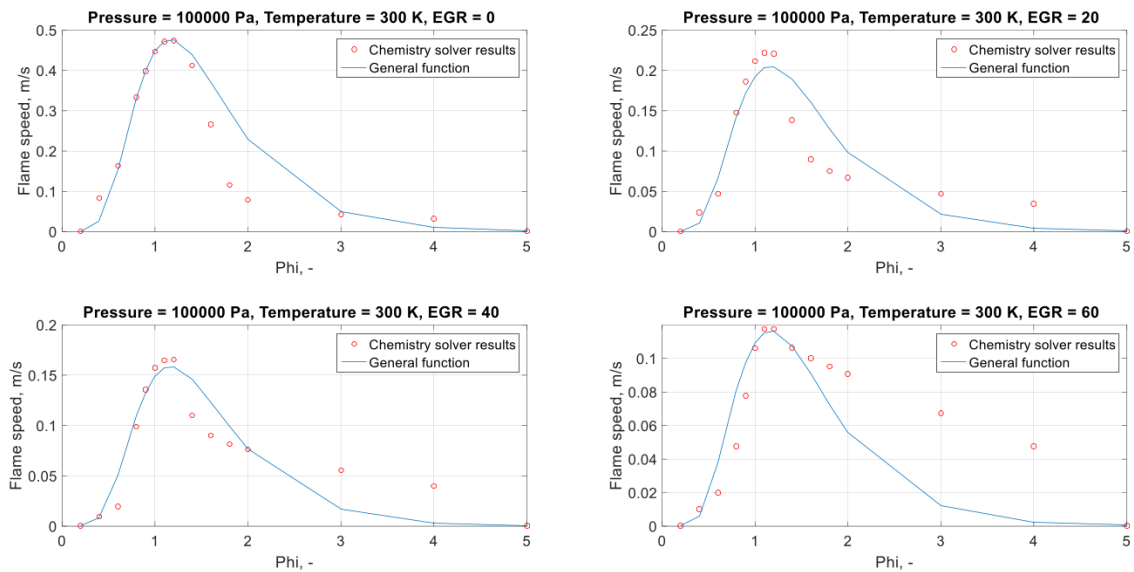
Figure 32   Chemistry solver results and laminar flame speed results with the correlation function at different EGR values

Figure 33 shows the coefficient of determination (R^2) values between the chemistry solver results and general function at different temperatures and EGR values. It can be seen that the best

53

agreement between chemistry solver results and general function is obtained around 500 K. the correlation decreases markedly with the increase of EGR and at high temperatures.
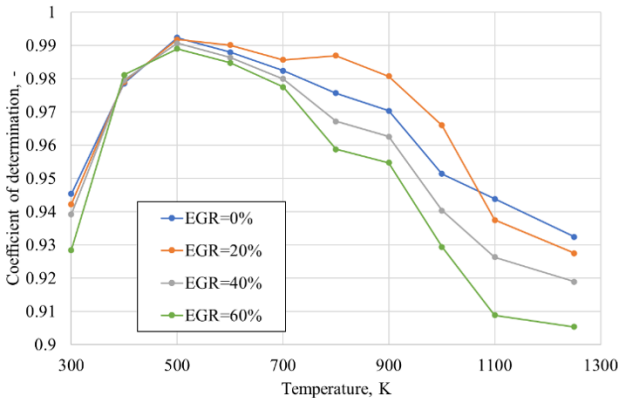
Figure 33   Coefficient of determination values between chemistry solver results and general function for different temperature and EGR values

Figure 34 shows the calculated and tuned laminar flame speed results with the correlation function in Equation (57) with Cai et al. chemical mechanism. For most autoignition delay time representation, a logarithmic scale is used in order to emphasize that the order of magnitude is sufficient for valid autoignition modeling. In Figure 34, the linear scale emphasizes a good agreement with the chemistry solver results at temperatures 1000 K and 1200 K.
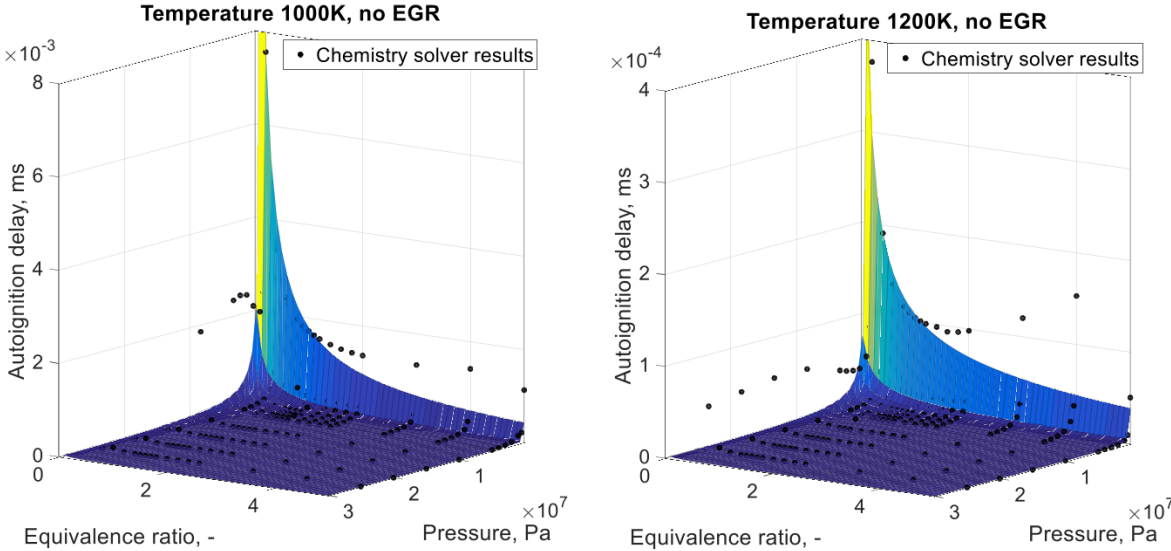
Figure 34   Calculated (black dots) and autoignition timing results with the correlation functions without EGR at 1000 and 1200 K

Figure 35 shows the same results as Figure 34 for 2D cuts at different pressure values. It can be seen that the agreement between the chemistry solver results and general function approach is better for the points around the stoichiometric equivalence ratio and around the fuel-rich region. In contrast, additional efforts are required for the lean air-fuel mixtures and the fuel-rich region at higher pressures.
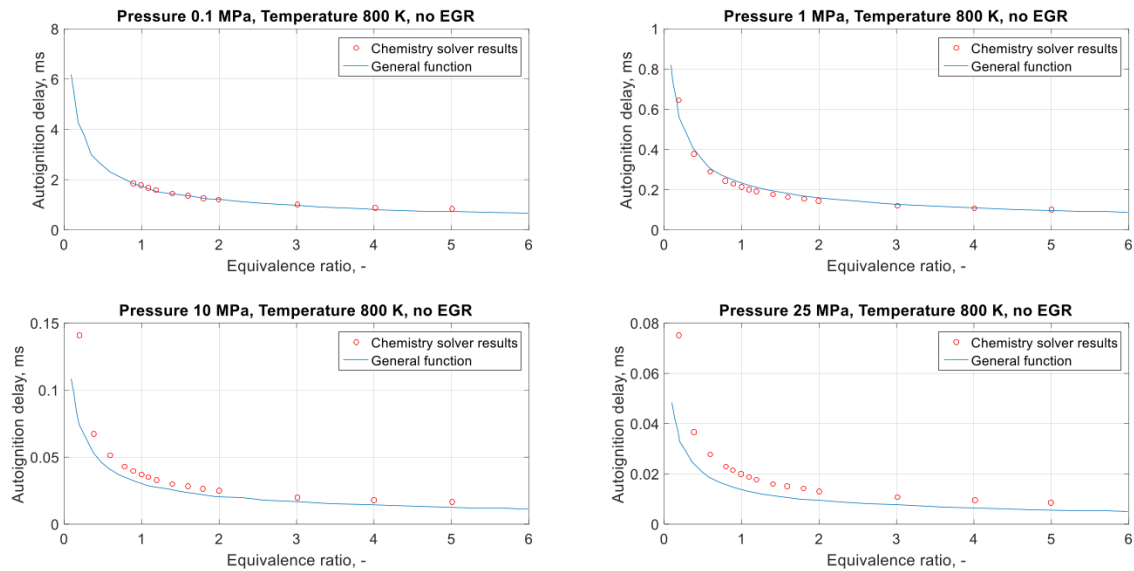
Figure 35   Chemistry solver results and autoignition results with the correlation function

In PAPER 5, the operating conditions and numerical setup for the calculation are presented, for which the results are shown. The performed engine operating point features a multi-injection strategy of four separate injections, where the OME-3 fuel was injected at 20 °C. Figure 36 compares the most detailed chemistry mechanism of OME-3 fuel, Cai et al., and ECFM-3Z combustion model with implemented autoignition and laminar flame speed databases for two operating injection strategies. A good trend was achieved for the temperature results, while the ignition timing was slightly delayed for the simulation of ECFM-3Z. That can also be attributed to the autoignition parameter for ECFM-3Z calculation, which was not calibrated but used as a default value of 1. The same ignition delay is observed for the rate of heat release results, while the peak of released heat is achieved with the same value. As seen from RoHR diagram, ECFM-3Z combustion is not so pronounced as with Cai et al. For the late-stage combustion, the biggest discrepancy is achieved, which can be mainly attributed to the simplified chemistry in the combustion model does not account for such detailed carbon-based reactions. A better agreement is reached for the single injection case than in a multi-injection strategy with four different injections, which calculates autoignition delay based on the whole chemistry reactions rather than

on interpolated conditions based on four parameters from the generated database. The ECFM-3Z in combination with the developed method for database generation of autoignition and laminar flame speed, has correctly described the ignition of each injection and its ignition and combustion process with significantly simpler chemistry and decreased computational demand. The computational discrepancy between the ECFM-3Z model and Cai et al. mechanism can be attributed mainly to the simplified chemistry description in the ECFM-3Z model, which accounts for transport equations for a dozen chemical species. In contrast, Cai accounts for transport equations for 322 chemical species. Finally, the computational time was decreased approximately 20 times with the ECFM-3Z model.

Figure 36   Comparison of temperature and rate of heat release results between detailed chemistry mechanism by Cai et al. and ECFM-3Z combustion model

3.5 Internal combustion engine results

This section confirms results from 3D CFD calculations on ICE operating cycles against the experimental ICE in-cylinder data. In PAPER 7, the numerical setup for analyzing ICE results is presented. Figure 37 shows the mean in-cylinder temperature for four observing operating ICE cases, including TRI for SLW and SLW-1 models. All models achieved a good trend for the single injection Case #1 and Case #2. The temperature difference between radiative absorption models was within 10 K for Case #1 and 20K for Case #2, which has a greater initial EGR ratio and temperature. The higher temperature difference between models in Case #2 is due to the higher mole fraction of participating gases CO_2 and H_2O in the cylinder. The best agreement with experimental results is achieved with the SLW results, while the lowest agreement is achieved with the WSGG model for all four operating cases. The highest discrepancy with experimental data is achieved around the peak temperature and during the cylinder expansion, where the combustion products CO2 and H2O are also increasing. For the multi-injection Case #3 and Case #4, a correct trend for autoignition detection of separated injections is achieved, which is visible in temperature inflexion points, where the temperature gradient arises. A higher discrepancy is achieved for the multi-injection cases, especially in Case #4, which has a higher EGR mass fraction. The model discrepancy goes up to approximately 27 K, with the highest difference achieved in expansion, similar to the single injection cases. The SLW-1 results for all operating cases are in good agreement with the SLW model and are notably better than the results obtained with WSGG. SLW-1 represent the compromise between WSGG and SLW models. SLW-1 considers spectral line gas properties for a single grey gas and transparent window but without solving additional time-consuming transport equations for the grey gases.

Figure 37   Mean temperature results for all observing ICE operating points, and radiative absorption coefficient models: WSGG, SLW, and SLW-1

The comparison between SLW-1 results with and without TRI for Case #1 and Case #2 is shown in Figure 38. A higher disagreement between simulation and experimental data with and without TRI is more pronounced for Case #2, which has a higher mean in-cylinder temperature and EGR ratio. The maximal mean temperature difference is approximately 8 K, while for Case #1, significantly lower. As expected, a more significant TRI influence is observed at higher temperatures. The temperature decrease for simulation with included TRI was also observed in the results obtained for Sanda Flame D simulation, shown in Figure 25.

58
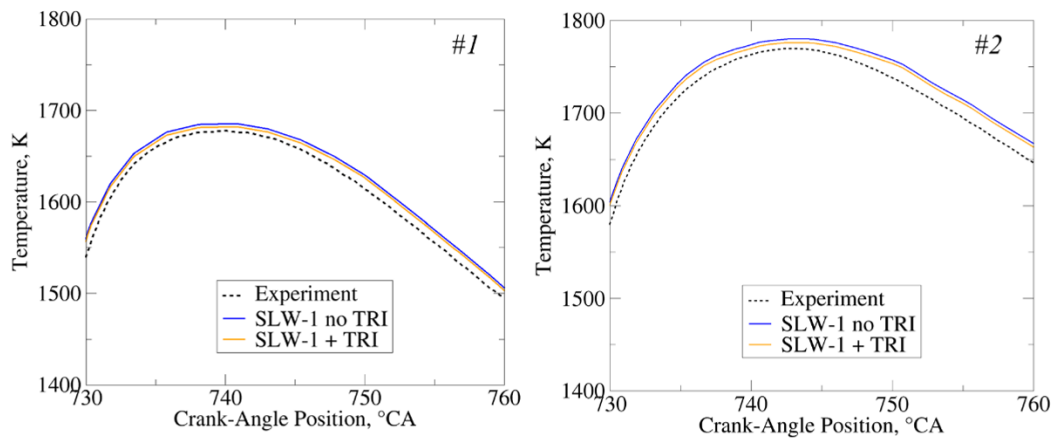
Figure 38   Mean temperature results of SLW-1 model with/without TRI for operating

Case #1 and Case #2

Figure 39 shows 3D profiles at 15 °CA after TDC for Case #2: The mean temperature, the temperature difference between simulation with and without TRI, radiative participating gases CO_2 and H_2O, and pollutant emissions for NO and soot. At 15 °CA after TDC, fuel injection is finished, and temperature distribution is developed, where the peak temperatures are achieved at the cylinder bowl. The peak NO mass fraction can also be observed in the same region. H_2O distribution significantly correlates to the temperature field. The CO_2 distribution shows the regions of the completed combustion where the area closer to the injector is still not fully combusted. The low-temperature part of the cylinder bowl is due to the cooling from injected fuel. Those regions are also the highest soot formation regions, primarily associated with lower temperatures and evaporated fuel-rich regions. Temperature difference distribution between simulations with and without radiation correlates to the right-hand diagram in Figure 38. The highest differences are in the regions of the highest temperature gradients.
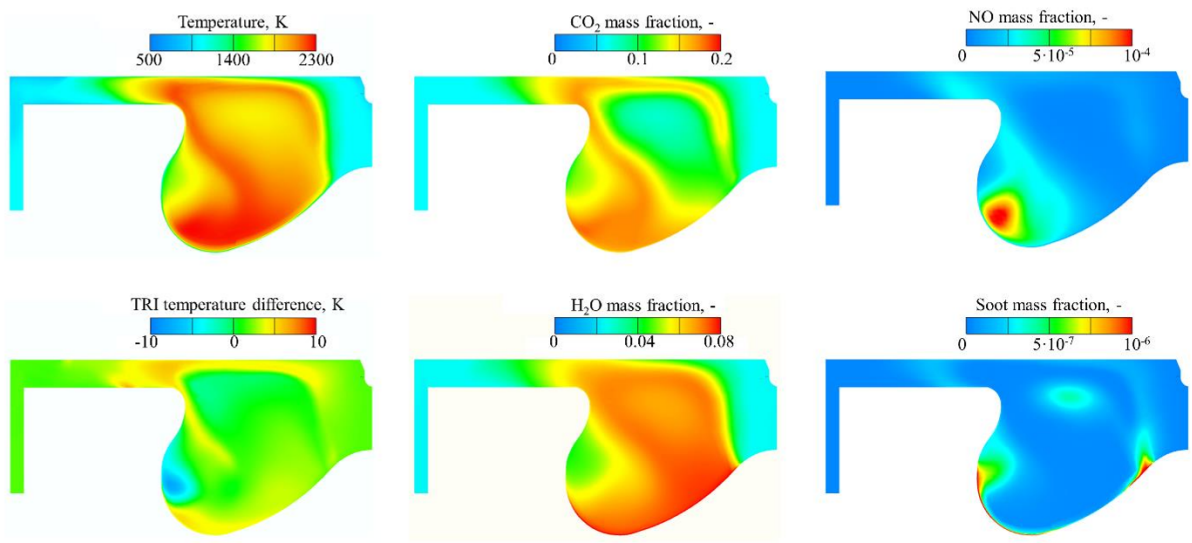
Figure 39   Different 3D profiles of Case #2 at 15 °CA after TDC (735 °CA)

Figure 40 shows the calculated boundary values of incident radiation for implemented periodic boundary connection boundary condition. The right segment has a slightly higher incident radiation value than the left segment due to the initial fluid flow swirling inside the cylinder. All radiative intensity that goes outside from a segment is transferred as input on its boundary connection segment.
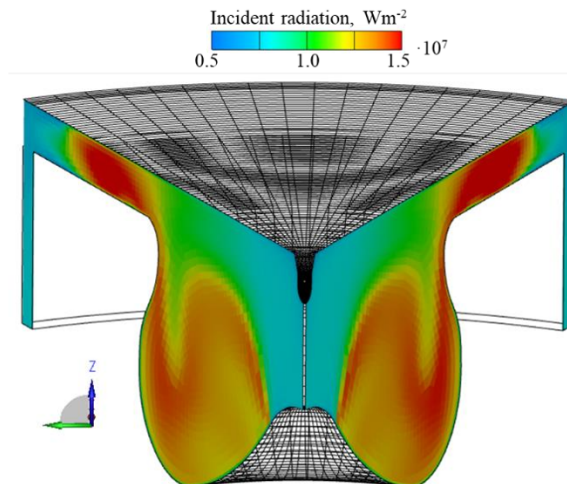
Figure 40   Incident radiation results at the boundary connection walls for Case #2 at 15 °CA after TDC

3.5.1 Pollutant emission results

Figure 41 shows NO formation described with the extended Zeldovich model for the operating Case #1 and Case #2. Despite the increased temperature, the initial EGR strongly reduces the mean NO emissions in the operating cycle. The NO emission results when exhaust values start to open are given in Figure 13 for all operating points and compared with available experimental data. The overprediction of NO emissions compared to the experimental data is achieved for both operating single injection cases. The overpredicted NO emissions also correlate to the higher mean temperatures in Figure 37 results. SLW-1 achieved an accuracy in-between WSGG and SLW models same as for the temperature results. The temperature is the primary generator of NO emissions in the extended Zeldovich model, due to that NO results from CFD simulations exceed the experimental NO concentrations in all four operating ICE cases. The temperature and NO emissions results are increased for all radiative absorption models. Additionally, TRI interaction on the final emissions is of minor importance compared to the differences in the radiative absorption models.
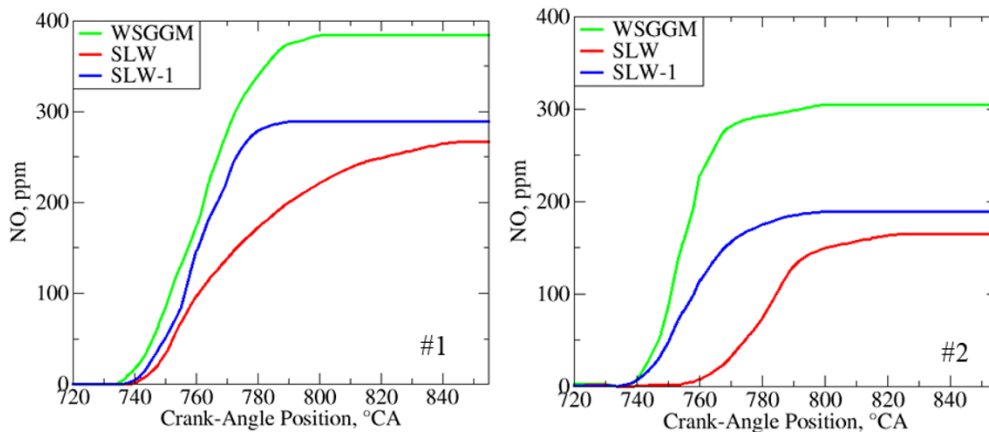
Figure 41   NO profile formation for concentration different

Figure 42   NO results at the exhaust system for ICE cases

Figure 43 shows soot results at the end of all operating cycles. The overall low concentrations of soot are achieved for Case #1 and Case #3, which feature a low initial EGR ratio. That is one of the reasons why radiative absorption of CO_2 and H_2O dominates soot absorption in Case #1 and Case #3. A higher difference between predicted soot emissions is achieved for the operating points with the higher initial EGR values. The impact of radiative heat transfer and TRI is also lower on exhaust soot results than on NO results, as seen in Figure 43.

Figure 43   Soot results at the exhaust system for ICE cases

Table III shows the average computational CPU time of each simulation. A simulation without RTE solver FVM is given as a reference. It can be concluded that the SLW model is computationally too demanding for the ICE simulations at the expense of not providing

62

significantly more accurate results than the SLW-1 model. Additionally, SLW-1 features a similar computational time as WSGG but gives additional accuracy with the consideration of spectral line properties. Although it does not add significantly increased accuracy in ICE, TRI is recommended for inclusion due to the non-significant increase in computational time.

Table III   Average CPU time in seconds

Without radiation	WSGG	SLW no TRI	SLW-1 no TRI	SLW + TRI	SLW-1 + TRI
25064	42157	69012	45129	70213	47001

4 CONCLUSIONS AND FUTURE WORK

The procedure of general functions for the generation of databases required for combustion modelling in the coherent flame models is developed. The procedure is general and applicable to every fuel, and under this thesis was mainly focused on the generation of laminar flame speed and autoignition databases for OME-3 fuel. Additionally, the developed procedure showed good potential for reducing the number of required grid points since a reasonable agreement can be achieved with a few calculated points around stoichiometric values of equivalence ratio. The procedure validation was performed on generated laminar flame speed and autoignition database for OME-3 fuel, where a good agreement was achieved compared to the available experimental results. For the engine operating cycles, verification was made compared to the most detailed chemistry mechanism available in the literature, Cai et al. The verification results showed a great agreement in the trend and autoignition timing between mean in-cylinder temperature and rate of heat release curves for both single and multi-injection strategies. In combination with coherent flame models, the developed method represents a robust and computationally low-demanding procedure for accurate ignition and combustion process calculations of new biofuels and e-fuels. Although not presented in this thesis, the procedure was also developed for fuel blends, dual fuel, and multiple fuel combustion, where the additional fuel composition parameter was added as the fifth grid parameter. An integrated simulation approach for more efficient estimation of pollutant formation in industrial multiphase reactive applications is presented in this thesis, which couples radiative heat transfer and pre-generated laminar flame speed and autoignition databases. For the calculation of the radiative absorption coefficient in participating multiphase media, the numerical model that calculates the spectral-line formulation using only a single grey gas and one transparent gas was implemented, called SLW-1 model is implemented in AVL FIREm™ CFD code using user routines. SLW-1 is implemented inside the finite volume method for radiative heat transfer that features periodic boundary conditions, moving mesh, rezone procedure and TRI for ICE calculations. A good agreement with 1D validation cases without radiation and for the 2D Sandia flame D is achieved, but also the verification with other radiative absorption coefficient models, WSGG and SLW. Different initial EGR cases were observed on complex 3D ICE cases with the single and multi-injection strategies with experimental data. It can be stated that the radiative heat

transfer shows a more significant discrepancy from the experimental data for operating cases loaded with more EGR. Additionally, NO_x results from CFD simulations exceed the experimental NO_x concentrations in all four operating ICE cases. Since the same conditions are applied for all operating conditions, the temperature is the primary generator of NO_x emissions, which results in proportional results between temperature and NO_x emissions for all radiative absorption models. It was observed that the participation of CO_2 and H_2O has a higher impact on the overall radiative heat transfer than soot. From the results, it can be concluded that the SLW model is too computationally demanding for the ICE simulations at the expense of not providing significantly higher accuracy than the SLW-1 model, which features similar computational time as WSGG. Although it does not add significantly increased accuracy in ICE, TRI is recommended for inclusion due to the non-significant increase in computational time. Future work is to adapt the implemented SLW-1 for calculating methane participation in radiative heat transfer for dual-fuel combustion.

5 LITERATURE

[1]   Stančin H, Mikulčić H, Wang X, Duić N. A review on alternative fuels in future energy system. Renewable and Sustainable Energy Reviews 2020;128:109927. https://doi.org/10.1016/j.rser.2020.109927.

[2]   Bohlooli Arkhazloo N, Bouissa Y, Bazdidi-Tehrani F, Jadidi M, Morin J-B, Jahazi M. Experimental and unsteady CFD analyses of the heating process of large size forgings in a gas-fired furnace. Case Studies in Thermal Engineering 2019;14:100428. https://doi.org/10.1016/j.csite.2019.100428.

[3]   Modest MF, Haworth DC. Radiative heat transfer in high-pressure combustion systems. SpringerBriefs in Applied Sciences and Technology, Springer Verlag; 2016, p. 137–48. https://doi.org/10.1007/978-3-319-27291-7_7.

[4]   Benajes J, Martin J, Garcia A, Villalta D, Warey A, Domenech V, et al. An Investigation of Radiation Heat Transfer in a Light-Duty Diesel Engine. SAE Int J Engines 2015;8. https://doi.org/10.4271/2015-24-2443.

[5]   Paul C, Ferreyro Fernandez S, Haworth DC, Roy S, Modest MF. A detailed modeling study of radiative heat transfer in a heavy-duty diesel engine. Combust Flame 2019;200:325–41. https://doi.org/10.1016/j.combustflame.2018.11.032.

[6]   Coelho PJ. Advances in the discrete ordinates and finite volume methods for the solution of radiative heat transfer problems in participating media. J Quant Spectrosc Radiat Transf 2014;145:121–46. https://doi.org/10.1016/j.jqsrt.2014.04.021.

[7]   Fernandez SF, Paul C, Sircar A, Imren A, Haworth DC, Roy S, et al. Soot and spectral radiation modeling for high-pressure turbulent spray flames. Combust Flame 2018;190:402–15. https://doi.org/10.1016/j.combustflame.2017.12.016.

[8]   Fernandez SF, Paul C, Sircar A, Imren A, Haworth DC, Roy S, et al. Soot and spectral radiation modeling for high-pressure turbulent spray flames. Combust Flame 2018;190:402–15. https://doi.org/10.1016/j.combustflame.2017.12.016.

[9]   Skeen S, Manin J, Pickett L, Dalen K, Ivarsson A. Quantitative spatially resolved measurements of total radiation in high-pressure spray flames. SAE Technical Papers 2014;1. https://doi.org/10.4271/2014-01-1252.

[10]   Yue Z, Reitz RD. Numerical investigation of radiative heat transfer in internal combustion engines. Appl Energy 2019;235:147–63. https://doi.org/10.1016/j.apenergy.2018.10.098.

[11]   Benajes J, Martín J, García A, Villalta D, Warey A. In-cylinder soot radiation heat transfer in direct-injection diesel engines. Energy Convers Manag 2015;106:414–27. https://doi.org/10.1016/j.enconman.2015.09.059.

[12] López JJ, García-Oliver JM, García A, Villalta D. Development of a soot radiation model for diesel flames. Appl Therm Eng 2019. https://doi.org/10.1016/j.applthermaleng.2019.04.120.

[13] Coelho PJ. Radiative Transfer in Combustion Systems. Handbook of Thermal Science and Engineering, Cham: Springer International Publishing; 2018, p. 1173–99. https://doi.org/10.1007/978-3-319-26695-4_61.

[14] Dorigon LJ, Duciak G, Brittes R, Cassol F, Galarça M, França FHR. WSGG correlations based on HITEMP2010 for computation of thermal radiation in non-isothermal, non-homogeneous H2O/CO2 mixtures. Int J Heat Mass Transf 2013;64:863–73. https://doi.org/10.1016/j.ijheatmasstransfer.2013.05.010.

[15] Cassol F, Brittes R, Centeno FR, da Silva CV, França FHR. Evaluation of the gray gas model to compute radiative transfer in non-isothermal, non-homogeneous participating medium containing CO2, H2O and soot. Journal of the Brazilian Society of Mechanical Sciences and Engineering 2015;37:163–72. https://doi.org/10.1007/s40430-014-0168-5.

[16] Granate P, Coelho PJ, Roger M. Radiative heat transfer in strongly forward scattering media using the discrete ordinates method. J Quant Spectrosc Radiat Transf 2016;172:110–20. https://doi.org/10.1016/j.jqsrt.2015.12.011.

[17] Ozen G, Selçuk N. SLW model for computational fluid dynamics modeling of combustion systems: Implementation and validation. Numerical Heat Transfer, Part B: Fundamentals 2016;70:47–55. https://doi.org/10.1080/10407790.2016.1173499.

[18] Pearson JT, Webb BW, Solovjov VP, Ma J. Efficient representation of the absorption line blackbody distribution function for H2O, CO2, and CO at variable temperature, mole fraction, and total pressure. J Quant Spectrosc Radiat Transf 2014;138:82–96. https://doi.org/10.1016/j.jqsrt.2014.01.019.

[19] Garten B, Hunger F, Messig D, Stelzner B, Trimis D, Hasse C. Detailed radiation modeling of a partial-oxidation flame. International Journal of Thermal Sciences 2015;87:68–84. https://doi.org/10.1016/j.ijthermalsci.2014.07.022.

[20] Webb BW, Ma J, Pearson JT, Solovjov VP. SLW modeling of radiation transfer in comprehensive combustion predictions. Combustion Science and Technology 2018;190:1392–408. https://doi.org/10.1080/00102202.2018.1452123.

[21] Solovjov VP, Andre F, Lemonnier D, Webb BW. The Generalized SLW Model. J Phys Conf Ser 2016;676. https://doi.org/10.1088/1742-6596/676/1/012022.

[22] Ozen G, Ates C, Selçuk N, Kulah G. Assessment of SLW-1 model in the presence of gray and non-gray particles. International Journal of Thermal Sciences 2019;136:420–32. https://doi.org/10.1016/j.ijthermalsci.2018.10.038.

[23] Viskanta R. Computation of radiative transfer in combustion systems. Int J Numer Methods Heat Fluid Flow 2008;18:415–42. https://doi.org/10.1108/09615530810853664/FULL/PDF.

[24] Benajes J, Martín J, García A, Villalta D, Warey A. In-cylinder soot radiation heat transfer in direct-injection diesel engines. Energy Convers Manag 2015;106:414–27. https://doi.org/10.1016/J.ENCONMAN.2015.09.059.

[25] Yoshikawa T, Reitz RD. Effect of radiation on diesel engine combustion and heat transfer. Journal of Thermal Science and Technology 2009;4:86–97. https://doi.org/10.1299/jtst.4.86.

[26] Benajes J, Martin J, Garcia A, Villalta D, Warey A, Domenech V, et al. An Investigation of Radiation Heat Transfer in a Light-Duty Diesel Engine. SAE Int J Engines 2015;8. https://doi.org/10.4271/2015-24-2443.

[27] Chishty MA, Bolla M, Hawkes E, Pei Y, Kook S. Assessing the Importance of Radiative Heat Transfer for ECN Spray A Using the Transported PDF Method. SAE Int J Fuels Lubr 2016;9:100–7. https://doi.org/10.4271/2016-01-0857.

[28] Paul C, Haworth DC, Modest MF. A simplified CFD model for spectral radiative heat transfer in high-pressure hydrocarbon-air combustion systems. Proceedings of the Combustion Institute 2019;37:4617–24. https://doi.org/10.1016/j.proci.2018.08.024.

[29] Geringer S. Influence of Radiative Heat Transfer on NOx and Soot Formation in Large Two-Stroke Marine Diesel Engines. 2021. https://doi.org/10.3929/ETHZ-B-000489745.

[30] Coelho PJ, Aelenei D. Application of high-order spatial resolution schemes to the hybrid finite volume/finite element method for radiative transfer in participating media. Int J Numer Methods Heat Fluid Flow 2008;18:173–84. https://doi.org/10.1108/09615530810846329/FULL/PDF.

[31] Jurić F, Petranović Z, Vujanović M, Duić N. Numerical assessment of radiative heat transfer impact on pollutant formation processes in a compression ignition engine. J Clean Prod 2020;275:123087. https://doi.org/10.1016/J.JCLEPRO.2020.123087.

[32] Mukut KM, Roy SP. Effect of O2 concentration in ambient mixture and multiphase radiation on pollutant formation in ECN spray-A. Combustion Theory and Modelling 2020;24:549–72. https://doi.org/10.1080/13647830.2020.1721561.

[33] Jurić F, Coelho PJ, Priesching P, Duić N, Honus S, Vujanović M. Implementation of the spectral line-based weighted-sum-of-gray-gases model in the finite volume method for radiation modeling in internal combustion engines. Int J Energy Res 2022. https://doi.org/10.1002/er.8177.

[34] Solovjov VP, Webb BW. Global Spectral Methods in Gas Radiation: The Exact Limit of the SLW Model and Its Relationship to the ADF and FSK Methods. J Heat Transfer 2011;133. https://doi.org/10.1115/1.4002775.

[35] Yadav R, Balaji C, Venkateshan SP. Implementation of SLW model in the radiative heat transfer problems with particles and high temperature gradients. Int J Numer Methods Heat Fluid Flow 2017;27:1128–41. https://doi.org/10.1108/HFF-03-2016-0095/FULL/PDF.

[36] Doner N, Selçuk N. An application of Spectral line-based weighted sum of grey gases (SLW) model with geometric optics approximation for radiative heat transfer in 3-D participating media. Appl Therm Eng 2013;50:89–93. https://doi.org/10.1016/j.applthermaleng.2012.05.035.

[37] Galtier M, Woelffel W, André F, Solovjov VP, Webb BW, Roy S. Assessment of narrow-band and full spectrum gas radiation methods in a real industrial glass furnace configuration. Appl Therm Eng 2022;216:119020. https://doi.org/10.1016/j.applthermaleng.2022.119020.

[38] Solovjov VP, Lemonnier D, Webb BW. The SLW-1 model for efficient prediction of radiative transfer in high temperature gases. J Quant Spectrosc Radiat Transf 2011;112:1205–12. https://doi.org/10.1016/j.jqsrt.2010.08.009.

[39] Solovjov VP, Lemonnier D, Webb BW. SLW-1 modeling of radiative heat transfer in nonisothermal nonhomogeneous gas mixtures with soot. J Heat Transfer 2011;133. https://doi.org/10.1115/1.4003903.

[40] Węcel G, Ostrowski Z, Kozozub P. Absorption line black body distribution function evaluated with proper orthogonal decomposition for mixture of CO2 and H2O. Int J Numer Methods Heat Fluid Flow 2014;24:932–48. https://doi.org/10.1108/HFF-04-2013-0142/FULL/PDF.

[41] Yasar MS, Ozen G, Selçuk N, Kulah G. Performance of banded SLW-1 in presence of non-gray walls and particles in fluidized bed combustors. J Quant Spectrosc Radiat Transf 2020;257:107370. https://doi.org/10.1016/j.jqsrt.2020.107370.

[42] Coelho PJ. Numerical simulation of the interaction between turbulence and radiation in reactive flows. Prog Energy Combust Sci 2007;33:311–83. https://doi.org/10.1016/j.pecs.2006.11.002.

[43] Coelho PJ. Turbulence-radiation interaction: From theory to application in numerical simulations. J Heat Transfer 2012;134. https://doi.org/10.1115/1.4005130.

[44] Bolla M, Farrace D, Wright YM, Boulouchos K, Mastorakos E. Influence of turbulence-chemistry interaction for n-heptane spray combustion under diesel engine conditions with emphasis on soot formation and oxidation. Combustion Theory and Modelling 2014;18:330–60. https://doi.org/10.1080/13647830.2014.898795.

[45] Lion S, Vlaskos I, Taccani R. A review of emissions reduction technologies for low and medium speed marine Diesel engines and their potential for waste heat recovery. Energy Convers Manag 2020;207:112553. https://doi.org/10.1016/j.enconman.2020.112553.

[46] López JJ, García A, Monsalve-Serrano J, Cogo V, Wittek K. Potential of a two-stage variable compression ratio downsized spark ignition engine for passenger cars under different driving conditions. Energy Convers Manag 2020;203:112251. https://doi.org/10.1016/j.enconman.2019.112251.

[47] Hao C, Lu Z, Feng Y, Bai H, Wen M, Wang T. Optimization of fuel/air mixing and combustion process in a heavy-duty diesel engine using fuel split device. Appl Therm Eng 2021;186:116458. https://doi.org/10.1016/j.applthermaleng.2020.116458.

[48] Cerinski D, Vujanović M, Petranović Z, Baleta J, Samec N, Hriberšek M. Numerical analysis of fuel injection configuration on nitrogen oxides formation in a jet engine combustion chamber. Energy Convers Manag 2020;220:112862. https://doi.org/10.1016/j.enconman.2020.112862.

[49] Geng L, Li S, Xiao Y, Xie Y, Chen H, Chen X. Effects of injection timing and rail pressure on combustion characteristics and cyclic variations of a common rail DI engine fuelled with F-T diesel synthesized from coal. Journal of the Energy Institute 2020;93:2148–62. https://doi.org/10.1016/j.joei.2020.05.009.

[50] Huang H, Zhu Z, Chen Y, Chen Y, Lv D, Zhu J, et al. Experimental and numerical study of multiple injection effects on combustion and emission characteristics of natural gas–diesel dual-fuel engine. Energy Convers Manag 2019;183:84–96. https://doi.org/10.1016/j.enconman.2018.12.110.

[51] Xu M, Cheng W, Zhang H, An T, Zhang S. Effect of diesel pre-injection timing on combustion and emission characteristics of compression ignited natural gas engine. Energy Convers Manag 2016;117:86–94. https://doi.org/10.1016/j.enconman.2016.02.054.

[52] Abdul Gafoor CP, Gupta R. Numerical investigation of piston bowl geometry and swirl ratio on emission from diesel engines. Energy Convers Manag 2015;101:541–51. https://doi.org/10.1016/j.enconman.2015.06.007.

[53] Shirvani S, Shirvani S, Shamekhi AH, Reitz RD. An Investigation of the Effects of the Piston Bowl Geometries of a Heavy-Duty Engine on Performance and Emissions Using Direct Dual Fuel Stratification Strategy, and Proposing Two New Piston Profiles. SAE Int J Engines 2020;13:03-13-03–0021. https://doi.org/10.4271/03-13-03-0021.

[54] Petranović Z, Edelbauer W, Vujanović M, Duić N. Modelling of spray and combustion processes by using the Eulerian multiphase approach and detailed chemical kinetics. Fuel 2017;191:25–35. https://doi.org/10.1016/j.fuel.2016.11.051.

[55] Józsa V, Hidegh G, Kun-Balog A, Ng J-H, Chong CT. Ultra-low emission combustion of diesel-coconut biodiesel fuels by a mixture temperature-controlled combustion mode. Energy Convers Manag 2020;214:112908. https://doi.org/10.1016/j.enconman.2020.112908.

[56] Pranoto H, Wahab A, Arifin Z, Siswanto I. Fuel filter condition monitoring (ffcm) devices innovation on truck diesel engine to prevent filter blocking due to use of bio diesel: b10-b20-b30. J Phys Conf Ser 2020;1700:012099. https://doi.org/10.1088/1742-6596/1700/1/012099.

[57] Lazaroiu G, Pană C, Mihaescu L, Cernat A, Negurescu N, Mocanu R, et al. Solutions for energy recovery of animal waste from leather industry. Energy Convers Manag 2017;149:1085–95. https://doi.org/10.1016/j.enconman.2017.06.042.

[58] Westbrook CK, Pitz WJ, Herbinet O, Curran HJ, Silke EJ. A comprehensive detailed chemical kinetic reaction mechanism for combustion of n-alkane hydrocarbons from n-octane to n-hexadecane. Combust Flame 2009;156:181–99. https://doi.org/10.1016/j.combustflame.2008.07.014.

[59] Novella R, García A, Pastor JM, Domenech V. The role of detailed chemical kinetics on CFD diesel spray ignition and combustion modelling. Math Comput Model 2011;54:1706–19. https://doi.org/10.1016/j.mcm.2010.12.048.

[60] Gopinath S, Devan PK, Sabarish V, Sabharish Babu BV, Sakthivel S, Vignesh P. Effect of spray characteristics influences combustion in DI diesel engine – A review. Mater Today Proc 2020;33:52–65. https://doi.org/10.1016/j.matpr.2020.03.130.

[61] Juric F, Vujanovic M, Zivic M, Holik M, Wang X, Duic N. Assessment of radiative heat transfer impact on a temperature distribution inside a real industrial swirled furnace. Thermal Science 2020:285–285. https://doi.org/10.2298/TSCI200407285J.

[62] Desantes JM, García-Oliver JM, Novella R, Pérez-Sánchez EJ. Application of a flamelet-based CFD combustion model to the LES simulation of a diesel-like reacting spray. Comput Fluids 2020;200:104419. https://doi.org/10.1016/j.compfluid.2019.104419.

[63] van Oijen JA, Donini A, Bastiaans RJM, ten Thije Boonkkamp JHM, de Goey LPH. State-of-the-art in premixed combustion modeling using flamelet generated manifolds. Prog Energy Combust Sci 2016;57:30–74. https://doi.org/10.1016/j.pecs.2016.07.001.

[64] Eder L, Ban M, Pirker G, Vujanovic M, Priesching P, Wimmer A. Development and Validation of 3D-CFD Injection and Combustion Models for Dual Fuel Combustion in Diesel Ignited Large Gas Engines. Energies (Basel) 2018;11:643. https://doi.org/10.3390/en11030643.

[65] Peters N. Laminar flamelet concepts in turbulent combustion. Symposium (International) on Combustion 1988;21:1231–50. https://doi.org/10.1016/S0082-0784(88)80355-2.

[66] Beeckmann J, Hesse R, Kruse S, Berens A, Peters N, Pitsch H, et al. Propagation speed and stability of spherically expanding hydrogen/air flames: Experimental study and asymptotics. Proceedings of the Combustion Institute 2017;36:1531–8. https://doi.org/10.1016/j.proci.2016.06.194.

[67] Colin O, Benkenida A, Angelberger C. 3D modeling of mixing, ignition and combustion phenomena in highly stratified gasoline engines. Oil and Gas Science and Technology 2003;58:47–62. https://doi.org/10.2516/ogst:2003004.

[68] Colin O, Benkenida A. The 3-zones Extended Coherent Flame Model (ECFM3Z) for computing premixed/diffusion combustion. Oil and Gas Science and Technology 2004;59:593–609. https://doi.org/10.2516/ogst:2004043.

[69] Tap FA, Hilbert R, Thévenin D, Veynante D. A generalized flame surface density modelling approach for the auto-ignition of a turbulent non-premixed system. Combustion Theory and Modelling 2004;8:165–93. https://doi.org/10.1088/1364-7830/8/1/009.

[70] Béard P, Colin O, Miche M. Improved modelling of di diesel engines using sub-grid descriptions of spray and combustion. SAE Technical Papers 2003. https://doi.org/10.4271/2003-01-0008.

[71] Catapano F, Costa M, Marseglia G, Sementa P, Sorge U, Vaglieco BM. Experimental and Numerical Investigation in a Turbocharged GDI Engine Under Knock Condition by Means of Conventional and Non-Conventional Methods. SAE Int J Engines 2015;8:437–46. https://doi.org/10.4271/2015-01-0397.

[72] Bohbot J, Colin O, Velghe A, Michel JB, Wang M, Senecal PK, et al. An Innovative Approach Combining Adaptive Mesh Refinement, the ECFM3Z Turbulent Combustion Model, and the TKI Tabulated Auto-Ignition Model for Diesel Engine CFD Simulations. SAE Technical Papers 2016. https://doi.org/10.4271/2016-01-0604.

[73] Hidegh G, Csemány D, Vámos J, Kavas L, Józsa V. Mixture Temperature-Controlled combustion of different biodiesels and conventional fuels. Energy 2021;234:121219. https://doi.org/10.1016/J.ENERGY.2021.121219.

[74] Hann S, Grill M, Bargende M. Laminar Flame Speed Engine Simulation of Lean Combustion and Exhaust Gas Recirculation at High Load. MTZ Worldwide 2018;79:26–33. https://doi.org/10.1007/s38313-018-0002-z.

[75] Koch J, Geringer S, Farrace D, Pandurangi S, Bolla M, Wright YM, et al. Assessment of Two Premixed LES Combustion Models in an Engine-Like Geometry. SAE Technical Papers 2018;2018-April. https://doi.org/10.4271/2018-01-0176.

[76] Fossi A, DeChamplain A. Large eddy simulation of spark ignition of a bluff-body stabilized burner using a subgrid-ignition model coupled with FGM-based combustion models. Int J Numer Methods Heat Fluid Flow 2017;27:400–27. https://doi.org/10.1108/HFF-07-2015-0299/FULL/PDF.

[77] Wang Z, Liu H, Reitz RD. Knocking combustion in spark-ignition engines. Prog Energy Combust Sci 2017;61:78–112. https://doi.org/10.1016/j.pecs.2017.03.004.

[78] Bougrine S, Richard S, Michel JB, Veynante D. Simulation of CO and NO emissions in a SI engine using a 0D coherent flame model coupled with a tabulated chemistry approach. Appl Energy 2014;113:1199–215. https://doi.org/10.1016/j.apenergy.2013.08.038.

[79] Sjerić M, Kozarac D, Schuemie H, Tatschl R. A new quasi-dimensional flame tracking combustion model for spark ignition engines. Energy Convers Manag 2018;165:263–75. https://doi.org/10.1016/j.enconman.2018.03.008.

[80] Mobasheri R, Peng Z, Mirsalim SM. Analysis the effect of advanced injection strategies on engine performance and pollutant emissions in a heavy duty DI-diesel engine by CFD modeling. Int J Heat Fluid Flow 2012;33:59–69. https://doi.org/10.1016/j.ijheatfluidflow.2011.10.004.

[81] Fossi A, DeChamplain A, Akih-Kumgeh B. Unsteady RANS and scale adaptive simulations of a turbulent spray flame in a swirled-stabilized gas turbine model combustor using tabulated chemistry. Int J Numer Methods Heat Fluid Flow 2015;25:1064–88. https://doi.org/10.1108/HFF-09-2014-0272/FULL/PDF.

[82] Jurić F, Ban M, Priesching P, Schmalhorst C, Duić N, Vujanović M. Numerical modeling of laminar flame speed and autoignition delay using general fuel-independent function. Fuel 2022;323:124432. https://doi.org/10.1016/j.fuel.2022.124432.

[83] Colin O, Benkenida A, Angelberger C. 3D Modeling of Mixing, Ignition and Combustion Phenomena in Highly Stratified Gasoline Engines. vol. 58. 2003.

[84] Oijen JA Van, Goey LPH De. Modelling of Premixed Laminar Flames using Flamelet-Generated Manifolds. Combustion Science and Technology 2000;161:113–37. https://doi.org/10.1080/00102200008935814.

[85] Donini A, M. Bastiaans RJ, van Oijen JA, H. de Goey LP. A 5-D Implementation of FGM for the Large Eddy Simulation of a Stratified Swirled Flame with Heat Loss in a Gas Turbine Combustor. vol. 98. Flow, Turbulence and Combustion; 2017. https://doi.org/10.1007/s10494-016-9777-7.

[86] Tvrdojevic M, Vujanovic M, Priesching P, Tap FA, Starikov A, Goryntsev D, et al. Implementation of the Semi Empirical Kinetic Soot Model within Chemistry Tabulation Framework for Efficient Emissions Predictions in Diesel Engines. Open Physics 2020;17:905–15. https://doi.org/10.1515/phys-2019-0096.

[87] Priesching P, Tvrdojevic M, Tap F, Meijer C. Prediction of the Combustion and Emission Processes in Diesel Engines Based on a Tabulated Chemistry Approach. SAE Tech Pap 2017. https://doi.org/10.4271/2017-01-2200.

[88] Mobasheri R. Analysis the ECFM-3Z Combustion Model for Simulating the Combustion Process and Emission Characteristics in a HSDI Diesel Engine. International Journal of

Spray and Combustion Dynamics 2015;7:353–71. https://doi.org/10.1260/1756-8277.7.4.353.

[89] Cai L, Jacobs S, Langer R, vom Lehn F, Heufer KA, Pitsch H. Auto-ignition of oxymethylene ethers (OMEn, n = 2–4) as promising synthetic e-fuels from renewable electricity: shock tube experiments and automatic mechanism generation. Fuel 2020;264:116711. https://doi.org/10.1016/j.fuel.2019.116711.

[90] Bradley D, Kalghatgi GT. Influence of autoignition delay time characteristics of different fuels on pressure waves and knock in reciprocating engines. Combust Flame 2009;156:2307–18. https://doi.org/10.1016/j.combustflame.2009.08.003.

[91] Wang W, Gowdagiri S, Oehlschlaeger MA. The high-temperature autoignition of biodiesels and biodiesel components. Combust Flame 2014;161:3014–21. https://doi.org/10.1016/j.combustflame.2014.06.009.

[92] Shahridzuan Abdullah I, Khalid A, Jaat N, Saputra Nursal R, Koten H, Karagoz Y. A study of ignition delay, combustion process and emissions in a high ambient temperature of diesel combustion. Fuel 2021;297:120706. https://doi.org/10.1016/j.fuel.2021.120706.

[93] Rajak U, Nashine P, Chaurasiya PK, Verma TN, Patel DK, Dwivedi G. Experimental & predicative analysis of engine characteristics of various biodiesels. Fuel 2021;285:119097. https://doi.org/10.1016/j.fuel.2020.119097.

[94] Rajak U, Nashine P, Dasore A, Balijepalli R, Kumar Chaurasiya P, Nath Verma T. Numerical analysis of performance and emission behavior of CI engine fueled with microalgae biodiesel blend. Mater Today Proc 2021. https://doi.org/10.1016/j.matpr.2021.02.104.

[95] Mullan Karishma S, Dasore A, Rajak U, Nath Verma T, Prahlada Rao K, Omprakash B. Experimental examination of CI engine fueled with various blends of diesel-apricot oil at different engine operating conditions. Mater Today Proc 2021. https://doi.org/10.1016/j.matpr.2021.02.105.

[96] Xuan T, Sun Z, EL-Seesy AI, Mi Y, Zhong W, He Z, et al. An optical study on spray and combustion characteristics of ternary hydrogenated catalytic biodiesel/methanol/n-octanol blends; part I: Spray morphology, ignition delay, and flame lift-off length. Fuel 2021;289:119762. https://doi.org/10.1016/j.fuel.2020.119762.

[97] Kobashi Y, Todokoro M, Shibata G, Ogawa H, Mori T, Imai D. EGR gas composition effects on ignition delays in diesel combustion. Fuel 2020;281:118730. https://doi.org/10.1016/j.fuel.2020.118730.

[98] Lawson R, Gururajan V, Movaghar A, Egolfopoulos FN. Autoignition of reacting mixtures at engine-relevant conditions using confined spherically expanding flames.

Proceedings of the Combustion Institute 2021;38:2285–93. https://doi.org/10.1016/j.proci.2020.06.224.

[99] Rahnama P, Arab M, Reitz RD. A Time-Saving Methodology for Optimizing a Compression Ignition Engine to Reduce Fuel Consumption through Machine Learning. SAE Int J Engines 2020;13:03-13-02–0019. https://doi.org/10.4271/03-13-02-0019.

[100] Vignesh R, Ashok B. Deep neural network model-based global calibration scheme for split injection control map to enhance the characteristics of biofuel powered engine. Energy Convers Manag 2021;249:114875. https://doi.org/10.1016/j.enconman.2021.114875.

[101] Han W, Sun Z, Scholtissek A, Hasse C. Machine Learning of ignition delay times under dual-fuel engine conditions. Fuel 2021;288:119650. https://doi.org/10.1016/j.fuel.2020.119650.

[102] Misdariis A, Vermorel O, Poinsot T. A methodology based on reduced schemes to compute autoignition and propagation in internal combustion engines. Proceedings of the Combustion Institute 2015;35:3001–8. https://doi.org/10.1016/j.proci.2014.06.053.

[103] Del Pecchia M, Breda S, D'Adamo A, Fontanesi S, Irimescu A, Merola S. Development of Chemistry-Based Laminar Flame Speed Correlation for Part-Load SI Conditions and Validation in a GDI Research Engine. SAE Int J Engines 2018;11:2018-01–0174. https://doi.org/10.4271/2018-01-0174.

[104] Del Pecchia M, Pessina V, Berni F, d'Adamo A, Fontanesi S. Gasoline-ethanol blend formulation to mimic laminar flame speed and auto-ignition quality in automotive engines. Fuel 2020;264:116741. https://doi.org/10.1016/j.fuel.2019.116741.

[105] D'Adamo A, Del Pecchia M, Breda S, Berni F, Fontanesi S, Prager J. Chemistry-Based Laminar Flame Speed Correlations for a Wide Range of Engine Conditions for Iso-Octane, n-Heptane, Toluene and Gasoline Surrogate Fuels, 2017. https://doi.org/10.4271/2017-01-2190.

[106] Verhelst S, T'Joen C, Vancoillie J, Demuynck J. A correlation for the laminar burning velocity for use in hydrogen spark ignition engine simulation. Int J Hydrogen Energy 2011;36:957–74. https://doi.org/10.1016/j.ijhydene.2010.10.020.

[107] Ji C, Liu X, Wang S, Gao B, Yang J. Development and validation of a laminar flame speed correlation for the CFD simulation of hydrogen-enriched gasoline engines. Int J Hydrogen Energy 2013;38:1997–2006. https://doi.org/10.1016/j.ijhydene.2012.11.139.

[108] Liu X, Ji C, Gao B, Wang S, Liang C, Yang J. A laminar flame speed correlation of hydrogen–methanol blends valid at engine-like conditions. Int J Hydrogen Energy 2013;38:15500–9. https://doi.org/10.1016/j.ijhydene.2013.09.031.

[109] Modest MF. Radiative Heat Transfer. 3rd ed. Elsevier; 2013. https://doi.org/10.1016/B978-0-12-503163-9.X5000-0.

[110] Coelho PJ. on the Convergence of the Discrete Ordinates and Finite Volume Methods for the Solution of the Radiative Transfer Equation 2013;M.

[111] Cassol F, Brittes R, Centeno FR, da Silva CV, França FHR. Evaluation of the gray gas model to compute radiative transfer in non-isothermal, non-homogeneous participating medium containing CO2, H2O and soot. Journal of the Brazilian Society of Mechanical Sciences and Engineering 2015;37:163–72. https://doi.org/10.1007/s40430-014-0168-5.

[112] Pearson JT, Webb BW, Solovjov VP, Ma J. Efficient representation of the absorption line blackbody distribution function for H2O, CO2, and CO at variable temperature, mole fraction, and total pressure. J Quant Spectrosc Radiat Transf 2014;138:82–96. https://doi.org/10.1016/j.jqsrt.2014.01.019.

[113] Pearson JT, Webb BW, Solovjov VP, Ma J. Efficient representation of the absorption line blackbody distribution function for H2O, CO2, and CO at variable temperature, mole fraction, and total pressure. J Quant Spectrosc Radiat Transf 2014;138:82–96. https://doi.org/10.1016/j.jqsrt.2014.01.019.

[114] Jurić F, Petranović Z, Vujanović M, Duić N. Numerical assessment of radiative heat transfer impact on pollutant formation processes in a compression ignition engine. J Clean Prod 2020;275. https://doi.org/10.1016/j.jclepro.2020.123087.

[115] Dorigon LJ, Duciak G, Brittes R, Cassol F, Galarça M, França FHR. WSGG correlations based on HITEMP2010 for computation of thermal radiation in non-isothermal, non-homogeneous H2O/CO2 mixtures. Int J Heat Mass Transf 2013;64:863–73. https://doi.org/10.1016/j.ijheatmasstransfer.2013.05.010.

[116] Jurić F, Vujanović M, Zivic M, Holik M, Wang X, Duic N. Assessment of radiative heat transfer impact on a temperature distribution inside a real industrial swirled furnace. Thermal Science 2020;24:3663–72. https://doi.org/10.2298/TSCI200407285J.

[117] Webb BW, Solovjov VP, André F. The spectral line weighted-sum-of-gray-gases (SLW) model for prediction of radiative transfer in molecular gases, 2019, p. 207–98. https://doi.org/10.1016/bs.aiht.2019.08.003.

[118] Colin O, Benkenida A. The 3-Zones Extended Coherent Flame Model \(Ecfm3z\) for Computing Premixed/Diffusion Combustion; The 3-Zones Extended Coherent Flame Model \(Ecfm3z\) for Computing Premixed/Diffusion Combustion 2004. https://doi.org/10.2516/ogst:2004043ï.

[119] Eder L, Ban M, Pirker G, Vujanovic M, Priesching P, Wimmer A. Development and validation of 3D-CFD injection and combustion models for dual fuel combustion in diesel ignited large gas engines. Energies (Basel) 2018;11. https://doi.org/10.3390/en11030643.

76

[120] Knop V, Jay S. Latest Developments in Gasoline Auto-Ignition Modelling Applied to an Optical CAI (Tm) Engine. Oil & Gas Science and Technology 2006;61:121–37. https://doi.org/10.2516/ogst:2006008x.

[121] da Cruz AP. THREE-DIMENSIONAL MODELING OF SELF-IGNITION IN HCCI AND CONVENTIONAL DIESEL ENGINES. Combustion Science and Technology 2004;176:867–87. https://doi.org/10.1080/00102200490428503.

[122] Crowe CT, Schwarzkopf JD, Sommerfeld M, Tsuji Y. Multiphase Flows with Droplets and Particles. Taylor & Francis Group; 2012.

[123] Ferziger JH, Peric M. Computational Methods for Fluid Dynamics. 2002. https://doi.org/10.1016/S0898-1221(03)90046-0.

[124] Schiller L, Naumann AZ. VDI 77 1933:318–20.

[125] Cunningham E. On the velocity of steady fall of spherical particles through fluid medium. Proceedings of the Royal Society of London Series A, Containing Papers of a Mathematical and Physical Character 1910;83:357–65. https://doi.org/10.1098/rspa.1910.0024.

[126] Reitz RD, Diwakar R. Structure of High-Pressure Fuel Sprays, 1987. https://doi.org/10.4271/870598.

[127] Liu AB, Mather D, Reitz RD. Modeling the Effects of Drop Drag and Breakup on Fuel Sprays, 1993. https://doi.org/10.4271/930072.

[128] Jiro S, Kobayashi M, Iwashita S, Fujimoto H. Modeling of Diesel Spray Impingement on a Flat Wall, 1994. https://doi.org/10.4271/941894.

[129] Abramzon B, Sazhin S. Convective vaporization of a fuel droplet with thermal radiation absorption. Fuel 2006;85:32–46. https://doi.org/10.1016/j.fuel.2005.02.027.

[130] Abramzon B, Sirignano WA. Droplet vaporization model for spray combustion calculations. Int J Heat Mass Transf 1989;32:1605–18. https://doi.org/10.1016/0017-9310(89)90043-4.

[131] Pang KM, Ng HK, Gan S. Investigation of fuel injection pattern on soot formation and oxidation processes in a light-duty diesel engine using integrated CFD-reduced chemistry. Fuel 2012;96:404–18. https://doi.org/10.1016/j.fuel.2012.01.002.

[132] Wu S, Zhou D, Yang W. Implementation of an efficient method of moments for treatment of soot formation and oxidation processes in three-dimensional engine simulations. Appl Energy 2019;254. https://doi.org/10.1016/j.apenergy.2019.113661.

[133] Fiveland WA. Discrete-Ordinates Solutions of the Radiative Transport Equation for Rectangular Enclosures. J Heat Transfer 1984;106:699. https://doi.org/10.1115/1.3246741.

[134] Dua SS, Ping C. Multi-dimensional radiative transfer in non-isothermal cylindrical media with non-isothermal bounding walls. Int J Heat Mass Transf 1975;18:245–59. https://doi.org/10.1016/0017-9310(75)90157-X.

[135] Denison MK. The Spectral-Line Weighted-Sum-of- Gray-Gases Model for Arbitrary RTE Solvers. PhD Dissertation, Brigham Young University, 1994.

[136] Ren S, Wang Z, Li B, Liu H, Wang J. Development of a reduced polyoxymethylene dimethyl ethers (PODEn) mechanism for engine applications. Fuel 2019;238:208–24. https://doi.org/10.1016/j.fuel.2018.10.111.

[137] Sun W, Wang G, Li S, Zhang R, Yang B, Yang J, et al. Speciation and the laminar burning velocities of poly(oxymethylene) dimethyl ether 3 (POMDME3) flames: An experimental and modeling study. Proceedings of the Combustion Institute 2017;36:1269–78. https://doi.org/10.1016/j.proci.2016.05.058.

[138] Lin Q, Tay KL, Zhou D, Yang W. Development of a compact and robust Polyoxymethylene Dimethyl Ether 3 reaction mechanism for internal combustion engines. Energy Convers Manag 2019;185:35–43. https://doi.org/10.1016/j.enconman.2019.02.007.

[139] Gülder ÖL. Correlations of Laminar Combustion Data for Alternative S.I. Engine Fuels, 1984. https://doi.org/10.4271/841000.

6 CURRICULUM VITAE

FILIP JURIĆ mag.ing.mech. was born on the 24th of March 1993 in Zagreb, Croatia. After finishing the high school "XV. Gymnasium" in Zagreb in 2011 as one of the best students in his generation, he received the right to direct enrolment at the Faculty of Mechanical Engineering and Naval Architecture (FMENA), University of Zagreb, where he finished the undergraduate studies in mechanical engineering in 2014 (with honours – Summa Cum Laude, and Faculty medal), and the graduate studies in 2016 (with honours – Summa Cum Laude, and Faculty medal). Immediately after finishing his studies, he got employed at the Faculty of Mechanical Engineering and Naval Architecture, University of Zagreb, at the Department of Power, Energy and Environmental Engineering as a research assistant and a PhD student. As a member of the CFD PowerLab group, he worked on an industrial project with the company AVL List GmbH from Graz, as part of which the topic of his PhD was defined. He has worked on several EU funded and Croatian-Chinese bilateral projects. He currently works as a team member on the RESIN project, financed by the European Regional Development Fund, Operational Programme Competitiveness and Cohesion 2014−2020.

He attended numerous international scientific conferences. He has been a part of the local organising committee of the 8th European Combustion Meeting 2017 and international SDEWES conferences in 2017, 2019, 2021, and 2022. He is the author of 10 scientific papers published in renowned (CC/SCI indexed) journals. His current Scopus h-index is 6. He serves as a reviewer for Renewable and Sustainable Energy Reviews, Journal of Cleaner Production, Fuel, Applied Thermal Engineering, International Journal of Thermal Science, Journal of Environmental Management, Combustion Science and Technology, Open Physics, Thermal Science, and Energy Sources, Part A: Recovery, Utilisation, and Environmental Effects. He speaks and writes English and German.

List of published scientific journal papers:

1. Jurić, Filip; Ban, Marko; Priesching, Peter; Schmalhorst, Carsten; Duić, Neven; Vujanović, Milan: Numerical modeling of laminar flame speed and autoignition delay using general fuel-independent function. // Fuel (Guildford), 323 (2022), 1-10 doi:10.1016/j.fuel.2022.124432

2. Jurić, Filip; Coelho, Pedro J.; Priesching, Peter; Duić, Neven; Honus, Stanislav; Vujanović, Milan: Implementation of the spectral line-based weighted-sum-of-gray-gases model in the finite volume method for radiation modeling in internal combustion engines. //

International journal of energy research, 46 (2022), 14; 20265-20278 doi:10.1002/er.8177

3. Jurić, Filip; Stipić, Marija; Samec, Niko; Hriberšek, Matjaž; Honus, Stanislav; Vujanović, Milan: Numerical investigation of multiphase reactive processes using flamelet generated manifold approach and extended coherent flame combustion model. // Energy Conversion and Management, 240 (2021), 114261, 12 doi:10.1016/j.enconman.2021.114261

4. Hrnčić, Boris; Pfeifer, Antun; Jurić, Filip; Duić, Neven; Ivanović, Vladan; Vušanović, Igor: Different investment dynamics in energy transition towards a 100% renewable energy system. // Energy (Oxford), 237 (2021), 121526, 11 doi:10.1016/j.energy.2021.121526

5. Bedoić, Robert; Jurić, Filip; Ćosić, Boris; Pukšec, Tomislav; Čuček, Lidija; Duić, Neven: Beyond energy crops and subsidised electricity – A study on sustainable biogas production and utilisation in advanced energy markets. // Energy, 201 (2020), 117651, 12 doi:10.1016/j.energy.2020.117651

6. Jurić, Filip; Petranović, Zvonimir; Vujanović, Milan; Duić, Neven: Numerical assessment of radiative heat transfer impact on pollutant formation processes in a compression ignition engine. // Journal of cleaner production, 275 (2020), 1-13 doi:10.1016/j.jclepro.2020.123087

7. Jurić, Filip; Vujanović, Milan; Živić, Marija; Holik, Mario; Wang, Xuebin; Duić, Neven: Assessment of radiative heat transfer impact on a temperature distribution inside a real industrial swirled furnace. // Thermal science, 24 (2020), 6A; 3663-3672 doi:10.2298/TSCI200407285J

8. Jurić, Filip; Petranović, Zvonimir; Vujanović, Milan; Katrašnik, Tomaž; Vihar, Rok; Wang Xuebin; Duić, Neven: Experimental and numerical investigation of injection timing and rail pressure impact on combustion characteristics of a diesel engine. // Energy conversion and management, 185 (2019), 1; 730-739 doi:10.1016/j.enconman.2019.02.039

9. Huzjan, Fran; Jurić, Filip; Lončarić, Sven; Vujanović, Milan: Deep Learning-based Image Analysis Method for Estimation of Macroscopic Spray Parameters. // Neural Computing and Applications, (2022)
doi: https://doi.org/10.1007/s00521-022-08184-3

10. Jurić, Filip; Vujanović, Milan; Petranović, Zvonimir: Coupling of Euler Eulerian and Euler Lagrangian Spray Methods with Chemistry Kinetics for Modeling of Reactive Flow and Pollutant Formation // International Multidisciplinary Conference on Computer and Energy Science (SpliTech) Bol, Hrvatska: IEEE, 2021. 1-6 doi:10.23919/splitech52315.2021.9566356

7 SUMMARY OF PAPERS

PAPER 1

Jurić, Filip; Petranović, Zvonimir; Vujanović, Milan; Katrašnik, Tomaž; Vihar, Rok; Wang Xuebin; Duić, Neven: Experimental and numerical investigation of injection timing and rail pressure impact on combustion characteristics of a diesel engine // Energy conversion and management, 185 (2019), https://doi.org/10.1016/j.enconman.2019.02.039

The comparison between two combustion modelling approaches in conjunction with experimental research was conducted on this scale for the first time. In addition to validating the results on both single and multi-injection systems in a real industrial diesel engine, the impacts of injection parameters, including injection timing and rail pressure, were also analysed using a combination of experimental research and numerical simulations. This research also revealed some key insights. The combustion process in diesel engines is mainly governed by chemistry, which leads to better agreement between the results of general gas phase reactions and experimental data in the premixed stage of combustion. Meanwhile, the ECFM-3Z model demonstrates superior prediction of the late combustion phase due to its more accurate representation of mixing time, which depends on turbulence quantities (turbulence kinetic energy and turbulence dissipation rate). The combination of experimental research and numerical simulations presented here can be effectively utilized for further investigation of both single injection and multi-injection parameters that influence the combustion process. Finally, calculated results such as mean pressure and RoHR were compared with experimental data.

In this paper, Jurić was responsible for writing, performing all steps of simulations, and graphical representation of the results. Petranović and Vujanović were responsible for reviewing paper. Katrašnik and Vihar were responsible for experimental measurement, writing and reviewing. Wang and Duić supervised the work.

PAPER 2

Jurić, Filip; Petranović, Zvonimir; Vujanović, Milan; Duić, Neven: Numerical assessment of radiative heat transfer impact on pollutant formation processes in a compression ignition engine // Journal of cleaner production, 275 (2020), https://doi.org/10.1016/j.jclepro.2020.123087

To date, there have been few CFD investigations of radiative heat transfer in internal combustion engines that have combined implemented models for evaluating compression ignition engine emissions and conducting a parameter study of wall emissivity factors and spatial discretization. This research has also uncovered some new insights regarding the impact of radiation on emission formation. The higher soot concentration affects the mean in-cylinder temperature during the combustion process, lowering the mean temperature during both the combustion and expansion phases of the IC engine. The regions with the highest gradients of soot concentration show the most significant difference in temperature profiles between calculations that exclude and include radiative heat transfer within the engine combustion chamber. Furthermore, radiative heat transfer reduces NOx formation concentrations due to the overall lower in-cylinder temperatures. The obtained mean pressure, mean temperature, and heat release results have been validated against experimental data. Finally, the implemented FVM and WSGG in combination with a combustion model in AVL FIRE™ are capable of numerically assessing radiative heat transfer phenomena in IC engines and evaluating their impact on pollutant formation.

In this paper, Jurić was responsible for writing, implementation, validation, numerical simulations and postprocessing of the results. Petranović was responsible for implementing the first version of FVM solver. The paper was reviewed by Vujanović and Duić.

PAPER 3

Jurić, Filip; Vujanović, Milan; Živić, Marija; Holik, Mario; Wang, Xuebin; Duić, Neven: Assessment of radiative heat transfer impact on a temperature distribution inside a real industrial swirled furnace // Thermal science, 24 (2020),
https://doi.org/10.2298/TSCI200407285J

This study aims to analyse radiative heat transfer in participating media using two different radiation models, DTRM and DOM, in conjunction with the Steady Combustion Model by employing the CFD code AVL FIRE™ on an industrial furnace that employs a swirled combustion process. Validation of both radiative heat transfer models demonstrated that the presented modelling procedures are capable of accurately predicting heat transport and can be utilized as a computationally efficient tool to facilitate the design and optimization of industrial

furnaces. The results obtained using both the DTRM and DOM models were in good agreement with experimental results during validation.

In this paper, Jurić was responsible for writing, implementation, validation, numerical simulations and postprocessing of the results. Vujanović was responsible for obtaining validation data, and swirl simulation setup. The paper was reviewed by Živić, Holik, Wang and Duić.

PAPER 4

Jurić, Filip; Stipić, Marija; Samec, Niko; Hriberšek, Matjaž; Honus, Stanislav; Vujanović, Milan: Numerical investigation of multiphase reactive processes using flamelet generated manifold approach and extended coherent flame combustion model // Energy Conversion and Management, **240** (2021), https://doi.org/10.1016/j.enconman.2021.114261

In the present study, the numerical investigation of the single and multi-injection strategy in a direct injection compression ignition engine by utilising the FGM and ECFM-3Z combustion modelling approaches were performed. To the best of our knowledge, a study that compares these two combustion modelling approaches in multiphase reactive systems has not been reported. Apart from the comparison of modelling approaches, the validation of the results on pressure, temperature, rate of heat release, and emission results for both single and multi-injection strategy were analysed in a compression ignition engine.

In this paper, Jurić and Stipić were responsible for writing, implementation, validation, numerical simulations and postprocessing of the results. The paper was reviewed by Samec, Hriberšek, Honus and Vujanović.

PAPER 5

Jurić, Filip; Ban, Marko; Priesching, Peter; Schmalhorst, Carsten; Duić, Neven; Vujanović, Milan: Numerical modeling of laminar flame speed and autoignition delay using general fuel-independent function // Fuel (Guildford), **323** (2022), https://doi.org/10.1016/j.fuel.2022.124432

In this work, the effects of complex chemistry kinetics are reproduced by developing efficient database creation consisting of the relevant ignition data used by existing combustion models. In the pre-processing stage, available reaction mechanisms of several fuels were investigated and validated against existing experimental data of autoignition and laminar flame velocities. The autoignition of fuel/air mixtures for different conditions is pre-tabulated from nondimensional constant pressure reactor calculation. At the same time, the laminar flame speed is pre-tabulated from premixed freely propagating reactors, for which the LOGEsoft™ and Cantera open-source software were used. The data imputation and extrapolation method was developed as a general fuel-independent function. The nonlinear least squares algorithm was employed to fill the unsuccessfully calculated points of databases in the post-processing. In this work, the novel general, fuel-independent procedure is developed and implemented into CFD software based on the lognormal distribution for laminar flame speed in equivalence ratio direction and exponential functions for pressure, temperature, and exhaust gas recirculation directions. Three parameters are used to determine the dependence of the laminar flame speed or autoignition results on pressure and equivalence ratio directions. Additionally, the method is also applicable to dual-fuel combustion. The ignition delay and laminar flame speed values of fuel blends are described with the additional parameter of the fuel composition. Finally, the database implementation is verified with the detailed chemical mechanism of complex internal combustion operating case in computational fluid dynamics and validated with experimental data.

In this paper, Jurić was responsible for writing, implementation, validation, numerical simulations and postprocessing of the results. Ban, Priesching and Schmalhorst were responsible for methodology and supervision. The paper was reviewed by Vujanović and Duić.

PAPER 6

Jurić, Filip; Coelho, Pedro J.; Priesching, Peter; Duić, Neven; Honus, Stanislav; Vujanović, Milan: *Implementation of the spectral line-based weighted-sum-of-gray-gases model in the finite volume method for radiation modeling in internal combustion engines* // International journal of energy research, 46 (2022), 14, https://doi.org/10.1002/er.8177

Based on previous research, the SLW radiative absorption model has been deemed an adequate solution for accurately predicting radiative heat transfer in IC engines with acceptable

computational cost, and was therefore implemented in this work for further investigation. In this paper, the SLW model was implemented in the CFD software AVL FIRE™ as a gas radiative heat transfer estimation approach for predicting the combined absorption coefficient of CO2, H2O, and soot. The SLW model was first validated against analytical data for simple geometries. The predictive accuracy of the AVL FIRE™ code with the SLW model was then assessed for a compression ignition engine operating with a complex 3D moving mesh and rezone procedure computed on multiprocessing units. To the authors' knowledge, the SLW model has not previously been used in conjunction with FVM to model radiative heat transfer in IC engine applications. The combination of SLW and FVM constitutes a robust and computationally feasible solution that is applicable to a wide range of complex industrial applications, such as moving meshes in internal combustion engines. Additionally, few studies have accounted for non-gray thermal radiation using accurate models in IC engines, but instead rely on accurate but time-consuming methods. While thermal radiation in IC engines may play a relatively minor role in light-duty vehicles, the SLW/FVM combination can provide insight into its effect on pollutant formation such as NOx and soot.

In this paper, Jurić was responsible for writing, implementation, validation, numerical simulations and postprocessing of the results. Priesching and Coelho were responsible for methodology and supervision. The paper was reviewed by Honus, Vujanović and Duić.

PAPER 7

Jurić, Filip; Coelho, Pedro J.; Priesching, Peter; Duić, Neven; Vujanović, Milan: Assessment of the Accuracy and Computational Efficiency of the SLW-1 Model in the Numerical Simulation of an Internal Combustion Engine // (Submitted to International Journal of Numerical Methods for Heat & Fluid Flow), under revision

The objective of the present work is to implement the SLW-1 model in combination with TRI for the calculation of radiative transfer in the AVL FIREm™ code. SLW-1 model, and TRI were never implemented in the CFD framework for a complex geometry that features a 3D moving mesh and periodic boundary conditions. The influence of radiative heat transfer and TRI on pollutant emissions in an ICE is investigated.

In this paper, Jurić was responsible for writing, implementation, validation, numerical simulations and postprocessing of the results. Coelho was responsible for writing, supervision

and methodology. Priesching was responsible for methodology and supervision. The paper was reviewed by Vujanović and Duić

PAPER 1

Experimental and Numerical Investigation of Injection Timing and Rail Pressure Impact on Combustion Characteristics of a Diesel Engine

Filip Jurić [*], [a]
e−mail: filip.juric@fsb.hr

Zvonimir Petranović [b]
e−mail: zvonimir.petranovic@avl.com

Milan Vujanović [a]
e−mail: milan.vujanovic@fsb.hr

Tomaž Katrašnik [c]
e−mail: tomaz.katrasnik@fs.uni-lj.si

Rok Vihar [c]
e−mail: rok.vihar@fs.uni-lj.si

Xuebin Wang [d]
e−mail: wxb005@mail.xjtu.edu.cn

Neven Duić [a]
e−mail: neven.duic@fsb.hr

[a] Faculty of Mechanical Engineering and Naval Architecture, University of Zagreb, Ivana Lučića 5, 10000 Zagreb, Croatia
[b] AVL List GmbH Hans-List-Platz 1, 8020 Graz, Austria
[c] Faculty of Mechanical Engineering, University of Ljubljana, Aškerčeva cesta 6 1000 Ljubljana, Slovenia
[d] MOE Key Laboratory of Thermo-Fluid Science and Engineering, Xi'an Jiaotong University, Xi'an, Shaanxi 710049, China
* Corresponding author

ABSTRACT

To explore the influence of fuel injection strategy on the combustion process, the Computational Fluid Dynamics (CFD) simulations were performed, and simulation results were validated against the experimental data measured at different rail pressures and injection timings. The experiments were conducted on a diesel engine equipped with an advanced injection system that allows full control over the injection parameters. To model the combustion process of EN590 diesel fuel, two different approaches were used: the General Gas Phase Reactions (GGPR) approach and the 3-zones Extended Coherent Flame Model (ECFM-3Z+). The calculated results, such as mean pressure and rate of heat release, were validated against experimental data in operating points with different injection parameters in order to prove the validity of spray and combustion sub-models. At the higher injected pressure, GGPR model showed better prediction capability in the premixed phase of combustion process, compared to the ECFM-3Z+ model. Nevertheless, in the rate-controlled phase of combustion process, ECFM-3Z+ model shows stronger diffusion of temperature field, due to the more detailed consideration of combustion diffusion phenomena in the ECFM-3Z+ governing equations. Furthermore, the results show that the rail pressure has a lower impact on the combustion process for injection timing after the Top Dead Centre (TDC). Both, single and multi-injection cases are found to be in a good agreement with the experimental data, while the GGPR approach was found to be suitable only for combustion delay determination and ECFM-3Z+ also for the entire combustion process.

KEYWORDS

Diesel engine, Injection, Combustion, General gas phase reactions, Coherent flame model, Spray

HIGHLIGHTS

- Numerical and experimental research of the single and multi-injection strategy

- Comparison between chemical mechanism n-heptane and combustion model ECFM-3Z+

- Better prediction of the GGPR in the premixed phase for a higher injection pressure

- Better predictions of the ECFM-3Z+ in the rate of heat release peak

- Lower impact of the rail pressure for injection timings after the TDC

NOMENCLATURE

Latin	**Description**	**Unit**
A	Constant in Arrhenius law	
c	Species concentration	mol m^{-3}
C_D	Drag coefficient	
C_P	Cunningham correction factor	
C_1	WAVE breakup model constant 1	
C_2	WAVE breakup model constant 2	
d	Droplet diameter	m
D	Effective diffusion coefficient	m^2 s^{-1}
E_a	Activation energy	J kg^{-1}
f	Frequency	Hz
F_d	Drag force	N
g_i	Cartesian component of the force vector	m s^{-2}
h	Enthalpy	kJ kg^{-1}
H	Total enthalpy interfacial exchange term	kJ kg^{-1}
l	Length of the nozzle	m
m	Mass	kg
$\dot{m}$	Mass flow	kg s^{-1}
M	Molar mass	kg kmol^{-1}
n_{cycl}	Number of cylinders	
n_{nh}	Number of nozzle holes	
p	Pressure	Pa
q	Heat flux	W m^{-2}
q^t	Turbulent heat flux	W m^{-2}
r	Droplet radius	m
R	Ideal gas constant	J (mol K)$^{-1}$
S	Source of extensive property	
t	Time	s
T	Temperature	K
u,v	Velocity	m s^{-1}
V	Volume	m^3

w	Molecular weight of species k	kg kmol^{-1}
x	Cartesian coordinates	m
Y	Mass fraction	

Greek	**Description**	**Unit**
α	Volume fraction	
β	Coefficient in Arrhenius law	
γ	Half outer cone angle	rad
Γ	Diffusion coefficient	
λ_w	Wavelength	m
μ^t	Turbulent viscosity	Pa s
ρ	Density	kg m^{-3}
τ_a	Breakup time	s
φ	Extensive property of general conservation equation	
ω	Reaction rate	
Ω	Wave growth rate	s

1. INTRODUCTION

Despite the increasingly strict emissions standards, diesel fuel continues to be the primary energy source for the transportation systems [1]. The main reason for that is diesel engine higher thermal efficiency when comparing to the spark ignition ones, especially for heavy load transport [2]. Currently, the consumption of diesel fuel in the transportation sector is three times larger than gasoline, with recorded increasing trend [3] which can be addressed to higher conversion efficiency, higher specific power output, and better reliability of diesel engines [4]. Therefore, the researches in more efficient engine operation are flourishing [5].

The overall energy efficiency of diesel engines regarding fuel consumption and pollutant emissions highly depends on the spray and combustion processes. Fuel evaporation, vapour interaction with the surrounding gases, and subsequent combustion are directly determined with the fuel injection strategy [6]. Therefore, to contribute to the diesel engine efficiency increase, the in-depth understanding of evaporation and combustion process is of great importance [7]. To examine the impact of the injection system on the combustion process, it is common to couple the CFD analyses with the experimental research [8]. This approach is capable of getting a validated insight of physical and chemical phenomena inside the cylinder such as temperature field, evaporated fuel, flame zones, emission concentrations, and spray

cloud shape [9]. With such insight and the in-depth understanding of combustion and spray processes, it could be possible to achieve the reduction of emission formation [10]. For example, in [11] the authors combined experimental and numerical approach to determine the possible enhancements of diesel engine design and operation. A detailed investigation of the multi-injection strategy was conducted in [12], where CFD analysis showed the capabilities to model the low-temperature combustion in order to achieve higher efficiency, lower nitric oxides, and lower soot emissions. In [13], the authors showed the possibilities to achieve the higher thermal efficiency of a dual fuel engine by optimising the fuel injection strategy. It is known that the fuel consumption efficiency and pollutant emissions depend on the injection system parameters, piston geometry parameters, and conditions inside the combustion chamber [14]. For example, in [15] the authors presented the optimization process of piston design. A similar procedure can be adopted for injection timing research and influence of fuel injection strategy on the combustion process, as shown in [8] and [16]. Recent numerical researches of diesel engines also focused on the swirl motion [17] and engine cooling influence [18] on the combustion and emission formation processes. Regarding the injection timing, several experimental investigations were carried out to show the influence of multi-injection strategies on the in-cylinder pressure [19]. Most of the experimental studies have been hitherto conducted with a constant injection parameters [20]. Similar experimental investigations for different percentage of animal fat in diesel fuel blends were carried out to quantify their impact on in-cylinder pressure and emissions [21].

The experimental measurements in this research were conducted on an upgraded four-cylinder PSA Diesel 1.6 HDi engine that allows full control over the fuel injection parameters. The multi-injection strategy features the separate pilot and main injections which results in reducing the emissions and engine combustion noise [22]. The Pilot Injection (PI) is used to produce a small amount of vapour that ignites and increases the mean in-cylinder temperature [23]. At later crank angle positions, the Main Injection (MI) follows. In this research, the EN590 diesel fuel that features low sulphur content and it is characterised by a cetane number 51 was used to power the experimental engine [24]. To model the combustion process with the GGPR approach, the n-heptane (C_7H_{16}) chemical mechanism was employed [25]. This mechanism contains skeletal general gas phase reactions of chemical species, where the chemical kinetic was described with the CHEMKIN tabulation [26]. Since the chemical and physical properties of the diesel fuel EN590 in experiments were different from n-heptane, fluid intensive properties were taken from the EN590 database [27]. Such an approach is commonly used in the literature [28].

The main novelty of this research is an analysis of ECFM-3Z+ and GGPR combustion modelling approaches coupled with the experimental investigation on the real industrial IC engine including both single injection and multi-injection strategy. To the best of our

knowledge, the comparison between two combustion modelling approaches together with the experimental research was examined on this scale for the first time. Apart from validating the results on both single and multi-injection system in a real industrial diesel engine, the impacts of injection parameters like injection timing and rail pressure were also analysed with the combination of experimental research and numerical simulations. Furthermore, the research revealed some specific point during the analysis. The combustion process in the Diesel engines is mainly dominated by the chemistry, which effects in the better agreement of the GGPR results with the experimental data in the premixed stage of the combustion. While the ECFM-3Z+ shows a better prediction in the late combustion due to the better description of the mixing time that depends on the turbulence quantities (turbulence kinetic energy and turbulence dissipation rate). The presented combination of experimental research and numerical simulations can be successfully used for further investigation of both single injection and multi-injection parameters that influence the combustion process. Finally, the calculated results such as the mean pressure and the rate of heat release (ROHR) were compared with the experimental data.

2. MATHEMATICAL MODEL

All simulations were performed using the Reynolds-Averaged Navier-Stokes (RANS) equation approach. For the turbulence modelling, the $k - \zeta - f$ turbulence model was employed [29].

2.1. Spray modelling

CFD simulations were performed by using the Euler Lagrangian (EL) modelling approach considering processes such as fuel atomization, droplet evaporation, and vapour combustion [30]. The definition of the EL spray approach is that the two-phase flow is described for a gas phase and a liquid fuel in a different manner. The gas phase is treated as a continuum while the liquid fuel is treated as discrete parcels. The continuum assumption is based on the conservation equations for the finite control volume approach where the fluid flow is divided into a selected number of control volumes [31].

The discrete parcels are tracked through the flow field by using the Lagrangian mechanics. In this research, authors considered only the drag force occurring due to the high relative velocities between the interacting phases. The parcel trajectories are described as:

$$F_{\mathrm{d}i} = m_{\mathrm{p}} \frac{du_{\mathrm{p}i}}{dt}, \tag{1}$$

where the drag force, $F_{\mathrm{d}i}$, is calculated by employing the Schiller Neumann drag law [32]:

$$F_{\text{d}i} = 0.5\pi \, r^2 \rho C_D {u_i}^2,\tag{2}$$

where the drag coefficient C_D is calculated depending on Reynolds number, Re [33]:

$$C_D = \begin{cases} \dfrac{24}{ReC_p}(1 + 0.15Re^{0.687}) & Re < 10^3 \\[2mm] \dfrac{0.44}{C_p} & Re \geq 10^3 \end{cases}.\tag{3}$$

In Equation (3), the C_p is the experimentally determined Cunningham correction factor [33]. When the fuel injection starts the liquid jet disintegrates into smaller droplets. To model the spray disintegration process, the WAVE breakup model was employed [34]. The assumptions of this model are the spherical shape of liquid droplets and proportionality of the wavelength of surface wave and growth of initial perturbations. Thus, the radius of a disintegrated droplet, r_{stable} can be expressed as:

$$r_{stable} = \lambda_w C_1,\tag{4}$$

where C_1 is the model constant, and λ_w is the wavelength of the fastest growing wave on the parcel surface. The rate of parcel radius reduction is calculated according to:

$$\frac{dr}{dt} = -\frac{(r - r_{stable})}{\tau_a},\tag{5}$$

where the modelled breakup time τ_a is defined as:

$$\tau_a = \frac{3.726r \, C_2}{\lambda_w \, \Omega}.\tag{6}$$

The term C_2 in Equation (6) is the constant used to tune the droplet breakup time. The wavelength λ_w and the wave growth rate Ω, occurring in Equation (6) depend on the local flow properties, as discussed in [34].

2.2. Combustion modelling

The combustion process is modelled by using two different approaches; General Gas Phase Reactions (GGPR) and combustion model ECFM-3Z+ [27]. The first approach uses various chemical mechanisms described through species chemical reactions and by using the Arrhenius

law. On the other hand, the ECFM-3Z+ model is one of the coherent flame approaches suitable for the modelling of the combustion process in diesel engines.

2.2.1. General gas phase reactions

The combustion process can be modelled by using chemical kinetics. With such an approach, a higher modelling accuracy can be achieved but with increased computational effort, comparing to the commonly used combustion models. In this work, the skeletal chemical mechanism for n-heptane (C_7H_{16}), described with 46 chemical species and 182 chemical reactions is employed [25]. To obtain the mass fraction of each chemical species in the gaseous phase, an additional transport equation is solved. The calculation of the source term in the species transport equation is calculated as:

$$\omega = A \cdot T^\beta \cdot e^{-\frac{E_a}{RT}}. \tag{7}$$

where the constants A, β and E_a are given in the CHEMKIN tabulation for each reaction and are derived from the experimental investigation [25]. The FIRE™ solver provides the input data of species mass fractions and their thermodynamic data in each cell and calculates their reaction rates based on the perfectly stirred 0D reactor model. The chemical species can originate in chemical reactions as products, but they also can be reactants. If the chemical species is a reactant, it will be modelled as a sink in the corresponding transport equation:

$$\frac{\partial}{\partial t}(\rho y_x) + \frac{\partial}{\partial x_i}(\rho \tilde{u}_i y_x) = \frac{\partial}{\partial x_i}\left(\Gamma_x \frac{\partial y_x}{\partial x_i}\right) + S_x \quad . \tag{8}$$

The species source term S_x in Equation (8) is expressed as a difference between all forward and backwards reactions, considering the concentration of chemical species in these reactions:

$$S_x = \frac{dc_i}{dt} \cdot M_i = \sum_{n=1}^{f} \omega_{n,f} \cdot c_{n,f} \cdot c_{oxy} - \sum_{n=1}^{b} \omega_{n,b} \cdot c_{n,b} \cdot c_{red} \quad , \tag{9}$$

where the index f is the number of forwarding chemical reaction, in which the chemical species are generated, and index b is the number of backwards chemical reactions. In Equation (9), c_{oxy} denotes the molar concentration of the oxidizer and c_{red} denotes the molar concentration of the redactor, and $c_{n,f}$ and $c_{n,b}$ represent molar concentrations of all species that participate in forward chemical reactions, i.e. backwards chemical reactions. The heat released from each reaction is summed up and it is included in the energy conservation equation.

For describing turbulence-chemistry interaction, Probability Density Function (PDF) approach was considered in this work. Probability Density Function in this model is based on the presumed Gaussian Probability Density Function. The temperature T is assumed to be the sum of mean temperature and temperature variance:

$$T = \bar{T} + x \sqrt{\overline{T'T'}} \quad , \tag{10}$$

where the probability density function of x is the standard Gaussian function $p(x)$. The mean value of temperature function can be calculated as approximate quadrature formula:

$$\overline{f(T)} \approx \sum_{k=1}^{n} \left(\bar{T} + x_k \sqrt{\overline{T'T'}} \right) c_k \quad , \tag{11}$$

where the c_k is a coefficient in each node x_k calculated using the formula:

$$c_k = \int_{-\infty}^{\infty} \left(\prod_{j \neq k} \frac{x - x_j}{x_k - x_j} \right)^2 p(x) \, dx \, . \tag{12}$$

Finally, temperature variance is calculated solving its transport equation with its correction factors:

$$\frac{\partial}{\partial t} \left(\rho \overline{T'T'} \right) + \frac{\partial}{\partial x_i} \left(\rho \tilde{u}_i \overline{T'T'} \right) = \frac{\partial}{\partial x_i} \left(\frac{20}{17} \mu_t \frac{\partial \overline{T'T'}}{\partial x_i} \right) + 2.86 \, \mu_t \left(\frac{\partial \bar{T}}{\partial x_i} \right)^2 - 2\rho \frac{\varepsilon}{k} \overline{T'T'} \, . \tag{13}$$

2.2.2. Three-zones Extended Coherent Flame Model

The 3-zones Extended Coherent Flame Model (ECFM-3Z+) is one of the coherent flame models suitable for modelling the combustion process in diesel engines. This model has a decoupled treatment of chemistry and turbulence, which makes it an attractive solution for combustion modelling [35]. Besides the standard species transport equations, the ECFM-3Z+ solves additionally transport equations of 11 chemical species: O_2, N_2, CO_2, CO, H_2, H_2O, O, H, N, OH and NO in each cell [27]:

$$\frac{\partial \bar{\rho} \tilde{y}_x}{\partial t} + \frac{\partial \bar{\rho} \tilde{u}_i \tilde{y}_x}{\partial x_i} - \frac{\partial}{\partial x_i} \left(\left(\frac{\mu}{Sc} + \frac{\mu_t}{Sc_t} \right) \frac{\partial \tilde{y}_x}{\partial x_i} \right) = \overline{\dot{\omega}_x} \, , \tag{14}$$

where $\tilde{y}_x$ is the averaged mass fraction of species x and $\overline{\dot{\omega}_x}$ is the corresponding combustion source term. Furthermore, three transport equation for the fuel mass fraction y_{fu}, mixture fraction f and residual gas mass g have to be solved [27]:

$$\frac{\partial}{\partial t}(\rho y_{fu}) + \frac{\partial}{\partial x_i}(\rho \tilde{u}_i y_{fu}) = \frac{\partial}{\partial x_i}\left(\Gamma_{fu}\frac{\partial y_{fu}}{\partial x_i}\right) + S_{fu} \, , \tag{15}$$

$$\frac{\partial}{\partial t}(\rho f) + \frac{\partial}{\partial x_i}(\rho \tilde{u}_i f) = \frac{\partial}{\partial x_i}\left(\Gamma_f \frac{\partial f}{\partial x_i}\right) , \tag{16}$$

$$\frac{\partial}{\partial t}(\rho g) + \frac{\partial}{\partial x_i}(\rho \tilde{u}_i g) = \frac{\partial}{\partial x_i}\left(\Gamma_g \frac{\partial g}{\partial x_i}\right) . \tag{17}$$

The fuel fraction is divided into two variables: fuel mass fraction in the fresh gases $\tilde{y}_{u.f.}$ and fuel mass fraction in burnt gases. Where the fuel mass fraction in the fresh gases $\tilde{y}_{u.f.}$ is calculated from the transport equation:

$$\frac{\partial \bar{\rho}\tilde{y}_{u.f.}}{\partial t} + \frac{\partial \bar{\rho}\widetilde{u_i}\tilde{y}_{u.f.}}{\partial x_i} = \frac{\partial}{\partial x_i}\left[\left(\frac{\mu}{Sc} + \frac{\mu_t}{Sc_t}\right)\frac{\partial \tilde{y}_{u.f.}}{\partial x_i}\right] + \bar{\rho}\tilde{S}_{u.f.} + \overline{\dot{\omega}_{u.f.}} \quad , \tag{18}$$

and the fuel mass fraction in burnt gases is calculated as the difference between the fuel mass fraction y_{fu} and fuel mass fraction in the fresh gases $\tilde{y}_{u.f.}$. Additionally, the mixing of evaporated fuel with fresh air is modelled with the transport equations for the unmixed fuel and the unmixed oxygen. The unmixed fuel $\tilde{y}_f$ and unmixed oxygen $\tilde{y}_{a.O2}$ are calculated as:

$$\frac{\partial \bar{\rho}\tilde{y}_f}{\partial t} + \frac{\partial \bar{\rho}\widetilde{u_i}\tilde{y}_f}{\partial x_i} - \frac{\partial}{\partial x_i}\left(\frac{\mu}{Sc}\frac{\partial \bar{\rho}\tilde{y}_f}{\partial x_i}\right)\frac{\partial \tilde{y}_f}{\partial x_i} = \bar{\rho}\tilde{S}_f - \frac{1}{\tau_m}\tilde{y}_f\left(1 - \tilde{y}_f\frac{\bar{\rho}M_{mix}}{\bar{\rho}_u M_f}\right), \tag{19}$$

$$\frac{\partial \bar{\rho}\tilde{y}_{a.O2}}{\partial t} + \frac{\partial \bar{\rho}\widetilde{u_i}\tilde{y}_{a.O2}}{\partial x_i} - \frac{\partial}{\partial x_i}\left(\frac{\mu}{Sc}\frac{\partial \bar{\rho}\tilde{y}_{a.O2}}{\partial x_i}\right)\frac{\partial \tilde{y}_{a.O2}}{\partial x_i} = \bar{\rho}\tilde{S}_f - \frac{1}{\tau_m}\tilde{y}_{a.O2}\left(1 - \frac{\tilde{y}_{a.O2}}{\tilde{y}_{\infty.O2}}\frac{\bar{\rho}M_{mix}}{\bar{\rho}_u M_f}\right), \tag{20}$$

where the source terms depend on the mixing time τ_m which considers turbulence quantities, and is defined as:

$$\frac{1}{\tau_m} = \beta\frac{\varepsilon}{k} \, , \tag{21}$$

where the β is a model factor with the value 1.

10

3. EXPERIMENTAL SETUP

The experimental investigation was performed on a modified four-cylinder, four-stroke, turbocharged 1.6 litre PSA light-duty Diesel engine. Main characteristics of the engine are given in Table 1. For this study, the engine was reworked in a way that one of the cylinders was thermodynamically separated along with the entire gas path and fuel supply system, as presented in Figure 1. This allowed a fully flexible control over thermodynamic states in the intake (IM) and exhaust manifolds (EM), and injection parameters of the observed cylinder, which allow for exploring a wide range of operating conditions in precisely controlled variation studies. For that purpose, the intake air for separated cylinder was externally supplied with compressed air from laboratory high pressure distribution system using a pressure regulator. The exhaust manifold pressure of the separated cylinder was regulated by a backpressure valve in the exhaust system of the cylinder. Remaining three cylinders, that were not the part of this study, were using original turbocharger and were controlled by an original electronic control unit (ECU).

Engine	PSA DV6 ATED4
Cylinders	4, inline
Displacement	1560 cm^3
Bore	75 mm
Stroke	88.3 mm
Compression ratio	18:1
Cooling system	Water cooled

Table 1   Engine characteristics.

Full control over the injection timing, fuel quantity, and injection pressure was performed with injection control system (National Instruments, Drivven system), which controlled energizing characteristics of the injectors, as well as the operation of separated common rail high-pressure pump to ensure a full and precise control over the injection parameters of the analysed cylinder. The main characteristics of the fuel injection system are given in Table 2.

The engine was coupled with a Zöllner B-350AC eddy-current dynamometer controlled by Kristel, Seibt & Co control system KS ADAC. In-cylinder pressure was measured with a calibrated piezo-electric pressure transducer (AVL GH14D) in combination with charge amplifier AVL MICROIFEM, connected to 16-bit, 4 channel National Instruments data-acquisition system with a maximum sampling frequency of 1 sample per second per channel (MS/s/ch). An optical shaft encoder Kistler CAM UNIT Type 2613B provided an external trigger and an external clock at 0.1 crank angle degree (° CA) for data acquisition and injection

control system. Top dead centre (TDC) was determined by capacitive sensor COM Type 2653. The maximum uncertainty of pressure measurement, which combines the uncertainties of pressure transducer, charge amplifier and data acquisition system, is 0.31% and maximum uncertainty of pressure measurement corresponding to crank angle was therefore 0.96%.

Fuel injection system	Common rail
Injector type	Solenoid
Number of holes	6
Hole diameter	0.115 mm
Spray angle	149 °
Nozzle diameter at hole centre position	2.05 mm

Table 2   Fuel injection system characteristics.

Data acquisition and injection control embedded system was based on National Instruments cRIO 9024 processing unit and 9114 chassis. The same system was used for indication of in-cylinder pressure traces and engine control. Fuel mass flow was measured with AVL 730 gravimetric balance while intake airflow was measured with Coriolis flowmeter Micro Motion, model F025.

Representative pressure trace was generated by averaging 100 consecutive pressure cycles in selected operational point at a sampling resolution of 0.1° CA. Representative in-cylinder pressure trace was generated through a two steps approach. First, 100 consecutive cycles of the individual operating point were averaged to eliminate Cycle-to-Cycle Variations (CCV) due to signal noise [36]. Second, pressure oscillations in the combustion chamber that occur as a result of partial auto-ignition of the fuel were eliminated by applying low-pass finite impulse response (FIR) filter [37]. The representative pressure trace was then used as an input for the ROHR analysis that was performed with the AVL Burn™ software [38]. The employed software tool is based on detailed 0D thermodynamic equations considering variable gas properties determined via the NASA polynomials and relevant partial derivatives of non-perfect gases as well as the compressibility factor. Detailed equations for 0D ROHR calculation, which are based on mass, enthalpy and species conservation, are presented in [39].
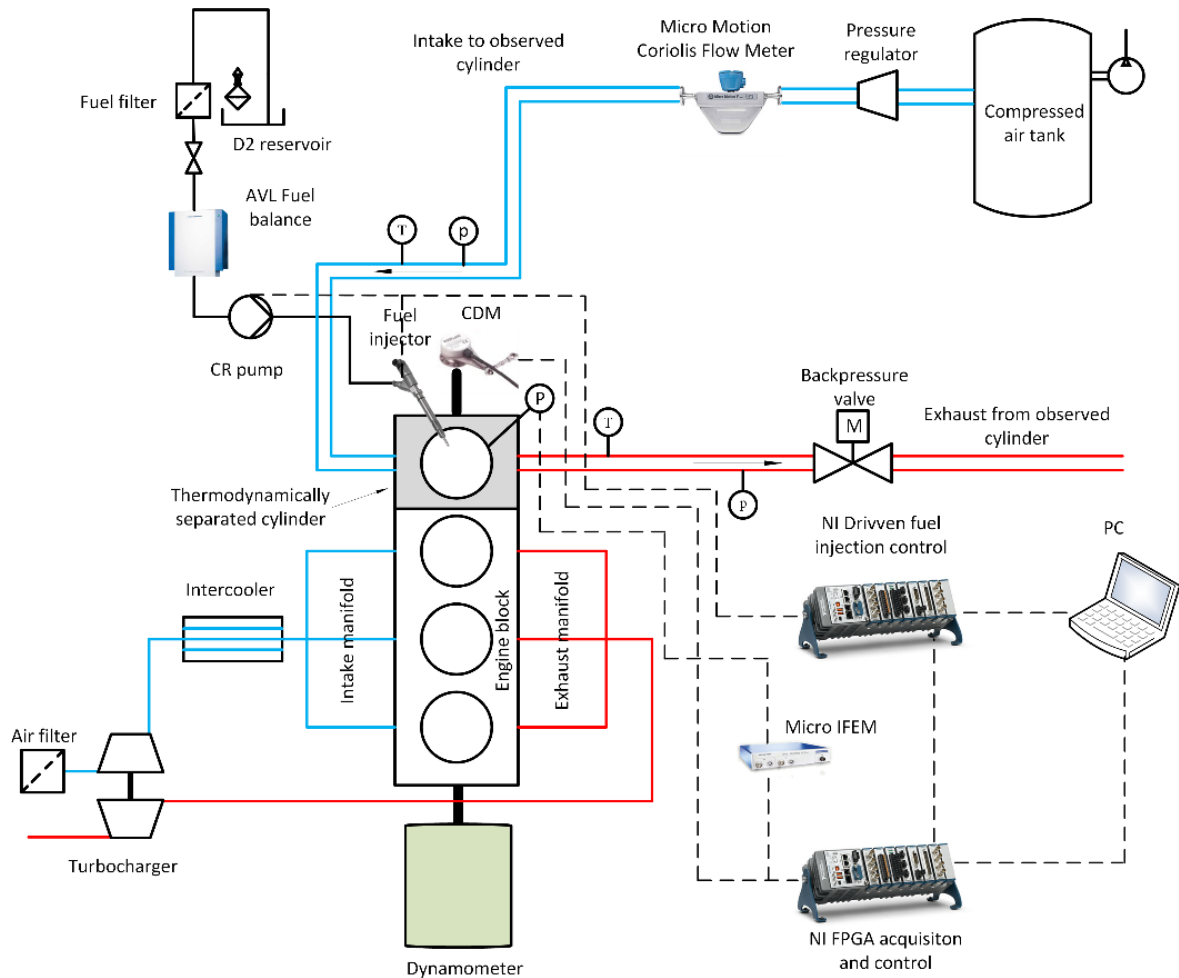
Figure 1   Scheme of the experimental system

To obtain the geometrical parameters, three-dimensional (3D) scan of the ω-shaped piston geometry was performed. The experiments were performed at 1500 1/min while varying start of energizing (SOE), energizing duration (ED), and rail pressure (RP) keeping constant indicated mean effective pressure (IMEP). The characteristics of the observed engine operating points are shown in Table 3.

#Case	En. Speed [rpm] [1/min]	p_IM [bar]	Fuel flow [kg/h]	IMEP [bar]	Air flow [kg/h]	RP [bar]	SOE [° CA]	ED [μs]
a	1500	1,40	0,42	4,17	17,93	600	705	545
b	1500	1,40	0,43	4,22	17,84	600	715	540
c	1500	1,40	0,45	4,18	17,57	600	725	570
d	1500	1,40	0,42	4,17	17,31	1200	705	365
e	1500	1,40	0,41	4,23	17,28	1200	715	356
f	1500	1,40	0,42	4,26	17,11	1200	725	370

Table 3   Operating single injection points with corresponding engine operating parameters

In order to prove high predictability of the proposed modelling approach, also the more demanding case with two separate injections (PI and MI) at the same rotation speed was observed. For this operating point different parameters, such as the start of the pilot injection energizing (SOPE), the start of main injection energizing (SOME), duration of pilot injection (PED), and the duration of the main injection (MED) are shown in Table 4.

#Case	En. Speed [rpm] [1/min]	p_IM [bar]	Fuel flow [kg/h]	IMEP [bar]	Air flow [kg/h]	RP [bar]	SOPE [° CA]	PED [μs]	SOME [° CA]	MED [μs]
g	1499,6	1,1702	2,42	4,8862	78,26	700	695	240	714	545

Table 4   Operating multi-injection point with corresponding engine operating parameters

4. NUMERICAL SETUP

Numerical simulations were performed by using the commercial 3D CFD software AVL FIRE™ for the closed valve period. The control volume mesh is covering $1/6^{th}$ of the cylinder bowl due to the 6 symmetrically distributed nozzle holes. Therefore, the injection from only one nozzle hole was considered. The computational domain was generated by using the AVL FIRE™ ESE DIESEL tool [27]. Initially, the piston geometry was scanned and the moving computational mesh was generated. The generated mesh contains 32500 control volumes at the Top Dead Centre (TDC), and 56412 control volumes in the Bottom Dead Centre (BDC). In order to correctly describe the fluid flow interaction with the wall, a two-cell thick boundary was created at the wall boundary selections declared in Table 5. The mesh movement was based on the interpolation between two meshes of identical topology, while the rezoning procedure was considered by exchanging meshes with same outer boundaries and with a different number of control volumes [40]. The mesh dependency study was conducted generating two additional moving meshes of same block structure with approximately 1.5 and 2 times more cells. The simulations with the same setup were run for all three meshes, where the obtained results were different for less than 1%. From that comparison, the presented mesh was selected for all calculations in this work, since it is capturing all the necessary flow features with satisfying accuracy in less computational time. All meshes in the mesh dependency study are generated with the first grid boundary nodes at approximately 1 mm from the wall, at *y+* value around 30-35 which fits the log-law profile for turbulent flows, according to literature [41].
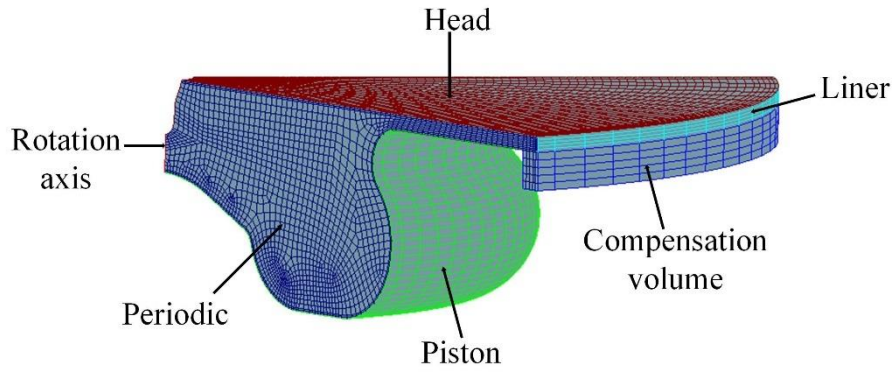
Figure 2   Computational domain at the top dead centre

The piston selection was defined as a moving part which resulted in deformation of specific computational cells. Therefore, the mesh was rezoned several times to satisfy pre-defined conditions of cell aspect ratio and orthogonality. The details regarding the boundary conditions are shown in Table 5. The engine head temperature was controlled by cooling water while cooling oil controlled the piston temperature. Those surfaces were assumed as isothermal boundary conditions with temperatures corresponding to the experimentally measured values. The cylinder geometry was assumed to be symmetric around the cylinder axis, and therefore the segment cut boundary was defined as the periodic inlet/outlet boundary condition. In order to compensate the geometric irregularities, the compensation volume was generated and it was defined as an adiabatic boundary condition. Mesh dependency tests were performed on three meshes with different cell size and with same block structure geometry where for all three meshes the converged results were matching. Therefore, the mesh with the lowest number of cells was selected for further calculations in order to save computational time and still provide reliable results.

Boundary condition	Type	Specific condition
Piston	Mesh movement wall	Temperature 560 K
Head	Fixed wall	Temperature 530 K
Liner	Fixed wall	Temperature from 360 K to 450 K
Cylinder axis	Symmetry	
Compensation volume wall	Mesh movement wall	Adiabatic
Periodic segment cut	Periodic inlet/outlet	Boundary connection

Table 5   Boundary conditions

Figure 3 shows the computational domain symmetry plane cut section, while the red rectangle shows a detailed view of the orifice refinement section that was generated in order to achieve more stable and robust calculations.
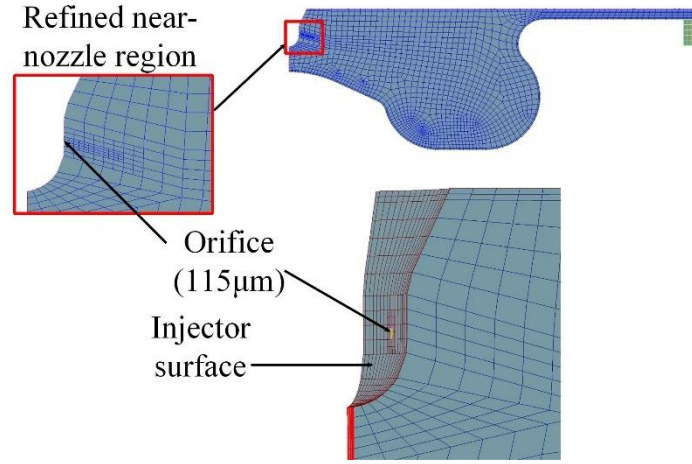
Figure 3   Computational domain with details on near-nozzle region refinement (left)

The initial pressure, temperature and gas composition were defined according to the available experimental data. The initial velocity field inside the cylinder was defined with swirl value of 4000 min^{-1} around the z-axis.

In both combustion modelling approaches, at the crank angle positions characteristic for the injection and combustion process, the smallest time step was defined as 0.1° CA, while the largest time step size of 1° CA was defined during the compression stroke. The Courant–Friedrichs–Lewy (CFL) criteria with a maximum CFL number of 1 was used to determine the instant time step and the time integration was done by the first order Euler implicit scheme. For turbulence and energy transport equations, the first order upwind differencing scheme was used, while for the momentum equation, the MINMOD Relaxed scheme was employed [27]. The convergence criteria were satisfied when normalised energy, momentum and pressure residuals reached a value lower than 10^{-4}. The pressure-velocity coupling was performed by employing the SIMPLE algorithm for solving the pressure correction equation.

4.1.   Injection parameters and spray setup

Fuel mass injected in each cycle is calculated from the total fuel consumption measured at the fuel tank. The connection is obtained from the mass conservation law, and can be expressed as:

$$m_{\text{cycle}} = \frac{2 \cdot \dot{m}_{ft}}{f \cdot n_{cycl} \cdot n_{nh}} \qquad , \tag{22}$$

16

where $\dot{m}_{ft}$ is the fuel consumption, f is the engine speed (Hz), n_{cycl} is the number of cylinders that engine has, and n_{nh} is the number of nozzle holes that injector has. The half outer cone angle γ, used for spray definition was calculated according to the following expression [42]:

$$\gamma = arctg\left[\frac{4\pi\sqrt{3}}{6\left(3+0.28\left(\frac{l}{d_{nh}}\right)\right)}\sqrt{\frac{\rho_g}{\rho_f}}\right] \quad , \tag{23}$$

where l is the length of the nozzle, and d_{nh} is the nozzle hole diameter, ρ_g is the gas density and ρ_f is the density of injected fuel. In Equation (23), the impact of l was neglected due to its small influence on the spreading angle. Within the EL spray model, WAVE breakup model was considered [43]. The WAVE model constant C_2 was varied between 6 and 12 in single injection cases, and for the multi-injection cases it was considered 15 during the PI, and 25 during the MI period. Additionally, for the case g with the multi injection strategy, the ratio between PI and MI fuel mass was not known in experimental research. This ratio was assumed the same as the ratio between the combustion areas of PI and MI under the experimental rate of heat release curve.

5. RESULTS

In this section, the experimental and CFD simulation results are presented. Firstly, the in-cylinder pressure and ROHR results of single-injection operating points are compared with the experimental results. Furthermore, for specific crank angle positions, the development of evaporated fuel and temperature field through the engine combustion chamber is described. At the end of the chapter, the results of multi-injection operating point are discussed.

5.1.   Single injection results

Figure 4 shows the differences in in-cylinder pressure and ROHR curves obtained by the combustion model, chemical mechanism and experiment for 6 operating points (cases) with a single injection strategy. The presented ROHR is calculated for the 1/6th of the cylinder bowl volume, indicating that for the entire engine, this value should be multiplied by a number of nozzle holes and number of engine cylinders.

The fuel autoignition point, or the start of combustion (SOC), is indicated by the initial departure of ROHR from the zero value. It is discernible from figures that SOC is predicted

well in the analysed case, indicating plausibility of the employed models also during the ignition delay period.

It is noticed that for cases *a*, *b,* and *f*, the GGPR model predicts higher peak values of ROHR in comparison with the combustion ECFM-3Z+ model and with the experimental data. This can be mostly attributed to a different combustion modelling approaches, where the turbulence fluctuations are differently described. Additionally, the ECMF-3Z+ features 3-mixing zones for the air and fuel, which lead to a more appropriate SOC and ROHR predictions in the premixed phase of combustion. In the GGPR approach, it is assumed that the reaction rates of the chemical mechanism are calculated based on mean quantities, which increases the uncertainty of a turbulent flame calculation. The high turbulent fluctuations obtained during spray injection and ignition of evaporated fuel produce the discrepancy in the ROHR results obtained for the cases fluid dynamics in Figure 4. In Equation (9) it can be noticed, that the products of mean and instantons species concentrations and chemical reaction rates are different. In the ECFM-3Z+ model, the turbulence fluctuations are considered inside the mixing model and are used for the modelling of the source term in Equation (14). For calculation of source terms in the Equation (14) for the fuel and oxygen, the mixing time-scale between 3-zones is required, which is assumed to be proportional to the turbulent time-scale given by the turbulence model.

The cases *a*, *b* and *c* have the same mass of injected fuel and injection timing but lower injection pressure as cases on their right-hand side. In the case *a*, it is noticed that the peak in-cylinder pressure in the premixed phase is lower for approximately 10 bar than in the case *d*, which is addressed to the lower injection pressure and lower droplet velocities. With lower droplet velocities, the spray droplets are larger and evaporate slower resulting in lower ROHR values and lower in-cylinder pressure.

For a higher rail pressure values, the rate of heat release curve exhibits higher gradients, which can be attributed to a better fuel disintegration process due to higher injection pressure, and thus higher share of evaporated fuel before the SOC. For cases *c* and *f*, the fuel injection occurs after the piston reached TDC, which leads to the SOC after the peak motoring pressure. For these cases, differences in peak values of ROHR are less noticeable. In the ECFM-3Z+ model, the auto-ignition and laminar flame speed model are considered, which can be the reason why the ROHR predictions show a more reliable result in the SOC phase when compared with the GGPR.

From the results presented in Figure 4, it can be concluded that for the fuel injection after the TDC, the injection pressure has a lower impact on the combustion process. Furthermore, it can be concluded that both the ECFM-3Z+ and chemical mechanism results show a good agreement with the experimental data. Additionally, GGPR shows a better prediction in the

18

premixed phase of the combustion process for higher injection pressure, but the ECFM-3Z+ shows better predictions of the peak rate of heat release than the GGPR.
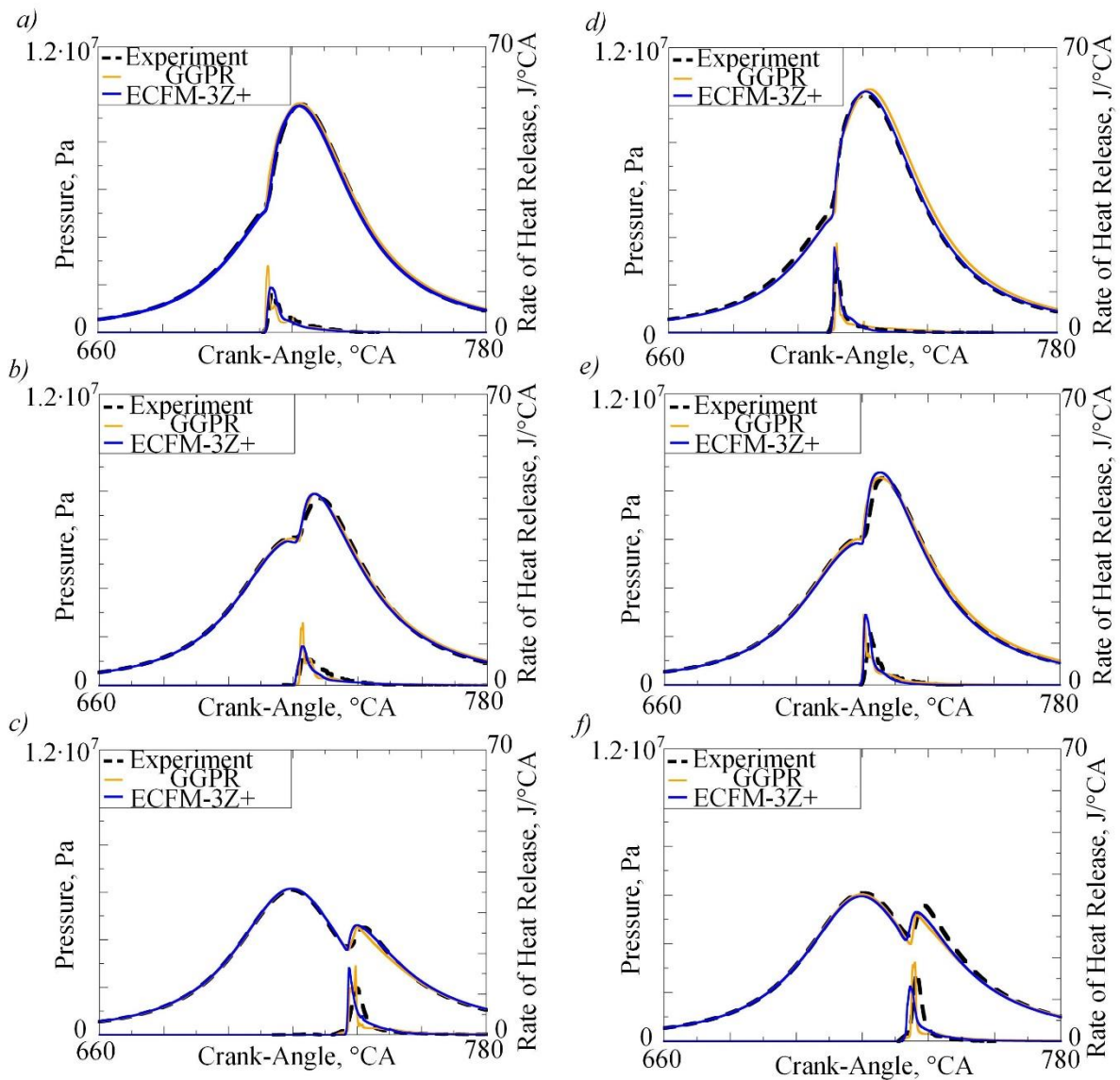
Figure 4   The in-cylinder pressure and rate of heat release for single injection cases defined in Table 3

In Figure 5, the injected droplet velocity is shown for case *a*. This view with six nozzle hole injections was obtained cloning the results for the 1/6th of the cylinder bowl volume around the z-axis, to envisage the actual injection process inside the whole cylinder. The droplet velocity results were obtained from the continuity equation, where the injection pressure was accelerating the droplets to the shown velocity results.

19
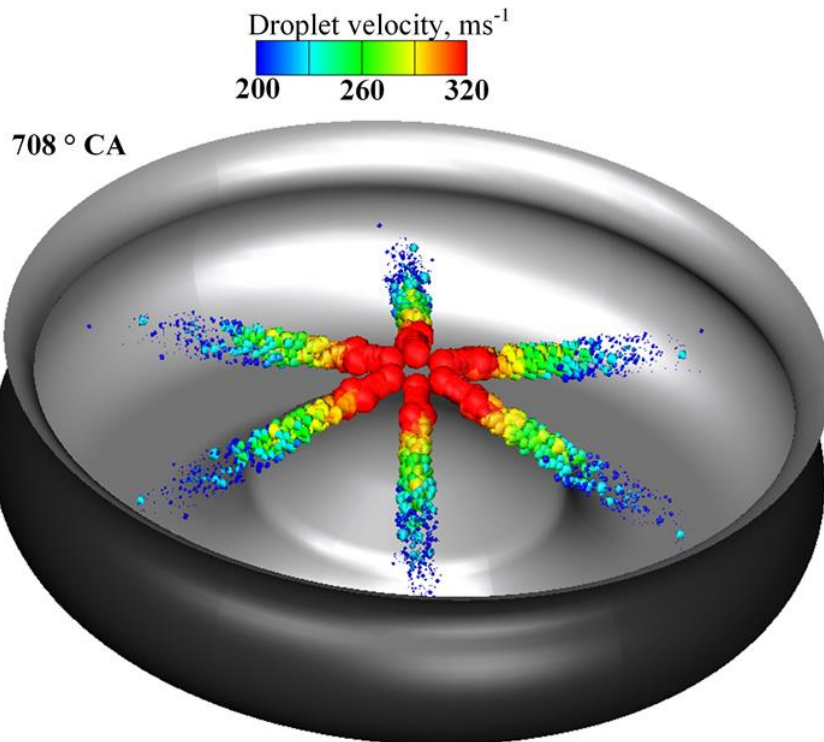
Figure 5   Injected parcel velocity for the whole cylinder of single injection case (case *a*)

The evaporated fuel distribution for the single injection case *a* is presented in Figure 6. The vapour fuel concentration is in direct relation to the temperature field shown in Figure 7 where the regions of lower temperature, due to the evaporation process are as well the regions of higher concentration of evaporated fuel. At 710° CA, the injection process ends, and the initial fuel vapour is produced. At 711° CA, the combustion process starts and the concentration of the evaporated fuel decreases. It can be noticed that the evaporated fuel is propagating towards the piston bowl where the combustion occurs with the largest share, as can be seen from temperature distribution in Figure 7. At 712° CA, the evaporated fuel is spread in the high-temperature region which propagates its combustion. In later crank angle positions, the evaporated fuel disappears in chemical reactions acting as a reactant. The results of evaporated fuel predicted with the ECFM-3Z+ show that the evaporation process is more intensive than in GGPR. But in Figure 4, it is shown that the burning process is faster in the GGPR. That can be attributed to the auto-ignition and laminar flame speed model in ECMF-3Z+ that slows down the combustion process.
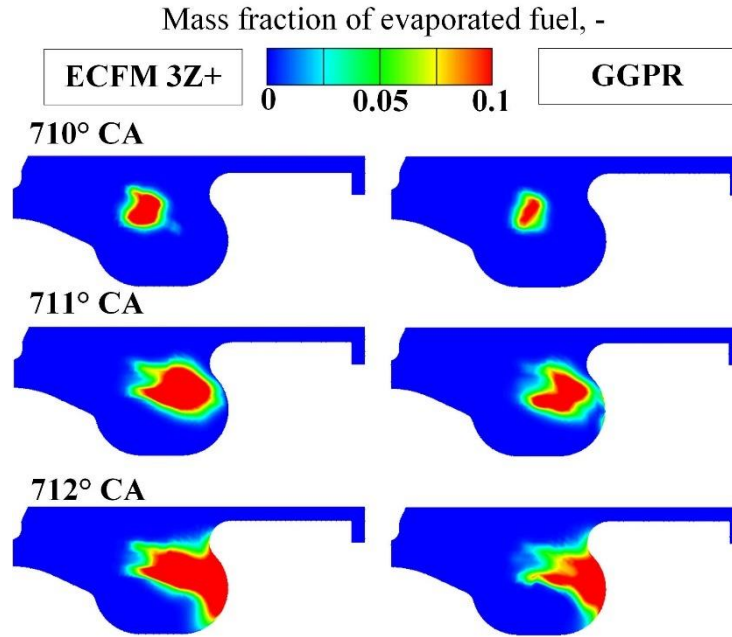
Figure 6   Temperature field for different combustion modelling approaches of single injection case (case *a*).

Figure 7 shows temperature fields for the case *a,* which is a representative case for analysis of calculated results for a single injection strategy. The 3D results are shown for the symmetry plane of the computational domain. The temperature field recorded at 710° CA clearly shows the influence of fuel injection process. The intense breakup promotes the evaporation process by enlarging the surface available for the mass transfer of the liquid fuel into the gaseous phase. The cooling of the gas phase is visible due to the evaporation process. At 717° CA, the combustion starts and the local temperature rise is visible. For that crank angle position, it can be noticed that with the ECFM-3Z+ model the higher share of fuel is burned resulting in the larger high-temperature region characterized by the lower peak value. It can be concluded, that in ECFM-3Z+ model fuel-air mixing is better described. The peak temperatures are recorded at 724° CA, where the maximum temperature is in a good agreement for the results obtained with both modelling approaches.
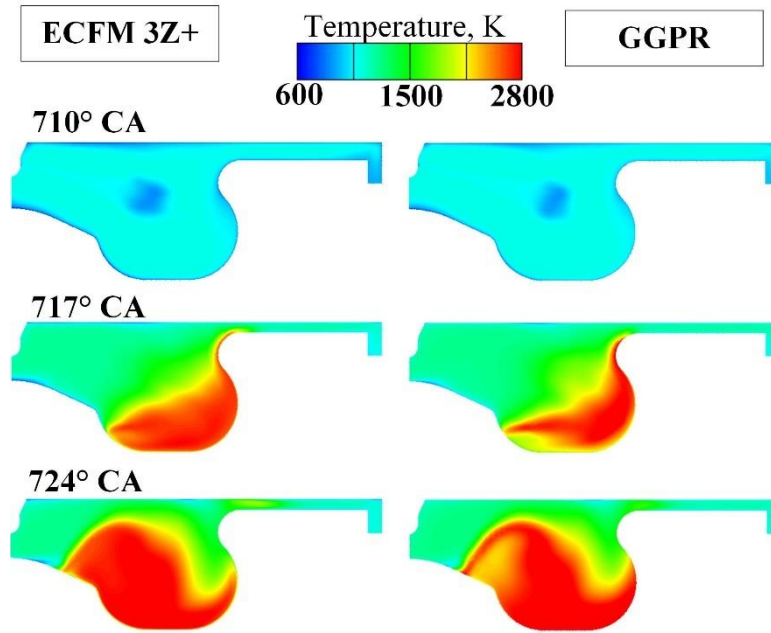
Figure 7   Temperature field for different combustion modelling approaches for operating point *a*.

5.2.   Multi-injection results

Figure 8 shows the in-cylinder pressure results obtained by the combustion model, GGPR approach, and experimental data for the multi-injection operating point. The comparison of the experimental and calculated ROHR during the injection period for the computational domain is also shown, where the area under curves represents the accumulated released energy. The ignition of the PI fuel predicted by the ECFM-3Z+ model is occurring slightly before recorded experimental data. For the PI fuel, using the GGPR approach a higher ignition delay is noticed when compared to the experimental data. From showed results in Figure 7, it can be stated, that in the rate-controlled of combustion process, ECFM-3Z+ model shows stronger diffusion of temperature field, due to the more detailed consideration of combustion diffusion phenomena. In Equation (14) of the ECFM-3Z+ combustion model, the consideration of Sc number improves interaction with the in-cylinder flow and which can be seen in the larger high-temperature region at 717° CA.
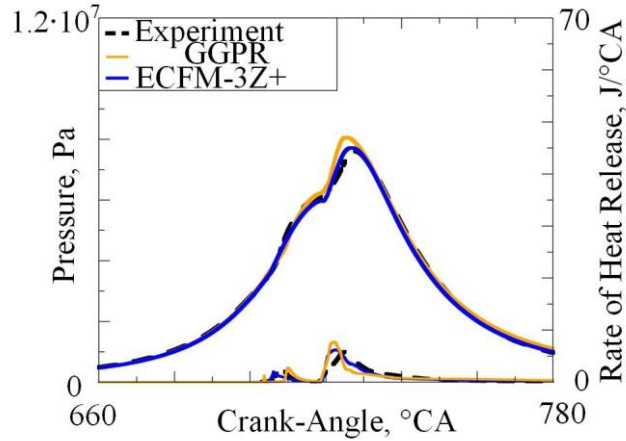
Figure 8   The mean in-cylinder pressure and the rate of heat release results obtained by experiment, GGPR and ECFM-3Z+ for multi-injection case defined in Table 4

Figure 9 shows the evaporated fuel distribution for different crank angle positions at the spray axis plane for the multi-injection case *g*. The fuel vapour is shown several crank angle degrees after 700° CA when the PI is finished. The concentrations of evaporated fuel predicted in ECFM-3Z+ simulations show a more intensive evaporation process during the PI. Such behaviour can be attributed to a better description of turbulence-chemistry interaction and faster ignition when comparing to the GGPR approach. This can also be seen in the ROHR curve in Figure 8. At 703° CA, the combustion process of the PI fuel occurs and the concentration of the evaporated fuel decreases. At later crank angle positions, the MI occurs. Compared to single injection cases faster evaporation is noticed, which can be addressed to the higher in-cylinder temperature achieved through PI combustion. Higher temperatures also accelerate chemical reactions and reduce the ignition delay of MI. Due to that, a premixed peak of MI combustion is not pronounced as in single injection cases. Such behaviour, characterised by lower temperatures and pressure increase gradients, is favourable for the engine noise and NO_x emissions. In the ECFM-3Z+ approach, due to auto-ignition model and laminar flame speed model that postpone the combustion process, the overall combustion process of evaporated fuel during the spray injection is slower than in the GGPR approach. At 724° CA, the combustion process of the MI fuel occurs and the concentration of the evaporated fuel decreases. The last remaining evaporated fuel is located in the near piston region, where the lower temperature of the piston postpones the combustion process.
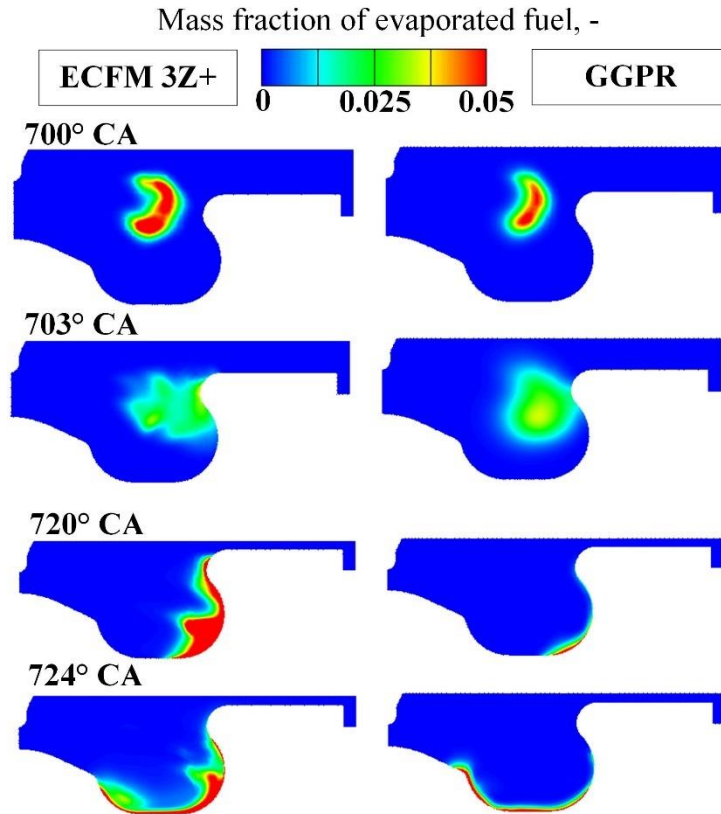
Figure 9   Temperature field for different combustion modelling approaches of the multi-injection case (case *g*).

In Figure 10 the temperature field for different crank angle positions of case *g* is shown. The temperature distribution at 697° CA shows the influence of PI where the cooling of the gas phase is visible due to the lower fuel temperature and fuel evaporation. At 714° CA, the combustion of vapour fuel from the PI occurs, and the rise in temperature is visible in the combustion regions. At 717° CA, the MI occurs, which is demonstrated with a lower temperature in the spray region. The peak temperatures are recorded at 730° CA, where the maximum temperature is higher for the results obtained with the GGPR approach.
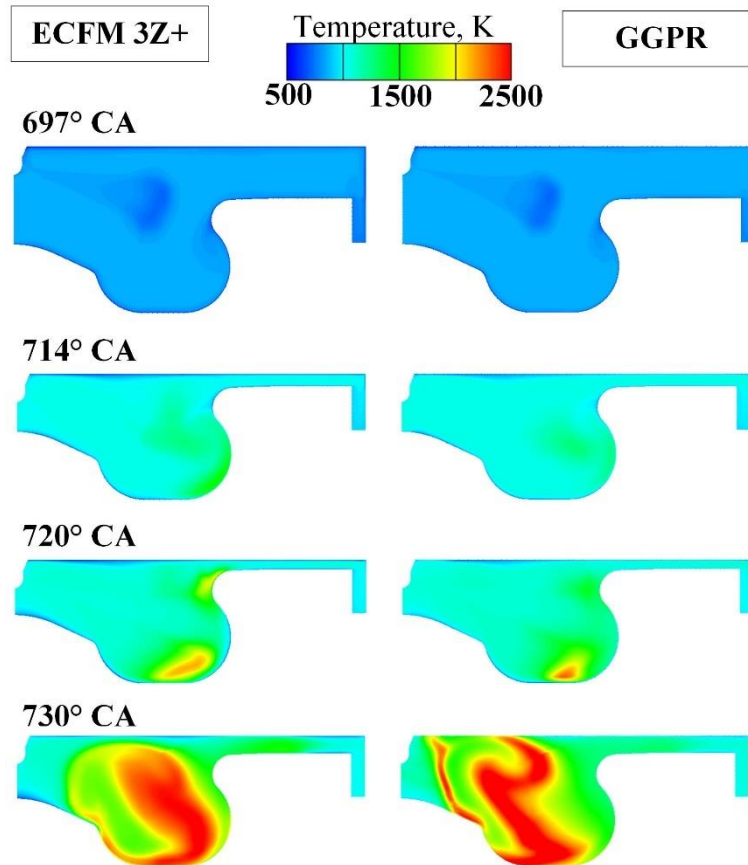
Figure 10   Temperature field for different combustion modelling approaches of the multi-injection case (case *g*).

6.   CONCLUSIONS

The purpose of this paper was to present the different 3D numerical approaches, applied on the IC diesel engine, with a good trade-off between computational efficiency and modelling depth to achieve a high level of predictability. The influence of injection timing and rail pressure on combustion characteristics was investigated with the presented analysis for CFD simulations. The experimental research and diesel engine combustion simulations performed with ECFM-3Z+ and GGPR combustion modelling approaches were conducted for several injection timings showing a good prediction capability. The experimental matrix was made to show the impact of rail pressure, in-cylinder pressure, in-cylinder temperature and chemical species concentrations on the overall combustion process. Measured results of ignition delays and ROHR indicate the change of air to fuel ratio in the premixed and in the mixture-controlled combustion, which was also proved by the 3D results of simulations. Furthermore, it was shown that the GGPR modelling approach is good for estimation of combustion delay and less accurate in the premixed and mixture-controlled combustion. The   ECFM-3Z+ modelling

approach, on the other hand, shows a good agreement of the mean in-cylinder pressure and ROHR also in the late combustion phase. This can be addressed to usage of the auto-ignition and the laminar flame speed models within this approach. Both combustion modelling approaches were validated on the operating point with a multi-injection strategy, and a good agreement with the experimental results was achieved, especially for the ECFM-3Z+ case. In the rate-controlled and late phase of the combustion process, the ECFM-3Z+ model shows a stronger diffusion of the temperature field, due to a more detailed consideration of combustion diffusion phenomena. It can be concluded that for the fuel injection after the TDC, the injection pressure has a lower impact on the combustion process.

Acknowledgements

References

[1]   Chong HS, Park Y, Kwon S, Hong Y. Analysis of real driving gaseous emissions from light-duty diesel vehicles. Transp Res Part D Transp Environ 2018;65:485–99. doi:10.1016/J.TRD.2018.09.015.

[2]   Katrašnik T. Hybridization of powertrain and downsizing of IC engine - A way to reduce fuel consumption and pollutant emissions - Part 1. Energy Convers Manag 2007;48:1411–23. doi:10.1016/j.enconman.2006.12.004.

[3]   https://www.fuelseurope.eu/knowledge/how-refining-works/diesel-gasoline-imbalance n.d.

[4]   Petranovic Z, Edelbauer W, Vujanović M, Priesching P, Tatschl R, Duić N. Modeling of Reactive Spray Processes in DI Diesel Engines. SAE Tech Pap Ser 2017.

[5]   Kılkış Ş, Krajačić G, Duić N, Rosen MA, Al-Nimr MA. Advancements in sustainable development of energy, water and environment systems. Energy Convers Manag 2018;176:164–83. doi:10.1016/J.ENCONMAN.2018.09.015.

[6]   Petranović Z, Edelbauer W, Vujanović M, Duić N. Modelling of spray and combustion processes by using the Eulerian multiphase approach and detailed chemical kinetics. Fuel 2017;191:25–35. doi:10.1016/j.fuel.2016.11.051.

[7]   Divekar PS, Chen X, Tjong J, Zheng M. Energy efficiency impact of EGR on organizing clean combustion in diesel engines. Energy Convers Manag 2016;112:369–81. doi:10.1016/j.enconman.2016.01.042.

[8]   Guo C, Song Y, Feng H, Zuo Z, Jia B, Zhang Z, et al. Effect of fuel injection characteristics on the performance of a free-piston diesel engine linear generator: CFD

simulation and experimental results. Energy Convers Manag 2018;160:302–12. doi:10.1016/j.enconman.2018.01.052.

[9]   Petranović Z, Sjerić M, Taritaš I, Vujanović M, Kozarac D. Study of advanced engine operating strategies on a turbocharged diesel engine by using coupled numerical approaches. Energy Convers Manag 2018;171:1–11. doi:10.1016/j.enconman.2018.05.085.

[10]   Zhao F, Yang W, Zhou D, Yu W, Li J, Tay KL. Numerical modelling of soot formation and oxidation using phenomenological soot modelling approach in a dual-fueled compression ignition engine. Fuel 2017;188:382–9. doi:10.1016/j.fuel.2016.10.054.

[11]   Petranović Z, Bešenić T, Vujanović M, Duić N. Modelling pollutant emissions in diesel engines, influence of biofuel on pollutant formation. J Environ Manage 2016:1–9. doi:10.1016/j.jenvman.2017.03.033.

[12]   Anand K, Reitz RD. Exploring the benefits of multiple injections in low temperature combustion using a diesel surrogate model. Fuel 2016;165:341–50. doi:10.1016/j.fuel.2015.10.087.

[13]   Sremec M, Taritaš I, Sjerić M, Kozarac D. Numerical Investigation of Injection Timing Influence on Fuel Slip and Influence of Compression Ratio on Knock Occurrence in Conventional Dual Fuel Engine. J Sustain Dev Energy, Water Environ Syst 2017;5:518–32. doi:10.13044/j.sdewes.d5.0163.

[14]   Baleta J, Mikulčić H, Vujanović M, Petranović Z, Duić N. Numerical simulation of urea based selective non-catalytic reduction deNOx process for industrial applications. Energy Convers Manag 2016;125:59–69. doi:10.1016/j.enconman.2016.01.062.

[15]   Taghavifar H, Khalilarya S, Jafarmadar S. Engine structure modifications effect on the flow behavior, combustion, and performance characteristics of di diesel engine. Energy Convers Manag 2014;85:20–32. doi:10.1016/j.enconman.2014.05.076.

[16]   Li XR, Zhou HQ, Zhao LM, Su L, Xu H, Liu FS. Effect of split injections coupled with swirl on combustion performance in DI diesel engines. Energy Convers Manag 2016;129:180–8. doi:10.1016/j.enconman.2016.09.011.

[17]   Abdul Gafoor CP, Gupta R. Numerical investigation of piston bowl geometry and swirl ratio on emission from diesel engines. Energy Convers Manag 2015;101:541–51. doi:10.1016/j.enconman.2015.06.007.

[18]   Hossain AK, Smith DI, Davies PA. Effects of engine cooling water temperature on performance and emission characteristics of a compression ignition engine operated with biofuel blend. J Sustain Dev Energy, Water Environ Syst 2017;5:46–57. doi:10.13044/j.sdewes.d5.0132.

[19]   Zhang Q, Hao Z, Zheng X, Yang W. Characteristics and effect factors of pressure oscillation in multi-injection DI diesel engine at high-load conditions. Appl Energy

2017;195:52–66. doi:10.1016/j.apenergy.2017.03.048.

[20] Lazaroiu G, Pană C, Mihaescu L, Cernat A, Negurescu N, Mocanu R, et al. Solutions for energy recovery of animal waste from leather industry. Energy Convers Manag 2017;149:1085–95. doi:10.1016/j.enconman.2017.06.042.

[21] Cernat A, Pana C, Negurescu N, Lazaroiu G, Nutu C. Aspects of the animal fat use at the diesel engine fuelling. Proc Univ Power Eng Conf 2015:1–6. doi:10.1109/UPEC.2015.7339917.

[22] Zhao H. Advanced Direct Injection Combustion Engine Technologies and Development - Volume 2: Diesel Engines. 2009. doi:10.1533/9781845697457.

[23] Hasse C, Barths H, Peters N. Modelling the Effect of Split Injections in Diesel Engines Using Representative Interactive Flamelets. SAE Tech Pap Ser 1999. doi:10.4271/1999-01-3547.

[24] EN 5902013AC2014 Automotive fuels - Diesel - Requirements and test methods 2014;1. doi:http://www.sciencedirect.com/science/article/pii/S0045782504000313.

[25] Liu S, Hewson JC, Chen JH, Pitsch H. Effects of strain rate on high-pressure nonpremixed n-heptane autoignition in counterflow. Combust Flame 2004;137:320–39. doi:10.1016/j.combustflame.2004.01.011.

[26] Zhang C, Wu H. The simulation based on CHEMKIN for homogeneous charge compression ignition combustion with on-board fuel reformation in the chamber. Int J Hydrogen Energy 2012;37:4467–75. doi:10.1016/j.ijhydene.2011.11.104.

[27] AVL FIRE Documentation 2017. Graz: 2017.

[28] Wu X, Deng J, Cui H, Xue F, Zhou L, Luo F. Numerical simulation of injection rate of each nozzle hole of multi-hole diesel injector. Appl Therm Eng 2016;108:793–7. doi:10.1016/j.applthermaleng.2016.07.136.

[29] Hanjalić K, Popovac M, Hadžiabdić M. A robust near-wall elliptic-relaxation eddy-viscosity turbulence model for CFD. Int J Heat Fluid Flow 2004;25:1047–51. doi:10.1016/j.ijheatfluidflow.2004.07.005.

[30] Crowe CT, Schwarzkopf JD, Sommerfeld M, Tsuji Y. Multiphase Flows with Droplets and Particles. Taylor & Francis Group; 2012.

[31] Ferziger JH, Peric M. Computational Methods for Fluid Dynamics. 2002. doi:10.1016/S0898-1221(03)90046-0.

[32] Schiller L, Naumann AZ. VDI 77 1933:318–20.

[33] Cunningham E. On the Velocity of Steady Fall of Spherical Particles through Fluid Medium. Proc R Soc A Math Phys Eng Sci 1910;83:357–65. doi:10.1098/rspa.1910.0024.

[34] Liu AB, Mather D, Reitz RD. Modeling the Effects of Drop Drag and Breakup on Fuel Sprays. SAE Tech Pap Ser 1993;298:4–7.

[35] Colin O, Benkenida A. The 3-zones Extended Coherent Flame Model (ECFM3Z) for computing premixed/diffusion combustion. Oil Gas Sci Technol 2004;59:593–609. doi:10.2516/ogst:2004043.

[36] Payri F, Luján JM, Martín J, Abbad a. Digital signal processing of in-cylinder pressure for combustion diagnosis of internal combustion engines. Mech Syst Signal Process 2010;24:1767–84. doi:10.1016/j.ymssp.2009.12.011.

[37] Rašić D, Vihar R, Žvar Baškovič U, Katrašnik T. Methodology for processing pressure traces used as inputs for combustion analyses in diesel engines. Meas Sci Technol 2017. doi:doi.org/10.1088/1361-6501/aa5f9e.

[38] AVL manual: Theory AVL BOOST. 2011.

[39] Prah I, Katrašnik T. Application of Optimization Techniques to Determine Parameters of the Vibe Combustion Model. J Mech Eng 2009;55:715–26.

[40] Tatschl R. Appendix 3D-CFD Simulation of IC-Engine Flow, Mixture Formation and Combustion with AVL FIRE. vol. 1542. 2012. doi:10.1007/978-3-642-14094-5.

[41] Popovac M, Hanjalic K. Compound Wall Treatment for RANS Computation of Complex Turbulent Flows and Heat Transfer. Flow, Turbul Combust 2007;78:177–202. doi:10.1007/s10494-006-9067-x.

[42] Kenneth Kuan-Yun Kuo RA. Applications of Turbulent and Multi-Phase Combustion. 2012. doi:10.1002/9781118127575.

[43] Liu AB, Mather D, Reitz RD. Modeling the Effects of Drop Drag and Breakup on Fuel Sprays 1993. doi:10.4271/930072.

PAPER 2

Numerical Assessment of Radiative Heat Transfer Impact on Pollutant Formation Processes in a Compression Ignition Engine

Filip Jurić[a]
e−mail: filip.juric@fsb.hr

Zvonimir Petranović[b]
e−mail: zvonimir.petranovic@avl.com

Milan Vujanović[*,a]
e−mail: milan.vujanovic@fsb.hr

Neven Duić[a]
e−mail: neven.duic@fsb.hr

[a] Faculty of Mechanical Engineering and Naval Architecture, University of Zagreb, Ivana Lučića 5, 10000 Zagreb, Croatia

[b] AVL AST List GmbH, Alte Poststraße 152, 8020 Graz, Austria

ABSTRACT

An imposed solution in the development process of compression ignition engines is the use of numerical research employing Computational Fluid Dynamics (CFD). At the high operating temperatures in compression ignition engines, the radiative heat transfer influences the overall temperature profile and heat transfer, which also affects the formation processes of pollutants. For the radiative transfer calculation in this work, method of discrete ordinates (DOM) employing Finite Volume Method (FVM) is implemented with user functions into the AVL FIRE™ CFD code. The absorptivity and emissivity are described with the implemented Weighted Sum of Grey Gases Model (WSGGM) based on non-isothermal and nonhomogeneous absorption coefficient correlations for carbon dioxide, water vapour and soot. The implemented procedure is extended to work with moving meshes, parallel computing and rezoning procedure, which are needed to account the radiative heat transport in internal combustion engines. Additionally, the focus of this work is on the performed validation of calculated mean temperature, pressure, rate of heat release and emission results against the compression ignition engine experimental measurements. Results with the implemented radiation model showed lower peak temperatures for approximately 10 K, which resulted in around 18 % lower nitrogen oxides concentrations, and up to 20 % higher soot concentrations at the end of engine operating cycle. The most

[*] Corresponding author

dominant impact of the radiative heat transfer on soot formation is visible at the crank angles, where peak temperatures occur. The performed parameter study of the piston and head wall emissivity values showed a reduction in mean in-cylinder pressure and NO mass fraction for a less reflective surface. From the conducted parameter analysis of ordinates number, the sufficient accuracy is achieved for simulations with eight ordinates, which resulted in approximately 50 % increased computational time. Finally, it may be concluded that the combination of implemented models is useful to predict the heat transfer of internal combustion engine focussing on the radiative heat transport, which can be an important factor for the development of forthcoming internal combustion engines.

KEYWORDS

Pollutant Emissions, Radiation, Engine, Participating Media

1. INTRODUCTION

Despite the development of new technologies in the transport and energy sector, most of the energy consumption is still provided by fuel consumption (Stančin et al., 2020). For this reason, the scientific investigations still aim to improve energy efficiency by controlling operation conditions, and adapt new more sustainable fuels to the existing energy systems (Bedoić et al., 2020) or additionally reduce the pollutants from conventional transport systems employing the new after-treatment technologies (Bešenić et al., 2020). The development and improvement of the combustion system is a great challenge that has been attempted to solve for many years (Mikulčić et al., 2020). The fossil fuel combustion process, as an exothermic process, is known to have a negative impact on the environment, and their reduction is crucial in the near future to reduce atmospheric pollution (Baleta et al., 2019). Currently, a significant source of harmful emissions is generated from gas turbines, internal combustion engines, industrial furnaces, and boilers, which still have room for improvement in current energy transition (Mikulčić et al., 2016). A promising approach for solving significant pollutant emissions is the utilisation of biofuels in conventional combustion systems, where the development of numerical models is of essential importance (Kun-Balog et al., 2017). Additional focus is also given on pollutants that are produced from the Internal Combustion (IC) engines, where the further developments of after-treatment, advanced combustion modelling, and alternative fuels are still ongoing (J Javier López et al., 2019). Recent researches investigated some unusual alternative fuels applicable for IC engine combustion such as from animal fat (Cernat et al., 2015), animal waste in leather industry (Lazaroiu et al., 2017) or methanol blends (Gupta and Mishra, 2019). An example of a modern approach for emission characteristics of a

2

compression ignition engine operated with biofuel blend is described in (Fajri et al., 2017). Contrarily, the current numerical research is providing solutions for improvement of the combustion process and engine efficiency, such as with the improvement of spray injection strategy (Sremec et al., 2017). Therefore, the combined approach of experimental research and Computational Fluid Dynamics (CFD) is utilised for more accurate calculation of temperature field inside combustion systems, that is a generator of pollutant formation processes (Bešenić et al., 2018). The employed CFD procedure in this work was performed for the analysis spray angle impact on combustion process in different piston design (Soni and Gupta, 2017). Fajri et al. utilise the CFD procedure for the determination of NO_x emissions from the compression ignition engines, where the emphasis was on the start of combustion and combustion duration of different fuel blends (Fajri et al., 2017). In (Lamas et al., 2019), authors showed the influence of injection strategy on emission results, where the reduction up to 30 % of NO_x emissions are achieved by the implementation of multi injection strategy. A promising solution for the determination of the NOx and soot emissions is a coupling of the CFD procedures with the neural networks to predict the emissions from different fuel blends as shown in (Taghavifar et al., 2016), where satisfactory prediction functions are achieved.

The additional complexity and computational demanding are the main reasons for not considering the impact of radiative heat transfer in IC engine numerical simulations (José J. López et al., 2019). With the development of the computational resources, the radiative heat transfer in the participating media can be approximated for the engineering applications. It is no longer sufficient not to include the impact of radiative heat transfer on pollutant formation processes to compute the amount of pollutant from IC engines (Paul et al., 2019). While the effect of radiation on the heat transfer in IC engines is in the most researches not considered, the radiation effect in the high-scale industrial application such as boilers and furnaces is commonly considered (Bohlooli Arkhazloo et al., 2019). Furthermore, the CFD procedure for calculating the radiative heat transport in jet engines is described in (Cerutti et al., 2008).

If the radiative heat transfer in participating media is assumed the Radiative Transfer Equation (RTE) needs to be solved. Approximated numerical models need to be employed in order to solve the RTE (Modest and Haworth, 2016). Among the many types of research on the topic of heat transfer by radiation in IC engines, just a few were carried out by solving the RTE (Benajes et al., 2015). All type of calculations that were conducted, where mainly using a Discrete Ordinate Method (DOM) radiative solver and the wide-band spectral model for calculating the absorption of the gas medium, including soot. The impact of radiative heat transfer and soot and NO_x formation process was investigated for the first time in the paper (Yoshikawa and Reitz, 2009), where the high values of absorption

coefficient inside the combustion chamber of the IC engine were achieved, due to the high soot concentrations and high-pressure. Although in small geometries, such as in passenger car IC engines, the impact of radiation on the whole heat transfer is not significant, the impact on the emission formation processes cannot still be ignored (Yildiz et al., 2019). It was evaluated, that the soot process formation depends greater on the radiation heat transfer in IC engines than the NO_x formation process (Fernandez et al., 2018). Numerical investigation of radiative heat transfer in IC engines employing DOM showed that radiation influences soot predictions by as much as 50 % (Yue and Reitz, 2019).

Of all the existing models, the DOM and its conservative modification Finite Volume Method (FVM) is the most utilised for calculation of radiative heat transfer in the CFD codes (Coelho, 2014a). That is why, for this analysis of radiative heat transfer in this work, the radiation model FVM is used, which can be applied for a wide range of industrial applications (Coelho, 2018). Nevertheless, the results on the IC engine with FVM radiation model have not been published briefly.

The DOM approximation, coupled with the conservative FVM, was implemented into the CFD software AVL FIRE™ in this work, based on the literature (Mishra et al., 2006). The implemented model considers all radiative heat transfer phenomena: absorption, emission, and scattering (Modest, 2013). The absorptivity and emissivity coefficients are calculated with the Weighted-Sum-of-Grey-Gases Model (WSGGM) base on non-isothermal and non-homogeneous correlations for H_2O and CO_2 mixtures in (Dorigon et al., 2013). With the development of exhaust particulate filters, the focus on soot modelling for the calculation of soot emissions in IC engines is no longer a priority (Guan et al., 2015). Although for the soot absorption coefficient modelling, it is essential to include the calculation of soot formation process, where the common correlation for soot modelling can be found in the (Cassol et al., 2015). The scattering phenomena can be neglected for the IC engine simulation, since it was neglected in all conducted IC engine calculations, due to the small size of soot particles and with an emissivity similar to grey gas model (Granate et al., 2016).

Furthermore, the algorithm for spatial angle discretisation with an arbitral number of theta and phi angles is implemented, where each spatial angle represents an ordinate. This algorithm is based on the procedure presented for regular geometries in the literature (Chai et al., 1994) and irregulated geometries (Chai et al., 1995). After Performing the spatial discretisation, the incident radiation can be calculated for each ordinate with corresponding transport equation, and then summarised in all ordinates to obtain the radiative source term in the energy conservation equation (Coelho, 2014b).

Since the radiative heat transfer directly influences the temperature field inside the combustion chamber, the numerical results of forming emission would also be affected by

4

the participating radiative media (Pang et al., 2016). The recent research for calculating emissions and optimising the combustion process by using the CFD in combustion chambers showed that the radiative properties of the gas inside the IC engine combustion chamber could not be neglected (Dec, 2009). For the definition of incident radiation at the boundary value, the implementation of symmetry, diffusive opaque and periodic boundary is performed for all ordinates directions based on the (Boulet et al., 2007). The implemented model is validated on simple geometry cases available in the literature. First validation case is parallel plates for which analytic result is available in (Fiveland, 1984), and the second one is the cylinder for which analytic result is available in (Dua and Ping, 1975). With the satisfactory agreement against the analytical results, the implemented radiation FVM DOM and radiative absorption coefficient model WSGGM are employed for IC simulations, where the combustion process is modelled with ECFM-3Z model as in (Jurić et al., 2019). Additionally, the results are compared with experimental measurements of the diesel engine from a production line passenger car, that were conducted by AVL GmbH.

According to the authors' knowledge, just a few papers are published regarding the CFD investigations of radiative heat transfer in internal combustion engines, and none of these has combined implemented models on an evaluation of compression ignition engine emissions and parameter study of wall emissivity factors, and spatial discretisation. Furthermore, the research revealed some new points regarding the impact of radiation on emission formation. The higher soot concentration influences the mean in-cylinder temperature during the combustion process and decreases the mean temperature during the combustion and expansion process of the IC engine. The regions of the highest soot concentration gradients showed the most significant difference in the temperature profiles between calculations that exclude and include the radiative heat transfer inside the engine combustion chamber. Additionally, the radiative heat transfer decreases the NO_x formation concentrations due to the overall lower in-cylinder temperatures. Obtain mean pressure, mean temperature, and heat release results are validated against the experiment. Finally, the implemented FVM DOM and WSGGM in combination with a combustion model in AVL FIRE™ are capable of numerical assessment of radiative heat transfer phenomena in IC engines and evaluation of its impact on the pollutant formation process.

2. MATHEMATICAL MODEL

In this section, the emphasis is on the mathematical modelling of the radiative heat transfer, where the implementation of the FVM DOM model is explained into details. All simulations in this work are calculated with Reynolds-Averaged Navier-Stokes (RANS) equations inside AVL FIRE™ v2019 CFD software. The Reynolds stress tensor is modelled by using the $k - \zeta - f$ turbulence model, which is considered as a suitable turbulence model

for modelling in compression ignition engines (Hanjalić et al., 2004), compared to the conventional $k - \varepsilon$ turbulence model described in (Honus et al., 2017). This model benefits with the robustness for modelling strong swirl motion and tolerance to a small value of dimensionless wall distance at the boundary cell-centre.

2.1. Spray modelling

In this work, Euler Lagrangian spray modelling approach is used, which assumes the liquid phase as parcels that move through continuum gas phase. Basic equations that describe the continuum phase are the conservation laws of mass, momentum and energy, which are calculated for the finite volumes. The motion of the liquid phase parcels is traced through the finite volume mesh by calculating their pathways, where the only observed force is drag force. The drag force is calculated by Schiller Neumman law, where the parcel trajectory is obtained from deceleration u_{pi} in the following term:

$$m_p \frac{du_{pi}}{dt} = 0.5\pi\, r^2 \rho C_D u_{rel}{}^2 \tag{1}$$

In Equation (1), the drag coefficient C_D is experimentally determined by the Cunningham correction factor. For the disintegration process of bulk liquid, WAVE disintegration model was employed. In such a model, liquid droplets or blobs are assumed to be spherical, and the increase of first perturbations on the surface of droplet is correlated to their wavelength (Gao et al., 2016).

The radius of the produced droplet, r_{stable} can be expressed as:

$$r_{stable} = \lambda_w C_1 u_{rel}{}^2 \tag{2}$$

where C_1 is the constant of WAVE model (assumed 0.61), λ_w is the wavelength on the droplet surface of the highest growing gradient. By using the WAVE model, the parcel size reduction rate is defined as:

$$\frac{dr}{dt} = -\frac{\lambda_w\, \Omega\, (r - r_{stable})}{3.726\, r\, C_2} \tag{3}$$

The term C_2 in Equation (3) is a modelling constant which is used to delay the droplet breakup time, which varies from type of injector, and in this work is modelled as a constant value of 15. In the WAVE model, the wave growth rate Ω and the wavelength λ_w are calculated as depending on the local flow characteristics (Petranović et al., 2015). Evaporation process was described with Abramzon-Sirignano evaporation model (Abramzon and Sirignano, 1989), which assumes Le number value of evaporation process

6

1. Evaporation process and breakup disintegration process were modelled for sphere parcels of constant temperature and physical properties through fluid parcel, where the first injected parcels are assumed of same size as nozzle orifice diameter. For the wall parcel interaction a Walljet1 model is employed together with turbulent dispersion model, which details can be found in the literature (AVL AST GmbH, 2019).

2.2. Combustion modelling

For the combustion modelling, three-zones Extended Coherent Flame (ECFM-3Z) model is employed, which is appropriate for IC engine. ECFM-3Z features decoupled turbulence and chemistry calculation, for which standard species transport equation has to be solved (Colin and Benkenida, 2004).

$$\frac{\partial \overline{\rho} \tilde{y}_k}{\partial t} + \frac{\partial \overline{\rho} \tilde{u}_i \tilde{y}_k}{\partial x_i} - \frac{\partial}{\partial x_i}\left(\left(\frac{\mu}{Sc} + \frac{\mu_t}{Sc_t}\right)\frac{\partial \tilde{y}_k}{\partial x_i}\right) = \overline{\dot{\omega}_k} \tag{4}$$

where $\tilde{y}_k$ is the average mass ratio of specie k, and $\overline{\dot{\omega}_x}$ is the specie's source term from combustion reactions. For the mixture fraction f, fuel mass fraction y_{fu}, and residual gas mass g transport equations are determined (AVL AST GmbH, 2019):

$$\frac{\partial}{\partial t}\left(\rho y_{fu}\right) + \frac{\partial}{\partial x_i}\left(\rho \tilde{u}_i y_{fu}\right) = \frac{\partial}{\partial x_i}\left(\Gamma_{fu}\frac{\partial y_{fu}}{\partial x_i}\right) + S_{fu} \tag{5}$$

$$\frac{\partial}{\partial t}\left(\rho f\right) + \frac{\partial}{\partial x_i}\left(\rho \tilde{u}_i f\right) = \frac{\partial}{\partial x_i}\left(\Gamma_f \frac{\partial f}{\partial x_i}\right) \tag{6}$$

$$\frac{\partial}{\partial t}\left(\rho g\right) + \frac{\partial}{\partial x_i}\left(\rho \tilde{u}_i g\right) = \frac{\partial}{\partial x_i}\left(\Gamma_g \frac{\partial g}{\partial x_i}\right) \tag{7}$$

For the autoignition of air-fuel mixture the ignition delay and heat release are perambulated on the 0D reactors. The further model description of the model and calculation procedure of fuel mass ratio in flue gases, and mass fraction of fuel in the fresh air is described in literature (Jurić et al., 2019). The main limitation of the model is reduced chemistry kinetics, that is only account for the transport of standard species and that there is no unburnt fuel in the burnt gas phase (Mobasheri, 2015).

2.3. Emission modelling

The NO_x emission formation in this work is modelled for prompt and thermal, employing the Extended Zeldovich model described in the literature (Vujanović et al., 2009). The Extended Zeldovich model also includes temperature fluctuations in its chemical

reactions employing probability density function with a two-moment function beta. The description of the Extended Zeldovich equations is described in (Petranović et al., 2016). Due to the high activation energy required to split the strong N_2 triple bond, the rate of formation of NO within this model is significant only at high temperatures (greater than 1800 K) (Rao and Honnery, 2013). Further NO_x modelling approaches can be found in the review paper (E et al., 2017).

The soot formation process is modelled with the reduced kinetic soot model, which is based on a detailed soot formation kinetic scheme (Pang et al., 2012). The reduced kinetic soot formation model incorporates seven gas phase reactions in the combustion model, with only one additional species for the soot (Wu et al., 2019). The reduced mechanism applied in this work is described with the following chemical reactions (AVL AST GmbH, 2019):

$$C_xH_y + \left(\frac{x}{2} + \frac{y}{4}\right)O_2 \rightleftarrows x\,CO + \frac{y}{2}H_2O$$

$$H_2 + H_2 + O_2 \rightleftarrows H_2O + H_2O$$
$$CO + CO + O_2 \rightleftarrows C_2O + C_2O$$
$$CO + H_2O \rightleftarrows C_2O + H_2$$
$$C_xH_y + C_xH_y \rightleftarrows 2x\,C + y\,H_2$$
$$C + C + O_2 \rightleftarrows CO + CO$$
$$C + H_2O \rightleftarrows CO + H_2$$
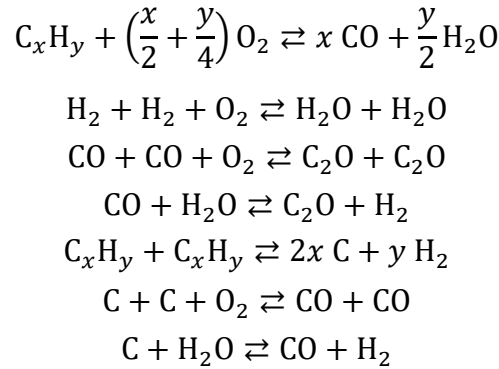
where C represents the soot. The reaction parameters for the primary soot formation reaction are changing with the air fuel ratio, while the presence of oxygen and water oxidizes the soot. The soot particle formation process is characterized by a gaseous-solid conversion, where the solid phase does not exhibit a uniform chemical and physical topology (AVL AST GmbH, 2019).

2.4. Radiative heat transfer modelling

The radiation in participating media is modelled by implementing DOM featuring FVM. The radiative heat transfer is consisting of three phenomena: absorption, emission and scattering. Figure 1 shows the scheme of incident radiation balance, where the media absorb the incoming radiation through participating media, enhanced by the emission of the media and scattered in different directions.
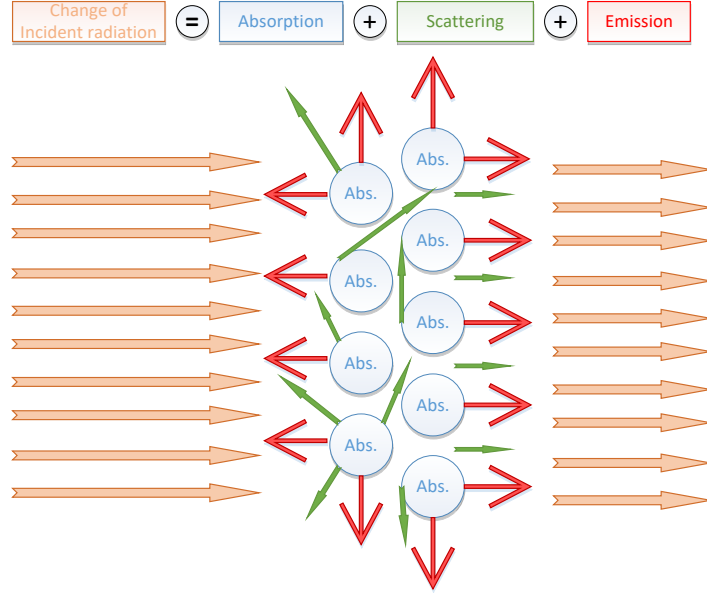
Figure 1   Scheme of radiative heat transfer in participating media

Such phenomena are specifed by the RTE, which in its full form can be written as

$$\frac{\mathrm{dI}(\vec{r},\vec{s})}{\mathrm{ds}} = \kappa(\vec{r})\mathrm{I_b}(\vec{r}) \text{-} (\kappa + \sigma_s)(\vec{r})\mathrm{I}(\vec{r},\vec{s}) + \frac{\sigma_s(\vec{r})}{4\pi}\int_{4\pi}\mathrm{I}(\vec{r},\vec{s}')\Phi(\vec{r},\vec{s},\vec{s}')\mathrm{d}\Omega' \tag{8}$$

which for the DOM featuring FVM gets the following expression for the spatial angle discretisation:

$$\frac{\partial \mathrm{I}^{\mathrm{l}}}{\partial s^{\mathrm{l}}} = \text{-}(\kappa + \sigma_s)\mathrm{I}^{\mathrm{l}} + \kappa\left(\frac{\sigma\mathrm{T}^4}{\pi}\right) + \frac{\sigma_s}{4\pi}\sum_{\mathrm{l}=1}^{\mathrm{M}}\mathrm{I}^{\mathrm{l}}\,\Phi^{\mathrm{l}}\Delta\Omega^{\mathrm{l}} \tag{9}$$

where I^l in the Equations (8) is the intensity of incident radiation in the l direction, κ is the absorption coefficient, σ_s is scattering coefficient, Φ is scattering phase function and s^l is an ordinate direction with its spatial angle $\Delta\Omega^l$. Spatial angle discretisation is showed in Figure 2, where the ordinate direction s^l is oriented perpendicular to its spatial angle.
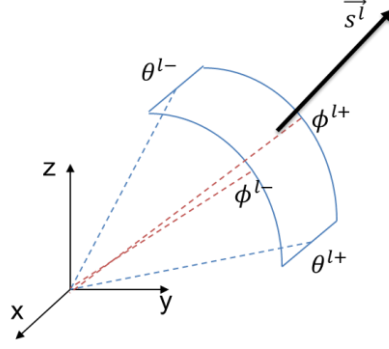
Figure 2   Spatial angle discretisation

Equation (9) has to be solved for each discretised spatial angle, but the minimal number is recommended to be eight (Modest, 2013). When the intensity of incident radiation in each ordinate direction is obtained, the incident radiation is calculated as:

$$G = \sum_{i=1}^{n} I^l \cdot \Delta\Omega^l \tag{10}$$

where n is the total number of control angles (spatial angle discretisation). It can be noticed from Equation (9) that the incident radiation depends on the temperature. The interaction between the radiation heat transfer and the energy conservation equation for each cell in the computational domain is then modelled as the radiative heat source term in the energy conservation equation. The radiative source term is defined as:

$$S_{rad} = \kappa(G\text{-}4\sigma T^4) \tag{11}$$

which then is considered as an input in the source term of energy conservation equation. If Equation (9) is applied to the computational domain with three dimensional discretised cells, the following equation is obtained:

$$\sum_{i=1}^{\text{number of all cell faces}} \Delta A_i\, I^l \int_{\Delta\Omega^l} \left(s^l_i\, n_i\right) d\Omega^l$$
$$= \left(\text{-}(\kappa + \sigma_s)I^l + \kappa\left(\frac{\sigma T^4}{\pi}\right) + \frac{\sigma_s}{4\pi} \sum_{k=1}^{\text{num\_dir}} I^k\, \Phi^k\, \Delta\Omega^k \right) \Delta\Omega^l \Delta V \tag{12}$$

The term on the left-hand side in Equation (12) presents the divergence of the incident radiation intensity, which can be affected by the three above mentioned phenomena. Equation (12) is calculated iteratively during the fluid flow iterations together with the fluid

flow calculation. The symmetry and diffusive opaque boundary conditions are implemented for the description of incident radiation in all ordinate's directions at the domain boundaries. The boundary condition for the diffusive walls is calculated only for the directions that are oriented into the computational domain and are calculated as (Coelho, 2013):

$$I_{bnd}^l = \varepsilon \frac{n_r^2 \sigma T^4}{\pi} + \frac{1-\varepsilon}{\pi} \sum_{(s^l \cdot n_i) < 0}^k I^k \cdot |n_i s_i| \Delta \Omega^k \tag{13}$$

where ε is the wall emissivity, and n_r is a refractive index which is for all surfaces in this work assumed one. The term on the left-hand side in Equation (13) represents the emission term, while on the right-hand side is the reflexion term. Diffusive reflection term is modelled as a reflection factor multiplied by the ratio between the radiation that hits the wall and geometrical characteristics of reflected directions.

The implemented algorithm for calculating spatial angle boundaries and directions is based on the upwind differencing scheme, and it is shown in Figure 3. Figure 3 shows how the intensities of incident radiation propagate in the computational domain with the global coordinate system.
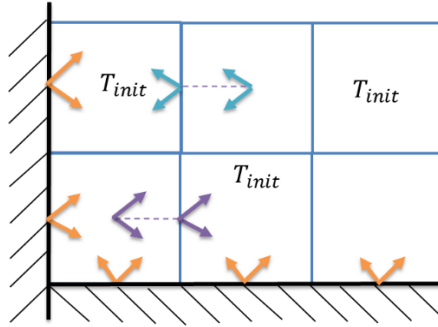
Figure 3   Algorithm for calculation of incident radiation.

Convergence criterium of Equation (11) is modelled with the following equation:

$$\frac{I_{new}^L - I_{old}^L}{I_{new}^L} < \text{ convergence criterium} \tag{14}$$

For all calculations presented in this paper, convergence criterium was 0.001.

2.4.1. Absorption coefficient modelling

Absorption coefficient in this work is modelled by implemented WSGGM for grey gases, which is based on the CO_2 and H_2O correlations in the literature (Dorigon et al., 2013). The correlations in [13] model the soot absorption coefficient, added to the gas

11

absorption coefficient based on superposition rule of RTE. The following equation, where the calculate the total absorption coefficient κ_s presents the soot absorption coefficient:

$$\kappa = -\frac{\ln(1-\varepsilon)}{s} + \kappa_s \tag{15}$$

The s in Equation (16) presents the thickness of absorption media, which is calculated by the following equation:

$$s = 3.6\frac{\Delta V}{A_{tot}} \tag{16}$$

where ΔV presents the cell volume and A_{tot} is the sum of all cell's faces. Emissivity ε in Equation (17) is calculated with the following equation of WSGGM:

$$\varepsilon = \sum_{i=0}^{2} \alpha_i \left(1 - e^{-a_i p s}\right) \tag{17}$$

where α_i is weight factor for the ith grey gas and is dependent only on temperature. The absorption coefficient a_i of the ith grey gas is determined by partial pressures p of the water vapour and carbon dioxide, which absorbs the incident radiation. For $i = 0$ the gas absorption coefficient has value α_o to resolve transparent windows in the spectrum between spectral regions of high absorption. For the transparent windows, the weight factor is calculated as:

$$\alpha_o = 1 - \sum_{i=0}^{2} \alpha_i \tag{18}$$

The other weighting factors are given by a polynomial of third order in the following form, where $b_{i,j}$ is the polynomial coefficient:

$$\alpha_i = \sum_{j=0}^{3} b_{i,j}\, T^j \tag{19}$$

The soot absorption coefficient is modelled as grey gas absorption, due to its the radiative properties, with the following equation:

$$\kappa_s = 0.672 \, T \, c \qquad\qquad (20)$$

where c is the soot mass fraction.

2.4.2. Model Validation

Validation of the implemented model is conducted on simple geometry cases for which the analytical results exist, where the good agreement with analytical results is obtained. The validation is firstly conducted on parallel plates for which analytic result is available in (Fiveland, 1984). From the unidimensional solution, the case with the absorption coefficient $a = 0.1 \, \mathrm{m}^{-1}$, and 1 m distance between two plates where the first plate is at 0 K and the second plate is at 2000 K. The numerical simulation is performed on 10x10x10 cells (1x1x1 m) cube mesh where the two opposing walls are set as black surface boundary conditions, where one plate does not emit any radiation due to its temperature 0 K. All remaining walls as symmetry boundary conditions, and the implemented FVM DOM was described with eight ordinates. Figure 4 shows the temperature field between two plates, where the good agreement with the implemented and the analytical result is achieved. For the second validation case, a cylinder of same height and diameter for which analytic result is available in (Dua and Ping, 1975) is selected. The cylinder has all walls assumed as black surfaces at 0 K, so there is not any emittance from cylinder walls. Only the absorption and emissivity of media at 500 K with absorption factor $a = 1 \, \mathrm{m}^{-1}$ inside the cylinder is assumed. Figure 5 shows the result of the unidimensional wall heat flux at the cylinder base on cylinder hexahedron mesh with 20 cells in each direction. The good agreement with the analytical result is achieved. The more details about validation cases can be found in cited references.
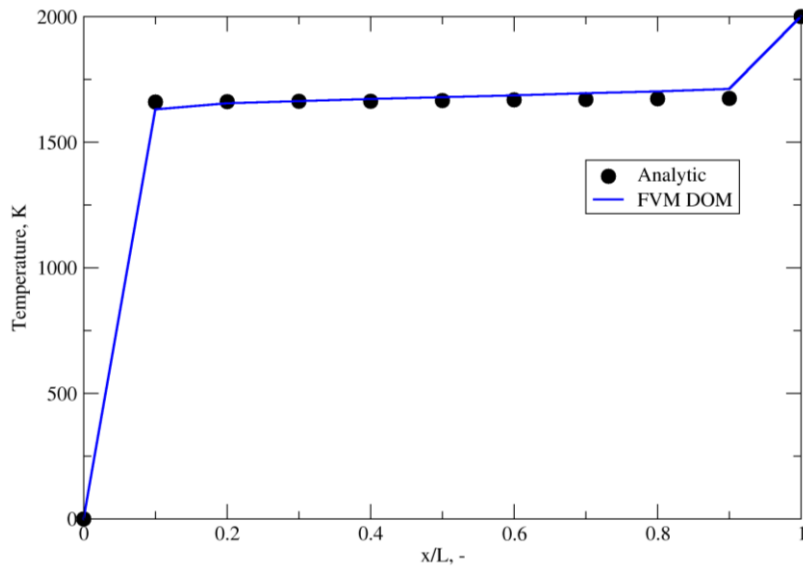
Figure 4   Validation results for the parallel plates (Fiveland, 1984).
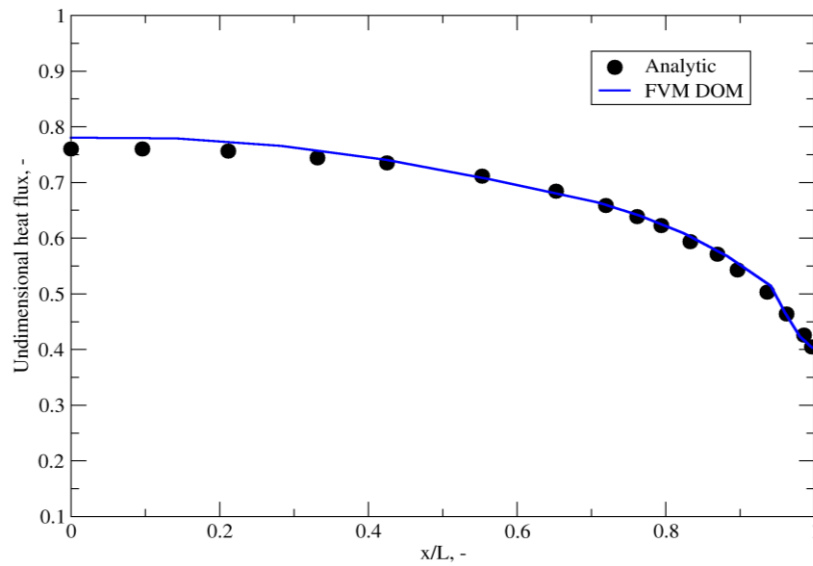
Figure 5 Validation results for cylinder case in (Dua and Ping, 1975).

3. EXPERIMENTAL DATA

The experimental measurements of the diesel engine from a production line passenger car are performed by AVL GmbH. The properties of the Volvo I5D engine and injection system are shown in Table 1.

Table 1   Engine and injection system specifications.

Type	Direct injection diesel
Bore (mm)	81
Compression ratio	16.5
Stroke (mm)	93.15
Spray Angle (°)	17.5
Number of nozzle holes	7
Diameter of nozzle hole (mm)	0.125

At the start of the experiment, the combustion chamber was initialised with a mixture of fresh air and Exhaust Gas Residuals (EGR) gas for each engine operating point. The injection temperature of the EN590 B7 fuel was set to 44°C, according to the experimental data.

The fuel inlet boundary condition was determined from the experimentally measured rate of injection, as shown in Figure 6. The rate of injection curve is given in non-dimensional parameters where the integral of the curve must be equalised with the injected liquid mass to obtain the injection velocity profile.
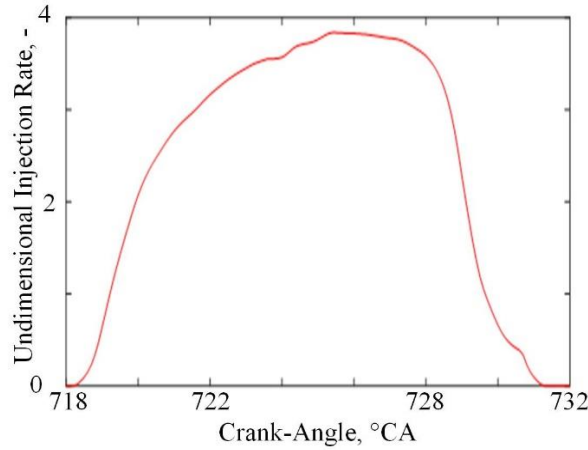
Figure 6   Injection rate profile.

4. NUMERICAL SETUP

Numerical calculations are performed with CFD code AVL FIRE^{TM}. The simulation time was set to the high-pressure cycle period when the inlet and exhaust valves are closed, particularly from 585°CA to 855°CA. Only the injection process from one nozzle hole is observed, and symmetric in-cylinder behaviour was assumed. During the calculation, a 1/7th segment of the complete engine cylinder was modelled, and the cyclic boundary conditions at the side surfaces were applied. The moving mesh was generated by the AVL FIRE^{TM} ESE DIESEL, and it contains around 35000 control volumes at the Top Dead Centre (TDC), and around 86000 cells in the Bottom Dead Centre (BDC). The generated computational domain with the defined boundary conditions, located at the TDC is shown in Figure 7. The mesh was generated with a 2-cell boundary layer, and in combination with wall functions, it was used to consider the wall impact on the fluid flow. The cylinder geometry is symmetric around the cylinder axis, and therefore, the cyclic (periodic) boundary conditions are applied at the sides. Mesh movement was described by rezoning procedure, where the meshes with the different number of cells, but same boundary conditions are exchanged during the compression and expansion (Tatschl, 2012). A compensation volume was added at the piston geometry to compensate geometry irregularities, and to conserve the exact compression ratio.
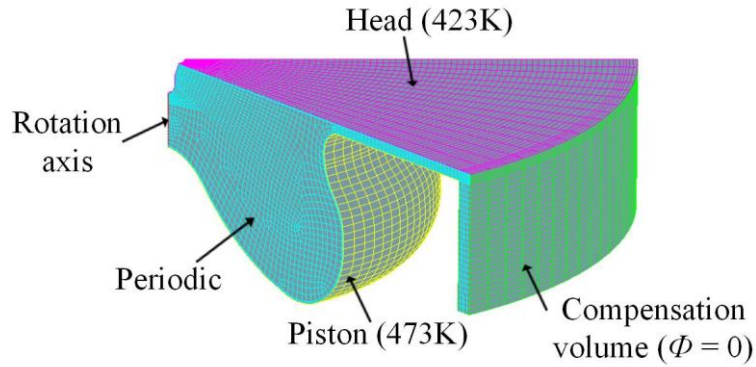
Figure 7   Computational domain positioned in the top dead centre.

Two additional meshes with smaller cell size, but with the same structure of block cells were generated in order to prove independency of the mesh on simulation results. The results on three meshes showed good agreement for mean in-cylinder pressure, temperature and Rate of Heat Release (RoHR) results, but also for the emission results.

For the mass conservation equation, the central differencing scheme is employed, while for the energy and turbulence conservation equations the upwind differencing scheme is applied. For the momentum equation, a combination of central differencing scheme and upwind differencing scheme was proposed by introducing a blending factor of 0.5. The convergence criteria for the solution are defined when the normalised pressure, momentum and energy residuals reach values lower than 10^{-4}. For turbulence and energy, the first order transport equations are solved using the upwind differencing scheme, while the central differencing scheme was employed for the mass conservation equation. The wall selections were defined as isothermal walls, and the air and fuel entrainments were prescribed with a constant temperature mass flow. All results showed in this work considered a maximum of 10 DOM FVM solver iterations, which were enough to achieve convergence. It was noticed, that the incident radiation results do not change significantly through each fluid flow iteration, and therefore the results calculated when the radiation solver is called each fluid flow iteration were compared when the solver was called every fifth and every tenth iteration. The results showed the approximately same values of mean pressure and pollutant mass fractions for all calculated incident radiations with every fluid flow iteration, every fifth and every tenth iteration. As a result, all simulations performed in this paper will be considered the calculation of incident radiation every tenth fluid flow iteration.

Selected ECFM-3Z combustion model parameters were extinction temperature at 200 K, autoignition time factor at the value of 1 and mixing parameter at the value of 1.

16

Operating points that are investigated in this paper feature a single injection, with the swirling motion inside the cylinder was defined as motion around symmetry axis with a value of 4740 min^{-1}, according to the experimental research. The initial conditions, combustion parameter and initial gas composition are shown in Table 2, where Case *a* and Case *b* are defined. The only differences between Case *a* and Case *b* is in the EGR mass fraction at the initial stage of the combustion, and initial temperature. From the initial conditions in Table 2, it is expected that Case *a* which features higher values of initial temperature and higher EGR mass fraction will show a more significant influence of radiative heat transfer than Case *b*. Both operating cycles have constant rotation speed and the same amount of injected fuel, for which the liquid properties of diesel EN590 B7 fuel are employed. The initial values of turbulent length scale and turbulent kinetic energy are estimated as 2 mm and 10 m^{2}s^2 following the setup presented in (Barbouchi and Bessrour, 2009).

Table 2   Initial conditions.

Operating point		Gas composition (kg/kg)	Case *a*	Case *b*
Engine speed (rpm)	2000	O_2	0.184638	0.2290
Number of injections	1	N_2	0.758305	0.7672
Injected mass (mg)	4.1	CO_2	0.03888	0.0331
Pressure (Pa)	210000	H_2O	0.01818	0.0155
		Temperature (K)	419	365

Numerical simulations were performed on Intel® Xeon® E5-2650 v4 @ 2.20 GHz which has 24 CPUs.

5. RESULTS AND DISCUSSION

In this section, important specific objectives, the major results, and the most significant conclusions of the paper are discussed. Firstly, the mean pressure, temperature and RoHR results for cases in Table 2 are presented, following with emission results. Finally, the parameter analysis of the piston and head emissivity factor is conducted and shown.

Figure 8 shows a comparison between temperature profile for the Case *a*, where the orange curve represents the results obtained for the numerical calculation without considering the radiative heat transfer, and the blue curve represents the results employing FVM DOM radiation model. The discrepancy between simulations with and without included radiation can be attributed mainly to the soot absorption, which has grey gas behaviour, that absorbs a high percentage of incident radiation in the high-temperature regions. The RoHR results (for the only 1/7th of the cylinder) shows a similar effect, where the energy loss due to the radiation is dominant for the highest RoHR values.

17
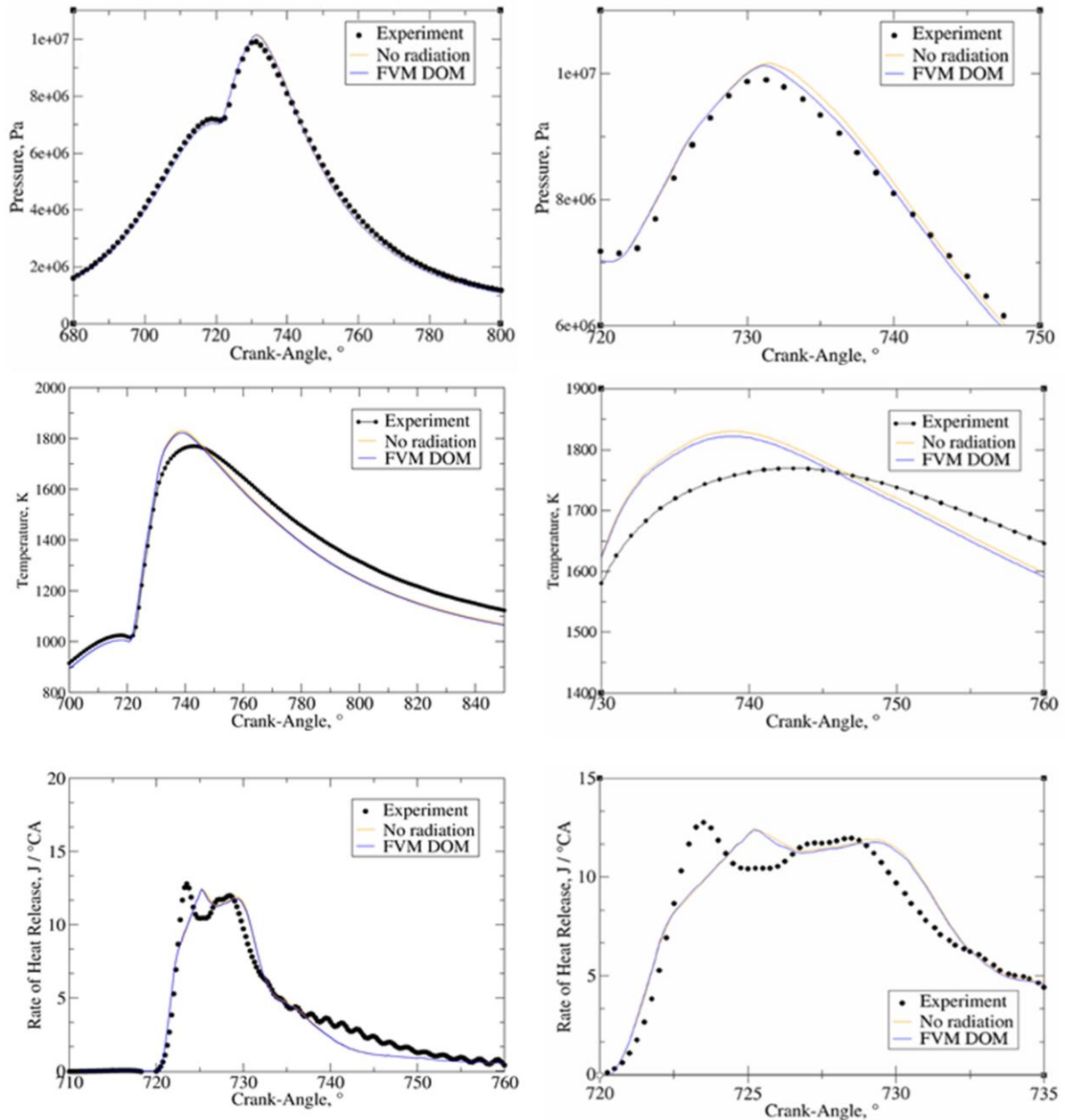
Figure 8   Case *a*: Mean pressure, temperature and rate of heat release curves for the results without considering radiative heat transfer and with FVM DOM (zoomed diagrams on right)

Figure 9 shows similar phenomena as Figure 8, but for the case without Exhaust Gas Recirculation in the initial phase of the operating point. The pressure curves of both operating conditions are in a good agreement with experimental results, but for Case *b* better agreement with the temperature results is achieved. The smaller discrepancy between result without radiation and with FVM can be attributed to the lower initial concentrations of CO_2 and H_2O, and the higher oxidising temperature of soot, due to better air to fuel ratio.

18
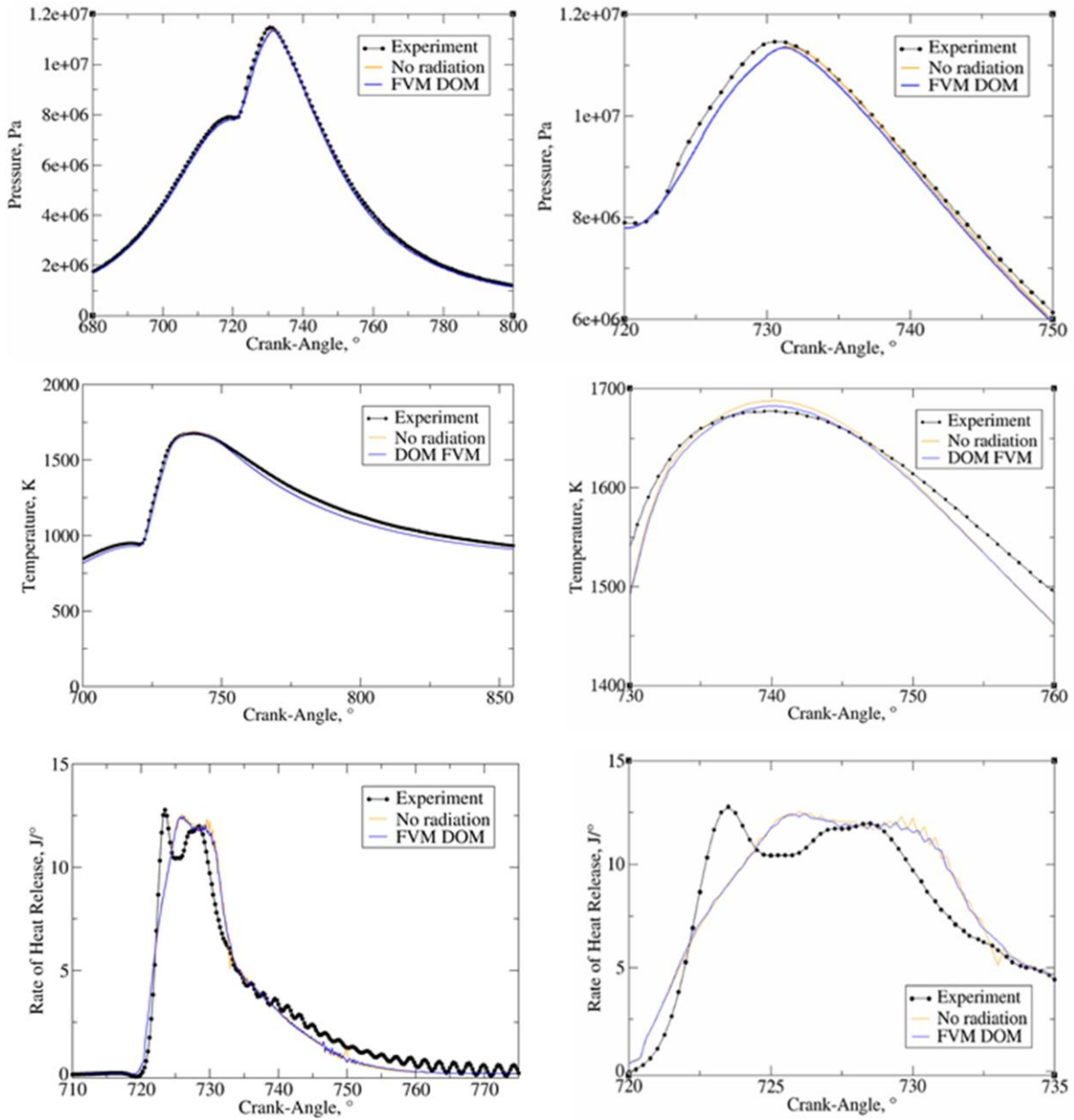
Figure 9   Case *b*: Mean pressure, temperature and rate of heat release curves for the results without considering radiative heat transfer and with FVM DOM (zoomed diagrams on right)

In both cases calculated RoHR curves underachieve the peak of firstly combusted regions and slightly postpone the combustion process. Although the same injected amount of fuel in both operating cases, significantly increased soot mass fraction at the end of the operating cycle is achieved in Case *a*, due to the lower initial oxygen concentrations. The difference between calculations without radiation and with the FVM DOM in Case *a* and Case *b* is mainly generated by soot concentrations inside the cylinder. Consequently, the higher soot concentrations in Case *a* resulted in a greater discrepancy between calculations without radiation and with the FVM DOM than in Case *b*.

19

Figure 10 shows 3D temperature profiles, where on the left side of diagram is the temperature field at the maximum soot mass fraction (740 °CA) for the simulation without radiation. On the right side is the temperature field for the included radiation. The highest difference between peak local temperature values for simulation without included radiation and with DOM FVM is around 15 K. Some discrepancy in temperature profiles is noticeable at the regions of high soot concentrations, which are also showed for 740 °CA in Figure 11. In the middle of the high-temperature region shown in Figure 10, the discrepancy between simulations is visible, which can be assigned to the H_2O and CO_2 absorption, since this region feature low values of soot mass fraction. Furthermore, CO_2 and H_2O as products of the combustion process are the most dominant exactly in the mentioned region where the first ignition is expected to occur. Figure 11 shows soot mass fraction profile inside the internal combustion engine, where the highest discrepancy between simulation without radiation and with FVM DOM is visible in the regions of highest temperature gradients. The distribution of soot mass fraction in Figure 11 shows a good agreement, where the regions of highest and lowest soot concentrations are preserved in calculations with and without radiative heat transfer. The total difference of soot mass fraction is achieved approximately 20 % higher with the calculations with FVM DOM than without considering radiation. Such a difference can have a great deal in the development process of new IC engines.
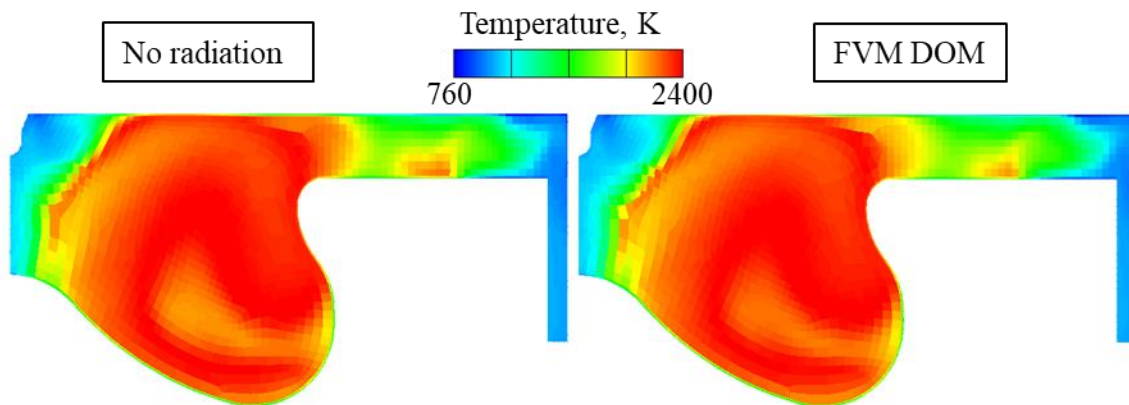
Figure 10   Temperature field for simulation without radiative heat transfer and with DOM FVM
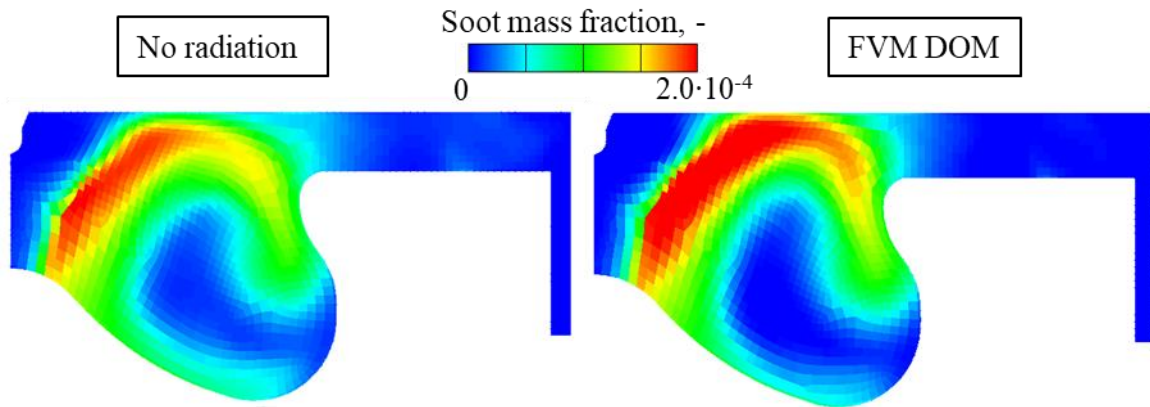
Figure 11   Soot mass fraction for simulation without radiative heat transfer and with FVM DOM

Table 3 shows the emission results for both operating conditions, where the more significant difference between simulations without radiation and with FVM DOM is achieved in Case *a*, due to the higher EGR value. Additionally, in both cases, the trend in emission formation is that the NO emissions are decreased with included radiative heat transfer, which can be ascribed to the lower temperature results, while the soot emissions are increased with the included radiative heat transfer, due to the lower temperature of in-cylinder gas that promotes the oxidation process of the soot.

Table 3   NO and soot emission results at the exhaust manifold.

Operating point		Experiment	No radiation	With radiation
Case *a*	NO mass fraction, ppm	136	367	317
	Soot mass fraction, ppm	36.6	29.7	37.3
Case *b*	NO mass fraction, ppm	252	621	508
	Soot mass fraction, ppm	2.1	0.89	0.91

In Table 6, the comparison of calculation time between simulations with and without radiation is shown, where the approximately 50 % more time consuming are the simulations when the radiative heat transfer is calculating.

Table 4   World clock computational time for simulations with and without radiation performed with 1 and 20 Central Processing Units (CPUs)

Number of CPUs	No radiation	With radiation
1	2 hours	3.5 hours
20	24 minutes	36 minutes

5.1. Parameter analyses

Impact of ordinates numbers on mean pressure during the operating cycle for eight, sixteen and thirty-two ordinates in Case *a* are shown in Figure 12. Each ordinate represents an additional direction for which the incident radiation is calculated, and for which an additional transport equation is calculated. As a result, the calculation with a higher number of ordinates have a numerically more accurate result but at the cost of higher computational demand. In Table 5, the world clock time of calculation time for simulations with eight, sixteen and thirty-two ordinates are shown, where an approximately linear increase in computational time is present with an increasing number of directions. It can be stated that for the calculation of radiative heat transfer in the IC engine 8 directions are enough to estimate the radiative impact on overall heat transfer.
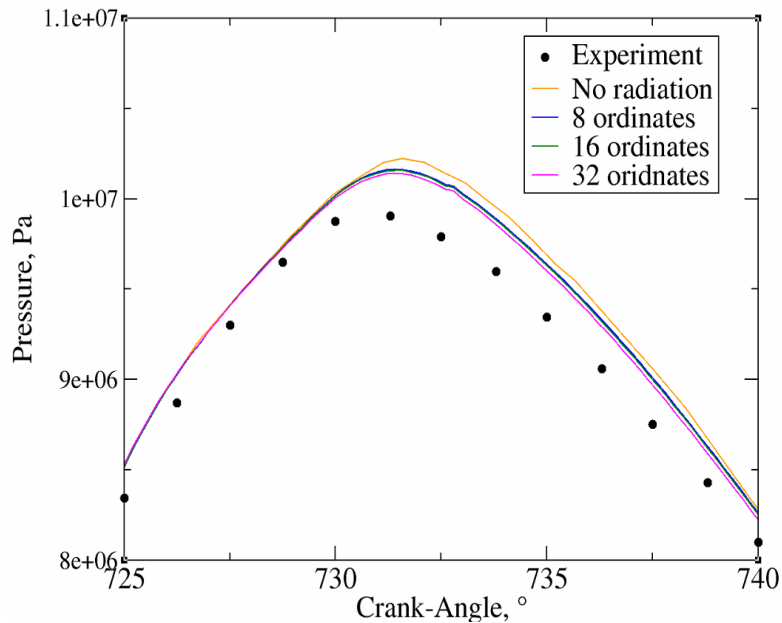
Figure 12   Mean pressure results for different number of ordinates

Table 5   World clock time for different number of ordinates in Case *a*

	Time, min
No radiation	24
8 ordinates	36
16 ordinates	49
32 ordinates	70

Figure 13 shows results obtained for the different values head and piston of the emissivity factor. Since the equivalent emissivity factor of the head and piston surface of

the experimental engine was not known, a parameter study was performed. The largest difference in mean pressure values can be noticed at the peak pressure values, which can be attributed to the highest temperatures at which the radiative heat transfer is more pronounced. Higher values of incident radiation filed inside the computational domain are achieved for the lower values of wall emissivity since the most of upcoming radiation is reflected into the domain, which results in higher incident radiation values at the piston and head selections. In all radiative heat transfer researches conducted in IC engine, a black surface emissivity was assumed. From Figure 13 it can be observed that with a lower emissivity, a better agreement with experimental results can be obtained, that can be attributed to metal surfaces in the experimental combustion chamber. Table 6 shows the impact of the piston and head emissivity values on exhaust emissions on Case *a* results, where a good trend in reducing of NO emissions can be attributed to the lower mean temperature inside the combustion chamber, that was observed in Figure 13. For the soot emissions, the higher soot mass fractions are achieved with lower emissivity values of head and piston wall.
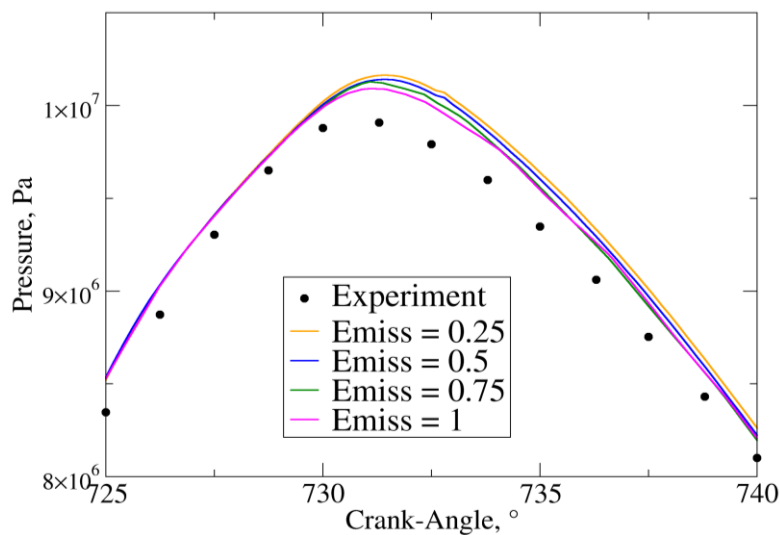
Figure 13   Mean pressure results for the different values of piston and head emissivity factors

Table 6   Impact of the piston and head emissivity factors on pollutant results at the end of Case *a*

	NO mass fraction, ppm	Soot mass fraction, ppm
Experiment	136	36.6
No radiation	367	29.7
Emissivity = 1	317	37.3
Emissivity = 0.75	316	37.8
Emissivity = 0.5	311	38.2
Emissivity = 0.25	301	39.2

6. CONCLUSIONS

The utilisation of the CFD for energy efficiency improvements and reduction of pollutant emissions in the industrial applications provides a valuable tool which provides feasibility to investigate different engine operating and design parameters. Discrete Ordinates Method employing Finite Volume Method is implemented by user functions into the AVL FIRE™ CFD software package. For the calculation of radiative absorption coefficient of participating radiative media, the implemented Weighted-Sum-of-Grey-Gases Model is employed featuring non-isothermal and non-homogeneous polynomial functions for H_2O, CO_2 and soot. The calculation procedure is adapted for computing on parallel units, rezoning process, and moving meshes, that are needed for calculation of IC engines. The validation of the implemented model on simple geometry cases showed a satisfactory agreement with the analytical results. After performed validation, the study was focused on the radiative heat transfer modelling in combination with the combustion process inside a diesel combustion chamber. Calculated mean pressure, mean temperature and the rate of heat release showed an agreement with the experimental traces. The most dominant impact on the radiative heat transfer is visible for the crank angles where the highest temperatures are achieved. The difference between calculations without radiation and with the FVM DOM in presented operating cases is mainly generated by soot concentrations in the regions of highest temperature gradients, where approximately 20 % lower total soot mass fraction is achieved with the simulations that account the radiative heat transfer. Parameter study of the piston and head wall emissivity values showed a reduction in mean in-cylinder pressure and NO mass fraction for a less reflective surface. The results obtained with the implemented radiation model predict lower peak temperatures for approximately 10 K, while the NO concentrations are decreased by 18 %, and soot concentration increased up to 20 %. From the conducted parameter analysis of ordinates number, the sufficient accuracy is achieved for simulations with eight ordinates, which resulted in approximately 50 % increased computational time. Finally, it can be concluded that if the additional physic phenomenon of radiative heat transfer is included in numerical simulations, a more accurate combustion and emission results are expected.

REFERENCES

Abramzon, B., Sirignano, W.A., 1989. Droplet vaporization model for spray combustion calculations. Int. J. Heat Mass Transf. 32, 1605–1618. https://doi.org/10.1016/0017-9310(89)90043-4

AVL AST GmbH, 2019. FIRE Documentation v2019.

Baleta, J., Mikulčić, H., Klemeš, J.J., Urbaniec, K., Duić, N., 2019. Integration of energy, water and environmental systems for a sustainable development. J. Clean. Prod. https://doi.org/10.1016/j.jclepro.2019.01.035

Barbouchi, Z., Bessrour, J., 2009. Turbulence study in the internal combustion engine 1, 194–202.

Bedoić, R., Jurić, F., Ćosić, B., Pukšec, T., Čuček, L., Duić, N., 2020. Beyond energy crops and subsidised electricity – A study on sustainable biogas production and utilisation in advanced energy markets. Energy 201. https://doi.org/10.1016/j.energy.2020.117651

Benajes, J., Martin, J., Garcia, A., Villalta, D., Warey, A., Domenech, V., Vassallo, A., 2015. An Investigation of Radiation Heat Transfer in a Light-Duty Diesel Engine. SAE Int. J. Engines 8. https://doi.org/10.4271/2015-24-2443

Bešenić, T., Baleta, J., Pachler, K., Vujanović, M., 2020. Numerical modelling of sulfur dioxide absorption for spray scrubbing. Energy Convers. Manag. 217, 112762. https://doi.org/10.1016/j.enconman.2020.112762

Bešenić, T., Mikulčić, H., Vujanović, M., Duić, N., 2018. Numerical modelling of emissions of nitrogen oxides in solid fuel combustion. J. Environ. Manage. 215, 177–184. https://doi.org/10.1016/J.JENVMAN.2018.03.014

Bohlooli Arkhazloo, N., Bouissa, Y., Bazdidi-Tehrani, F., Jadidi, M., Morin, J.-B., Jahazi, M., 2019. Experimental and unsteady CFD analyses of the heating process of large size forgings in a gas-fired furnace. Case Stud. Therm. Eng. 14, 100428. https://doi.org/10.1016/j.csite.2019.100428

Boulet, P., Collin, A., Consalvi, J.L., 2007. On the finite volume method and the discrete ordinates method regarding radiative heat transfer in acute forward anisotropic scattering media. J. Quant. Spectrosc. Radiat. Transf. 104, 460–473. https://doi.org/10.1016/j.jqsrt.2006.09.010

Cassol, F., Brittes, R., Centeno, F.R., da Silva, C.V., França, F.H.R., 2015. Evaluation of the gray gas model to compute radiative transfer in non-isothermal, non-homogeneous participating medium containing CO2, H2O and soot. J. Brazilian Soc. Mech. Sci. Eng. 37, 163–172. https://doi.org/10.1007/s40430-014-0168-5

Cernat, A., Pana, C., Negurescu, N., Lazaroiu, G., Nutu, C., 2015. Aspects of the animal fat use at the diesel engine fuelling. Proc. Univ. Power Eng. Conf. 1–6. https://doi.org/10.1109/UPEC.2015.7339917

Cerutti, M., Andreini, A., Facchini, B., Mangani, L., 2008. Modeling of turbulent combustion and radiative heat transfer in a object-oriented cfd code for gas turbine application, in: Proceedings of the ASME Turbo Expo. pp. 809–822. https://doi.org/10.1115/GT2008-51117

Chai, J.C., Lee, H.S., Patankar, S. V., 1994. Finite Volume Method for Radiation Heat Transfer. J. Thermophys. Heat Transf. 8, 419–425. https://doi.org/10.2514/3.559

Chai, J.C., Parthasarathy, G., Lee, H.S., Patankar, S. V., 1995. Finite volume radiative heat transfer procedure for irregular geometries. J. Thermophys. Heat Transf. 9, 410–415. https://doi.org/10.2514/3.682

Coelho, P.J., 2018. Radiative Transfer in Combustion Systems, in: Handbook of Thermal Science and Engineering. Springer International Publishing, Cham, pp. 1173–1199. https://doi.org/10.1007/978-3-319-26695-4_61

Coelho, P.J., 2014a. Advances in the discrete ordinates and finite volume methods for the solution of radiative heat transfer problems in participating media. J. Quant. Spectrosc. Radiat. Transf. 145, 121–146. https://doi.org/10.1016/j.jqsrt.2014.04.021

Coelho, P.J., 2014b. Advances in the discrete ordinates and finite volume methods for the solution of radiative heat transfer problems in participating media. J. Quant. Spectrosc. Radiat. Transf. 145, 121–146. https://doi.org/10.1016/j.jqsrt.2014.04.021

Coelho, P.J., 2013. on the Convergence of the Discrete Ordinates and Finite Volume Methods for the Solution of the Radiative Transfer Equation M.

Colin, O., Benkenida, A., 2004. The 3-zones Extended Coherent Flame Model (ECFM3Z) for computing premixed/diffusion combustion. Oil Gas Sci. Technol. 59, 593–609. https://doi.org/10.2516/ogst:2004043

Dec, J.E., 2009. Advanced compression-ignition engines—understanding the in-cylinder processes. Proc. Combust. Inst. 32, 2727–2742. https://doi.org/10.1016/j.proci.2008.08.008

Dorigon, L.J., Duciak, G., Brittes, R., Cassol, F., Galarça, M., França, F.H.R., 2013. WSGG correlations based on HITEMP2010 for computation of thermal radiation in non-isothermal, non-homogeneous H2O/CO2 mixtures. Int. J. Heat Mass Transf. 64, 863–873. https://doi.org/10.1016/j.ijheatmasstransfer.2013.05.010

Dua, S.S., Ping, C., 1975. Multi-dimensional radiative transfer in non-isothermal cylindrical media with non-isothermal bounding walls. Int. J. Heat Mass Transf. 18, 245–259. https://doi.org/10.1016/0017-9310(75)90157-X

E, J., Pham, M., Zhao, D., Deng, Y., Le, D.H., Zuo, W., Zhu, H., Liu, T., Peng, Q., Zhang, Z., 2017. Effect of different technologies on combustion and emissions of the diesel engine fueled with biodiesel: A review. Renew. Sustain. Energy Rev. https://doi.org/10.1016/j.rser.2017.05.250

Fajri, H.R., Jafari, M.J., Shamekhi, A.H., Jazayeri, S.A., 2017. A numerical investigation of the effects of combustion parameters on the performance of a compression ignition engine toward NOx emission reduction. J. Clean. Prod. 167, 140–153. https://doi.org/10.1016/j.jclepro.2017.08.146

Fernandez, S.F., Paul, C., Sircar, A., Imren, A., Haworth, D.C., Roy, S., Modest, M.F., 2018. Soot and spectral radiation modeling for high-pressure turbulent spray flames. Combust. Flame 190, 402–415. https://doi.org/10.1016/j.combustflame.2017.12.016

Fiveland, W.A., 1984. Discrete-Ordinates Solutions of the Radiative Transport Equation for Rectangular Enclosures. J. Heat Transfer 106, 699. https://doi.org/10.1115/1.3246741

Gao, H., Li, X., Xue, J., Bai, H., He, X., Liu, F., 2016. A modification to the WAVE breakup model for evaporating diesel spray. Appl. Therm. Eng. 108, 555–566. https://doi.org/10.1016/j.applthermaleng.2016.07.152

Granate, P., Coelho, P.J., Roger, M., 2016. Radiative heat transfer in strongly forward scattering media using the discrete ordinates method. J. Quant. Spectrosc. Radiat. Transf. 172, 110–120. https://doi.org/10.1016/j.jqsrt.2015.12.011

Guan, B., Zhan, R., Lin, H., Huang, Z., 2015. Review of the state-of-the-art of exhaust particulate filter technology in internal combustion engines. J. Environ. Manage. 154, 225–258. https://doi.org/10.1016/j.jenvman.2015.02.027

Gupta, A., Mishra, P.C., 2019. Optimization of emission characteristics of spark ignition engine with chambered straight muffler running in methanol blend:An engine development technique for environmental sustainability. J. Clean. Prod. 238. https://doi.org/10.1016/j.jclepro.2019.117778

Hanjalić, K., Popovac, M., Hadžiabdić, M., 2004. A robust near-wall elliptic-relaxation eddy-viscosity turbulence model for CFD. Int. J. Heat Fluid Flow 25, 1047–1051. https://doi.org/10.1016/j.ijheatfluidflow.2004.07.005

Honus, S., Pospíšilík, V., Jursová, S., Šmída, Z., Molnár, V., Dovica, M., 2017. Verifying the Prediction Result Reliability Using k-ε, Eddy Dissipation, and Discrete Transfer Models Applied on Methane Combustion Using a Prototype Low-Pressure Burner. Adv. Sci. Technol. Res. J. 11, 252–259. https://doi.org/10.12913/22998624/80922

Jurić, F., Petranović, Z., Vujanović, M., Katrašnik, T., Vihar, R., Wang, X., Duić, N., 2019. Experimental and numerical investigation of injection timing and rail pressure impact on combustion characteristics of a diesel engine. Energy Convers. Manag. 185, 730–739. https://doi.org/10.1016/j.enconman.2019.02.039

Kun-Balog, A., Sztankó, K., Józsa, V., 2017. Pollutant emission of gaseous and liquid aqueous bioethanol combustion in swirl burners. Energy Convers. Manag. 149, 896–903. https://doi.org/10.1016/j.enconman.2017.03.064

Lamas, M.I., Rodríguez, J. de D., Castro-Santos, L., Carral, L.M., 2019. Effect of multiple

injection strategies on emissions and performance in the Wärtsilä 6L 46 marine engine. A numerical approach. J. Clean. Prod. 206, 1–10. https://doi.org/10.1016/j.jclepro.2018.09.165

Lazaroiu, G., Pană, C., Mihaescu, L., Cernat, A., Negurescu, N., Mocanu, R., Negreanu, G., 2017. Solutions for energy recovery of animal waste from leather industry. Energy Convers. Manag. 149, 1085–1095. https://doi.org/10.1016/j.enconman.2017.06.042

López, José J., García-Oliver, J.M., García, A., Villalta, D., 2019. Development of a soot radiation model for diesel flames. Appl. Therm. Eng. https://doi.org/10.1016/j.applthermaleng.2019.04.120

López, J Javier, García, A., Monsalve-serrano, J., Cogo, V., Wittek, K., 2019. Potential of a two-stage variable compression ratio downsized spark ignition engine for passenger cars under different driving conditions. Energy Convers. Manag. 112251. https://doi.org/10.1016/j.enconman.2019.112251

Mikulčić, H., Baleta, J., Klemeš, J.J., 2020. Sustainability through combined development of energy, water and environment systems. J. Clean. Prod. https://doi.org/10.1016/j.jclepro.2019.119727

Mikulčić, H., Klemeš, J.J., Duić, N., 2016. Shaping sustainable development to support human welfare. Clean Technol. Environ. Policy 18, 1633–1639. https://doi.org/10.1007/s10098-016-1269-x

Mishra, S.C., Chugh, P., Kumar, P., Mitra, K., 2006. Development and comparison of the DTM, the DOM and the FVM formulations for the short-pulse laser transport through a participating medium. Int. J. Heat Mass Transf. 49, 1820–1832. https://doi.org/10.1016/j.ijheatmasstransfer.2005.10.043

Mobasheri, R., 2015. Analysis the ECFM-3Z Combustion Model for Simulating the Combustion Process and Emission Characteristics in a HSDI Diesel Engine. Int. J. Spray Combust. Dyn. 7, 353–371. https://doi.org/10.1260/1756-8277.7.4.353

Modest, M.F., 2013. Radiative Heat Transfer, 3rd ed, Elsevier. Elsevier. https://doi.org/10.1016/B978-0-12-503163-9.X5000-0

Modest, M.F., Haworth, D.C., 2016. Radiative heat transfer in high-pressure combustion systems, in: SpringerBriefs in Applied Sciences and Technology. Springer Verlag, pp. 137–148. https://doi.org/10.1007/978-3-319-27291-7_7

Pang, K.M., Karvounis, N., Walther, J.H., Schramm, J., 2016. Numerical investigation of soot formation and oxidation processes under large two-stroke marine diesel engine-like conditions using integrated CFD-chemical kinetics. Appl. Energy 169, 874–887. https://doi.org/10.1016/j.apenergy.2016.02.081

Pang, K.M., Ng, H.K., Gan, S., 2012. Investigation of fuel injection pattern on soot formation and oxidation processes in a light-duty diesel engine using integrated CFD-reduced

chemistry. Fuel 96, 404–418. https://doi.org/10.1016/j.fuel.2012.01.002

Paul, C., Ferreyro Fernandez, S., Haworth, D.C., Roy, S., Modest, M.F., 2019. A detailed modeling study of radiative heat transfer in a heavy-duty diesel engine. Combust. Flame 200, 325–341. https://doi.org/10.1016/j.combustflame.2018.11.032

Petranović, Z., Bešenić, T., Vujanović, M., Duić, N., 2016. Modelling pollutant emissions in diesel engines, influence of biofuel on pollutant formation. J. Environ. Manage. 1–9. https://doi.org/10.1016/j.jenvman.2017.03.033

Petranović, Z., Vujanović, M., Duić, N., 2015. Towards a more sustainable transport sector by numerically simulating fuel spray and pollutant formation in diesel engines. J. Clean. Prod. 88, 272–279. https://doi.org/10.1016/j.jclepro.2014.09.004

Rao, V., Honnery, D., 2013. A comparison of two NO x prediction schemes for use in diesel engine thermodynamic modelling. Fuel 107, 662–670. https://doi.org/10.1016/j.fuel.2013.01.071

Soni, D.K., Gupta, R., 2017. Numerical analysis of flow dynamics for two piston bowl designs at different spray angles. J. Clean. Prod. 149, 723–734. https://doi.org/10.1016/j.jclepro.2017.02.142

Sremec, M., Taritaš, I., Sjerić, M., Kozarac, D., 2017. Numerical Investigation of Injection Timing Influence on Fuel Slip and Influence of Compression Ratio on Knock Occurrence in Conventional Dual Fuel Engine. J. Sustain. Dev. Energy, Water Environ. Syst. 5, 518–532. https://doi.org/10.13044/j.sdewes.d5.0163

Stančin, H., Mikulčić, H., Wang, X., Duić, N., 2020. A review on alternative fuels in future energy system. Renew. Sustain. Energy Rev. 128, 109927. https://doi.org/10.1016/j.rser.2020.109927

Taghavifar, Hadi, Taghavifar, Hamid, Mardani, A., Mohebbi, A., Khalilarya, S., Jafarmadar, S., 2016. Appraisal of artificial neural networks to the emission analysis and prediction of CO2, soot, and NOx of n-heptane fueled engine. J. Clean. Prod. 112, 1729–1739. https://doi.org/10.1016/j.jclepro.2015.03.035

Tatschl, R., 2012. Appendix 3D-CFD Simulation of IC-Engine Flow, Mixture Formation and Combustion with AVL FIRE, Combustion Engines Development. https://doi.org/10.1007/978-3-642-14094-5

Vujanović, M., Duić, N., Tatschl, R., 2009. Validation of reduced mechanisms for nitrogen chemistry in numerical simulation of a turbulent non-premixed flame. React. Kinet. Catal. Lett. 96, 125–138. https://doi.org/10.1007/s11144-009-5463-2

Wu, S., Zhou, D., Yang, W., 2019. Implementation of an efficient method of moments for treatment of soot formation and oxidation processes in three-dimensional engine simulations. Appl. Energy 254. https://doi.org/10.1016/j.apenergy.2019.113661

Yildiz, I., Açıkkalp, E., Caliskan, H., Mori, K., 2019. Environmental pollution cost analyses

of biodiesel and diesel fuels for a diesel engine. J. Environ. Manage. 243, 218–226. https://doi.org/10.1016/j.jenvman.2019.05.002

Yoshikawa, T., Reitz, R.D., 2009. Effect of Radiation on Diesel Engine Combustion and Heat Transfer. J. Therm. Sci. Technol. 4, 86–97. https://doi.org/10.1299/jtst.4.86

Yue, Z., Reitz, R.D., 2019. Numerical investigation of radiative heat transfer in internal combustion engines. Appl. Energy 235, 147–163. https://doi.org/10.1016/j.apenergy.2018.10.098

PAPER 3

ASSESSMENT OF RADIATIVE HEAT TRANSFER IMPACT ON A TEMPERATURE DISTRIBUTION INSIDE A REAL INDUSTRIAL SWIRLED FURNACE

by

Filip JURIĆ[a], Milan VUJANOVIĆ[a], Marija ŽIVIĆ[b], Mario HOLIK[b], Xuebin WANG[c], and Neven DUIĆ[a]*

[a]Faculty of Mechanical Engineering and Naval Architecture, University of Zagreb, Zagreb, Croatia;
[b]Mechanical Engineering Faculty, Josip Juraj Strossmayer University of Osijek, Slavonski Brod, Croatia
[c]MOE Key Laboratory of Thermo-Fluid Science and Engineering, Xi'an Jiaotong University, Xi'an, Shaanxi, China

Combustion systems will continue to share a portion in energy sectors along the current energy transition, and therefore the attention is still given to the further improvements of their energy efficiency. Modern research and development processes of combustion systems are improbable without the usage of predictive numerical tools such as CFD. The radiative heat transfer in participating media is modelled in this work with discrete transfer radiative method (DTRM) and discrete ordinates method (DOM) by finite volume discretisation, in order to predict heat transfer inside combustion chamber accurately. The DTRM trace the rays in different directions from each face of the generated mesh. At the same time, DOM is described with the angle discretisation, where for each spatial angle the radiative transport equation needs to be solved. In combination with the steady combustion model in AVL FIRE™ CFD code, both models are applied for computation of temperature distribution in a real oil-fired industrial furnace for which the experimental results are available. For calculation of the absorption coefficient in both models weighted sum of grey gasses model is used. The focus of this work is to estimate radiative heat transfer with DTRM and DOM models and to validate obtained results against experimental data and calculations without radiative heat transfer, where approximately 25% higher temperatures are achieved. The validation results showed good agreement with the experimental data with a better prediction of the DOM model in the temperature trend near the furnace outlet. Both radiation modelling approaches show capability for the computation of radiative heat transfer in participating media on a complex validation case of the combustion process in oil-fired furnace.

Keywords: *radiative heat transfer, participating media, furnace, radiative absorption, combustion*

Introduction

It is known that the radiative heat transfer as a fundamental heat transfer mechanism is not negligible in the overall heat transfer of the energy systems that work at the high tem-

---

Jurić, F., *et al.*: Assessment of Radiative Heat Transfer Impact …
THERMAL SCIENCE: Year 2020, Vol. 24, No. 6A, pp. 1-10

2

perature conditions. Recent researches show that if emissions concentrations are to be calculated, it is not enough to exclude the impact of radiation on overall heat transfer and consequently, on emission formation [1]. In numerical modelling of engineering systems that operate at high temperatures such as furnaces, boilers, jet engines and internal combustion engines the consideration of radiative heat transfer in calculations significantly influence the energy efficiency [2]. As one of the predictive tools in energy efficiency investigation, the CFD is frequently utilised for the research of combustion system designs to evaluate the heat transfer impact on their energy efficiency [3]. With the development of the computational resources, the radiative heat transfer models within CFD are commonly applied to evaluate the impact of the radiative heat transfer impact on total heat transfer and temperature distribution [4]. For the calculation of radiative heat transfer in participating media of furnace combustion chamber, in this work, two radiation models have been applied: DTRM and DOM approximation with a finite volume approach. Both models are employed within the CFD software AVL FIRE™. These two models have different modelling approach in solving the radiative transfer equation (RTE) of participating media by their definition [5]. The DTRM model is based on the raytracing, which calculates the radiation intensity through the computational domain and has an utterly different modelling procedure from DOM featuring finite volume method [6]. In the pre-processing stage, the raytracing procedure is executed for each ray that is shot from the boundary face. The path through the computational domain is being calculated [7]. The input data of DTRM is a number of rays shot from the face, where for a greater number of rays, the more precise results will be obtained but will require more computational time [8]. For the DOM model, the input number of azimuthal and polar angles needs to be defined. After the spatial discretisation is conducted, the radiative heat transfer equation is calculated with transport equations for incident radiation in each spatial angle that represents one ordinate. Contributions of each ordinate are summed and added as input for calculation of the radiative source term in the energy conservation equation [9]. The authors of [10] show universality of DOM to be applied to a whole range of applications. The algorithm for obtaining ordinates directions and their spatial angles is described in [11]. Both modelling approaches (DTRM and DOM) are equally computationally demanding, and their accuracy is adjustable with input parameters [12]. Additionally, in this work, the absorptivity and emissivity are modelled as for isotropic media while the scattering phenomenon was not considered in observed simulations, since the soot participation in radiative heat transfer is well described by the grey-body model [13].

The recent research for optimising the combustion process by using CFD in combustion chambers showed that the application of radiative properties of the gas inside the steady system such as jet engine combustion chamber cannot be neglected [14]. The similar approach for investigating radiative heat transfer impact was used in the numerical modelling of heat transfer in strong swirl flow of furnaces [15]. Wang *et al.* [16], performed analysis of thermal efficiency with emphasis on the radiative impact calculated by DOM in reheating furnace. The AVL FIRE™ was already employed for steady calculations in biomass combustion in a rotary kiln in [17], where the similar framework is applied for the simulations in this work.

For the assessment of radiative heat transfer impact on temperature distribution in this work, IJmuiden furnace is selected for which dimensions and experimental data is available in [18]. The combustion process is modelled with steady combustion model (SCM) based on literature [19], where it was applied with and without heat transport by radiation. This SCM features fast convergence and steady solution of the combustion process and is applicable for the combustion process in oil-fired utility [20]. It is computationally less demanding

compared to the extended combustion models generally utilised in combustion systems like in [21]. A similar approach was applied for experimental oil furnace for emission predictions, but without radiation [22]. For the boundary conditions, diffusive opaque and inlet/outlet boundary conditions were applied for the calculation of incident radiation in directions that are oriented into the computational domain, based on the [23]. Similar approach was employed in [24], where the furnace gas temperature is predicted in reheating furnace with the P-1 radiation model. In [25], the estimation of radiative heat transfer in pulverised coal combustion is performed with the P-1, where the impact of particulate impact on incident radiation scattering is assumed.

Finally, this work aims to present the analysis of the radiative heat transfer in participating media with two different radiation models, DTRM and DOM in combination with SCM by employing CFD code AVL FIRE™ on an industrial furnace which includes the swirled combustion process. The performed validation of both radiative heat transfer models has shown that the presented modelling procedures are capable of predicting heat transport and can be used as a computationally fast tool that facilitates design and optimisation of industrial furnaces. The results with DTRM and DOM showed agreement in the validation against the experimental results. The results with DTRM and DOM showed agreement in the validation against the experimental results.

Mathematical model

All simulations performed in this paper are described with Reynolds-Averaged Navier-Stokes equations. The Reynolds stress tensor was modelled by using the k-ε turbulence model, which details can be found in [26].

Combustion modelling

The combustion process was modelled by SCM, which calculates a fast solution for the combustion process in oil-fired furnaces [20]. The SCM is based on empirical correlations for considering the impact of droplet evaporation, swirl motion, spray disintegration, chemistry kinetics on the oil combustion in an extended Arrhenius type expression. Additionally, SCM is applicable for the wide range of conventional oil flames. In SCM, the oil fuel is assumed in pre-mixed regime with the primary air-flow, due to consideration of the mixing time in combustion velocity. The model considers different reaction rate calculation:

$$\bar{r} = -\rho \frac{\partial \bar{y}_{\text{fu}}}{\partial t} = -k\rho \bar{y}_{\text{fu}} \bar{y}_{\text{O}_2} \tag{1}$$

where k is the reaction rate constant, $\bar{y}_{\text{fu}}$ – the average fuel mass fraction, and $\bar{y}_{\text{O}_2}$ – the average oxygen mass fraction, which is considered in the eq. (1) if $\bar{y}_{\text{O}_2}$ is lower than 0.03. Constant k could be characterized as a combustion velocity and is obtained from the following equation:

$$k = \frac{b}{t_{\text{ei}} + t_{\text{ox}}} \tag{2}$$

where the combustion velocity coefficient b is considered 33 for the $\bar{y}_{\text{O}_2}$ lower than 0.03 and 1 for $\bar{y}_{\text{O}_2}$ higher than 0.03, due to the influence of enough oxygen. The denominator of the eq. (2) is called total time, and it consists of two terms. The first term is time of evaporation and induction, t_{ei}:

$$t_{ei} = A \exp\left(\frac{10^5}{RT}\right) + 0.45695 d_{init}^2 \tag{3}$$

with T as local temperature, R – the universal gas constant, and d_{init} – the initial droplet diameter of value 0.3 mm. The second term is time of oxidation, which is calculated by following term:

$$t_{ox} = \frac{d_{init}^2}{0.0032(T - T_0) - 1.79} \tag{4}$$

In SCM fluid-flow is calculated only for one gaseous phase, which results that the evaporation process of inlet fuel is modelled inside the evaporation and induction time in eq. (3). Further description about evaporation time calculation can be found in literature [27]. This model gives good coverage of kinetic combustion for the lean region and for the burning of evaporated fuel in the region of disintegrated droplets. In SCM, the *b* is adjusted for different values of oxygen concentrations, which makes the reaction rate dependent on the availability of oxygen [20]. The mixing process of air and evaporated fuel in this work is amplified by the swirl motion of the primary inlet air. The inlet swirl velocity of primary air is defined by user-functions in the AVL FITE™, where the swirl ratio of 0.8 value around the *x*-axis is used. Additionally, this model is also suitable for calculating the flames formed in furnaces with the additional secondary inlet of air.

Radiative heat transfer modelling

In this subsection, two different modelling approaches that are used in this paper for the calculation of radiative heat transfer are presented: DTRM and DOM.

Discrete transfer radiative method

The primary assumption of the DTRM is that a single ray can approximate the radiation leaving the surface element in a specific range of solid angles. Such an assumption of DTRM is made by employing raytracing, where the change of incident radiation of each ray is only followed until the ray hit the wall [28]. The shift in incident radiation along a ray path can be written:

$$\frac{dI}{ds} = \frac{a\sigma T^4}{\pi} - aI \tag{5}$$

where a change of incident radiation I through path s is equivalent to a difference of the emitted and absorbed incident radiation, described with the absorption coefficient a. For this research, the refractive index is assumed 1. The DTRM integrates eq. (5) along with a series of rays leaving the boundary faces. The incident radiation is defined as I is calculated as [29]:

$$I = \frac{\sigma T^4}{\pi}[1 - \exp(-as)] + I_0 e^{-as} \tag{6}$$

In the pre-processing, the raytracing paths are computed and saved before the start of fluid-flow calculations. An azimuthal angle from which the rays are shot is varied from 0 to π and polar from 0 to 2π. For each ray, length within each control volume that it intercepts is calculated and stored. All wall boundaries are taken as black and diffuse. Thus, the intensity leaving the wall is given:

$$I_{bnd} = \frac{\sigma T_w^4}{\pi} \tag{7}$$

where T_w is the wall temperature and σ – the Stefan-Boltzmann constant. That means that the outgoing radiation flux is composed only of the directly emitting. The incident radiation at inlets and outlets leaves the calculation domain. Therefore, it is not reflected on inlet and outlet boundaries, and it is calculated:

$$I_{of} = \frac{\sigma T_{of}{}^4}{\pi} \tag{8}$$

where T_{of} is the temperature of the outflow boundary. The incident radiation flux at the boundary element is then calculated as the sum of incident intensities for all rays. In participating media, the energy gain or loss in internal cells due to radiation is given through the radiation source term. The radiation source term is then inserted as source term of the enthalpy conversation equation. The overall energy gain or loss for a specific internal cell is calculated from the sum of all rays the contributions crossing the cell.

Discrete ordinates method

The radiation in participating media was also modelled by the DOM model featuring a finite volume approach. The radiative heat transfer in the DOM is based on solving RTE, which is consisting of two mechanisms: absorption and emission. Participating media absorbs the incoming radiation, which is then enhanced by the emission of the media in j direction:

$$\frac{dI_j}{ds_j} = -(a + \sigma_s)I_j + a\left(\frac{\sigma T^4}{\pi}\right) \tag{9}$$

where I_j is the intensity of incident radiation in the j direction, a – the absorption coefficient, and s_j – the ordinate direction with its spatial angle $\Delta\Omega j$. Spatial angle discretization is defined as the ordinate direction s^l is oriented perpendicular to its spatial angle. The eq. (9) has to be solved for each discretised spatial angle, but the minimal number is recommended to be eight [13]. When the intensity of incident radiation in each ordinate direction is obtained, the incident radiation is calculated:

$$G = \sum_{j=1}^{n} I_j \Delta\Omega_j \tag{10}$$

where n is the total number of control angles that is defined by discretisation of spatial angles. It can be noticed from eq. (10) that the incident radiation depends mainly on the temperature, where the interaction between the radiation heat transfer and the radiative power source is modelled:

$$S_{rad} = a(G - 4\sigma T^4) \tag{11}$$

The boundary conditions in this work are assumed as the diffusive walls and are calculated only for the ordinates that have an orientation in the computational mesh. Diffusive opaque walls are defined as [10]:

$$I_{bnd\,j} = \epsilon \frac{n_r}{\pi}(\sigma T^4) + (1-\epsilon)\frac{\sum\limits_{(s_j \cdot n_i)>0} I_j |n_i D_{ci}|}{\sum\limits_{(s_j \cdot n_i)<0} n_i D_{ci}} \tag{12}$$

where ϵ is the wall emissivity and D_{ci} – the auxiliary variable for solving orientations of spatial angles in regard to cell face orientation. For the calculation intensities of incident radiation in

eq. (9), the upwind differencing scheme (UDS) is applied. Convergence criterium is defined as the ratio of the difference between the new and old value of incident radiation divided by the old incident radiation value, and in the following simulations equals 0.001.

Absorption coefficient modelling

Absorption coefficient in this work is modelled by implemented weighted sum of gray gases model (WSGGM) for grey gases, which is based on the CO_2 and H_2O correlations in the literature [30]. The total absorption coefficient a is defined:

$$a = -\frac{\ln(1-\varepsilon)}{s} \tag{13}$$

Emissivity ε in eq. (13) is defined in eq. (14):

$$\varepsilon = \sum_{i=0}^{2} \alpha_i \left[1 - \exp\left(-a_i ps\right) \right] \tag{14}$$

where α_i is weight factor of the grey gas i, a_i is its radiative absorption coefficient, p – the partial pressures of the of ith grey gas. The weighting factors of grey gas i are defined by the polynomial term for which the polynomial coefficients $b_{i,j}$ are tabulated:

$$\alpha_i = \sum_{j=0}^{3} b_{i,j} T^j \tag{15}$$

For i equals zero, the transparent gas is assumed. The weight factor of transparent gas is defined as:

$$\alpha_0 = 1 - \sum_{i=0}^{2} \alpha_i \tag{16}$$

Numerical setup

In fig. 1, the computational mesh with around 177000 control volumes is generated, for which the mesh dependency test was performed on two finer meshes with the input cell size 66% and 50% of the initial cell size. Simulation performed on all three meshes showed flow, temperature and turbulence quantities with the relative deviation lower than 0.5%. For the mass conservation equation, the central differencing scheme (CDS) was employed. In contrast, for the turbulence, energy and volume fraction transport equations, the first order UDS was applied. For the momentum equation, a combination of CDS and UDS was proposed by introducing a blending factor of 0.5. The convergence of the solution was achieved when the normalised pressure residual reached values lower than 5×10^{-4} also, momentum and energy residuals lower than 10^{-4}. For turbulence, energy and volume fraction transport equations the first-order UDS was used, while for the continuity equation, the CDS was employed. For the momentum equation, the MINMOD Relaxed scheme was employed [20]. The convergence criteria were satisfied when normalised energy, momentum and pressure residuals reached a value lower than 10^{-4}. For the DOM the RTE was solved each twentieth fluid-flow iterations. For the numerical simulations in this work crude oil fuel was modelled as a chemical compound with the average chemical formula $C_{13}H_{23}$, where the lower heating value is set to 41.1 MJkg^{-1}, and physical properties as density and viscosity are adopted from the AVL FIRE™ fuel database.
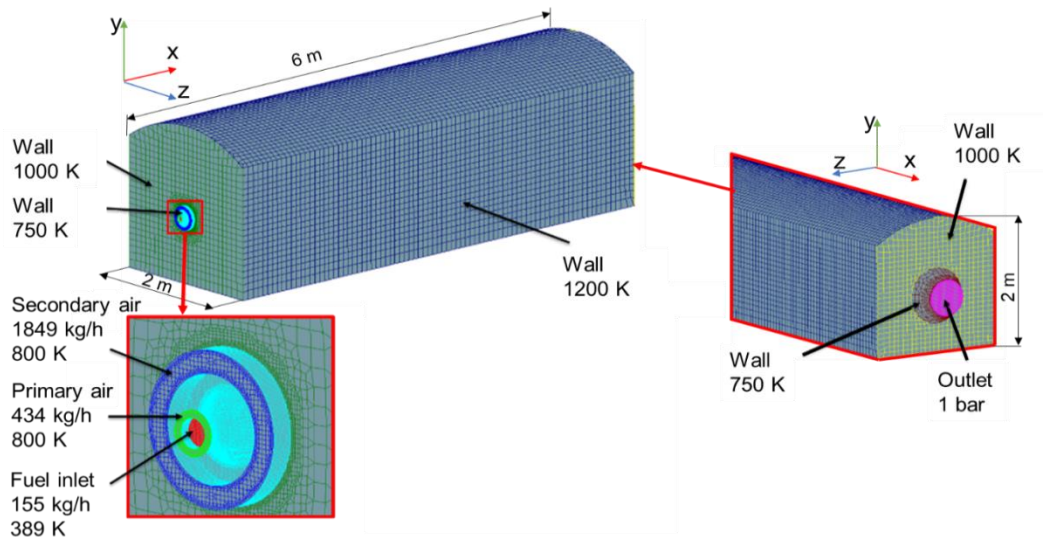
Figure 1. Computational domain with the boundary conditions

The boundary selections are shown in fig. 1, with the wall, inlet and outlet boundary conditions. The wall selections were defined as Dirichlet boundary condition of fixed temperature, and the air and fuel entrainment were prescribed with a constant temperature mass-flow. In the following case, all wall boundaries are set with an emissivity value 1. At the outlet selection, the static pressure was prescribed. Characteristic for the IJmuiden furnace is the secondary air with four times larger mass-flow. Spray parameters are considered inside the combustion model, which resulted in deficient computational time. That is precisely why this model is chosen for the combustion modelling in the furnace, to have an emphasis on the radiative heat transfer. For the DTRM raytracing, local hemisphere discretization was achieved with discretising boundary hemisphere with two polar angles and eight azimuthal angles. Thermal boundary under-relaxation factor was set to 0.5, and the tolerance was set to 0.01.

Results

In this section, critical specific objectives, the significant findings, and the most significant conclusions of the paper are presented. The presented temperature results for the verification furnace case are calculated for the steady-state, where the convergence of results is achieved after approximately 3000 fluid-flow iterations.

Figure 2 shows the results at the line connecting the centre of the inlet and centre of the outlet. The black dots represent experimental temperature measurements that are used for validation of radiation models. The blue curve shows results without radiation, that indicate overprediction of temperature results, and pronounced radiative gas emission losses in the furnace. The orange curve shows results obtained with the DTRM, while the green curve represents the results obtained with the DOM. The main difference between DTRM and DOM results is visible at the outlet of the domain, and it can be attributed to the outlet geometry that makes uncertainty raytracing. Furthermore, the better trend with calculation without radiation is achieved with the DTRM, which can be assign to lack of rays that hit the cells in the near outlet region.

Figure 3 shows measured distributions of unidirectional radiation intensity through a steady-state oil flame, where the results with radiation are showed against experimental re-

Jurić, F., *et al.*: Assessment of Radiative Heat Transfer Impact …
THERMAL SCIENCE: Year 2020, Vol. 24, No. 6A, pp. 1-10

8
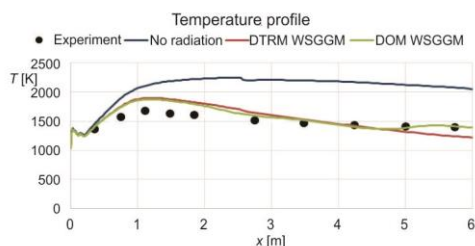
Figure 2. Temperature profile comparison between experimental data, combustion model without radiation and with DTRM and with DOM *(for color image see journal web site)*
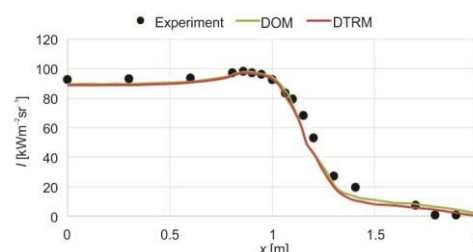
Figure 3. Comparison between calculated and measured distributions of unidirectional radiation intensity through a steady-state oil flame *(for color image see journal web site)*

sults. Both models show good agreement with experimental results and with their trend. The DOM results have slightly overprediction compare to the DTRM results during the whole region, which is especially pronounced between 1.5 m and 2 m of flame. The difference in these results is the outcome from the model equations, that differently calculate the gas emission in the flame cells.

In fig. 4, at the top, the temperature field results are shown for the case where the radiative heat transfer was not considered. The colder fuel region is visible near the inlet due to the lower air and fuel temperature. Inside the combustion chamber after the spray region, the practically uniform temperature field is achieved with the temperature of around 2200 K.

The DTRM and DOM results show a good agreement in a temperature distribution inside the combustion chamber. Difference between results with included radiative heat transfer and without radiation is in the near-wall temperatures and around the inlet, due to no presence of gas emissions in heat transfer. That can be attributed to the low temperature region of the injected fuel and the high emissivity of the media near the walls. The lower mean temperature obtained in the simulations with included DTRM has a slightly broader and shorter flame region, which is especially visible in the area near the outlet, which is also evident in fig. 2 diagram. The computational time of the showed results is four times more expensive for DTRM case compared to the case without calculation of the radiative heat transfer in participating media. The DTRM pre-processing of raytracing contributes most to that difference, which needs to be calculated only once before the start of the first calculation. Additional computational demand of DTRM is also obtained due to low CPU parallelisation potential, where the communication between CPU is aggravated by waiting for raytracing information, unlike the DOM where the parallelisation is faster.
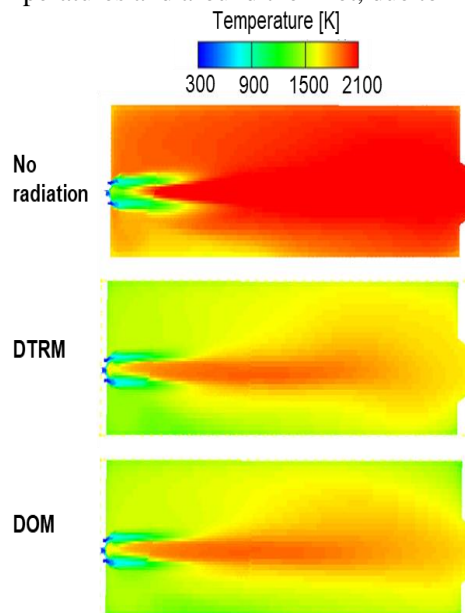
Figure 4. Temperature field results at the symmetry plane of the computational domain

Conclusion

The radiative heat transfer analysis in CFD of the steady combustion process provides a valuable tool that can be used to investigate more accurate and better understand the combustion process. The feasibility of DTRM and DOM radiative heat transfer models in the AVL FIRE™ code is examined, where the focus is on their comparison and application in combination with the combustion process inside a furnace combustion chamber. Simulations performed with SCM are presented for three cases: without radiative heat transfer, with radiation calculated by DTRM, and with radiation calculated by implemented DOM. The comparison of the CPU execution time showed that the calculation with DTRM is 3.8 times, and with DOM 2.3 times more time consuming than the case without calculation of the radiative heat transfer in participating media. The validation results showed good agreement with the experimental data with a better prediction of DOM model in the temperature trend near furnace outlet, which can be attributed to the shortcomings of DTRM raytracing in the near outlet region. The comparison of temperature distribution shows that the temperature field predicted with the DOM approach has a good agreement with the DTRM results, where a similar trend to the simulation without radiation is achieved. Furthermore, the main difference between DTRM and DOM results is visible at the outlet of the furnace, where the outlet geometry impacts the DTRM raytracing uncertainty. While for the DOM calculation, the incident radiation is calculated in every cell, which results in a better agreement with the experimental temperature profile along with the furnace. The calculations with the DTRM and DOM model are compared with the simulation without calculating radiative heat transfer, where approximately 25% higher temperatures are reached. Finally, it can be stated that the presented method with DTRM and DOM models can serve as a solution for a swift investigation of the radiative heat transfer in participating media of real industrial furnaces.

Acknowledgment

References

[1] Ren, T., *et al*., Machine Learning Applied to Retrieval of Temperature and Concentration Distributions From Infrared Emission Measurements, *Appl. Energy*, *252* (2019), Oct., pp. 1-15
[2] Modest, M. F., Haworth, D. C., Radiative Heat Transfer in High-Pressure Combustion Systems, in: *Springer Briefs in Applied Sciences and Technology*, Springer, New York, USA, 2016, pp. 137-148
[3] Vujanović, M., *et al*., Sustainable Energy Technologies and Environmental Impacts of Energy Systems, *Appl. Energy*, *256* (2019), Dec., pp. 1-11
[4] Maginot, P. G., *et al*., High-Order Solution Methods for Grey Discrete Ordinates Thermal Radiative Transfer, *J. Comput. Phys.*, *327* (2016), C, pp. 719-746
[5] Mishra, S. C., *et al*., Development and Comparison of the DTM, the DOM and the FVM Formulations for the Short-Pulse Laser Ttransport Through a Participating Medium, *Int. J. Heat Mass Transf.*, *49* (2006), 11-12, pp. 1820-1832
[6] Coelho, P. J., Advances in the Discrete Ordinates and Finite Volume Methods for the Solution of Radiative Heat Transfer Problems in Participating Media, *J Quant Spectrosc Radiat Transf*, *145* (2014), pp. 121-146
[7] Honus, S., Juchelková, D., Mathematical Models of Combustion, Convection and Heat Transfer in Experimental Thermic Device and Verification, *Teh. Vjesn.*, *21* (2014), 1, pp. 115-122

Jurić, F., *et al.*: Assessment of Radiative Heat Transfer Impact …
THERMAL SCIENCE: Year 2020, Vol. 24, No. 6A, pp. 1-10

10

[8] Coelho, P. J., Carvalho, M. G., A Conservative Formulation of the Discrete Transfer Method, *J. Heat Transfer*, *119* (1997), 1, pp. 118-128

[9] Chai, J. C., *et al.*, Finite Volume Method for Radiation Heat Transfer, *J. Thermophys Heat Trans.*, *8* (1994), 3, pp. 419-425

[10] Coelho, P. J., Advances in the Discrete Ordinates and Finite Volume Methods for the Solution of Radiative Heat Transfer Problems in Participating Media, *J Quant Spectrosc Radiat Transf*, *145* (2014), Sept., pp. 121-146

[11] Mishra, S. C., Roy, H. K., Solving Transient Conduction and Radiation Heat Transfer Problems Using the Lattice Boltzmann Method and the Finite Volume Method, *Jou. Comput. Phys.*, *223* (2007), 1, pp. 89-107

[12] Coelho, P. J., Radiative Transfer in Combustion Systems, in: *Handbook of Thermal Science and Engineering*, Springer, New York, USA, 2017, pp. 1173-1199

[13] Modest, M. F., *Radiative Heat Transfer Elsevier* (3rd ed.). Elsevier, Amsterdam, The Netherlands, 2013

[14] Tulwin, T., A Coupled Numerical Heat Transfer in the Transient Multicycle CFD Aircraft Engine Model, *Procedia Eng.*, *157* (2016), Dec., pp. 255-263

[15] Silva, J., *et al.*, CFD Modeling of Combustion in Biomass Furnace, *Energy Procedia*, *120* (2017), Aug., pp. 665-672

[16] Wang, J., *et al.*, Analysis of Slab Heating Characteristics in a Reheating Furnace, *Energy Convers. Manag.*, *149* (2017), Oct., pp. 928-936

[17] Mikulčić, H., *et al.*, Sustainability Through Combined Development of Energy, Water and Environment Systems, *J. Clean. Prod.*, *251* (2020), Apr., pp. 1-35

[18] Johnson, T. R., Beer, J. M., Radiative Heat Transfer in Furnaces: Further Development of the Zone Method of Analysis, *Proceedings of Symposium (International) on Combustion*, *14* (1973), 1, pp. 639-649

[19] Vujanović, M., *et al.*, User Function Approach in Modelling of Nitrogen Oxides in Commercial CFD Code FIRE, *Proceedings*, ECCOMAS Thematic Conference on Computational Combustion, Lisbon, Portugal, 2004, pp.1-8

[20] ***, AVL AST GmbH, FIRE Documentation v2019, Graz, Austria, 2019

[21] Jurić, F., *et al.*, Experimental and Numerical Investigation of Injection Timing and Rail Pressure Impact on Combustion Characteristics of a Diesel Engine, *Energy Convers. Manag.*, *185* (2019), Apr., pp. 730-739

[22] Jozsa, V., Kun-Balog, A., Stability and Emission Analysis of Crude Rapeseed Oil Combustion, *Fuel Process. Technol.*, *156* (2017), Nov., pp. 204-210

[23] Baburić, M., *et al.*, Application of the Conservative Discrete Transfer Radiation Method to a Furnace with Complex Geometry, *Numerical Heat Transfer, Part A: Applications*, *48* (2005), 4, pp. 297-313

[24] Qi, F., *et al.*, Numerical Study on Characteristics of Combustion and Pollutant Formation in a Reheating Furnace, *Thermal Science*, *22* (2018), 5, pp. 2103-2112

[25] Filkoski, R., *et al.*, Optimization of Pulverised Coal Combustion by Means of CFD/CTA Modeling, *Thermal Science*, *10* (2006), 3, pp. 161-179

[26] Honus, S., *et al.*, Verifying the Prediction Result Reliability Using k-ε, Eddy Dissipation, and Discrete Transfer Models Applied on Methane Combustion Using a Prototype Low-Pressure Burner, *Adv. Sci. Technol. Res. J.*, *11* (2017), 4, pp. 252-259

[27] Csemany, D., Jozsa, V., Fuel Evaporation in an Atmospheric Premixed Burner: Sensitivity Analysis and Spray Vaporization, *Processes*, *5* (2017), 80, pp. 1-16

[28] Abraham, J., Magi, V., Application of the Discrete Ordinates Method to Compute Radiant Heat Loss in a Diesel Engine, *Numerical Heat Transfer, Part A: Applications*, *31* (1997), 6, pp. 597-610

[29] Hosseini Sarvari, S. M., Solution of Multi-Dimensional Radiative Heat Transfer in Graded Index Media Using the Discrete Transfer Method, *Int. J. Heat Mass Transf.*, *112* (2017), Sept., pp. 1098-1112

[30] Dorigon, L. J., *et al.*, WSGG Correlations Based on HITEMP2010 for Computation of Thermal Radiation in Non-Isothermal, Non-Homogeneous H_2O/CO_2 Mixtures, *Int. J. Heat Mass Transf.*, *64* (2013), Sept., pp. 863-873

PAPER 4

Numerical Investigation of Multiphase Reactive Processes Using Flamelet Generated Manifold Approach and Extended Coherent Flame Combustion Model

Filip Jurić[1], Marija Stipić[2], Niko Samec[3], Matjaž Hriberšek[3], Stanislav Honus[4], Milan Vujanović[1,*]

[1] Faculty of Mechanical Engineering and Naval Architecture, University of Zagreb, Ivana Lučića 5, 10000 Zagreb, Croatia

[2] AVL List GmbH, Waagner-Biro-Straße 98a, 8020 Graz, Austria

[3] Faculty of Mechanical Engineering, University of Maribor, Smetanova ulica 17, 2000 Maribor, Slovenia

[4] Faculty of Mechanical Engineering, VŠB-Technical University of Ostrava, 17. listopadu 2172/15, 708 00 Ostrava-Poruba, Czech Republic

Corresponding author e−mail: milan.vujanovic@fsb.hr

ABSTRACT

For the calculation of multiphase reactive processes in computational fluid dynamics (CFD), detailed chemical kinetics and simplified combustion models are commonly applied. An appropriate modelling approach to overcome the high computational demand of chemical kinetics is the Flamelet generated manifold (FGM), which prescribe the calculation of chemical kinetics in preprocessor for the generation of the look-up databases that are used during CFD simulations with interpolation procedure. For the calculation of the chemistry kinetics in processor, combustion models are commonly applied, such as Three-zones extended coherent flame model (ECFM-3Z) that features calculation of flame speed in turbulent conditions. The primary goal of the research is to investigate and validate FGM and ECFM-3Z models on the multiphase reactive process inside a compression ignition engine for single and multiple injection strategies. Additionally, an overview of the modelling methodology and capability of FGM and ECFM-3Z models is presented, where the impact of their features is analysed on the results inside a compression ignition engine. For the numerical simulations, CFD code AVL FIRE™ was used, where the calculated results such as in-cylinder pressure, temperature, rate

---

of heat release, and nitric oxide emissions are computed. The FGM modelling approach showed higher ignition delay compared to the ECFM-3Z model for single-injection strategy, which can be attributed to the pretabulated autoignition conditions in three zones of the ECFM-3Z model. For the multi-injection strategy, such an ignition delay difference between FGM and ECFM-3Z is not observed since the small amount of injected fuel in pilot injections tends to have quicker ignition, which then creates better conditions for combustion of the more significant amount of injected fuel in the main injection. The experimental nitric oxide emission trend is achieved with both combustion modelling approaches, where the CFD calculation time for cases with FGM is reduced approximately by half. In comparison against the experimental values, both FGM and ECFM-3Z combustion modelling approaches showed the capability of predicting the influence of fuel injection strategy on the combustion process in passenger car compression ignition engines.

KEYWORDS

Combustion modelling, Flamelet generated manifold, Tabulation, Coherent flame combustion model, Engine, Emissions

NOMENCLATURE

Latin	**Description**	**Unit**
c	progress variable	
c_{var}	Progress variable variance	
C_1	WAVE breakup model constant 1	
C_2	WAVE breakup model constant 2	
d	Droplet diameter	m
D	Effective diffusion coefficient	$m^2 \, s^{-1}$
f	Mixture fraction	
g	Residual gas mass fraction	
h	Enthalpy	$kJ \, kg^{-1}$
H	Total enthalpy interfacial exchange term	$kJ \, kg^{-1}$
k	Turbulent kinetic energy	$m^2 \, s^{-2}$
m	Mass	kg
$\dot{m}$	Mass flow	$kg \, s^{-1}$

M	Molecular weight	kg kmol^{-1}
p	Pressure	Pa
r	Droplet radius	m
R	Ideal gas constant	J (mol K)$^{-1}$
S	Source of extensive property	
Sc	Schmidt number	
S_c	Segregation of progress variable	
S_Z	Segregation of mixture fraction	
t	Time	s
T	Temperature	K
u,v	Velocity	m s^{-1}
V	Volume	m^3
W_k	Molecular weight of species k	kg kmol^{-1}
x	Cartesian coordinates	m
y_i	Mass fraction of species i	
Z	Mixture fraction	
Z_{var}	Mixture fraction variance	

Greek	**Description**	**Unit**
β	ECFM-3Z+ model constant/	
ε	Dissipation rate	m^2 s^{-3}
ζ	Velocity scale ratio	
Γ	Diffusion coefficient	
λ_w	Wavelength	m
μ	Dynamic viscosity	Pa s
μ^t	Turbulent viscosity	Pa s
ρ	Density	kg m^{-3}
Σ	Turbulent flame surface density	1 m^{-1}
τ_a	Breakup time	s
τ_m	Mixing time	s
φ	Extensive property of general conservation equation	
χ	Scalar dissipation rate	1 s^{-3}
ω_i	Chemical source of species i	kg m^{-3} s^{-1}

| ω_{heat} | Chemical heat source | W |
| Ω | Wave growth rate | s |

1. Introduction

Currently, compression ignition engines represent the majority of truck engines, heavy-duty and marine engines, which are producers of a significant amount of harmful pollutants [1]. The more stringent regulations that enforce the reduction of pollutant emissions led to an extensive study of the combustion characteristics in internal combustion engines [2]. However, the numerical modelling of combustion systems is also challenging since the interaction of the fluid flow, turbulence, heat transfer, and chemical reactions need to be solved simultaneously [3]. That is applicable not only for the internal combustion engines but also for the combustion system such as jet engines [4].

Potential for the reduction of emission is observed in the controlling of fuel injection influence on combustion characteristics with the application of the injection system and rail pressure [5]. In [6], the author experimentally and numerically studied the multiple-injection strategy on the emission formation and combustion processes at underload conditions, where the rate of heat release (RoHR) results show a good agreement with the multiple injection strategies. The pre-injection timing in such multiple injection strategies can dominantly influence the combustion and emission characteristics, from which the NO_x are influenced the most, owing to the different temperature changes over time [7]. Another parameter that has the potential for lowering the emission is the piston bowl design, which can be easily assessed with the employment of the CFD simulations [8,9].

For the mathematical description of the combustion process several different modelling approaches can be employed, such as computational demanding detailed chemical mechanisms [10], reduced mechanisms, which are limited to a specific purpose, and combustion models [11]. In order to accurately describe a combustion process, specific mechanisms for each fuel are necessary [12]. With the development of numerous new alternative fuels, new mechanisms are required in order to describe their combustion process numerically [13]. Such modern fuels are commonly biodiesel fuels made from vegetable oils [14], animal oil [15] or waste [16]. The number of chemical species and elementary reactions included in the detailed chemical mechanisms is generally quite large [17]. As an illustration, a detailed reaction mechanism of diesel fuel can consist of 2900 chemical species and 15000 elementary reactions [18]. Such large mechanisms require significant computational resources for the simulation of industrial

combustion systems to calculate all interactions between elementary reactions that govern the combustion process [19]. This computational demand arises from the number of transport equations that need to be solved for each chemical species and the number of mesh elements [20].

One way to reduce the required number of equations that have to be solved is assuming that the chemical time and length scale in most flames are a small-scale [21]. Chemical reduction techniques and laminar flamelet models represent two main approaches that are based on the idea to model the detailed dynamics and structure of chemically reacting flow [22]. Laminar flamelet methods assume that the flame structures are considerably thinner compared to other scales of the distortions in the flow [23]. Furthermore, this implies that the chemical reactions are faster than all other time scales [24]. All flamelet models rely on the assumption that the chemical reaction occurs within relatively thin layers that separate the fresh unburned gas from the fully bunt gas. The internal structure of the flame is approximately frozen while it moves around in the flow. The dynamics of the thin flame front is predicted by computing a kinematic equation for the propagation of the flame front, a mixture fraction equation for the mixing, and a CFD solver for the fluid flow [25]. One of the several laminar flamelet models, which has proven an ability to accurately describe the combustion process in internal combustion engines, is the extended coherent flame model (ECFM) developed by Colin et al. [26]. The ECFM belongs to the flame surface density type of approaches, which was first proposed in the context of diffusion flames in the work of Marble and Broadwell [27]. More recently, this approach has been extended by considering a generalised flame surface density, including all possible values of the mixture fraction. In contrast, reaction rates per unit of flame surface are provided by a library of transient diffusion flames [28]. Based on the ECFM model, the unified diesel/petrol three-zones extended coherent flame model (ECFM-3Z) was briefly presented in [29]. In the ECFM-3Z, the description of unburned/burned gas is inherited from ECFM. The model is based on the flame surface density equation, and it can be employed to describe premixed and diffusion flames. In order to account for diffusion flame and mixing processes, each computational cell is split into three mixing zones: unmixed fuel zone, unmixed air plus possible residual gases (EGR) zone and completely mixed fuel-air mixture zone. This model is formulated and later validated by various researchers for partially-premixed and highly stratified combustion cases, as in the case of gasoline direct injection [30] and combustion cases with a high amount of exhaust gas recirculation [31]. In the work of [32], the capability of the ECFM-3Z combustion model to predict the combustion process and emission formation in a high-speed direct injection diesel engine is introduced. The ECFM-3Z applies to all types of

combustion processes without the need for predefining the type of combustion that is encountered [33].

Chemical reduction techniques rely on the assumption that the chemical time scales are short scale. A time scale analysis can be conducted if all transport processes are neglected, and the fastest time scales are assumed to be in the steady state. That means all variables can be stored in a database as a function of a few controlling variables. During the CFD solving procedure, only the equations for the controlling variables are solved. The computational singular perturbation method from Lam and Goussis [34] and the intrinsic low-dimensional manifold approach of Maas and Pope [35] are examples of such reduction methods.

Van Oijen and de Goey introduced a reduction method that can be interpreted as combining the flamelet and the manifold approaches, namely the flamelet generated manifold (FGM) technique [36]. An overview of the general FGM technique can be found in [37]. Successful application of the FGM combustion model, used in this work, for diesel engine was reported in[38]. A correct prediction of the combustion process in a diesel engine case using FGM as well as the emission processes based on a large number of chemical reactions is presented in the work of Priesching et al.[39]. In the work of Goryntsev et al. [40], successful application of the FGM combustion model in gasoline engine simulations and knock analysis was reported. The utilisation of the FGM approach for simulating an ignition timing of diesel spray was shown in the work of Bakdemir et al. [41]. The most critical characteristics like ignition delay and flame lift-off were well captured, demonstrating the potential of the FGM technique. Keum et al.[42] applied the FGM combustion model with the most detailed chemical reaction mechanism as well as different surrogates to a canonical homogeneous charge compression ignition engine experiment from Sandia National Laboratory. Additionally, an application of various numerical approaches to access the knocking phenomena has been reported in publication [43].

In the present study, the numerical investigation of the single and multi-injection strategy in a direct injection compression ignition engine by utilising the FGM and ECFM-3Z combustion modelling approaches were performed. To the best of our knowledge, a study that compares these two combustion modelling approaches in multiphase reactive systems has not been reported. Apart from the comparison of modelling approaches, the validation of the results on pressure, temperature, rate of heat release, and emission results for both single and multi-injection strategy were analysed in a compression ignition engine.

2. Mathematical model

For modelling turbulent flow Reynolds averaged Navier-Stokes equations approach with the $k - \zeta - f$ turbulence model is employed [44].

2.1. Spray modelling

The fuel injection is a necessary process used to disperse the liquid fuel in a broader area and to increase the surface needed for the more intensive evaporation process. In IC engines, the spray is produced by introducing liquid fuel into the combustion chamber through a nozzle under high injection pressure. Detailed understanding of the spray formation in diesel engines and its interaction with the surrounding air in the cylinder is necessary in order to achieve more efficient, complete combustion and lower pollutant emissions. In this work, Euler-Lagrangian method was employed, which is based on a statistical approach where each droplet is a component of a group of similar in size non-interacting droplets called parcels. The motion and the transport properties of the parcels are tracked in Lagrangian form through the computational mesh used for solving the gas phase Eulerian partial differential equations.

The standard Wave break-up model is employed to model injected liquid fuel jet break-up regime [45]. The basis of the Wave break-up model is the Kelvin-Helmholtz instability model. According to this model, new droplets are formed from the unstable surface waves caused by surface tension. Waves grow on the droplet surface with rate Ω and a wavelength λ_w. The size of the newly formed droplets is determined from the wavelength and growth rate of this instability. The break-up of the initial droplets results in the production of new droplets and the reduction of the size of the parent droplets[46]. For the radius reduction of the parent drops a rate approach is applied:

$$\frac{dr}{dt} = \frac{(r - r_0)}{\tau_a} \tag{1}$$

where r_0 is the droplet radius of the product droplet and τ_a is the break-up time of the model, which can be expressed as:

$$\tau_a = \frac{(3.726 \cdot C_2 \cdot r)}{\lambda_w \cdot \Omega} \tag{2}$$

and r_0 is proportional to the wavelength λ_w of the fastest-growing surface wave:

$$r_0 = \lambda_w \cdot C_1 \tag{3}$$

where C_1 is the Wave model constant determining the stable droplet size is set to the recommended default value of 0.61 [45]. The second Wave model constant C_2 is usually varied in order to adjust

break-up time and penetration length to the different nozzles. The higher the value, the slower the break-up time and the penetration length. Besides the liquid ligaments and droplets break-up, simultaneously in the spray region, the evaporation process has to be calculated. The mathematical model used in this thesis to perform the calculation of the evaporation process is Abramzon and Sirignano approach [47].

2.2. Combustion modelling

The combustion modelling is a complicated phenomenon that accounts for hundreds of different compounds of chemical scalars and reactions in the calculation domain. The process can be described through combustion models with different level of complexity or by employing detailed chemical mechanisms. The following section introduces a short description of two combustion modelling approaches.

2.2.1. Three-zones extended coherent flame model

The coherent flame models are based on the flamelet hypothesis, which states that the chemical reactions take place much faster than the turbulent mixing process. The reactions occur within relatively thin layers that separate the fresh gas from the wholly burnt gas. In addition, the turbulent flame is interpreted as an ensemble of small laminar flames denoted by the name flamelets. Using these assumptions, the reaction rate is computed as the product of the flame surface density and reacting rate per unit flame surface:

$$\overline{\rho \dot{r}_{fu}} = -\omega_L \Sigma \tag{4}$$

where ω_L represents the mean laminar fuel consumption rate per unit surface along the flame front and Σ the flame surface density. The three-zones extended coherent flame model can be considered as the further improvement of the coherent flame model, and it was developed especially for Diesel combustion. The model relies on a three-zones mixing description. Each cell of computational mesh is split into three mixing zones to account for diffusion and mixing processes: unmixed air plus possible residual gases, unmixed fuel and completely mixed fuel-air mixture.

When utilising the ECFM-3Z model, besides the standard species transport equations, additional transport equations for the following eleven chemical species are solved in each cell $O_2, N_2, CO_2, CO, H_2, H_2O, O, H, N, OH$ and NO [48]:

$$\frac{\partial \overline{\rho} y_x}{\partial t} + \frac{\partial \overline{\rho} u_i y_x}{\partial x_i} - \frac{\partial}{\partial x_i}\left(\left(\frac{\mu}{Sc} + \frac{\mu_t}{Sc_t}\right)\frac{\partial y_x}{\partial x_i}\right) = \overline{\dot{\omega}_x}, \tag{5}$$

where y_x and $\overline{\dot{\omega}_x}$ denote the averaged species mass fraction and the chemical source term for species i, respectively. Here, averaged means these quantities are the global quantities for the three mixing zones. In addition, transport equations for the fuel mass fraction y_{fu}, mixture fraction f and residual gas mass g have to be solved [48]:

$$\frac{\partial}{\partial t}(\rho y_{fu}) + \frac{\partial}{\partial x_i}(\rho u_i y_{fu}) = \frac{\partial}{\partial x_i}\left(\Gamma_{fu}\frac{\partial y_{fu}}{\partial x_i}\right) + S_{fu} \tag{6}$$

$$\frac{\partial}{\partial t}(\rho f) + \frac{\partial}{\partial x_i}(\rho u_i f) = \frac{\partial}{\partial x_i}\left(\Gamma_f \frac{\partial f}{\partial x_i}\right) \tag{7}$$

$$\frac{\partial}{\partial t}(\rho g) + \frac{\partial}{\partial x_i}(\rho u_i g) = \frac{\partial}{\partial x_i}\left(\Gamma_g \frac{\partial g}{\partial x_i}\right) \tag{8}$$

The fuel mass fraction is divided into fuel mass fraction present in the fresh gases $y_{u.f.}$ and fuel mass fraction present in burnt gases $y_{u.b.}$ This introduces an additional transport equation to calculate the $y_{u.f.}$:

$$\frac{\partial \overline{\rho} y_{u.f.}}{\partial t} + \frac{\partial \overline{\rho} u_i y_{u.f.}}{\partial x_i} = \frac{\partial}{\partial x_i}\left(\left(\frac{\mu}{Sc} + \frac{\mu_t}{Sc_t}\right)\frac{\partial y_{u.f.}}{\partial x_i}\right) \tag{9}$$

and the fuel mass fraction in burnt gases is calculated as the difference between the fuel mass fraction y_{fu} and fuel mass fraction in the fresh gases $y_{u.f.}$. Two new quantities are introduced to describe the mixing zones: the unmixed fuel y_{Fu}^F and the unmixed oxygen $y_{O_2}^A$. The equations for these unmixed species are [45]:

$$\frac{\partial \overline{\rho} y_{Fu}^F}{\partial t} + \frac{\partial \overline{\rho} u_i y_{Fu}^F}{\partial x_i} - \frac{\partial}{\partial x_i}\left(\frac{\mu}{Sc}\frac{\partial y_{Fu}^F}{\partial x_i}\right) = \overline{\rho}\dot{S}_f - \frac{1}{\tau_m}y_{Fu}^F\left(1 - y_{Fu}^F\frac{\overline{\rho M_{mix}}}{\overline{\rho_u M_f}}\right) \tag{10}$$

$$\frac{\partial \overline{\rho} y_{O_2}^A}{\partial t} + \frac{\partial \overline{\rho} u_i y_{O_2}^A}{\partial x_i} - \frac{\partial}{\partial x_i}\left(\frac{\mu}{Sc}\frac{\partial y_{O_2}^A}{\partial x_i}\right) = -\frac{1}{\tau_m}y_{O_2}^A\left(1 - \frac{y_{O_2}^A}{y_{O_2}^\infty}\frac{\overline{\rho M_{mix}}}{\overline{\rho_u M_{air+EGR}}}\right) \tag{11}$$

the source terms are depended on the mixing time, which considers turbulence quantities and is expressed as:

$$\frac{1}{\tau_m} = \beta\frac{\varepsilon}{k} \tag{12}$$

where the β denotes a model factor.

2.2.2. Flamelet generated manifold

When the mechanism of detailed chemistry that feature a large number of chemical reactions and species are observed, the use of the flamelet generated manifold method results in a reduction

of computational cost with a few orders of magnitude. This reduction method can be interpreted as a combination of classic flamelet and manifold methods [49]. The method is based on the idea that a multi-dimensional flame can be observed as an ensemble of thin, laminar, locally one-dimensional flames embedded in a flow field and denoted by the name flamelet. This assumption remains valid even for the turbulent flames. The flamelet method assumes that most variables, like species concentrations and temperature, are dependent on a small number of control variables relevant for one-dimensional flame structures. The FGM method generates a multi-dimensional chemical manifold out of flamelets computed for specific initial conditions using detailed chemistry. The thermochemical variables of flamelets are tabulated as a function of only two independent control variables: mixture fraction and progress variable. The generated table is then linked to a CFD code, and during the numerical simulation transport equations are solved only for the control variables and their variances. At the same time, the required thermochemical data is interpolated from the FGM table. The probability density function closure method is adopted to model the influence of the turbulence effects on combustion chemistry. In the present study, combustion chemistry is pre-computed, and the FGM database is generated based on the 0D perfectly stirred reactors (PSR). Figure 1 visualises the output of 0D PSR simulations for two table boundary temperatures: 700 K and 1800 K, where CO and CH_2O mass faction data is mapped on a predefined progress variable and mixture fraction grid. It is visible that the CO mass fraction increases as the combustion process propagates from the fresh to burnt gas. Furthermore, the peak values are achieved at a mixture fraction value which approximately corresponds to the value of the stoichiometric mixture. The increase in temperature also leads to an increase in CO but a decrease in CH_2O mass fraction.
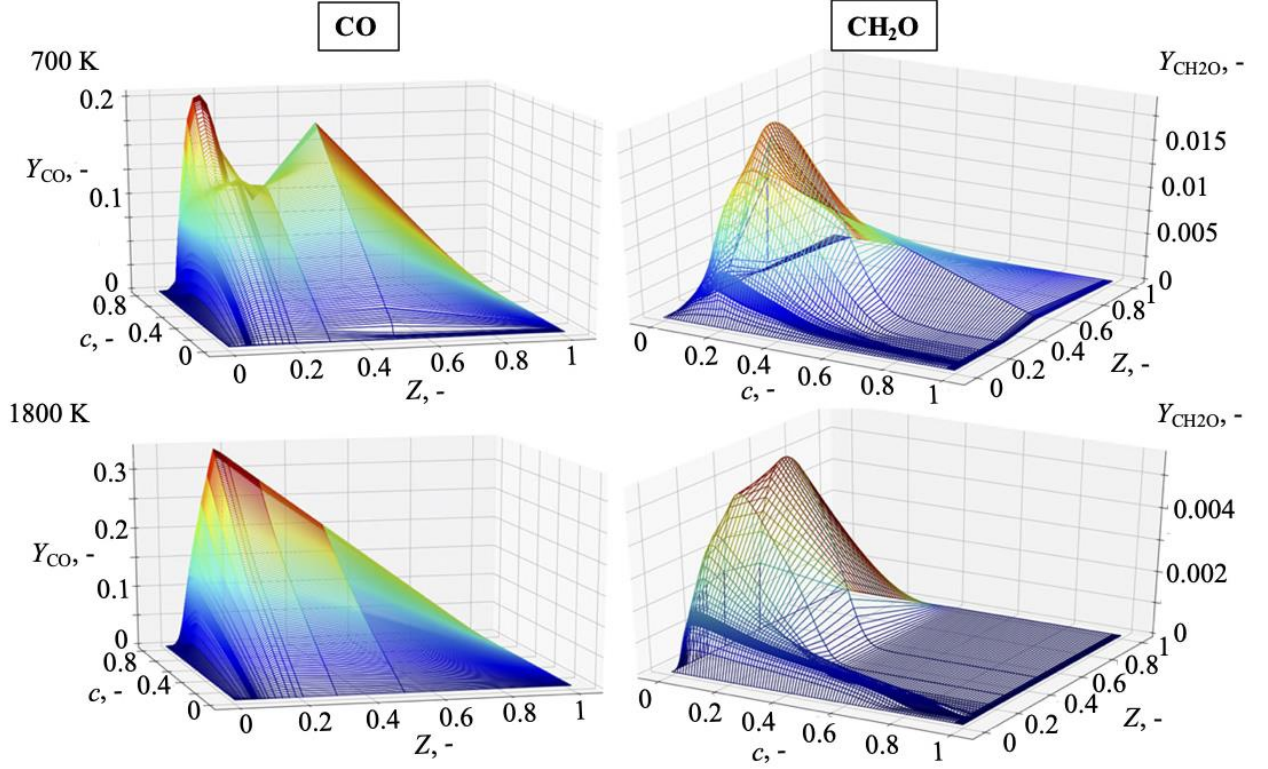
Figure 1. FGM table visualisation at temperatures 700 K and 1800 K

In addition to the transport equations of the turbulence model, four scalar transport equations for progress variable c, progress variable variance c_{var} mean mixture fraction Z, and mixture fraction variance Z_{var} need to be solved. Mixture fraction is a conserved scalar used to describe the mixing process between fuel and air. It equals zero in the oxidiser and unity in the fuel. The mixture fraction is not consumed by chemical reactions, and it is equal to the fuel in a non-reacting case. When using liquid fuels, the mixture fraction equation has a spray source term. The mean mixture fraction and its variance equations can be described as follows [45]:

$$\frac{\partial}{\partial t}\left(\bar{\rho}\tilde{Z}\right) + \frac{\partial}{\partial x_i}\left(\bar{\rho}\tilde{u}_i\tilde{Z}\right) = \frac{\partial}{\partial x_i}\left(\bar{\rho}(D + D_T)\frac{\partial \tilde{Z}}{\partial x_i}\right) + \overline{\dot{S}_{vap}}, \tag{13}$$

$$\frac{\partial}{\partial t}\left(\bar{\rho}\widetilde{Z''^2}\right) + \frac{\partial}{\partial x_i}\left(\bar{\rho}\tilde{u}_i\widetilde{Z''^2}\right) = \frac{\partial}{\partial x_i}\left(\bar{\rho}(D + D_T)\frac{\partial \widetilde{Z''^2}}{\partial x_i}\right) + 2\bar{\rho}D_T\left(\frac{\partial \widetilde{Z''}}{\partial x_i}\right)^2 + \bar{\rho}\tilde{\chi}_Z, \tag{14}$$

where the scalar dissipation rate is:

$$\tilde{\chi}_Z = 2\frac{\varepsilon}{k}\widetilde{Z''^2} \tag{15}$$

Progress variable is a scalar describing the reaction progress from fresh to burnt gas. When normalised, it is zero in fresh gas and unity in the burnt gas, and it has a source term from

chemistry. The progress variable is often defined as a linear combination of certain species, for example:

$$Y_C = \frac{Y_{CO}}{W_{CO}} + \frac{Y_{CO2}}{W_{CO2}} \tag{16}$$

where dominant species CO and CO_2 are used, weighted by their respective molecular weights. The progress variable can be normalised as follows:

$$c = \frac{Y_C}{Y_C^{EQ}} \tag{17}$$

The transport equations for the normalised mean progress variable and its variance is written as:

$$\frac{\partial}{\partial t}\left(\bar{\rho}\tilde{c}\right) + \frac{\partial}{\partial x_i}\left(\bar{\rho}\tilde{u}_i\tilde{c}\right) = \frac{\partial}{\partial x_i}\left(\bar{\rho}(D + D_T)\frac{\partial \tilde{c}}{\partial x_i}\right) + \overline{\dot{S}_c} \tag{18}$$

$$\frac{\partial}{\partial t}\left(\bar{\rho}\widetilde{c''^2}\right) + \frac{\partial}{\partial x_i}\left(\bar{\rho}\tilde{u}_i\widetilde{c''^2}\right) = \frac{\partial}{\partial x_i}\left(\bar{\rho}(D + D_T)\frac{\partial \widetilde{c''^2}}{\partial x_i}\right) + 2\bar{\rho}D_T\left(\frac{\partial \tilde{c''}}{\partial x_i}\right)^2 + \bar{\rho}\tilde{\chi}_c \tag{19}$$

where the scalar dissipation rate is:

$$\tilde{\chi}_c = 2\frac{\varepsilon}{k}\widetilde{c''^2} \tag{20}$$

The look-up tables enable reduction of the number of species to five, with the retention of correct thermochemistry. The used chemical species are O_2, CO_2, H_2O, N_2 and virtual fuel. Virtual fuel is an artificial species with the same physical and thermochemical properties as the actual fuel, and it burns in one single step. The virtual fuel [50] allows imposing species mass fractions from the look-up table, thus comprising all combustible matter present in the real burning mixture. The rate of change of the virtual fuel mass fraction is computed using:

$$\dot{Y}_{VF} = \frac{Y_{VF}(c(t+\Delta t),coords) - Y_{VF}(c(t),coords)}{\Delta t} \tag{21}$$

The rate of change of the other species of the virtual system is calculated by the CFD code, based on stoichiometric coefficients. The chemical heat source term is computed from species change rates $\overline{\dot{\omega}_i}$ and their partial enthalpies h_s:

$$\dot{\omega}_{heat} = \rho \sum_i \dot{\omega}_i h_i \tag{22}$$

2.3. Emission formation

Nitric oxide (NO_x) formation is divided into three mechanisms: thermal, prompt and fuel. The fuel NO_x mechanism can be neglected since diesel fuels contain negligible amounts of nitrogen. Due to the high in-cylinder temperatures in internal combustion engines, the thermal formation

mechanism is dominant in the production of NO_x concentrations. According to[51], the NO formation inside the engine cylinder is superior to other oxides of nitrogen, such as NO_2 and N_2O that are negligible for diesel engines. Therefore, in this work, only thermal and prompt mechanisms are considered in the calculation procedure. For the modelling of the emissions, the extended Zeldovich model was used, which considers the effect of oxygen, nitrogen and hydrogen radicals on NO formation. The following equation describes the extended Zeldovich model:

$$N_2 + O \rightarrow NO + N \qquad (23)$$

$$N + O_2 \rightarrow NO + O \qquad (24)$$

$$N + OH \rightarrow NO + H \qquad (25)$$

The chemical reaction of Equation (23) is the dissociation of nitrogen molecules in the air by the oxygen radicals, while Equation (24) describes oxidation of dissociated nitrogen. Finally, Equation (25) is the reaction in which OH radicals generate NO chemical species, which are present mostly in high-temperature regions. It is essential to point out that all three chemical reactions that represent the extended Zeldovich mechanism exhibit strong temperature dependency [52]. The prompt NO formation process in this work was calculated by employing the de Soete model, as in [53]. In engines, the influence of the turbulence on temperature and NO formation is not linear. That is why the temperature fluctuations were considered, as in [54], assuming the Probability Density Function as a beta distribution. The transport equation of NO is described with the following term:

$$\frac{\partial}{\partial t}(\rho y_{NO}) + \frac{\partial}{\partial x_i}(\rho u_i y_{NO}) = \frac{\partial}{\partial x_i}\left(\Gamma_{NO}\frac{\partial y_{NO}}{\partial x_i}\right) + S_{NO} \qquad (26)$$

Where the source term S_{NO} was described by the following Equation (27):

$$S_{NO} = M_{NO}\frac{dc_{NO}}{dt} \qquad (27)$$

For the FGM model, the extended Zeldovich mechanism equation was incorporated in the diesel fuel mechanism from which the look-up databases were generated.

3. Numerical setup

In the present study, the 3D-CFD simulations were performed using the commercial CFD code AVL FIRE™. The mesh generator AVL™ ESE Diesel tool [45] was used to create the computational mesh based on the provided piston bowl geometry data. The experimental data of the direct injection diesel engine configuration are provided by AVL GmbH. The main specifications of the diesel engine are given in Table 1, while the properties of used Diesel EN590B7 fuel are given in Table 2. The generated mesh with corresponding boundary selections is displayed in Figure 2. The generated computational domain is only seventh of the combustion chamber since the diesel injector has seven nozzle holes. A compensation volume is added to the original computational domain to get the correct compression ratio of the mesh and to compensate for all inconsistency in the geometry of the cylinder head. The final mesh consists of hexahedral elements with the number of cells in the mesh 54 663 and 112 854 at TDC and BDC, respectively. A 2-cell thick boundary layer was created in the vicinity of wall selections declared to capture the wall influence on the simulation results. In any numerical simulation, it is important to ensure that the results are not dependent on the mesh resolution. Hence the mesh sensitivity study was performed. For this purpose, two additional moving meshes with the same block structure, but approximately 1.3 and 2 times denser, were pre-investigated. Simulations with the same numerical setup were performed in order to study the capability of these computational meshes. The differentiation of calculated mean in-cylinder pressure and RoHR curves of individual domains from the measured data is shown in Figure 3. As can be seen, the mesh dependency results exhibited similar values for all computational meshes. Thus, the presented mesh is used for all further calculations.

Table 1. Engine specifications

Engine type	4-stroke DI diesel engine
Model	Volvo I5D
Number of cylinders	5, Inline
Displacement (cm^3)	2400
Bore (mm)	81
Stroke (mm)	93.15
Compression ratio	15.6

Table 2. Diesel EN590B7 specifications[55]

Flashpoint, min	55°C
Water, max	200 mg/kg
Total contamination, max	24 mg/kg
Kinematic viscosity	2.0-4.5 mm^2/s
Density	820-845 kg/m^3
Ester content, max % vol	7% FAME
Ash, max	0.01% wt
Sulfur, max (by mass)	10 mg/kg
Cetane number, min	51.0
PAH, max	11% wt
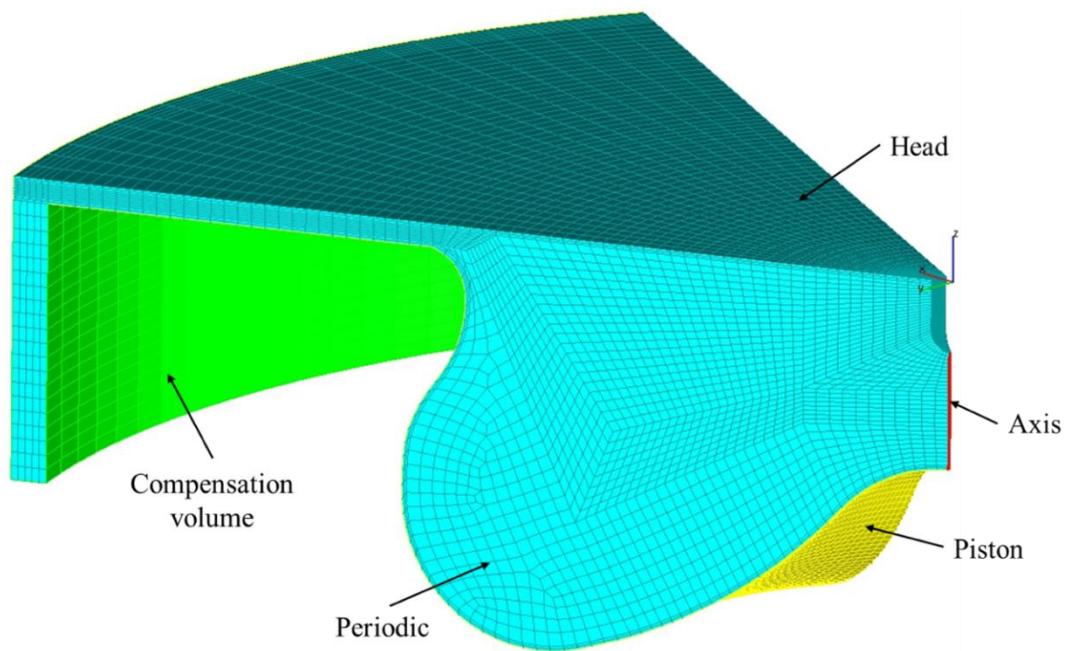
Figure 2. Computational mesh with corresponding boundary selections
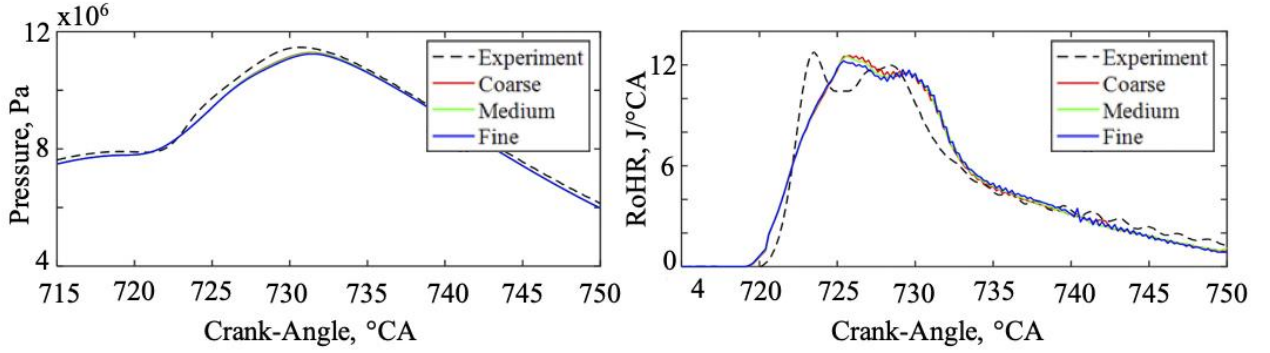
Figure 3. Mesh dependency of pressure and RoHR

Table 3 provides an overview of defined boundary conditions. A moving, constant temperature wall boundary condition was applied to the piston surface, while the constant temperature condition is prescribed for the fixed cylinder head selection. The cylinder geometry can be assumed as cyclic symmetrical hence the periodic boundary condition was applied to both sides of the mesh. In addition, for the compensation volume, an adiabatic boundary condition was considered.

Table 3. Computational mesh boundary conditions

Selection	Boundary Type	Specific condition
Piston	Mesh movement	Temperature 473 K
Segment	Periodic inlet/outlet	Periodic
Cylinder Head	Wall	Temperature 443 K
Comp. Volume	Mesh movement/Wall	Adiabatic boundary
Cylinder Axis	Symmetry	-

Relevant initial conditions such as pressure, temperature and the mass fraction of the species were specified according to available experimental data. Table 4 provides an overview of defined initial conditions for the two investigated engine operating points. The calculations were carried out for the engine rotational speed 2000 min^{-1}. The initial swirl velocity inside the combustion chamber was set to value 4740 min^{-1} around the cylinder axis. Single represents an operating point with a single-injection strategy. In addition to the single-injection engine operating point, a case with three injection pulses per cycle was investigated to prove the high accuracy of utilised modelling approaches. Parameters such as the start and the end of injections together with

corresponding injected fuel mass for both cases are shown in the following section. Initial mass fractions of the species Y_i in the combustion chamber at the beginning of the calculation are given in Table 5.

Table 4. Initial conditions of the observed operating points

	Single	Multi
Pressure (Pa)	219284	210867
Temperature (K)	427.2	418.9
Turbulent length scale (m)	0.002	0.002
Turbulent kinetic energy (m^2/s^2)	10	10

Table 5. Initial values of species

	Single	Multi
Y_{O2}	0.1855	0.1830
Y_{N2}	0.7579	0.7580
Y_{CO2}	0.0415	0.04021
Y_{H2O}	0.0151	0.01880

3.1. Spray setup

Properties of the liquid fuel utilised in performed calculations, namely Diesel EN590 B7, are already available in FIRE™. The term B7 implies that there is up to 7% biodiesel content in the fuel[55]. The temperature of injected fuel was measured in the experimental research, and it is defined by 317 K. The size of introduced particles at the fuel inlet is considered 125 μm. The main characteristic of the fuel injection system is shown in

Table 6, where the injector geometry required for simulation was taken over by the manufacturer. Spray angle delta 1 introduced in Table 6specifies the spray direction for each hole of the nozzle in degrees.

Table 6. Injector geometry

Position	(0.5, 0, -1.5) mm
Direction	(0, 0, 1)
Spray angle delta 1	145
Nozzle diameter at hole centre position	1.84 mm

| Nozzle hole diameter | 0.125 mm |

The Wave break-up model is employed in order to model liquid fuel break-up downstream of the injector. For the single-injection case, the Wave model constant C_2 was considered 5 during the ECFM-3Z simulation and 20 during the FGM simulation, as for the multi-injection case, it was varied between 6 and 36, with the three injection pulses being considered separately. Since the C_2 parameter is the tuning parameter of the model, which strictly influence the disintegration process of injected fuel and injector properties, the selected values of C_2 were based on the sensitivity parametric analysis of the injection process, where the C_2 parameter was tuned to have the best agreement with the experimentally measured pressure data. The total mass of injected fuel is 4.09 mg in the single-injection case and 3.95 mg in the multi-injection case. Figure 4 shows the injection rate for single-injection and multi-injection case, respectively.
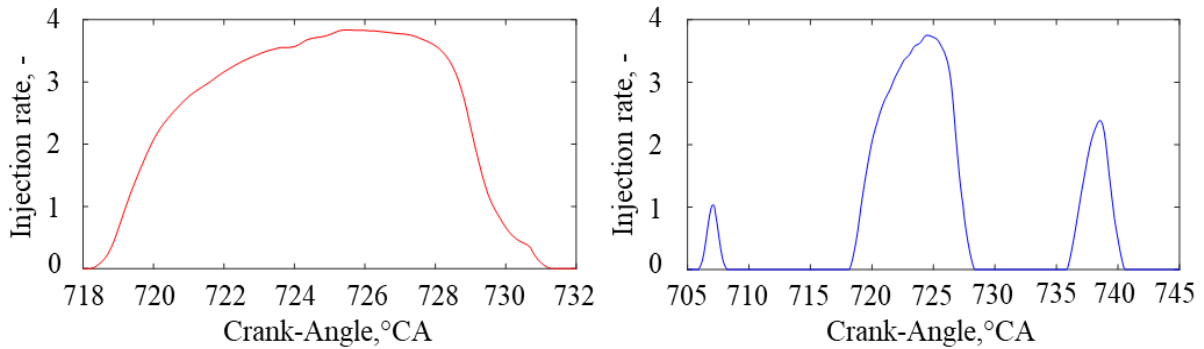
Figure 4.Injection rate for single (left) and multi (right) injection cases

3.2. Combustion setup

When modelling the combustion process with the ECFM-3Z combustion model, some parameters have to be adjusted. The mixing model parameter influences the fuel transfer from the pure fuel zone to the mixed zone. For modelling autoignition, the Two-Stage model was employed, where the autoignition delay time is interpolated from pre-computed tabulated values. For the multi-injection case, the autoignition model parameter was considered 1.2 during the pilot injection, while for the main and post-injection, it was set to the value 0.9. For the single-injection case, the autoignition model parameter was set to a value of 4. The autoignition parameter values are selected based on the preliminary analysis of the combustion process, where the ignition delay is adjusted to have autoignition timing similar to the experimentally measured RoHR data. Chemical reaction time influences the rate of reaction of the fuel during the combustion process. In the present study, it was considered 1 for the single-injection case and 10000 for the multi-

injection case, according to AVL FIRE™ recommendations [45]. Extinction temperature is set to 300 K.

The FGM table generation tool contains three steps: preprocessing of textual input, PSR simulations, and post-processing of the output. The preprocessor translates the script into valid input for the PSR solver and launches the individual simulations. The input data of a PSR table are summarised in Table 7, where pressure points are 40, 80, 120, 140, and temperatures are selected in the interval from 700 to 1800 K with the linear distribution. Mixture fraction grid is generated with 38 points where the refinement is around stoichiometric mixture fraction, 0.0451. For the generation of PSR table, a reduced reaction mechanism LLNL Diesel reduced NOx, with 181 species and 1432 reactions is used [56].

Table 7. The input of PSR simulation

Input variable		Points
Z	Mixture fraction	38
S	Mixture fraction segregation	10
T	Temperature	12
p	Pressure	4

4. Results and discussion

Within this section, the results of two 3D CFD combustion modelling approaches applied to the industrial diesel engine are shown. First, the calculated results, such as mean in-cylinder pressure and RoHR of the single-injection operating point, are compared with the experimental results. Afterwards, the equivalent comparison is presented for the operating point with a multi-injection strategy. Furthermore, the results for spray development and temperature field inside the engine combustion chamber for single-injection and multi-injection operating point are presented. Furthermore, the calculated NO_x emissions are compared with the experimental data. Finally, the comparison of calculation times for different combustion modelling approaches is shown.

4.1. Single-injection results

The in-cylinder pressure results for the single-injection case are shown in Figure 5. It is noticed that the FGM simulation underpredicts the experimental pressure curve. Furthermore, the numerical results of the ECFM-3Z combustion model show better agreement during the simulation with the experimental results of mean in-cylinder pressure than the results with the FGM. The

inflexion points visible around the TDC represent the start of the combustion. The pressure gradient increases due to the compression process until the evaporation of the spray during the pressure values are decreased. At the inflexion point, the heat from the chemical energy of the fuel is released, and the pressure gradient continues to rise to the maximum pressure. The inflexion points correspond to the initial declination of RoHR from the zero value, as visible in Figure 6. In [49], the FGM method was tested on numerous operating cases, where the agreement between the experimental and calculated peak pressures was detailly analysed. The obtain results in this work are within the interval of the difference between experimental and numerical simulations, which were published [49]. Better agreement of the ECFM model in the single-injection case can be mainly accounted to the better description of the air-fuel mixing process. The ECFM model divides each cell into three mixing zones to account for diffusion and mixing processes. The transport equation of the standard species used in the model is calculated for unmixed air with residual gases, unmixed fuel, and thoroughly mixed fuel-air mixture regions. Such an approach gives a better explanation of the mixing process, which is relevant for a more accurate description of the combustion process, especially in the operating cases that feature injection of a large amount of fuel in the short interval as in single-injection case. The accuracy of the ECFM model compared to the FGM model was achieved at the expense of the computational demand.

Figure 5. Mean pressure results for the single-injection case

Figure 6 shows a comparison of the RoHR results obtained by the ECFM-3Z and FGM combustion approaches with the experimental data for the single-injection case. The presented RoHR results represent only one-seventh of RoHR value for the entire cylinder. The start of the combustion or the autoignition point of the fuel-air mixture corresponds to the initial increase of

RoHR from the zero value. After the beginning of fuel injection into the cylinder, a specific delay of combustion start is present due to the mixing process, this delay is called ignition delay. It is notable from the presented results that the ECFM-3Z combustion model predicts the ignition earlier than the experimental data. On the contrary, the FGM combustion model predicts more extensive ignition delay. The earlier ignition in the ECFM-3Z model compared to the FGM model can be prescribed to a better description of the air-fuel mixing process, which is relevant for a more accurate description of ignition delay. The ability to capture the mixture of fuel and air in three mixing regions of the ECFM-3Z model shows a lower RoHR gradient compared to the experiment and FGM model. In the FGM, RoHR gives the increased ignition delay, which is compensated by a higher gradient of the released heat. That can be mainly attributed to the simplified chemistry in the FGM model that describes combustion progress with fewer transport equations than the detailed mechanism that describes each interim chemical species' transport and reaction. Furthermore, the results obtained by the FGM combustion model show a higher peak value of RoHR in comparison with the experiment, while the ECFM-3Z model predicts a lower peek value of RoHR. Calculated RoHR profiles have a good trend in comparison to the experimental curve for both combustion modelling approaches. It can be noticed that the higher gradient of RoHR curve after the ignition exist in the FGM calculations, together with more pronounced local maximum values.
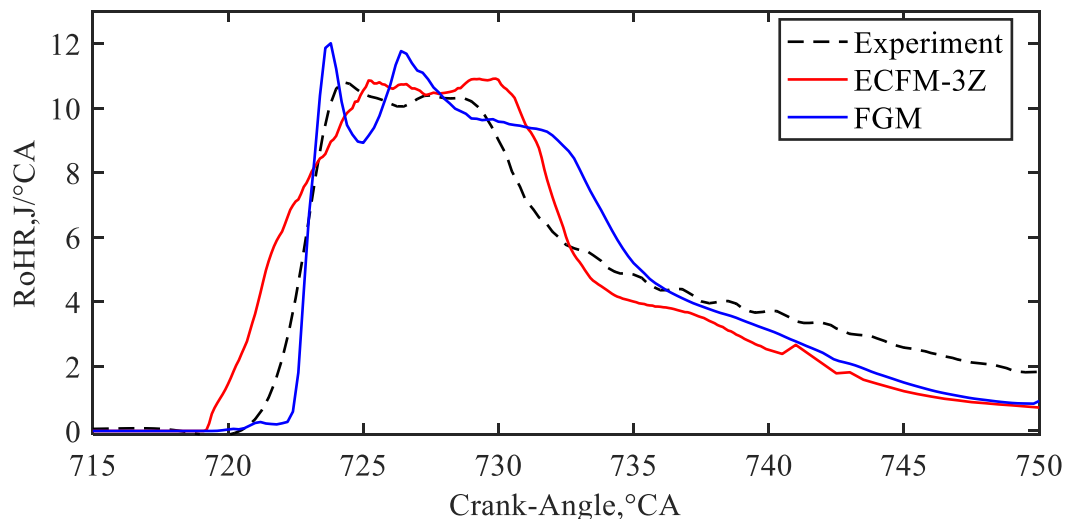
Figure 6. RoHR results for the single-injection case

4.2. Multi-injection results

Figure 7 shows the differences in mean pressure curves obtained with the combustion models and experiment for the multi-injection case. In this case, the results obtained with the ECFM-3Z

model show a larger underprediction of the experimental curve than the results obtained with the FGM model. The same underprediction of the peak pressure with FGM is achieved in the multi-injection operating point as in the single-injection point shown in Figure 5. In [39], the multi-injection engine operating point was observed with the FGM model, where the similar underachievement of the pressure rise in the pilot injection is present as in Figure 7. Compared to the ECFM results in the single-injection case, the underprediction in the multi-injection case is mainly due to the higher uncertainty of the model for lean conditions due to the description of unmixed fuel in transport Equation (10).
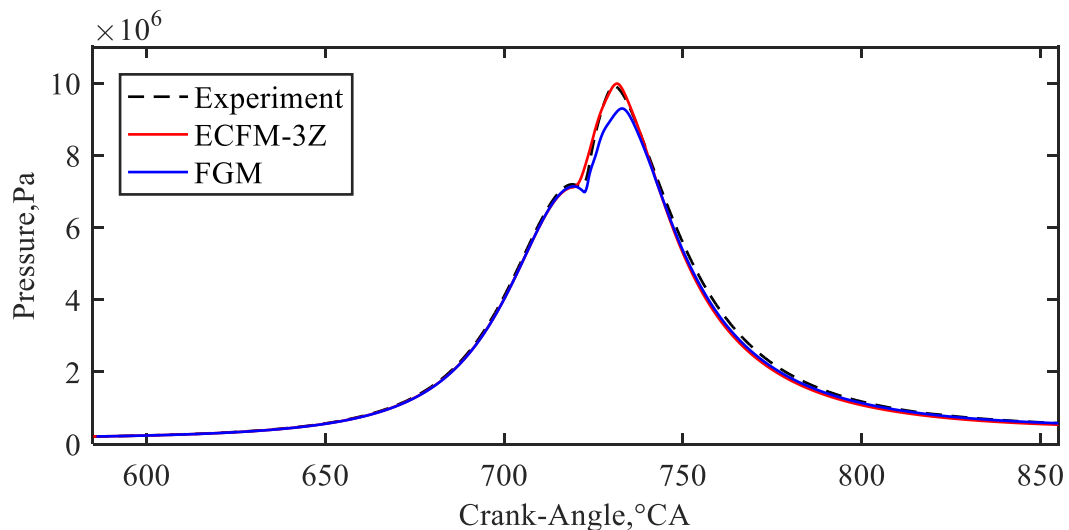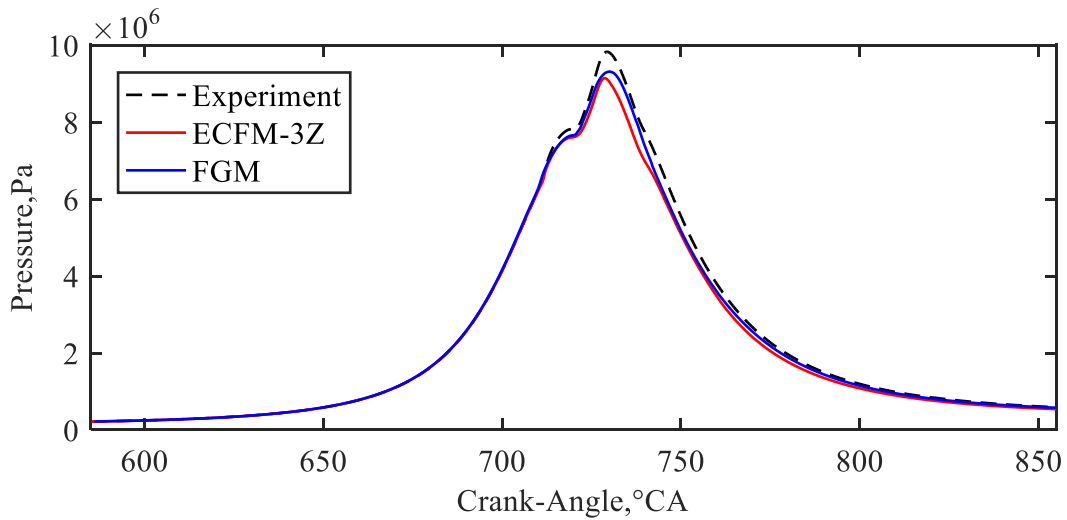

Figure 7. Mean pressure results for multi-injection case

Figure 8 shows the comparison of RoHR results obtained with the ECFM-3Z model and FGM model with the experimental data for the multi-injection case. The area under the curves represents the accumulated energy, the energy realised from the fuel oxidation. The ignition of the fuel injected in the pilot injection predicted by the ECFM-3Z has a more significant delay than experimental data. Still, the combustion of pilot injected fuel is faster than in experiment and FGM results. Also, the model overpredicts the peak value of the pilot heat release with ECFM-3Z. The ignition of the fuel injected in post-injection is well predicted, together with the peak value of RoHR. Apart from that, the shape of the calculated RoHR curve fits well with the experimental data. Furthermore, the injection of the fuel injected in the main injection and the magnitude of heat release corresponds to the experimental data. The ignition of the fuel injected in the pilot injection predicted by the FGM model occurs slightly after recorded experimental data, and the peak value of the first heat release is underpredicted. In the part when the main injection occurs, RoHR curve

obtained with the FGM exhibit a similar shape and magnitude as the one obtained with the ECFM-3Z model, while the peak value of the post-heat release is underpredicted.
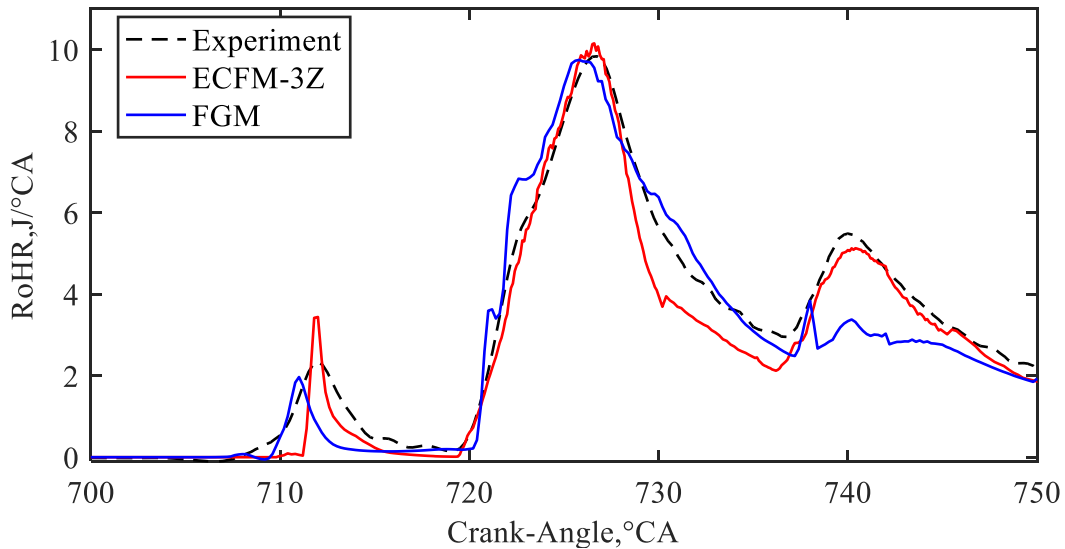
Figure 8. RoHR results for multi-injection case

One of the advantages of the multi-injection strategy compared to the single-injection strategy is the better control over the combustion process and the better overall efficiencies due to the lower amounts of the unburned fuel. For the approximately same injected mass in the single and multi-injection cases, the RoHR in the multi-injection case has permanent heat release during the operating cycle, which can be seen in Figure 8 compared to Figure 6. Moreover, the multi-injection strategy effectively reduces the NOx and PM and diesel engine combustion noise [57]. Overall, it can be concluded that both combustion modelling approaches have a suitable description of spray and combustion phenomena, with the computational demand acceptable for the industrial purposes of investigating the internal combustion engines that feature the multi-injection strategy.

4.3. Comparison of temperature fields

In Figure 9, the temperature field for different crank angle positions of the single-injection case is shown. Liquid fuel is injected into the cylinder at the 718 °CA, few degrees before the TDC. As the liquid fuel jet leaves the nozzle, it breaks up into small diameter droplets and evaporates, which is visible in temperature reduction. After the fuel vapour is produced and mixed with the hot oxidising gas media in the cylinder, ignition occurs, and in-cylinder pressure and temperature rise rapidly. Notably, at 720 °CA, the ECFM-3Z model predicts a more intensive evaporation process, while the FGM spray region less spreader, which can be addressed to the

higher value of Wave break-up constant C_2, but also to the lower ignition delay due to the better description of the air-fuel mixing process for the fuel-rich regions. The faster ignition is the primary reason for this, compared to the FGM model, which can also be seen in the RoHR curve in Figure 6. At 728 °CA and 740 °CA, it is visible that the ECFM-3Z model predicts a broader high-temperature region characterised by the higher peak pressures, which is also visible in Figure 5. The maximum temperature is higher for the results obtained with the FGM model, and it is recorded at 740 °CA. The temperature regions of both combustion modelling approaches are captured in good agreement between both models, where the main combustion exists in the cylinder bowl. The lower ignition delay of the ECFM-3Z model visible from the RoHR curve in Figure 6 agrees with the more developed combustion regions in the ECFM-3Z results compared to the FGM results. Such regions of the higher temperature with the ECFM-3Z model will obtain higher concentrations of NO and promoted NO formation process than with FGM results.
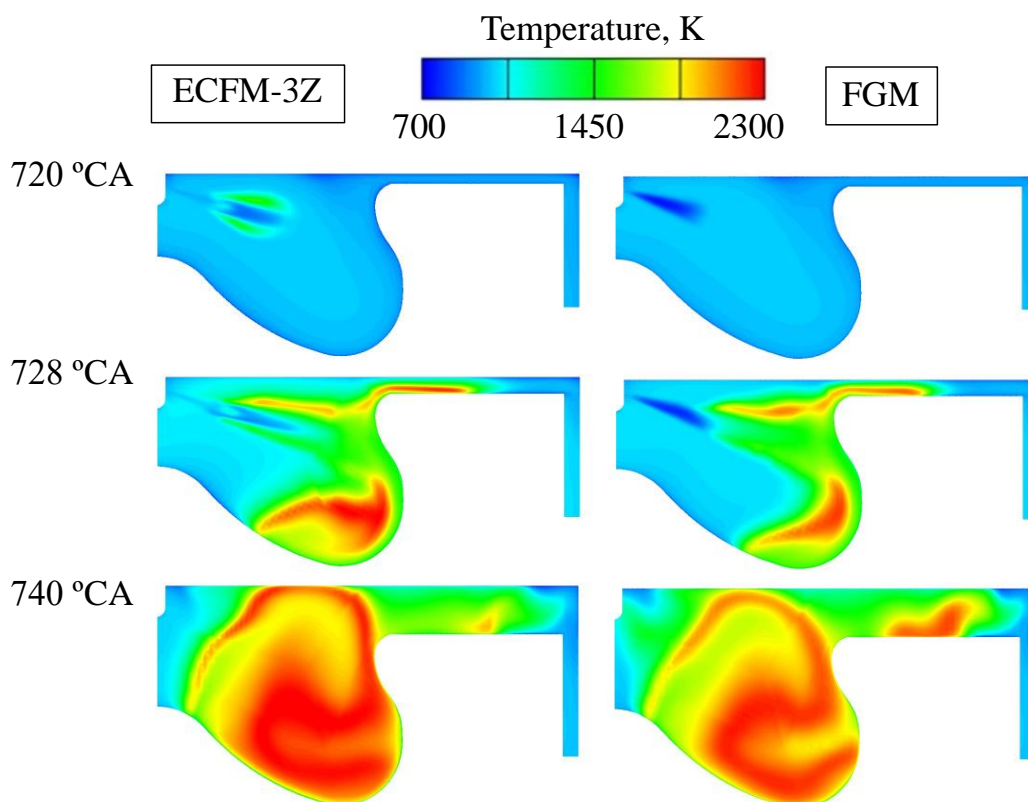
Figure 9. Temperature field ECFM-3Z and FGM of the single-injection case

Figure 10 shows the temperature field of the multi-injection case at crank angle positions that illustrate phases of the combustion process. Few degrees after the pilot injection, at 709 °CA, the low-temperature gas phase can be observed for the region where liquid fuel prevails. This phenomenon can be attributed to the evaporation process of injected fuel. At 721 °CA, the start of

combustion appears as temperature increase due to the ignition of vapour fuel from the pilot injection. The pilot injected fuel shows a pronounced evaporation process for FGM results, where the high-temperature conditions for the main injection were developed in the piston bowl, while for the ECFM-3Z model, they are more toward the nozzle. That can be mainly attributed to the direct influence of the near nozzle turbulence on the combustion process in the ECFM-3Z model via turbulent Schmidt number. Contrary to the FGM, for which the turbulence was considered indirectly via solving of two transport equations for mixture fraction variance and progress variable variance. At the same crank angle, a low-temperature spray region is noticeable due to the evaporation of the main injected fuel. If the multi-injection case is correlated to the single-injection case in Figure 9, the faster evaporation process is noticed. That can be attributed to the increased in-cylinder temperatures achieved through pilot-injection combustion that further reduce the autoignition timing of the fuel-air mixture from the main injection. Several degrees later, at 730 °CA, the developed combustion process occurs, which is generated from the combustion of the fuel-air mixture from the main injection, and the high-temperature region is formed. The post-injection occurs at 735 °CA, which is visible as the low-temperature spray region, while the expanded high-temperature region is more comprehensive for the results obtained with the ECFM-3Z combustion model.
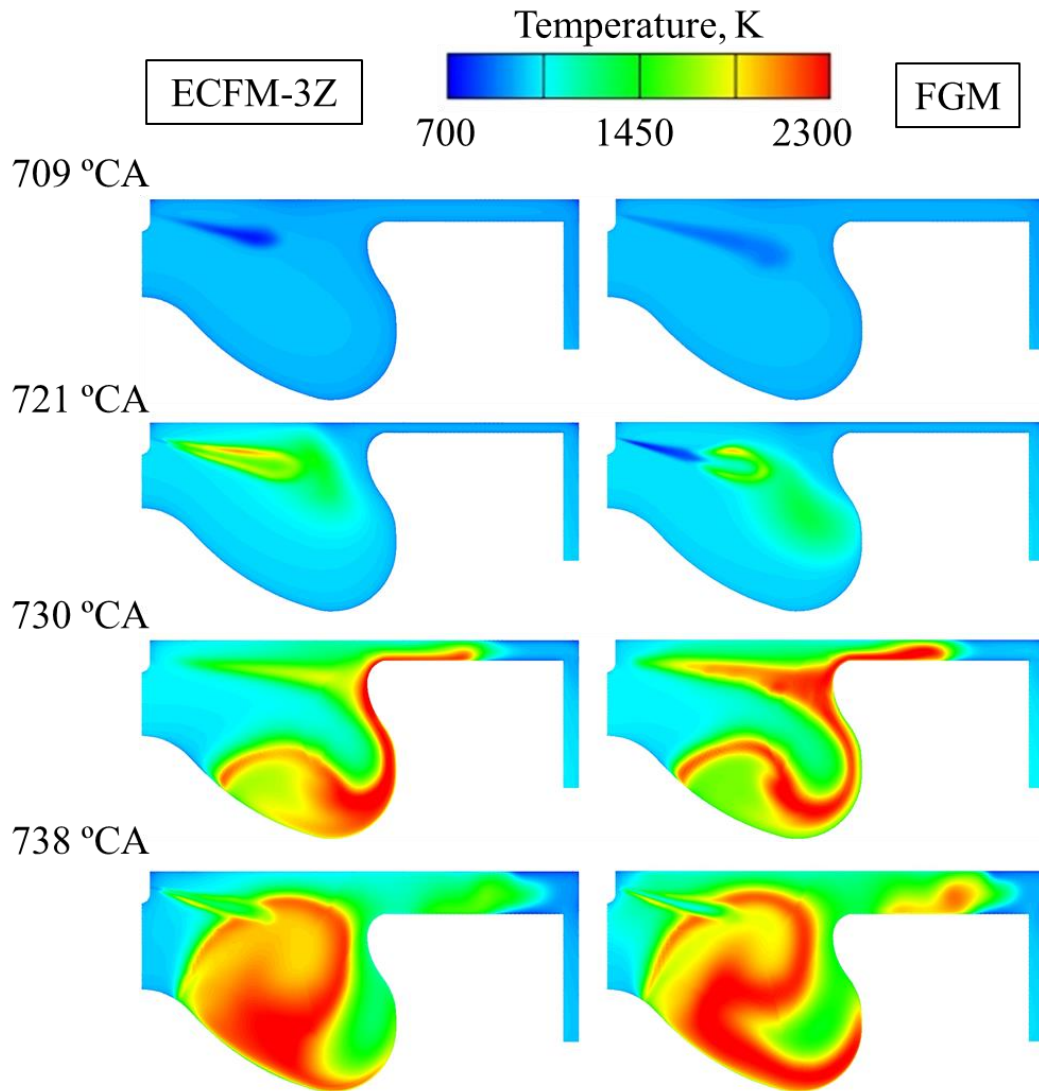
Figure 10. Temperature field for ECFM-3Z and FGM of the multi-injection case

4.4. Emission results

The NO pollutant species are formed under high-temperature conditions within the flame region, where the NO formation is generated pronouncedly at higher temperatures and the higher flame propagation rates, which generate thermal NO formation. The in-cylinder high-temperature regions mainly determined the NO formation in this work. Generally, the lower temperatures have been obtained with the FGM model in both single and multi-injection case, which resulted in the underprediction of NO concentrations with the FGM model, as can be seen in Table 8. When using the FGM combustion model, all NO-related chemistry is computed during lookup table generation, from which the interpolation procedure based on progress variable is made. Therefore, the accuracy of the FGM model for NO formation is expected to be lower than the ECFM-3Z, which calculates the chemical reactions during the 3D fluid flow iterations. The stored values of NO in

lookup tables are based on 0D PSR calculation which is retrieved during the CFD simulation. Table 8 shows a comparison of the calculated NO emissions with the experimental data. In the single-injection case, the ECFM-3Z model overpredicts the measured value of NO emission, which was expected from the mean pressure results in Figure 5, where the overprediction of NO concentrations is correlated to the mean pressure values which also have overprediction compared to the experimental results. Contrary, in comparison with the single-injection ECFM-3Z case, the FGM results have the same underprediction of NO concentrations as the mean pressure results. In the multi-injection case, the computed results with both combustion models are lower than the experimental data, which is once again correlated to the mean in-cylinder pressure results in Figure 7. Furthermore, in both cases, the ECFM-3Z model showed higher values of NO emission than the FGM, which can also be attributed to the direct influence of turbulence in CFD simulations on the combustion results and NO formation, rather than approximating it from the lookup tables. As can be seen, the trend in the experimental NO reduction between single and multi-injection case is well reproduced with both modelling approaches in CFD simulations. The calculated emission results indicate that both combustion models can perform the fast emission calculations in IC engine with reasonable accuracy.

Table 8. NO concentrations at the end of the operating cycle

	Single	Multi
Experiment (gm^{-3})	135.6	119.1
ECFM-3Z (gm^{-3})	160.8	98.2
FGM (gm^{-3})	70.9	67.5

4.5. Calculation time comparison

The FGM model allows including skeletal mechanisms as well as detailed reaction mechanisms in CFD simulations at a reasonable cost. Hence, the use of 3D CFD combustion models based on tabulated chemistry is becoming increasingly popular. In terms of computational time, the present study was executed on Intel® Xeon® E5-2650 processor, using four CPU cores per case. A comparison of the turnaround times for one single-injection and one multi-injection operating point is presented in Table 9. As can be noticed from the table, a reduction in the computational times is meaningful - approximately two times. That can be mainly attributed to the extensive calculation of the air-fuel mixing in the ECFM-3Z model, which separate each cell in 3 additional mixing regions for which the model transport equations are required to be solved.

Table 9. Comparison of calculation times for ECFM-3Z and FGM

	Single	Multi
ECFM-3Z (hh:mm)	1:25	2:16
FGM (hh:mm)	0:42	1:18

5. Conclusion

The investigation and comparison of ECFM-3Z and FGM combustion modelling approaches against the experimental results for a compression ignition engine are performed. The single and multiple injection strategies were examined to prove the high predictability of proposed modelling approaches. It is shown that the FGM modelling approach shows higher ignition delay compared to the ECFM-3Z model for single-injection case, which can be prescribed to the better description of the air-fuel mixing process, which is relevant for a more accurate description of ignition delay. Furthermore, pressure results obtained with the FGM model exhibit under prediction of the experimental pressure curve for both cases, while the opposite presented RoHR curves fitting well with the experimental data. In both single and multiple injection cases, the results obtained with the ECFM-3Z model showed a more uniform temperature region across the combustion chamber, while for the FGM narrow region of higher temperature is obtained. Higher mean temperatures and then mean pressures were achieved in the ECFM-3Z have a reasonable correlation with NO concentrations at the end of the cycle. The experimental NO reduction trend between the observed cases is well reproduced with both modelling approaches in CFD simulations. In both cases, the ECFM-3Z model showed higher values of NO emission in comparison with the FGM, which can also be attributed to the lower accuracy of the FGM model for NO formation than with the ECFM-3Z model, which calculates the chemical reactions during the fluid flow solver iterations. The calculated emission results tend to show a good trend with the measured emission concentration. Finally, it should be noted that the runtime for CFD simulations with FGM is approximately two times decreased due to the extensive calculation of the air-fuel mixture in the ECFM-3Z model, which separates each cell into three additional mixing regions.

REFERENCES

[1]   Lion S, Vlaskos I, Taccani R. A review of emissions reduction technologies for low and medium speed marine Diesel engines and their potential for waste heat recovery. Energy Convers Manag 2020;207:112553. doi:10.1016/j.enconman.2020.112553.

[2]   López JJ, García A, Monsalve-Serrano J, Cogo V, Wittek K. Potential of a two-stage variable compression ratio downsized spark ignition engine for passenger cars under different driving conditions. Energy Convers Manag 2020;203:112251. doi:10.1016/j.enconman.2019.112251.

[3]   Hao C, Lu Z, Feng Y, Bai H, Wen M, Wang T. Optimization of fuel/air mixing and combustion process in a heavy-duty diesel engine using fuel split device. Appl Therm Eng 2021;186:116458. doi:10.1016/j.applthermaleng.2020.116458.

[4]   Cerinski D, Vujanović M, Petranović Z, Baleta J, Samec N, Hriberšek M. Numerical analysis of fuel injection configuration on nitrogen oxides formation in a jet engine combustion chamber. Energy Convers Manag 2020;220:112862. doi:10.1016/j.enconman.2020.112862.

[5]   Geng L, Li S, Xiao Y, Xie Y, Chen H, Chen X. Effects of injection timing and rail pressure on combustion characteristics and cyclic variations of a common rail DI engine fuelled with F-T diesel synthesized from coal. J Energy Inst 2020;93:2148–62. doi:10.1016/j.joei.2020.05.009.

[6]   Huang H, Zhu Z, Chen Y, Chen Y, Lv D, Zhu J, et al. Experimental and numerical study of multiple injection effects on combustion and emission characteristics of natural gas–diesel dual-fuel engine. Energy Convers Manag 2019;183:84–96. doi:10.1016/j.enconman.2018.12.110.

[7]   Xu M, Cheng W, Zhang H, An T, Zhang S. Effect of diesel pre-injection timing on combustion and emission characteristics of compression ignited natural gas engine. Energy Convers Manag 2016;117:86–94. doi:10.1016/j.enconman.2016.02.054.

[8]   Abdul Gafoor CP, Gupta R. Numerical investigation of piston bowl geometry and swirl ratio on emission from diesel engines. Energy Convers Manag 2015;101:541–51. doi:10.1016/j.enconman.2015.06.007.

[9]   Shirvani S, Shirvani S, Shamekhi AH, Reitz RD. An Investigation of the Effects of the Piston Bowl Geometries of a Heavy-Duty Engine on Performance and Emissions Using Direct Dual Fuel Stratification Strategy, and Proposing Two New Piston Profiles. SAE Int J Engines 2020;13:03-13-03–0021. doi:10.4271/03-13-03-0021.

[10]   Yang J, Johansson M, Naik C, Puduppakkam K, Golovitchev V, Meeks E. 3D CFD Modeling of a Biodiesel-Fueled Diesel Engine Based on a Detailed Chemical Mechanism, 2012. doi:10.4271/2012-01-0151.

[11]   Petranović Z, Bešenić T, Vujanović M, Duić N. Modelling pollutant emissions in diesel engines, influence of biofuel on pollutant formation. J Environ Manage 2016:1–9. doi:10.1016/j.jenvman.2017.03.033.

[12]   Stančin H, Mikulčić H, Wang X, Duić N. A review on alternative fuels in future energy system. Renew Sustain Energy Rev 2020;128:109927. doi:10.1016/j.rser.2020.109927.

[13]   Petranović Z, Edelbauer W, Vujanović M, Duić N. Modelling of spray and combustion processes by using the Eulerian multiphase approach and detailed chemical kinetics. Fuel 2017;191:25–35. doi:10.1016/j.fuel.2016.11.051.

[14]   Józsa V, Hidegh G, Kun-Balog A, Ng J-H, Chong CT. Ultra-low emission combustion of diesel-coconut biodiesel fuels by a mixture temperature-controlled combustion mode. Energy Convers Manag 2020;214:112908. doi:10.1016/j.enconman.2020.112908.

[15]   Pranoto H, Wahab A, Arifin Z, Siswanto I. Fuel filter condition monitoring (ffcm) devices innovation on truck diesel engine to prevent filter blocking due to use of bio diesel: b10-b20-b30. J Phys Conf Ser 2020;1700:012099. doi:10.1088/1742-6596/1700/1/012099.

[16]   Lazaroiu G, Pană C, Mihaescu L, Cernat A, Negurescu N, Mocanu R, et al. Solutions for energy recovery of animal waste from leather industry. Energy Convers Manag 2017;149:1085–95. doi:10.1016/j.enconman.2017.06.042.

[17]   Westbrook CK, Pitz WJ, Herbinet O, Curran HJ, Silke EJ. A comprehensive detailed chemical kinetic reaction mechanism for combustion of n-alkane hydrocarbons from n-octane to n-hexadecane. Combust Flame 2009;156:181–99. doi:10.1016/j.combustflame.2008.07.014.

[18]   Novella R, García A, Pastor JM, Domenech V. The role of detailed chemical kinetics on CFD diesel spray ignition and combustion modelling. Math Comput Model 2011;54:1706–19. doi:10.1016/j.mcm.2010.12.048.

[19]   Gopinath S, Devan PK, Sabarish V, Sabharish Babu BV, Sakthivel S, Vignesh P. Effect of spray characteristics influences combustion in DI diesel engine – A review. Mater Today Proc 2020;33:52–65. doi:10.1016/j.matpr.2020.03.130.

[20]   Juric F, Vujanovic M, Zivic M, Holik M, Wang X, Duic N. Assessment of radiative heat transfer impact on a temperature distribution inside a real industrial swirled

furnace. Therm Sci 2020:285–285. doi:10.2298/TSCI200407285J.

[21] Desantes JM, García-Oliver JM, Novella R, Pérez-Sánchez EJ. Application of a flamelet-based CFD combustion model to the LES simulation of a diesel-like reacting spray. Comput Fluids 2020;200:104419. doi:10.1016/j.compfluid.2019.104419.

[22] van Oijen JA, Donini A, Bastiaans RJM, ten Thije Boonkkamp JHM, de Goey LPH. State-of-the-art in premixed combustion modeling using flamelet generated manifolds. Prog Energy Combust Sci 2016;57:30–74. doi:10.1016/j.pecs.2016.07.001.

[23] Eder L, Ban M, Pirker G, Vujanovic M, Priesching P, Wimmer A. Development and Validation of 3D-CFD Injection and Combustion Models for Dual Fuel Combustion in Diesel Ignited Large Gas Engines. Energies 2018;11:643. doi:10.3390/en11030643.

[24] Peters N. Laminar flamelet concepts in turbulent combustion. Symp Combust 1988;21:1231–50. doi:10.1016/S0082-0784(88)80355-2.

[25] Beeckmann J, Hesse R, Kruse S, Berens A, Peters N, Pitsch H, et al. Propagation speed and stability of spherically expanding hydrogen/air flames: Experimental study and asymptotics. Proc Combust Inst 2017;36:1531–8. doi:10.1016/j.proci.2016.06.194.

[26] Colin O, Benkenida A, Angelberger C. 3D modeling of mixing, ignition and combustion phenomena in highly stratified gasoline engines. Oil Gas Sci Technol 2003;58:47–62. doi:10.2516/ogst:2003004.

[27] Colin O, Benkenida A. The 3-zones Extended Coherent Flame Model (ECFM3Z) for computing premixed/diffusion combustion. Oil Gas Sci Technol 2004;59:593–609. doi:10.2516/ogst:2004043.

[28] Tap FA, Hilbert R, Thévenin D, Veynante D. A generalized flame surface density modelling approach for the auto-ignition of a turbulent non-premixed system. Combust Theory Model 2004;8:165–93. doi:10.1088/1364-7830/8/1/009.

[29] Béard P, Colin O, Miche M. Improved modelling of di diesel engines using sub-grid descriptions of spray and combustion. SAE Tech Pap 2003. doi:10.4271/2003-01-0008.

[30] Catapano F, Costa M, Marseglia G, Sementa P, Sorge U, Vaglieco BM. Experimental and Numerical Investigation in a Turbocharged GDI Engine Under Knock Condition by Means of Conventional and Non-Conventional Methods. SAE Int J Engines 2015;8:437–46. doi:10.4271/2015-01-0397.

[31] Bohbot J, Colin O, Velghe A, Michel JB, Wang M, Senecal PK, et al. An Innovative Approach Combining Adaptive Mesh Refinement, the ECFM3Z Turbulent Combustion Model, and the TKI Tabulated Auto-Ignition Model for Diesel Engine CFD Simulations. SAE Tech Pap 2016. doi:10.4271/2016-01-0604.

[32] Mobasheri R. Analysis the ECFM-3Z Combustion Model for Simulating the Combustion Process and Emission Characteristics in a HSDI Diesel Engine. Int J Spray Combust Dyn 2015;7:353–71. doi:10.1260/1756-8277.7.4.353.

[33] Jurić F, Petranović Z, Vujanović M, Duić N. Numerical assessment of radiative heat transfer impact on pollutant formation processes in a compression ignition engine. J Clean Prod 2020;275, 12308. doi:10.1016/j.jclepro.2020.123087.

[34] Lam SH, Goussis D a. Understanding complex chemical kinetics with computational singular perturbation. Symp Combust 1989;22:931–41. doi:10.1016/S0082-0784(89)80102-X.

[35] Maas U, Pope SB. Simplifying chemical kinetics: Intrinsic low-dimensional manifolds in composition space. Combust Flame 1992;88:239–64. doi:10.1016/0010-2180(92)90034-M.

[36] Oijen JA Van, Goey LPH De. Modelling of Premixed Laminar Flames using Flamelet-Generated Manifolds. Combust Sci Technol 2000;161:113–37. doi:10.1080/00102200008935814.

[37] Donini A, M. Bastiaans RJ, van Oijen JA, H. de Goey LP. A 5-D Implementation of FGM for the Large Eddy Simulation of a Stratified Swirled Flame with Heat Loss in a Gas Turbine Combustor. vol. 98. Flow, Turbulence and Combustion; 2017. doi:10.1007/s10494-016-9777-7.

[38] Tvrdojevic M, Vujanovic M, Priesching P, Tap FA, Starikov A, Goryntsev D, et al. Implementation of the Semi Empirical Kinetic Soot Model within Chemistry Tabulation Framework for Efficient Emissions Predictions in Diesel Engines. Open Phys 2020;17:905–15. doi:10.1515/phys-2019-0096.

[39] Priesching P, Tvrdojevic M, Tap F, Meijer C. Prediction of the Combustion and Emission Processes in Diesel Engines Based on a Tabulated Chemistry Approach. SAE Tech Pap 2017. doi:10.4271/2017-01-2200.

[40] Goryntsev D, Tap F, Tvrdojevic M, Priesching P. SI engine combustion and knock modelling using detailed fuel surrogate models and tabulated chemistry. SAE Tech Pap 2019;2019-April:1–14. doi:10.4271/2019-01-0205.

[41] Bekdemir C, Rijk E, Somers B, De Goey P, Albrecht B. On the application of the flamelet generated manifold (FGM) approach to the simulation of an igniting diesel spray. SAE Tech Pap 2010. doi:10.4271/2010-01-0358.

[42] Keum S, Grover RO, Meijer C, Tap F. CFD Modelling of Partial Fuel Stratification Combustion Using Detailed Fuel Surrogate Models and Tabulated Chemistry. Vol. 2

Emiss. Control Syst. Instrumentation, Control. Hybrids; Numer. Simulation; Engine Des. Mech. Dev., American Society of Mechanical Engineers; 2017. doi:10.1115/ICEF2017-3632.

[43]   D'Adamo A, Breda S, Iaccarino S, Berni F, Fontanesi S, Zardin B, et al. Development of a RANS-Based Knock Model to Infer the Knock Probability in a Research Spark-Ignition Engine. SAE Int J Engines 2017;10. doi:10.4271/2017-01-0551.

[44]   Durbin PA. Near-wall turbulence closure modeling without "damping functions." Theor Comput Fluid Dyn 1991;3:1–13. doi:10.1007/BF00271513.

[45]   AVL AST GmbH. AVL FIRE™ Documentation v2019. Graz, Austria: AVL AST GmbH; 2019.

[46]   Turner MR, Sazhin SS, Healey JJ, Crua C, Martynov SB. A breakup model for transient Diesel fuel sprays. Fuel 2012;97:288–305. doi:10.1016/j.fuel.2012.01.076.

[47]   Abramzon B, Sirignano WA. Droplet vaporization model for spray combustion calculations. Int J Heat Mass Transf 1989;32:1605–18. doi:10.1016/0017-9310(89)90043-4.

[48]   Jurić F, Petranović Z, Vujanović M, Katrašnik T, Vihar R, Wang X, et al. Experimental and numerical investigation of injection timing and rail pressure impact on combustion characteristics of a diesel engine. Energy Convers Manag 2019;185:730–9. doi:10.1016/j.enconman.2019.02.039.

[49]   Tap F, Meijer C, Goryntsev D, Starikov A, Tvrdojevic M, Priesching P. Predictive CFD Modeling of Diesel Engine Combustion Using an Efficient Workflow Based on Tabulated Chemistry. Vol. 2 Emiss. Control Syst. Instrumentation, Control. Hybrids; Numer. Simulation; Engine Des. Mech. Dev., American Society of Mechanical Engineers; 2018. doi:10.1115/ICEF2018-9758.

[50]   Tap F, Schapotschnikow P. Efficient combustion modeling based on Tabkin® CFD look-up tables: A case study of a lifted diesel spray flame. SAE Tech Pap 2012. doi:10.4271/2012-01-0152.

[51]   Rößler M, Koch T, Janzer C, Olzmann M. Mechanisms of the NO2 Formation in Diesel Engines. MTZ Worldw 2017;78:70–5. doi:10.1007/s38313-017-0057-2.

[52]   Józsa V. Mixture temperature-controlled combustion: A revolutionary concept for ultra-low NOX emission. Fuel 2021;291:120200. doi:10.1016/j.fuel.2021.120200.

[53]   Cao H, Sun S, Liu Y, Wall TF. Computational Fluid Dynamics Modeling of NO x Reduction Mechanism in Oxy-Fuel Combustion †. Energy & Fuels 2010;24:131–5. doi:10.1021/ef900524b.

[54]   Vujanović M, Duić N, Tatschl R. Validation of reduced mechanisms for nitrogen chemistry in numerical simulation of a turbulent non-premixed flame. React Kinet Catal Lett 2009;96:125–38. doi:10.1007/s11144-009-5463-2.

[55]   Hoekman SK, Broch A, Robbins C, Ceniceros E, Natarajan M. Review of biodiesel composition, properties, and specifications. Renew Sustain Energy Rev 2012;16:143–69. doi:10.1016/j.rser.2011.07.143.

[56]   Pei Y, Mehl M, Liu W, Lu T, Pitz WJ, Som S. A multicomponent blend as a diesel fuel surrogate for compression ignition engine applications. J Eng Gas Turbines Power 2015;137:1–9. doi:10.1115/1.4030416.

[57]   Mendez S, Thirouard B. Using multiple injection strategies in diesel combustion: Potential to improve emissions, noise and fuel economy trade-off in low CR engines. SAE Int J Fuels Lubr 2009;1:662–74. doi:10.4271/2008-01-1329.

PAPER 5

Numerical Modeling of Laminar Flame Speed and Autoignition Delay Using General Fuel-Independent Function

Filip Jurić[a], Marko Ban[b], Peter Priesching[c], Carsten Schmalhorst[d], Neven Duić[a], Milan Vujanović[a, *]

[a] University of Zagreb, Faculty of Mechanical Engineering and Naval Architecture, Ivana Lučića 5, 10000 Zagreb, Croatia

[b] SDEWES Centre, Ivana Lučića 5, 10000 Zagreb, Croatia

[c] AVL List GmbH, Alte Poststraße 152, 8020 Graz, Austria

[d] AVL Deutschland GmbH, Frankfurter Ring 213, 80807 Munich, Germany

[*] Corresponding author e-mail: milan.vujanovic@fsb.hr

ABSTRACT

The impact of the transport sector on climate change and carbon dioxide emissions into the atmosphere can be decreased by the utilization of biofuels and e-fuels. The chemical kinetics for calculating the combustion process of new biofuels and e-fuels is often excessively computationally demanding for numerical simulations, leading to the development and employment of combustion models, such as flamelet models. Such models require precalculated data of laminar flame speed and autoignition timing. The developed procedure in this work scrutinizes available reaction mechanisms of several fuels with the validation against existing experimental data of autoignition and laminar flame velocities, aiming for the generation of lookup databases. The autoignition of fuel/air mixtures for different conditions is pre-tabulated from nondimensional calculations of constant pressure reactor. Simultaneously, the laminar flame speed is pre-tabulated from premixed freely propagating reactors, for which calculation chemical kinetics software are applied. The ignition delay of cold flame and primary ignition was calculated using inflection point criteria implemented in the proposed method. The developed imputations method is based on the lognormal distribution for laminar flame speed in equivalence ratio direction and exponential functions for pressure, temperature, and exhaust gas recirculation directions. The laminar flame speed and autoignition databases generation procedure was demonstrated on prospective e-fuel three-oxyethylene dimethyl ether (OME-3) fuel by validating the available mechanism against the experimental data. Finally, the generated

databases are implemented into the computational fluid dynamics software and verified with the detailed chemical mechanism of OME-3 fuel.

KEYWORDS

Laminar flame speed; autoignition; flamelet model; chemical kinetics; combustion; e-fuels

1. INTRODUCTION

One way to mitigate the transport sector's impact on climate change and carbon dioxide emissions into the atmosphere is the utilization of biofuels and e-fuels in the transport sector [1]. Therefore, the implementation of biofuels [2] and e-fuels [3] in conventional internal combustion engines is of great importance to accelerate the transition of the transport sector to renewable energy sources. One approach to achieving greener transport [4] and the energy sector [5] is the application of biofuels. The impact on the generation of emissions such as nitrogen oxides is still not fully explored. Therefore, numerous researches are conducted to obtain biofuel impact on emissions when they substitute conventional fuel in existing combustion systems [6]. Other modern approaches are the implementation of alternative fuels, such as ammonia and its blends with natural gas [7], synthesized kerosine from coal [8], and gasoline substitutes like ethanol in passenger car engines [9] and marine engines[10], and toluene reference fuel [11].

There are already numerous biofuels and e-fuels, some similar and some less to conventional petrol and diesel fuels, but each with different physical properties, chemistry kinetics, and combustion characteristics [12]. In order to predict the fuel combustion under different fuel/air mixtures, loads, and temperatures, Computational Fluid Dynamics (CFD) with the chemical kinetics or combustion models are commonly employed [13]. The chemical kinetics is often too computationally demanding for numerical simulations, leading to the frequent use of combustion models, such as coherent flame models [14]. In coherent flame models, ignition delay and laminar flame velocities for different operating conditions must be precalculated in the form of a database or correlation formula [15]. The standard correlations for new biofuels and e-fuels are not accurate enough to validate their combustion process, primarily the low-temperature auto-ignition phenomenon [16]. In [17], the correlation functions between autoignition timing and flame speed propagation were developed based on the temperature gradients measured from the rapid compression.

Correlation functions for the autoignition of biodiesel fuels that feature ignition of fuel-air mixtures at high temperatures and their validation with the chemistry kinetic mechanisms were presented by the authors in [18], where the excellent agreement between the previously published mechanism was achieved. The dependency of autoignition timing and pollutant emissions results was demonstrated in [19], where the convenient diesel fuels with some percentage of biodiesel were observed at high-temperature conditions. The investigation results are that the rise in the ambient temperature lowers the ignition delay for all diesel fuel, which was expected. Recent publications have also investigated the investigation of biodiesel fuels produced by different sources [20]. For example, the autoignition delay of microalgae biodiesel blends was investigated numerically to determine combustion efficiency and pollutant emissions [21]. Additionally, an experimental autoignition investigation of biodiesel produced from the plant oil and its impact on the combustion process inside a compression ignition engine was observed [22]. The results showed that the biodiesel blend at 20% of the content exhibited better combustion performance and emission characteristics than other blend proportions.

In [23], the authors performed an experimental optical study of biodiesel ignition delay, where the correlation between autoignition timing and combustion process was demonstrated. A similar approach for determining the influence of pollutant concentrations of nitrogen oxides and carbon monoxide on autoignition timing under different exhaust gas recirculation (EGR) mass fractions was examined by the authors [24], where the diesel fuel with a small share of biodiesel was used. For the internal combustion engine operating conditions, a numerical method named spherically expanded flames was used to determine the autoignition and laminar flame speed propagation for a different share of e-fuel (dimethyl-ether), air, and helium [25]. The simulation results adequately captured the physics of unsteady flame propagation, autoignition, and the controlling reactions, but not at the early ignition stages.

Lately, the penetration of machine learning techniques has accelerated enormously in all science areas, so in this area too. Rahnama et al. [26] proposed the machine learning neural network for fuel consumption reduction in internal combustion engines, where the start of injection and its influence on autoignition timing was observed. Deep neural networks for internal combustion engines were also employed to determine emissions from the biodiesel combustion process [27]. In [28], the authors published the results of dual-fuel autoignition, which were predicted by the machine learning technique. The sensitivity analysis showed that the fuel ratio between the primary and secondary fuels has the most significant effect on dual-fuel ignition. Furthermore, an exciting approach, similar to the developed procedure in this work, was published by the authors of [29], where the calculation of the autoignition and

laminar flame speed was modeled by ignition to propagation reduced scheme, which was upgraded to additionally calculate the autoignition timing. Another approach that aims to obtain laminar flame speed with general formula is presented in [30]. The authors introduced a term that depends on polynomial, exponential factors, with additional constant defined from the precomputed database. Additionally, the same procedure was applied for obtaining ethanol/gasoline blends databases, where high accuracy in correlation is achieved [31]. Other researchers tend to determine laminar flame speed correlations for a single fuel. In [32], the authors proposed correlation functions for surrogate gasoline fuels as an exponential function in temperature and pressure direction. An exceptional scientific contribution was conducted to developing correlation functions of hydrogen fuel for spark ignition operating conditions [33]. Furthermore, additional research has been undertaken to develop correlation functions capable of describing hydrogen mixture with gasoline [34] and methanol [35] for combustion inside spark-ignition engines.

In this work, the effects of complex chemistry kinetics are reproduced by developing efficient database creation consisting of the relevant ignition data used by existing combustion models. In the pre-processing stage, available reaction mechanisms of several fuels were investigated and validated against existing experimental data of autoignition and laminar flame velocities. The autoignition of fuel/air mixtures for different conditions is pre-tabulated from nondimensional constant pressure reactor calculation. At the same time, the laminar flame speed is pre-tabulated from premixed freely propagating reactors, for which the LOGEsoft™ and Cantera open-source software were used. The ignition delay of cold flame and main ignition was calculated using the inflection point criteria presented in [35] and implemented in the proposed method. The data imputation and extrapolation method was developed as a general fuel-independent function. The nonlinear least squares algorithm was employed to fill the unsuccessfully calculated points of databases in the post-processing.

In this work, the novel general, fuel-independent procedure is developed and implemented into CFD software based on the lognormal distribution for laminar flame speed in equivalence ratio direction and exponential functions for pressure, temperature, and exhaust gas recirculation directions. Three parameters are used to determine the dependence of the laminar flame speed or autoignition results on pressure and equivalence ratio directions. Additionally, the method is also applicable to dual-fuel combustion. The ignition delay and laminar flame speed values of fuel blends are described with the additional parameter of the fuel composition. Finally, the database implementation is verified with the detailed chemical mechanism of complex internal

combustion operating case in computational fluid dynamics and validated with experimental data.

2. MATHEMATICAL MODEL

In this section, the mathematical model for calculating the correlation function and models used in the validation and verification are presented. For chemistry calculation, commercial LOGEsoft™ and Cantera open-source software were used, while for CFD simulation AVL FIRE™ was used.

2.1. Laminar flame speed

For the definition of the correlation function of the laminar flame speed points, firstly, the calculation on chemistry solvers was performed. The chemistry solver calculations were defined with the four-dimensional grid: temperature, pressure, equivalence ratio, and EGR. The calculations were performed on premixed freely propagating reactors, where each combination of four previously mentioned parameters was calculated as a separated reactor. The raw calculated data were sorted in the five-dimensional matrix, on which the correlation function is performed. Figure 1 shows the procedure of the developed method for the generation of a laminar flame speed database for the coherent flame models.
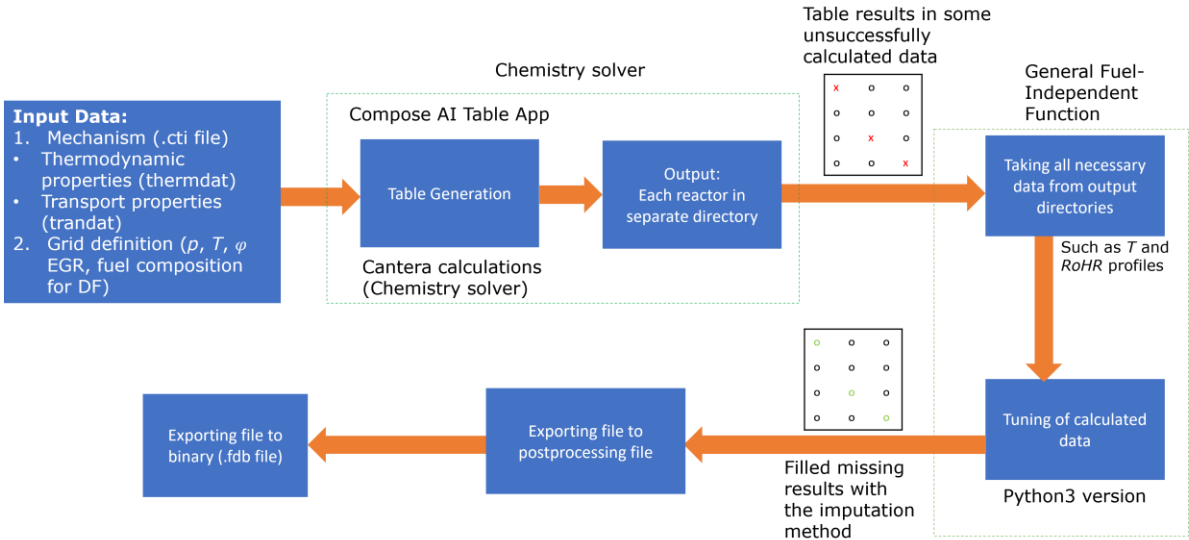
Figure 1   Flowchart of the developed procedure for generation of laminar flame speed and autoignition databases

The correlation function was tuned for calculated data, which was defined as the lognormal distribution for equivalence ratio (φ) and as the exponential function for the pressure (p) direction. The tuning equation has the following form:

$$S_L(p, \varphi) = S_{L,ref} \left[\frac{1}{\varphi \sigma \sqrt{2\pi}} \exp\left(-\frac{(\ln \varphi - \mu)^2}{2\sigma^2} \right) \right] \left(\frac{p}{p_{ref}} \right)^{\beta} \tag{1}$$

where μ and σ are two tuning parameters that are calculated for each combination of the temperature and EGR. For the calculation of μ and σ parameters that have the lowest disagreement with the raw computed data, the nonlinear least-squares method was employed with the Levenberg-Marquardt algorithm. p_{ref} is reference pressure of 0.1 MPa, while $S_{L,ref}$ is referent laminar flame speed at selected calculated point, which was in this case at equivalence ratio 1, and pressure 0.1 MPa. The algorithm was based on SciPy open-source package and its function scipy.optimize.least_squares that accounts for the optimized parameters of general function for each temperature point. In order to obtain the optimized parameters, the objective function is defined as:

$$f_{S_L} = \min \sum_{i=1}^{m} \left[S_{L_i} - S_L(p_i, \varphi_i) \right]^2 \tag{2}$$

where S_{L_i} is the calculated laminar flame speed from the chemistry solver, and m is the number of points used for obtaining the formula of laminar flame speed. The objective function is approximated by the linearization in each iteration step. The φ is changed with the estimation $\varphi + \delta$, and to determine δ the following term has to be calculated:

$$f_{S_L} \approx S_L(p_i, \varphi_i + \delta) + \frac{\partial S_L(p_i, \varphi_i)}{\partial \varphi} \delta \tag{3}$$

2.2. Autoignition timing

For the definition of the correlation function of the autoignition points, firstly, the calculation on chemistry solvers was performed. The chemistry solver calculations were also defined with the four-dimensional grid, where the parameters were temperature, pressure, equivalence ratio, and EGR, the same as in the laminar flame speed calculations. The calculations were performed on

nondimensional, perfectly stirred reactors, where each combination of four previously mentioned parameters was calculated as a separated reactor. The raw calculated data were sorted in the eight-dimensional matrix, where the four additional output parameters were autoignition timing, cold flame autoignition timing, released heat, and heat released by cold flame. The procedure of the developed method for generating the autoignition (τ) database is similar to the laminar flame speed database for the coherent flame models.

$$\tau(p, \varphi) = \tau_{ref} \left(\frac{p}{p_{\text{ref}}}\right)^{\alpha} (\varphi)^{\beta} \tag{4}$$

where α and β are two tuning parameters calculated for each combination of the temperature and EGR. For the calculation of α and β parameters that have the lowest disagreement with the raw calculated data, the nonlinear least-squares method was employed with the Levenberg-Marquardt algorithm. The objective function is defined as

$$f_\tau = \min \sum_{i=1}^{m} [\tau_i - \tau(p_i, \varphi_i)]^2 \tag{5}$$

Where the objective function is approximated by the linearization in each iteration step. The φ is changed with the estimation $\varphi + \delta$, and to determine δ the following term has to be calculated:

$$f_\tau \approx \tau(p_i, \varphi_i + \delta) + \frac{\partial \tau(p_i, \varphi_i)}{\partial \varphi} \delta \tag{6}$$

As in the case of the laminar flame speed algorithm was set to bisquare robust regression.

2.3. Coherent flame model – ECFM-3Z

An alternative to modeling combustion via chemical kinetics is using a coherent flame model suitable for simulating combustion inside diesel engines. One of such models is the extended coherent flame model in 3 zones (ECFM-3Z). It has a decoupled treatment of chemistry and turbulence [36].

In the model, the following equation is solved for the flame surface density Σ:

$$\frac{\partial \Sigma}{\partial t} + \frac{\partial}{\partial x_j}(\bar{u}_j \Sigma) - \frac{\partial}{\partial x_j}\left(\frac{v_t}{Sc_t}\frac{\partial \Sigma}{\partial x_j}\right) = S_\Sigma \tag{7}$$

where t is time, x_j are Cartesian coordinates, $\bar{u}_j$ is averaged velocity in Cartesian coordinates, v_t is the turbulent kinematic viscosity, Sc is unidimensional Schmidt number, and S_Σ is the source term in which laminar flame speed contribution is added through three phenomena, flame propagation, flame destruction and flame straining. In the model, transport equations for the following species are solved: O_2, N_2, NO, CO_2, CO, H_2, H_2O, O, H, N, OH:

$$\frac{\partial \bar{\rho} \tilde{Y}_X}{\partial t} + \frac{\partial \bar{\rho} \tilde{u}_i \tilde{Y}_X}{\partial x_i} = \frac{\partial}{\partial x_i}\left(\left(\frac{\mu}{Sc} + \frac{\mu_t}{Sc_t}\right)\frac{\partial \tilde{Y}_X}{\partial x_i}\right) + \bar{\dot{\omega}}_X \tag{8}$$

Where $\bar{\dot{\omega}}_X$ is the average combustion source term and $\tilde{Y}_X$ is the average mass fraction of species X, while $\bar{\rho}$ is averaged density. The fuel is divided into two parts: the unburned ($\tilde{Y}_{Fu}^u$) and burned ($\tilde{Y}_{Fu}^b$) fuel. For both of them, additional transport equations are solved:

$$\frac{\partial \bar{\rho} \tilde{Y}_{Fu}^u}{\partial t} + \frac{\partial \bar{\rho} \tilde{u}_i \tilde{Y}_{Fu}^u}{\partial x_i} = \frac{\partial}{\partial x_i}\left(\left(\frac{\mu}{Sc} + \frac{\mu_t}{Sc_t}\right)\frac{\partial \tilde{Y}_{Fu}^u}{\partial x_i}\right) + \bar{\rho}\tilde{S}_{Fu}^u + \bar{\dot{\omega}}_{Fu}^u - \bar{\dot{\omega}}_{Fu}^{u \to b} \tag{9}$$

$$\frac{\partial \bar{\rho} \tilde{Y}_{Fu}^b}{\partial t} + \frac{\partial \bar{\rho} \tilde{u}_i \tilde{Y}_{Fu}^b}{\partial x_i} = \frac{\partial}{\partial x_i}\left(\left(\frac{\mu}{Sc} + \frac{\mu_t}{Sc_t}\right)\frac{\partial \tilde{Y}_{Fu}^b}{\partial x_i}\right) + \bar{\rho}\tilde{S}_{Fu}^b + \bar{\dot{\omega}}_{Fu}^b + \bar{\dot{\omega}}_{Fu}^{u \to b} \tag{10}$$

where $\tilde{S}_{Fu}^u$ is a source term representing fuel evaporation. $\bar{\dot{\omega}}_{Fu}^u$ and $\bar{\dot{\omega}}_{Fu}^b$ represent oxidation of (un)burned fuel, while $\bar{\dot{\omega}}_{Fu}^{u \to b}$ represents fuel mass transfers between various zones. μ and μ_t are laminar and turbulent dynamic viscosity.

The combustion area can be divided into three zones: a pure fuel zone, a pure air plus possible EGR zone, and mixed air and fuel zone. The model describes autoignition and premixed and diffusion flames. A schematic showing these zones is shown in Figure 2 [37].
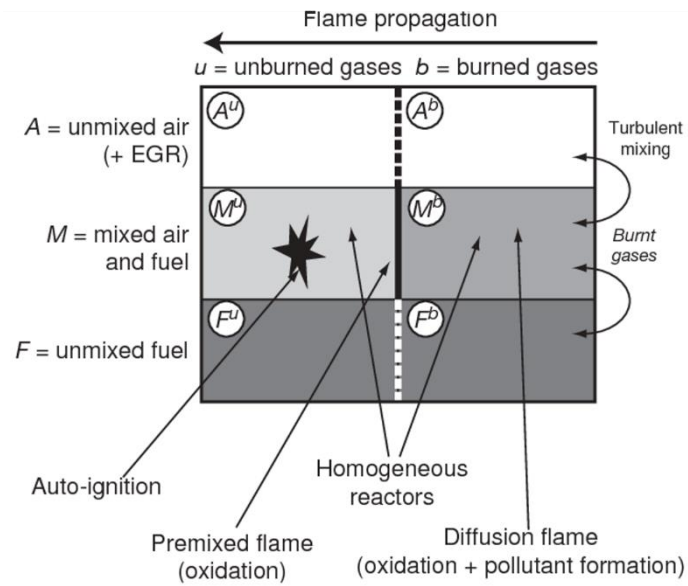
Figure 2   Schematic of the ECFM-3Z model cell [37]

3. VALIDATION

For the validation of the calculated data from chemistry solvers, four mechanisms of e-fuel OME-3 were compared with the experimental data: Cai et al. [16], Ren et al. [38], Sun et al. [39], and Lin et al. [40]. Figure 3 shows the calculated laminar flame results at a pressure of 0.1013 MPa and temperature of 408 K, and with four previously mentioned chemical mechanisms, where good agreement was achieved with all data.

9
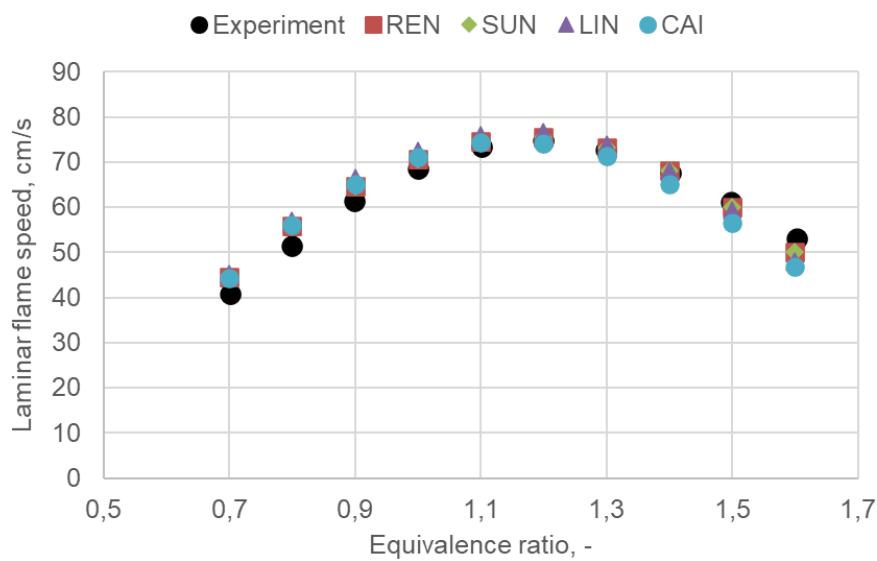
For the exact mechanism, the validation of results was performed on the autoignition results, where the best agreement with experimental data was achieved with the Lin et al. mechanism. The autoignition results were performed in Figure 4, where the results are shown at the pressure of 2 MPa for equivalence ratio values of 0.5, 1.0, and 2.0. The experimental autoignition results are taken from [16]. According to the performed validation, the Cai et al. chemical mechanism was selected to further investigate the correlation function since it features the highest number of chemical reactions and chemical species.
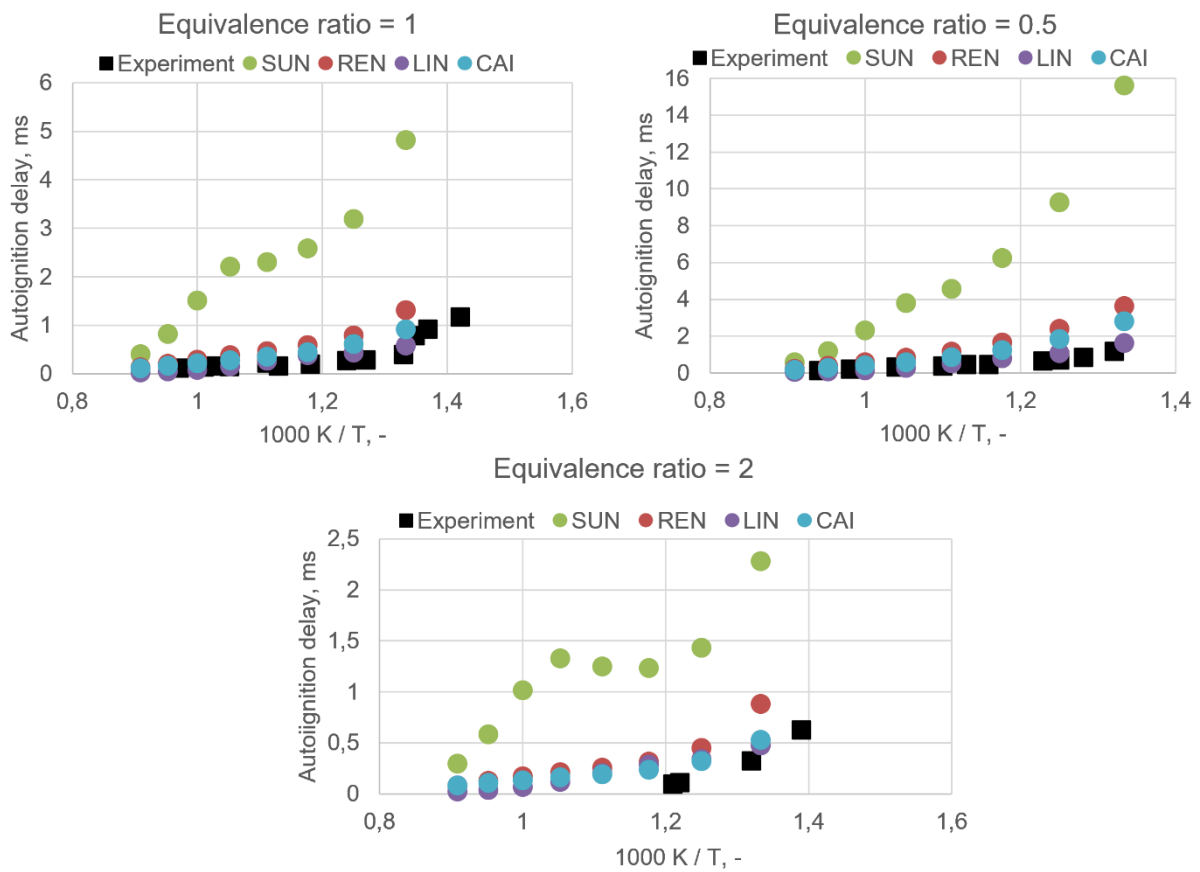
Figure 4   Comparison of calculated autoignition data with four chemical mechanisms and
experimental data at 2 MPa for equivalence ratios: 0.5, 1.0 and 2.0

4. NUMERICAL SETUP

This chapter presents the numerical setup of the verification case for generated laminar flame speed and autoignition tables of OME-3 fuel. The verification case was performed on Volvo I5D engine, for which the detailed description of mesh dependency is available in [13]. The engine and injector data are shown in Table 1.

Table 1 Engine and injector specifications

Engine data	
Bore	81 mm
Stroke	93.15 mm
Connecting rod length	147 mm
Compression ratio	16.5 : 1
Displacement	2.4 dm^3
Number of cylinders	5
Injector data	
Number of nozzle holes	7
Spray cone angle	145°
Flow rate (at 100 bar Δp)	440 cm^3 / 30 s
The shape of the nozzle dome	Micro Sac

The calculation of a moving computational mesh shown in Figure 5 was generated with the defined boundary selections. Due to the cyclic symmetry, the computation mesh is the cylinder part that features a single nozzle hole. Mesh details, like volume and number of cells, are given in Table 2. In Table 3, the boundary conditions of the engine operating cases are shown.
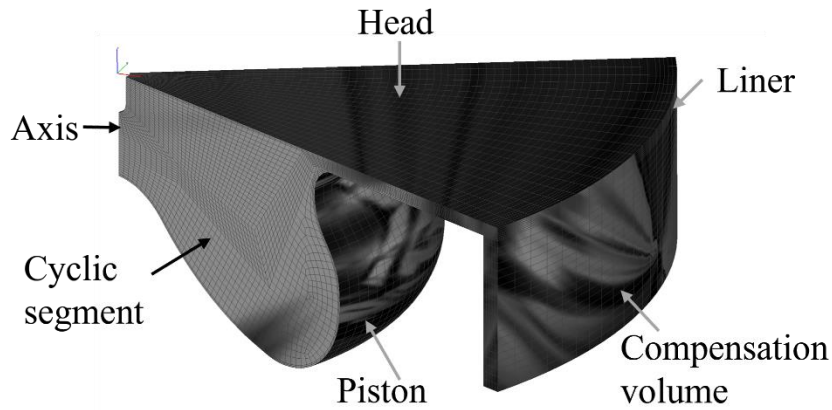
Figure 5   Boundary selections of the computational mesh

Table 2 Mesh details

	Top Dead Centre	Bottom Dead Centre
Volume, cm^3	4.67	75.88
Number of cells	54 663	112 854

Table 3 Boundary conditions for the verification operating case

Face selection	Boundary Condition
Piston	Type: Wall Temperature: 473 K
Liner	Type: Wall Temperature: 423 K
Axis	Type: Symmetry
Segment	Type: Inlet/Outlet
Compensation volume	Type: Wall, Mesh movement
Head	Type: Wall Temperature: 443 K

In Table 4, injection parameters for two observed operating cases are shown. Two cases that feature single and multi-injection strategies are selected in order to prove the capability of valid autoignition and combustion process modeling for both modeling strategies.

Table 4 Injection parameters for the verification operating cases

	Multi injection	**Single injection**
Injected mass	0.4, 0.4, 5.8, 0.8 mg	4.12 mg
Injection timing	683.9 - 740.7 °CA	718.2 - 731.3 °CA

For the time discretization, an automatic time step was used, where the maximum value of the local CFL number was set to 1. For the calculation of the spray process, the Euler Lagrangian model was used [41], with the Wave breakup model [42] and Abramzon evaporation model [43]. The CFD verification simulations are performed using the AVL AST software package, which has implemented the ECFM-3Z model and detail chemistry solvers. In Table 5, the grid definition of generated lookup databases for CFD implementation is given.

Table 5 Grid definition for laminar flame speed and autoignition timing databases

Laminar flame speed	**Grid points**
Temperature, K	300, 400, 500, 600, 700, 800, 900, 1000, 1100, 1250
Pressure, MPa	0.1, 0.2, 0.5, 1, 2, 5, 10, 15, 20, 25, 30
Equivalence ratio, -	0.2, 0.4, 0.6, 0.8, 0.9, 1, 1.1, 1.2, 1.4, 1.6, 1.8, 2, 3, 4, 5
EGR, -	0, 0.2, 0.4, 0.6
Autoignition	**Grid points**
Temperature, K	600, 620, …, 740, 760, 800, 840, …, 1400, 1440, 1500
Pressure, MPa	0.1, 0.2, 0.5, 1, 2, 5, 10, 15, 20, 25, 30
Equivalence ratio, -	0.2, 0.4, 0.6, 0.8, 0.9, 1, 1.1, 1.2, 1.4, 1.6, 1.8, 2, 3, 4, 5
EGR, -	0, 0.1, 0.2, 0.3, 0.4, 0.5, 0.6, 0.7, 0.8

5. RESULTS AND DISCUSSION

In this section, the results of the developed correlation functions and calculated data were compared on three-dimensional and two-dimensional diagrams. Figure 6 shows the calculated and tuned laminar flame speed results with the correlation function in Equation (1) at 1100 K with Cai et al. chemical mechanism. The a) diagram of Figure 6 shows the surface of raw data calculated from the chemistry solver, which is tuned with the correlation function, and where the results at the b) diagram of Figure 6 are obtained.
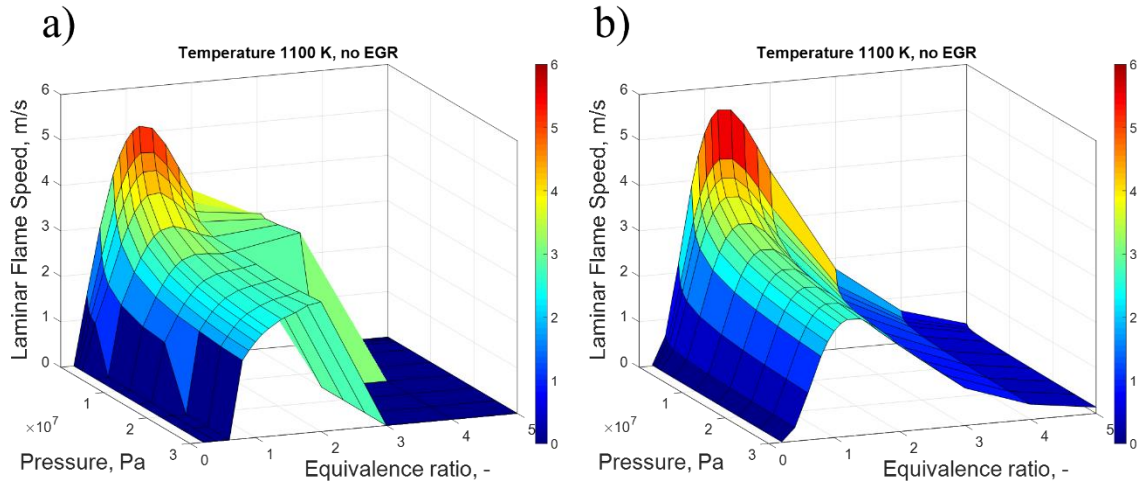
Figure 6   Calculated chemistry solver results (a) and laminar flame speed results with the correlation functions (b) at 1100K

Figure 8 shows the calculated results from the chemistry solver used as input to obtain the shape of laminar flame speed data and the shape obtained by the correlation function procedure on four parameters: temperature, equivalence ratio, pressure, and EGR mass fraction. The calculated laminar flame speed data is shown as the black dots, while the surface shows the results with the correlation function in Equation (1). From Figure 8**Error! Reference source not found.**, a good trend is achieved between calculated results and the results obtained from the general function approach. For the highest temperature, 1250 K, only 6 points are obtained from chemistry solver reactions, compared to the lower temperatures where the chemistry solver is more stable. The general function approach shows a robust extrapolation solution for such cases since it only needs 3 points to determine the whole laminar flame speed shape in pressure and equivalence ratio directions. In Figure 8, the same results for different pressure values. It can be seen that the agreement between the general function approach and calculated data using the conventional Gülder approach for extrapolation [44] is better for the lean mixtures and around the stoichiometric equivalence ratio. At the same time, a more significant discrepancy was achieved for the fuel-rich region.

Figure 9 shows the same results as in Figure 7 for temperature of 800 K, at different pressure values. Additionally, the number of successfully calculated data from the chemistry solver (red circles) is reduced with pressure and equivalence ration increase. Nevertheless, as shown, the general function method shows good robustness with fewer obtained points. Additionally, the method was also validated against calculated laminar flame speeds at different EGR values in Figure 10. With increased EGR, a more significant discrepancy with chemistry solver data is

obtained, which has unexpectedly high values in fuel rich regions. Such high values can also be attributed to the drawback of a chemical mechanism not intended to calculate the laminar flame speed for such conditions or to chemistry solver converging deficiency.
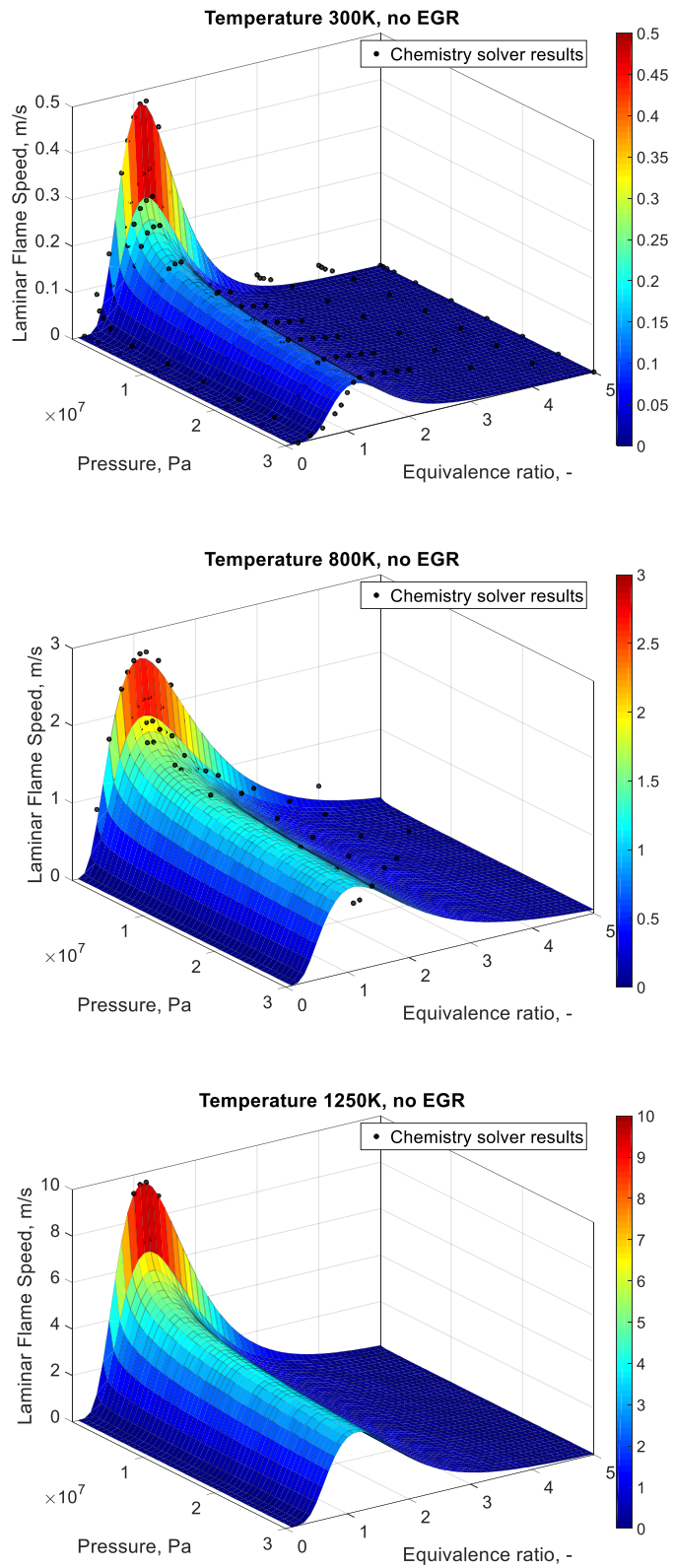
Figure 7   Lminar flame speed results with the correlation functions at 300, 800 and 1250 K and without EGR
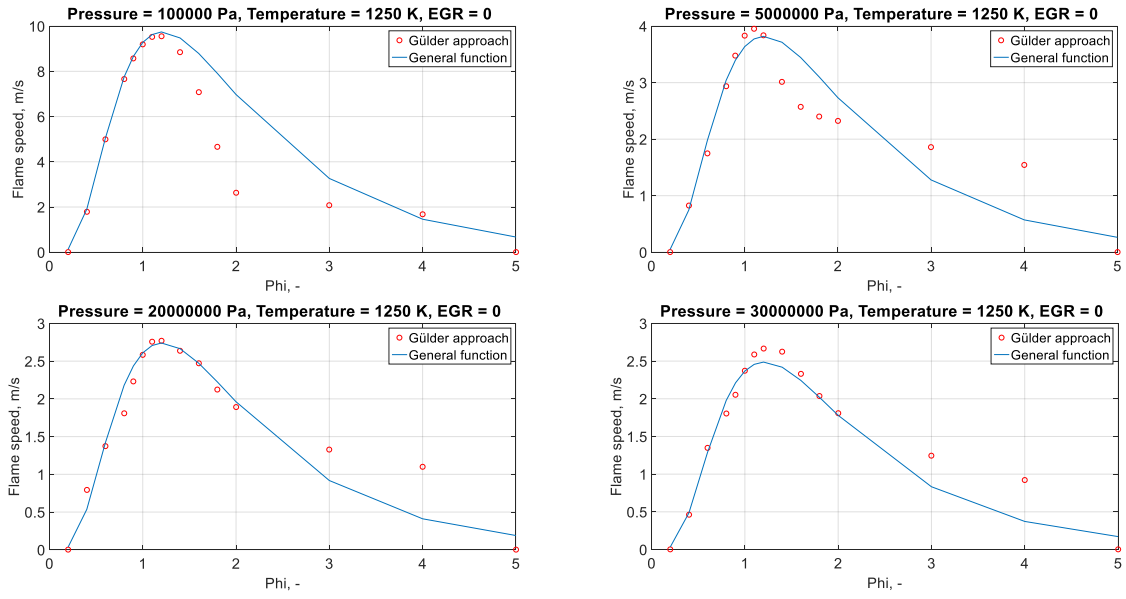
Figure 8   Calculated results with Gülder approach and laminar flame speed results with the correlation function at 1250 K
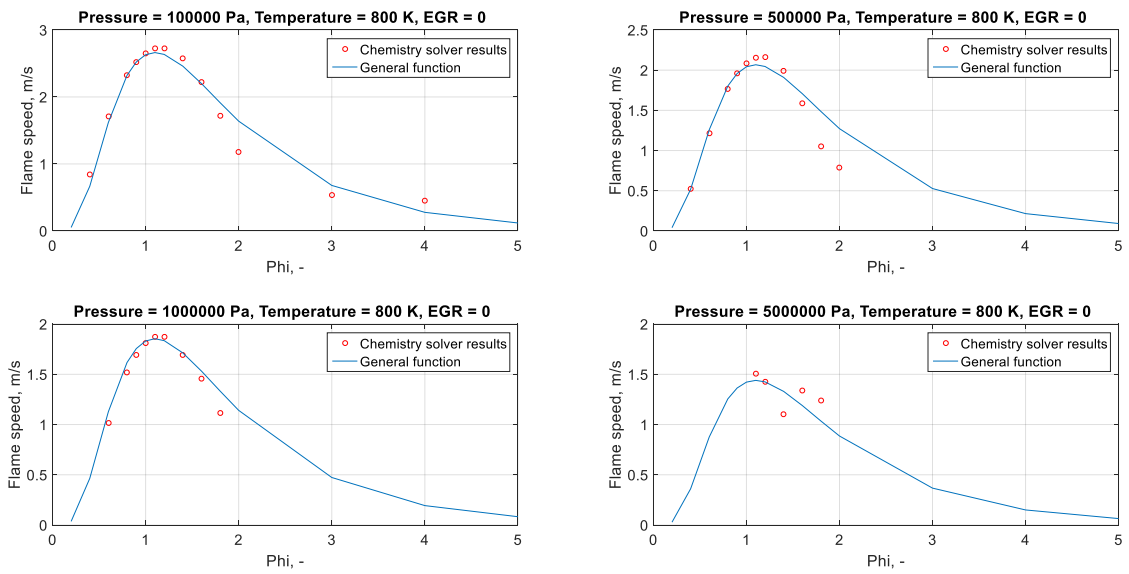
Figure 9   Chemistry solver results and laminar flame speed results with the correlation function at 800 K
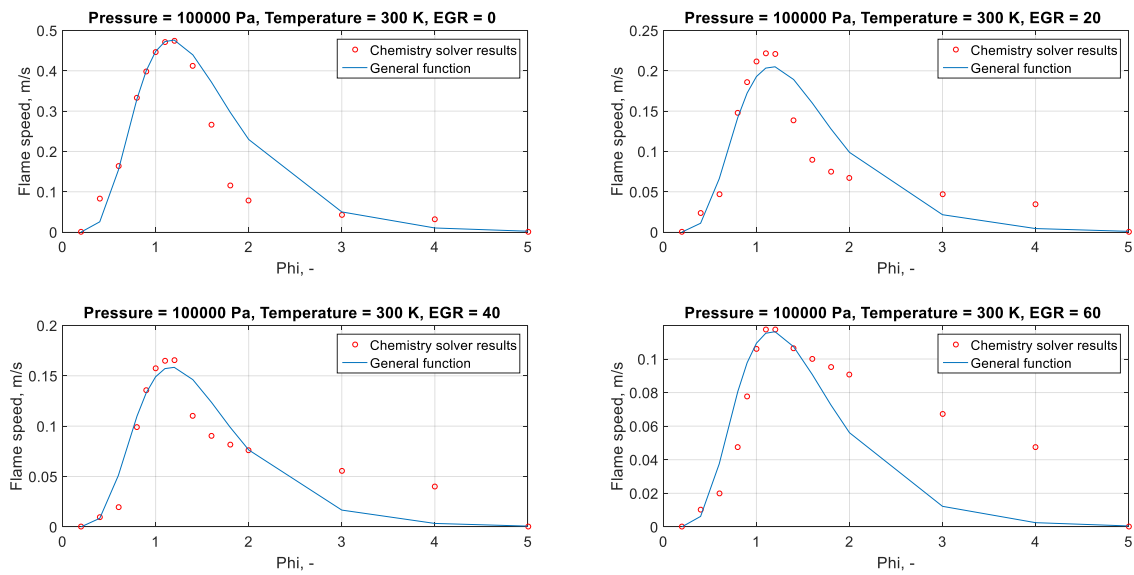
Figure 10　Chemistry solver results and laminar flame speed results with the correlation function at different EGR values

Figure 11 shows the coefficient of determination (R^2) values between the chemistry solver results and general function at different temperatures and EGR values. It can be seen that the best agreement between chemistry solver results and general function is obtained around 500 K. the correlation decreases markedly with the increase of EGR and at high temperatures.
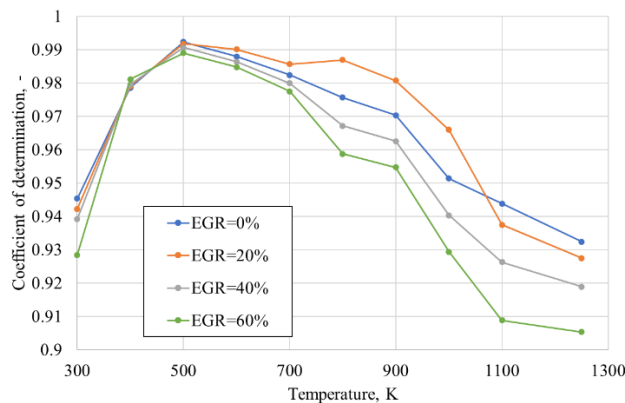
Figure 11　Coefficient of determination values between chemistry solver results and general function for different temperature and EGR values

Error! Reference source not found. Figure 12 shows the calculated and tuned laminar flame speed results with the correlation function in Equation (4) with Cai et al. chemical mechanism. For most autoignition delay time representation, a logarithmic scale is used in order to emphasize that

the order of magnitude is sufficient for valid autoignition modeling. In Figure 12, the linear scale emphasizes a good agreement with the chemistry solver results at temperatures 1000 K and 1200 K.
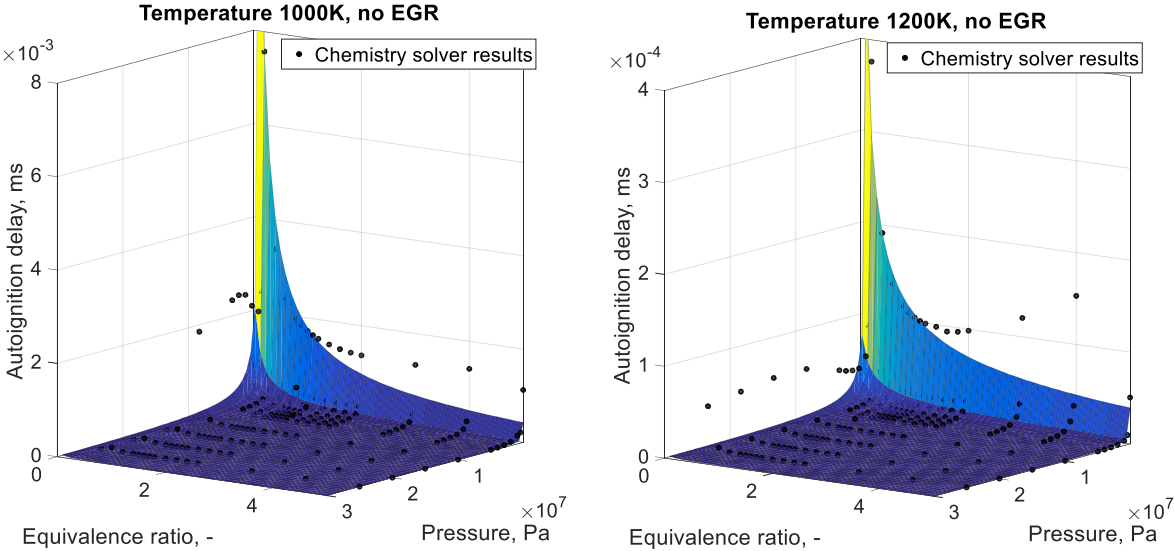
Figure 12   Calculated (black dots) and autoignition timing results with the correlation functions without EGR at 1000 and 1200 K

Figure 13 shows the same results as Figure 12 for 2D cuts at different pressure values. It can be seen that the agreement between the calculated data and obtained results is better for the points around the stoichiometric equivalence ratio and around the fuel-rich region. In contrast, additional efforts are required for the lean air-fuel mixtures and the fuel-rich region at higher pressures.
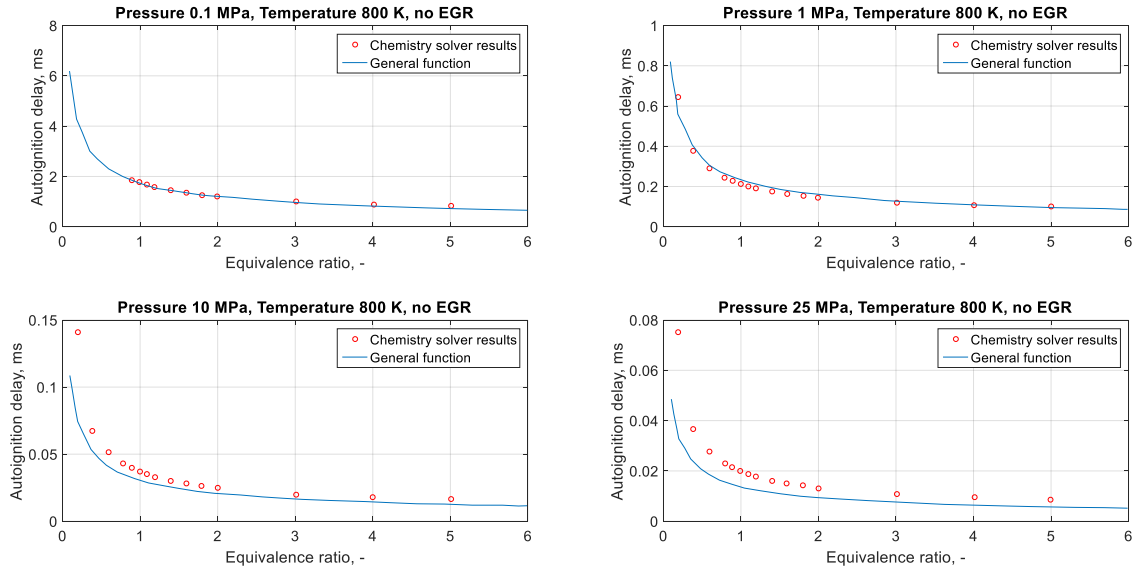
Figure 13   Chemistry solver results and autoignition results with the correlation function

In section 4., the operating conditions and numerical setup for the calculation are presented, for which the results are shown. The performed engine operating point features a multi-injection strategy of four separate injections, where the OME-3 fuel was injected at 20 °C. Figure 14 compares the most detailed chemistry mechanism of OME-3 fuel, Cai et al., and ECFM-3Z combustion model with implemented autoignition and laminar flame speed databases for two operating injection strategies shown in Table 4. A good trend was achieved for the temperature results, while the ignition timing was slightly delayed for the simulation of ECFM-3Z. That can also be attributed to the autoignition parameter for ECFM-3Z calculation, which was not calibrated but used as a default value of 1. The same ignition delay is observed for the rate of heat release results, while the peak of released heat is achieved with the same value. As seen from RoHR diagram, ECFM-3Z combustion is not so pronounced as with Cai et al. For the late-stage combustion, the biggest discrepancy is achieved, which can be mainly attributed to the simplified chemistry in the combustion model does not account for such detailed carbon-based reactions. A better agreement is reached for the single injection case than in a multi injection strategy with four different injections, which calculates autoignition delay based on the whole chemistry reactions rather than on interpolated conditions based on four parameters from the generated database. The ECFM-3Z in combination with the developed method for database generation of autoignition and laminar flame speed has correctly described the ignition of each injection and its ignition and combustion process with significantly simpler chemistry and decreased computational demand. The computational discrepancy between the ECFM-3Z model and Cai et al. mechanism can be attributed mainly to the simplified chemistry description in the ECFM-3Z model, which accounts

20

for transport equations for a dozen chemical species. In contrast, Cai accounts for transport equations for 322 chemical species. Finally, the computational time was decreased approximately 20 times with the ECFM-3Z model.

Figure 14   Comparison of temperature and rate of heat release results between detailed chemistry mechanism by Cai et al. and ECFM-3Z combustion model

6. CONCLUSIONS

The procedure of general functions for the generation of databases required for combustion modeling in the coherent flame models is developed in this work. The procedure is general and applicable to every fuel, and this work was mainly focused on the generation of laminar flame speed and autoignition databases for OME-3 fuel. Additionally, the developed procedure showed a good potential for reducing the number of required grid points since a reasonable agreement can be achieved with a few calculated points around stoichiometric values of equivalence ratio. The procedure validation was performed on generated laminar flame speed and autoignition database for OME-3 fuel, where a good agreement was achieved compared to the available experimental results. For the engine operating cycles, verification was made compared to the most detailed

chemistry mechanism available in the literature, Cai et al. The verification results showed a great agreement in the trend and autoignition timing between mean in-cylinder temperature and rate of heat release curves for both single and multi injection strategy. In combination with coherent flame models, the developed method represents a robust and computationally low demanding procedure for accurate ignition and combustion process calculations of new biofuels and e-fuels. Although not presented in this work, the procedure was also developed for fuel blends, dual fuel, and multiple fuel combustion, where the additional fuel composition parameter was added as the fifth grid parameter. Therefore, the future work investigates the obtained databases for dual fuel and the impact of generated databases on the whole operating cycle in CFD software.

REFERENCES

[1]   Stančin H, Mikulčić H, Wang X, Duić N. A review on alternative fuels in future energy system. Renew Sustain Energy Rev 2020;128:109927. doi:10.1016/j.rser.2020.109927.

[2]   E J, Pham M, Zhao D, Deng Y, Le DH, Zuo W, et al. Effect of different technologies on combustion and emissions of the diesel engine fueled with biodiesel: A review. Renew Sustain Energy Rev 2017;80:620–47. doi:10.1016/j.rser.2017.05.250.

[3]   Hänggi S, Elbert P, Bütler T, Cabalzar U, Teske S, Bach C, et al. A review of synthetic fuels for passenger vehicles. Energy Reports 2019;5:555–69. doi:10.1016/j.egyr.2019.04.007.

[4]   Hossain A, Smith D, Davies P. Effects of Engine Cooling Water Temperature on Performance and Emission Characteristics of a Compression Ignition Engine Operated with Biofuel Blend. J Sustain Dev Energy, Water Environ Syst 2017;5:46–57. doi:10.13044/j.sdewes.d5.0132.

[5]   Bešenić T, Mikulčić H, Vujanović M, Duić N. Numerical modelling of emissions of nitrogen oxides in solid fuel combustion. J Environ Manage 2018;215:177–84. doi:10.1016/j.jenvman.2018.03.014.

[6]   Zhang Y, Zhong Y, Wang J, Tan D, Zhang Z, Yang D. Effects of Different Biodiesel-Diesel Blend Fuel on Combustion and Emission Characteristics of a Diesel Engine. Processes 2021;9:1984. doi:10.3390/pr9111984.

[7]   Mikulčić H, Baleta J, Wang X, Wang J, Qi F, Wang F. Numerical simulation of ammonia/methane/air combustion using reduced chemical kinetics models. Int J Hydrogen Energy 2021;46:23548–63. doi:10.1016/j.ijhydene.2021.01.109.

[8]   Geng L, Li S, Xiao Y, Xie Y, Chen H, Chen X. Effects of injection timing and rail pressure on combustion characteristics and cyclic variations of a common rail DI engine fuelled with F-T diesel synthesized from coal. J Energy Inst 2020;93:2148–62. doi:10.1016/j.joei.2020.05.009.

[9]   Dirrenberger P, Glaude PA, Bounaceur R, Le Gall H, da Cruz AP, Konnov AA, et al. Laminar burning velocity of gasolines with addition of ethanol. Fuel 2014;115:162–9. doi:10.1016/j.fuel.2013.07.015.

[10]   Davis GW. Addressing Concerns Related to the Use of Ethanol-Blended Fuels in Marine Vehicles. J Sustain Dev Energy, Water Environ Syst 2017;5:546–59. doi:10.13044/j.sdewes.d5.0175.

[11]   Di Lorenzo M, Brequigny P, Foucher F, Mounaïm-Rousselle C. Validation of TRF-E as gasoline surrogate through an experimental laminar burning speed investigation. Fuel 2019;253:1578–88. doi:10.1016/j.fuel.2019.05.081.

[12]   Hidegh G, Csemány D, Vámos J, Kavas L, Józsa V. Mixture Temperature-Controlled combustion of different biodiesels and conventional fuels. Energy 2021;234:121219. doi:10.1016/j.energy.2021.121219.

[13]   Jurić F, Stipić M, Samec N, Hriberšek M, Honus S, Vujanović M. Numerical investigation of multiphase reactive processes using flamelet generated manifold approach and extended coherent flame combustion model. Energy Convers Manag 2021;240:114261. doi:10.1016/j.enconman.2021.114261.

[14]   Colin O, Benkenida A. The 3-zones Extended Coherent Flame Model (ECFM3Z) for computing premixed/diffusion combustion. Oil Gas Sci Technol 2004;59:593–609. doi:10.2516/ogst:2004043.

[15]   Mobasheri R. Analysis the ECFM-3Z Combustion Model for Simulating the Combustion Process and Emission Characteristics in a HSDI Diesel Engine. Int J Spray Combust Dyn 2015;7:353–71. doi:10.1260/1756-8277.7.4.353.

[16]   Cai L, Jacobs S, Langer R, vom Lehn F, Heufer KA, Pitsch H. Auto-ignition of oxymethylene ethers (OMEn, n = 2–4) as promising synthetic e-fuels from renewable

electricity: shock tube experiments and automatic mechanism generation. Fuel 2020;264:116711. doi:10.1016/j.fuel.2019.116711.

[17]   Bradley D, Kalghatgi GT. Influence of autoignition delay time characteristics of different fuels on pressure waves and knock in reciprocating engines. Combust Flame 2009;156:2307–18. doi:10.1016/j.combustflame.2009.08.003.

[18]   Wang W, Gowdagiri S, Oehlschlaeger MA. The high-temperature autoignition of biodiesels and biodiesel components. Combust Flame 2014;161:3014–21. doi:10.1016/j.combustflame.2014.06.009.

[19]   Shahridzuan Abdullah I, Khalid A, Jaat N, Saputra Nursal R, Koten H, Karagoz Y. A study of ignition delay, combustion process and emissions in a high ambient temperature of diesel combustion. Fuel 2021;297:120706. doi:10.1016/j.fuel.2021.120706.

[20]   Rajak U, Nashine P, Chaurasiya PK, Verma TN, Patel DK, Dwivedi G. Experimental & predicative analysis of engine characteristics of various biodiesels. Fuel 2021;285:119097. doi:10.1016/j.fuel.2020.119097.

[21]   Rajak U, Nashine P, Dasore A, Balijepalli R, Kumar Chaurasiya P, Nath Verma T. Numerical analysis of performance and emission behavior of CI engine fueled with microalgae biodiesel blend. Mater Today Proc 2021. doi:10.1016/j.matpr.2021.02.104.

[22]   Mullan Karishma S, Dasore A, Rajak U, Nath Verma T, Prahlada Rao K, Omprakash B. Experimental examination of CI engine fueled with various blends of diesel-apricot oil at different engine operating conditions. Mater Today Proc 2021. doi:10.1016/j.matpr.2021.02.105.

[23]   Xuan T, Sun Z, EL-Seesy AI, Mi Y, Zhong W, He Z, et al. An optical study on spray and combustion characteristics of ternary hydrogenated catalytic biodiesel/methanol/n-octanol blends; part I: Spray morphology, ignition delay, and flame lift-off length. Fuel 2021;289:119762. doi:10.1016/j.fuel.2020.119762.

[24]   Kobashi Y, Todokoro M, Shibata G, Ogawa H, Mori T, Imai D. EGR gas composition effects on ignition delays in diesel combustion. Fuel 2020;281:118730. doi:10.1016/j.fuel.2020.118730.

[25]   Lawson R, Gururajan V, Movaghar A, Egolfopoulos FN. Autoignition of reacting mixtures at engine-relevant conditions using confined spherically expanding flames. Proc Combust Inst 2021;38:2285–93. doi:10.1016/j.proci.2020.06.224.

[26]   Rahnama P, Arab M, Reitz RD. A Time-Saving Methodology for Optimizing a Compression Ignition Engine to Reduce Fuel Consumption through Machine Learning. SAE Int J Engines 2020;13:03-13-02–0019. doi:10.4271/03-13-02-0019.

[27] Vignesh R, Ashok B. Deep neural network model-based global calibration scheme for split injection control map to enhance the characteristics of biofuel powered engine. Energy Convers Manag 2021;249:114875. doi:10.1016/j.enconman.2021.114875.

[28] Han W, Sun Z, Scholtissek A, Hasse C. Machine Learning of ignition delay times under dual-fuel engine conditions. Fuel 2021;288:119650. doi:10.1016/j.fuel.2020.119650.

[29] Misdariis A, Vermorel O, Poinsot T. A methodology based on reduced schemes to compute autoignition and propagation in internal combustion engines. Proc Combust Inst 2015;35:3001–8. doi:10.1016/j.proci.2014.06.053.

[30] Del Pecchia M, Breda S, D'Adamo A, Fontanesi S, Irimescu A, Merola S. Development of Chemistry-Based Laminar Flame Speed Correlation for Part-Load SI Conditions and Validation in a GDI Research Engine. SAE Int J Engines 2018;11:2018-01–0174. doi:10.4271/2018-01-0174.

[31] Del Pecchia M, Pessina V, Berni F, d'Adamo A, Fontanesi S. Gasoline-ethanol blend formulation to mimic laminar flame speed and auto-ignition quality in automotive engines. Fuel 2020;264:116741. doi:10.1016/j.fuel.2019.116741.

[32] D'Adamo A, Del Pecchia M, Breda S, Berni F, Fontanesi S, Prager J. Chemistry-Based Laminar Flame Speed Correlations for a Wide Range of Engine Conditions for Iso-Octane, n-Heptane, Toluene and Gasoline Surrogate Fuels, 2017. doi:10.4271/2017-01-2190.

[33] Verhelst S, T'Joen C, Vancoillie J, Demuynck J. A correlation for the laminar burning velocity for use in hydrogen spark ignition engine simulation. Int J Hydrogen Energy 2011;36:957–74. doi:10.1016/j.ijhydene.2010.10.020.

[34] Ji C, Liu X, Wang S, Gao B, Yang J. Development and validation of a laminar flame speed correlation for the CFD simulation of hydrogen-enriched gasoline engines. Int J Hydrogen Energy 2013;38:1997–2006. doi:10.1016/j.ijhydene.2012.11.139.

[35] Liu X, Ji C, Gao B, Wang S, Liang C, Yang J. A laminar flame speed correlation of hydrogen–methanol blends valid at engine-like conditions. Int J Hydrogen Energy 2013;38:15500–9. doi:10.1016/j.ijhydene.2013.09.031.

[36] Cerinski D, Vujanović M, Petranović Z, Baleta J, Samec N, Hriberšek M. Numerical analysis of fuel injection configuration on nitrogen oxides formation in a jet engine combustion chamber. Energy Convers Manag 2020;220:112862. doi:10.1016/j.enconman.2020.112862.

[37] Colin O, Benkenida A. The 3-Zones Extended Coherent Flame Model \(Ecfm3z\) for Computing Premixed/Diffusion Combustion; The 3-Zones Extended Coherent Flame

Model \(Ecfm3z\) for Computing Premixed/Diffusion Combustion 2004. doi:10.2516/ogst:2004043ï.

[38]   Ren S, Wang Z, Li B, Liu H, Wang J. Development of a reduced polyoxymethylene dimethyl ethers (PODEn) mechanism for engine applications. Fuel 2019;238:208–24. doi:10.1016/j.fuel.2018.10.111.

[39]   Sun W, Wang G, Li S, Zhang R, Yang B, Yang J, et al. Speciation and the laminar burning velocities of poly(oxymethylene) dimethyl ether 3 (POMDME3) flames: An experimental and modeling study. Proc Combust Inst 2017;36:1269–78. doi:10.1016/j.proci.2016.05.058.

[40]   Lin Q, Tay KL, Zhou D, Yang W. Development of a compact and robust Polyoxymethylene Dimethyl Ether 3 reaction mechanism for internal combustion engines. Energy Convers Manag 2019;185:35–43. doi:10.1016/j.enconman.2019.02.007.

[41]   Gopinath S, Devan PK, Sabarish V, Sabharish Babu BV, Sakthivel S, Vignesh P. Effect of spray characteristics influences combustion in DI diesel engine – A review. Mater Today Proc 2020;33:52–65. doi:10.1016/j.matpr.2020.03.130.

[42]   Gao H, Li X, Xue J, Bai H, He X, Liu F. A modification to the WAVE breakup model for evaporating diesel spray. Appl Therm Eng 2016;108:555–66. doi:10.1016/j.applthermaleng.2016.07.152.

[43]   Abramzon B, Sirignano WA. Droplet vaporization model for spray combustion calculations. Int J Heat Mass Transf 1989;32:1605–18. doi:10.1016/0017-9310(89)90043-4.

[44]   Gülder ÖL. Correlations of Laminar Combustion Data for Alternative S.I. Engine Fuels, 1984. doi:10.4271/841000.

PAPER 6

Implementation of the Spectral Line-Based Weighted-Sum-of-Gray-Gases Model in the Finite Volume Method for Radiation Modeling in Internal Combustion Engines

Filip Jurić[a], Pedro Coelho[b], Peter Priesching[c], Neven Duić[a], Stanislav Honus[d], Milan Vujanović[a,*]

[a] University of Zagreb, Faculty of Mechanical Engineering and Naval Architecture, Ivana Lučića 5, 10000 Zagreb, Croatia

[b] IDMEC, Instituto Superior Técnico, Universidade de Lisboa, Av. Rovisco Pais 1, 1049-001 Lisbon, Portugal

[c] AVL List GmbH, Alte Poststraße 152, 8020 Graz, Austria

[d] Faculty of Mechanical Engineering, VŠB-Technical University of Ostrava, Ostrava-Poruba, Czech Republic

[*] Corresponding author e-mail: milan.vujanovic@fsb.hr

ABSTRACT

It is well-known that the pollutant formation processes and temperature distribution in various combustion systems that operate at high temperatures are influenced by radiation heat transport. Detailed modeling of radiation transport in internal combustion (IC) engines demands additional computational power, and hence the calculation of radiation phenomenon is not commonly applied in IC engines. At the same time, current operating conditions in IC engines consider high temperatures and recirculation of exhaust gases that enhance gas radiation. Therefore, the application of radiation models is needed to increase the correctness of radiative absorption, combustion characteristics, and the formation of pollutant emissions. In this paper, the implementation and validation of the spectral line-based weighted-sum-of-gray-gases (SLW) model for calculating soot and gas radiation are performed. The SLW model is implemented in the computational fluid dynamics code AVL FIRE™ by programable user routines. The radiative transfer equation was calculated employing the finite volume method applicable for multiprocessing, moving meshes, and a mesh rezone procedure required for IC engine modeling. The validation of the SLW model is performed on one-dimensional geometric cases that include analytical results of radiation intensity, for which agreement within 10 % of the relative error was achieved. Additionally, the SLW model is applied to compression ignition

---

engine simulations, where the obtained results are compared with the measured pressure and concentrations of NO and soot emissions. The calculated heat losses through the wall boundary layer were around 12 % of the total fuel energy, approximately 9.5 % of the total fuel energy was lost due to the convective flow. 7-8 % of convection heat loss was due to the higher emission than absorption of participating CO_2 and H_2O gasses, and the rest are net soot losses. For the observed operating cases, the computational time is increased nearly double for SLW model than in the simulation without radiation. Finally, the results calculated using SLW indicate an improved agreement with the experimental mean pressure, temperature, soot, and NO concentrations compared to simulations without radiation.

KEYWORDS

Radiative Absorption, Radiative Heat Transfer, Participating Media, Gas Radiation, Internal Combustion Engine

1. INTRODUCTION

It is well-known that radiative heat transfer is intensified at the high operating temperatures present in combustion systems [1]. A dominant share of total heat transfer is accomplished by radiation for systems that feature larger sizes, such as boilers, furnaces, and jet engines [2]. According to recent publications, the impact of radiation heat transport on pollutant formations needs to be considered if the correct calculation of emissions is demanded [3]. Most pollutant formation models are affected by temperature distribution, which arises from the heat transfer calculation [4]. Owing to that, it is necessary to correctly calculate radiative heat transfer for the participating radiative medium in combustion systems [5]. In addition to developing complex numerical models, the increasing research in alternative fuels that feature lower emissions is present, such as research on alternative fuels in the transportation sector made from waste [6], torrefied biomass [7], biomass oils [8] and ammonia [9].

Computational Fluid Dynamics (CFD) is a standard tool to simulate combustion systems and account for the effect of radiative heat transport on the temperature and its influence on the pollutants formation process [10]. When the participation of the medium in the radiative heat transport is considered, the solution of the integrodifferential Radiative Transfer Equation (RTE) is required [11]. A numerical approximation to solve the RTE has led to the development of numerous radiation models [12]. Thermal radiation is often neglected in internal combustion

2

(IC) engines due to the relatively small size of the combustion chamber, but a few works have taken radiation into account [3,13–15]. Even though it may have a relatively small impact on temperature, it affects the highly temperature-dependent NO emissions, as pointed out above.

In this work, the radiation model Finite Volume Method (FVM) is employed to approximate the RTE. FVM radiation model, in combination with CFD software AVL FIRE™, is modeled by user functions, which implementation was published on an IC engine [14] and a furnace [16]. One of the advantages of FVM model is its capability to model the impact of radiative heat transport in moving meshes as in IC engines, compared to the discrete transfer radiative method, which would be computationally demanding with mesh rezone [17]. The FVM is a generalized method in CFD that applies to a wide range of engineering projects that feature radiative heat transport [18]. Compared to the line-by-line models, in FVM, spectral line properties of carbon dioxide (CO_2), water vapor (H_2O), and soot are required to be calculated [19]. However, these models are too time-consuming for practical application due to the complex spectral dependence of the absorption coefficients of CO_2 and H_2O. Hence, the radiative heat exchange in participating media often relies on the utilization of global models to calculate the radiative properties of the medium [20,21].

The most recent work regarding absorption coefficient modeling was done on developing the radiative absorption coefficient models based on the weighted-sum-of-gray-gases model [22]. Recently developed weighted-sum-of-gray-gases models mainly aim to determine the radiative heat transfer of the participating media in oxy-fuel combustion conditions [23,24].

In this work, the Spectral line-based Weighted-sum-of-gray-gases (SLW) model is used to calculate the radiative properties in IC engines. This is an improved version of the classical weighted-sum-of-gray-gases model that considers the spectral line properties of H_2O and CO_2 [25]. Ozen and Selçuk [26] were the first to implement the discrete ordinates method along with the SLW model in CFD code. The implemented model performed an increased accuracy when the gas combustion was included, verifying that the spectral radiative properties of participating media are dominant in the overall radiative heat transport.

The SLW model was also employed for the three-dimensional (3D) combustion of partial-oxidation methane flame, where SLW provided valid results at sufficient computational demand [27]. Webb et al. [28] performed additional validation of SLW in a coal-fired furnace and revealed differences between gray and non-gray calculations. A comprehensive comparison between the weighted-sum-of-gray-gases method and the SLW model was performed by Ali et al. [29] in order to evaluate radiative transfer from a single participating gas at a uniform temperature and a non-isothermal mixture of gases inside a two-dimensional enclosure. Sun

and Zhang [30] showed that different gray gases have completely different contributions in SLW model. In combination with different RTE solving models (FVM and P_1 approximation), different accuracies for the gray gases are obtained. The authors proposed a hybrid FVM/P_1 model combined with SLW and stated that further investigation of this hybrid method is required. Other applications of the SLW model for two-dimensional calculations showed that the temperature field inside a radiant furnace contributed to inaccurate results of the radiative heat transfer through the medium [31–33]. The first published investigation that analyzed radiative heat transfer in oxy-fuel combustion with the model based on SLW was performed by Ströhle [34], where only the radiative absorption properties of gaseous H_2O and CO_2 were analyzed.

In the review paper [35], the influence of radiative heat transfer in turbulent flames with the SLW model was investigated. It was concluded that the SLW model has a good perspective for engineering applications for calculating the radiative heat transfer of participating media. In another review paper [36], a historical overview of the mathematical model, implementation, and application of the SLW model is given. Additional work was performed to investigate the SLW model compared to narrowband and wideband radiative absorption coefficient models in one-dimensional cases [30], where the authors compared FVM and P1 models for solving the RTE in combination with the SLW model. The better accuracy was achieved with the FVM. Ozen and Selçuk [37] performed a sensitivity analysis of several gas radiative property models, including the SLW model, where the SLW and DOM demonstrated efficient and accurate simulations for determining energy source terms and wall intensities inside fluidized bed combustors. From the literature review, SLW radiative absorption model is imposed as adequate solution for accurate and computationally acceptable solutions and was therefore implemented in this work for further investigation of radiative heat transfer in IC engines.

In this paper, the SLW model is implemented in the CFD software AVL FIRE™ as a gas radiative heat transfer estimation computation approach for predicting the combined CO_2, H_2O, and soot absorption coefficient. The SLW was firstly validated against the analytical data for simple geometries. The predictive accuracy of the AVL FIRE™ code with the SLW model is assessed for a compression ignition engine operation that features a complex 3D moving mesh and rezone procedure computed on multiprocessing units. According to the authors' knowledge, the SLW model was never employed in combination with FVM to model radiative heat transfer in IC engine applications. The combination of SLW and FVM constitutes a robust and computationally reasonable solution that applies to wide-range of complex industrial applications, such as moving meshes in internal combustion engines. Additionally, very few

papers [3,15] account for non-gray thermal radiation using accurate models in IC engines, but they use accurate and time-consuming methods. Although thermal radiation in IC engines may play a relatively minor role for light-duty vehicles, the SLW/FVM can provide an insight into its effect on emissions pollutant formation, such as NO_x and soot.

2.   MATHEMATICAL MODEL

In this work, the Reynolds-Averaged Navier-Stokes equations were solved using the *k-zeta-f* turbulence model. The *k-zeta-f* turbulence model is a robust turbulence model that allows the modeling of swirl motions inside IC engines and small wall distance values at boundary layers [38]. For calculating the gaseous phase, Eulerian specification of the fluid flow is assumed, for which the conservation equations of mass, momentum, and energy must be solved. Equation (1) describes energy conservation for the finite volume method, where the energy terms are integrated over the volume or each face of a control volume.

$$\frac{\partial}{\partial t}(\rho e) + u_i \frac{\partial}{\partial x_i}(\rho e) = \rho f_i u_i + \frac{\partial \tau_{ij} u_j}{\partial x_i} - \frac{\partial (u_i p)}{\partial x_i} + \frac{\partial}{\partial x_i}\left(\lambda \frac{\partial T}{\partial x_i}\right) + S_{rad} \tag{1}$$

Where *e* is total energy, the first term on the left side represents the total energy rate, the second represents the total energy transfer across the control volume boundaries. The first term on the right side is the power of volume forces, and the second term is the surface power forces on the control volume boundaries. The third term on the right side is pressure forces, while the fourth term is the heat transfer rate through the control volume boundaries. At the end is the source term, which is described as the radiative heat source of participating media. The implemented radiation model and absorption coefficient model aim to determine the radiative heat source term.

2.1. Radiative Transfer Calculation

The FVM radiation model was employed for the solution of RTE, as mentioned above. The FVM was considered only for absorption and emission phenomena. The participating medium absorbs the incident radiation, which is then augmented with the radiative emission of the medium, and scattering is neglected. The FVM features angular discretization that involves the calculation of the radiation intensity through the solution of a transport equation for each control

angle. The absorption coefficient of the medium was computed with the SLW model, which requires a transport equation for each gray gas. The following equation describes the RTE:

$$\frac{dI_{l,j}}{ds_l} = \kappa_j \left(a_j \frac{\sigma T^4}{\pi} - I_{l,j} \right) \tag{2}$$

In Equation (2), the $I_{l,j}$ is the radiation intensity that propagates along s_l direction, l denotes the control angle, κ_j is the absorption coefficient, where j denotes the jth gray gas for a mixture of H_2O and CO_2 and soot, and a_j denotes the combined gray gas weights of H_2O and CO_2, which are calculated as the product of the two individual gray gas weights [25]:

$$a_j = a_{H2O} \, a_{CO2} \tag{3}$$

Equation (2) is required to be solved for all control angle $\Delta\Omega_l$, where the transient term was not considered as in previous IC engine research [3,15]. The spatial discretization was carried out using the upwind scheme to calculate the radiation intensity at the downstream cell faces of a control volume. The marching procedure for solving the FVM equation was employed. The total incident radiation in each cell can be described as the sum of the incident radiation across all control angles and gray gases:

$$G_j = \sum_{l=1}^{L} I_{l,j} \cdot \Delta\Omega_l \tag{4}$$

where L is the total number of control angles. The radiative source for each gray gas is solved independently, and the total radiative source term is the sum of each gray gas contribution in the participating medium, which is calculated by [27]:

$$S_{rad} = \sum_{j=1}^{J} \kappa_j \left(G_j - 4\sigma T^4 \right) \tag{5}$$

where J is the total number of gray gases. The radiative source term in Equation (5) is implemented as a source term in the enthalpy transport equation. The boundary condition for an opaque nonreflecting wall may be written as follows [27]:

$$I_{bnd}^l = \epsilon \frac{\sigma T^4}{\pi} + (1 - \epsilon) \frac{\sum_{(s_l \cdot n_w) > 0} I_{l,j} \, |n_i D_{ci}|}{\sum_{(s_l \cdot n_w) < 0} n_i D_{ci}} \tag{6}$$

where ϵ denotes the wall emissivity, which is assumed to be 1, n_w is the outer wall unit vector, D_{ci} denotes auxiliary terms that depend on the orientation of the face wall and the control angle. Additionally, cyclic boundary conditions are applied to two IC engine boundaries, such

that the outgoing radiation intensity values that exit the calculation domain through a cyclic boundary are set equal to the incoming radiation intensities entering the domain at the other cyclic boundary. The convergence of RTE is reached when the difference between the new and the last iteration is less than 0.01%.

For the calculations with the SLW model, several gray gases are utilized as the replacement for non-gray gas, where each contribution is symbolized with the supplemental absorption cross-section $\bar{C}_{abs,j}$ and correlate the weight of gray gas a_j. The absorption cross-section ranges between $3 \cdot 10^{-5}$ and 60 m^{2}mol^{-1} for water vapor, while for CO_2, the range is between $3 \cdot 10^{-5}$ and 120 m^{2}mol^{-1} [39]. These limits of the absorption cross-sections, $C_{\min}$ and $C_{\max}$ are used for the calculation of a supplemental absorption cross-section $\bar{C}_{abs,j}$ of each gray gas:

$$\bar{C}_{abs,j} = C_{\min} \left(\frac{C_{\max}}{C_{\min}} \right)^{\frac{j}{J}} \tag{7}$$

The absorption cross-section domain is divided into intervals equally spaced on a logarithmic scale, and the range between two consecutive supplemental absorption cross-sections, $\bar{C}_{abs,j}$ and $\bar{C}_{abs,j+1}$, treated as an independent gray gas, whose absorption cross-section $C_{abs,j}$, is defined as follows::

$$C_{abs,j} = \sqrt{\bar{C}_{abs,j} \, \bar{C}_{abs,j+1}} \tag{8}$$

The gray gas weights, a_j can be obtained from the absorption-line blackbody distribution functions F, which is determined by the high-resolution HITRAN database that accounts for the radiative participation of CO_2 and H_2O [39]. The distribution function F is defined as:

$$F(C_{abs,j}) = \frac{\pi}{\sigma T^4} \int_{\{\eta: C_{\eta,j} < C_{abs,j}\}} I_{b\eta}(T) d\eta \tag{9}$$

where the integral is calculated over the spectral wavenumber η. The weight of the jth gray gas can be calculated as the difference distribution function F at the supplemental cross-section interval limits:

$$a_j = F(\bar{C}_{abs,j+1}) - F(\bar{C}_{abs,j}) \tag{10}$$

The combined absorption coefficient of CO_2 and H_2O, $\kappa_{CO2+H2O}$ is defined as the sum of the contributions of the two species [27]:

$$\kappa_{CO2+H2O} = N_{H_2O} \, C_{abs,k,CO_2} + N_{H_2O} \, C_{abs,k,CO_2} \tag{11}$$

where N is the molar density of the gas, which is determined from the local cell temperature and the species mass fraction. In this work, ten gray gases were used to compute non-gray radiative properties used in the SLW model. For the calculation of soot participation in radiative transport, the gray gas absorption model is assumed, due to its smoothly varying radiative properties, with the following equation [40]:

$$\kappa_s = 0.672 \, Tc \tag{12}$$

In Equation (12), the term c denotes the mass fraction of soot. For calculating the total absorption coefficient, the absorption coefficient of the soot is added to the combined absorption coefficient of CO_2 and H_2O, as shown in Equation (13).

$$\kappa_j = \kappa_{CO2+H2O} + \kappa_s \tag{13}$$

2.2. Combustion and pollutants emission modelling

A coherent flame model, ECFM-3Z combustion model, was employed for the modeling of the combustion process. The ECFM-3Z combustion model governing equations can be found in [41], where the ECFM-3Z was also used for the modeling of combustion inside a combustion chamber of an industrial diesel engine. The constant autoignition and mixing parameters were assumed to have the default value of 1.

For the calculation of turbulence chemistry interaction (TCI), Probability Density Function (PDF) approach was considered in this work, which equations and details can be found in [20]. PDF is based on the presumed standard Gaussian Probability Density Function, where the temperature T is assumed to be the sum of mean temperature and temperature variance.

$$T = \bar{T} + x \sqrt{\overline{T'T'}} \tag{14}$$

The mean value of the temperature function was calculated as approximate quadrature formula,

$$\overline{f(T)} \approx \sum_{k=1}^{n} \left(\overline{T} + x_k \sqrt{\overline{T'T'}} \right) c_k \tag{15}$$

The temperature variance was calculated by solving its transport equation with its correction factors in each node

$$\frac{\partial}{\partial t} \left(\rho \overline{T'T'} \right) + \frac{\partial}{\partial x_i} \left(\rho \tilde{u}_i \overline{T'T'} \right)$$
$$= \frac{\partial}{\partial x_i} \left(\frac{20}{17} \mu_t \frac{\partial \overline{T'T'}}{\partial x_i} \right) + 2.86 \, \mu_t \left(\frac{\partial \overline{T}}{\partial x_i} \right)^2 - 2\rho \frac{\varepsilon}{k} \overline{T'T'} \tag{16}$$

Furthermore, the spray process was modeled by the Euler Lagrangian approach. The liquid phase of an injected droplet is modeled as parcels, and the gas phase is modeled as a continuum. For each parcel, trajectories are calculated from the deacceleration of injected droplets due to the drag force, where drag coefficient C_D is calculated by Schiller Naumann drag law:

$$m_{\mathrm{p}} \frac{du_{\mathrm{p}i}}{dt} = 0.5\pi \, r^2 \rho C_D u_i^{\,2} \tag{17}$$

The Euler Lagrangian model assumes spherical symmetry, uniformity, and liquid-vapor thermal equilibrium of all droplets. Additionally, the quasi-steady and uniform surrounding around the droplets is assumed. The breakup model of the droplet parcel is modeled with the Wave breakup model, where the droplet disintegration is calculated by:

$$\frac{dr}{dt} = -\frac{\lambda_w \, \Omega \, (r - 0.61\lambda_w)}{3.726 \, r \, C_2} \tag{18}$$

Further description of Wave breakup model is described in the literature [42]. The constant C_2 of Wave model that dictates the breakup time of parcels specific for each injector system is set to eighteen. The half of nozzle diameter is assumed for the initial radius of droplet parcels. The Abramzon model was employed to model fuel evaporation, which governing equation can be found in [43]. In recent publications, such a model has also been applied to calculate the multi-component evaporation process [44].

Special attention has been given to the NO_x and soot formation process. The Extended Zeldovich Model was employed for thermal NO emissions [45], while a kinetic soot model was employed for the soot formation process. The prompt NO formation process in this work was calculated by employing the de Soete model, as in [46]. The method described in Vujanović et

al. [47] was used to determine the temperature fluctuations. The kinetic soot model is based on the detailed soot oxidation and agglomeration model. The source term calculation is determined from the probability density function of the mixture fraction [48,49], which is a function of the scalar dissipation rate, pressure, and temperature on the oxidizer side. The surface growth, oxidation, particle inception, and fragmentation are considered to calculate of soot volume fraction.

3. EXPERIMENTAL DATA AND NUMERICAL SETUP

The experimental validation data of the compression ignition engine was acquired from AVL GmbH [50]. In Table 1, the engine and injector properties are presented. For the generating computational mesh domain, the automatic masher AVL™ ESE Diesel tool is employed. The observed engine features a ω-shape piston bowl, which denotes the shape of the combustion chamber, and by its shape, promotes combustion. Figure 1 shows a 1/8th segment of a cylinder with generated boundary selections at the top dead center (TDC), respectively 720°CA is demonstrated. In this work, simulations only for one eight engine cylinder were calculated since the fuel injector possesses eight nozzle orifices. A piston rim compensation volume is generated to satisfy the compression ratio for all discrepancies and leakage present in the actual experimental engine, as shown in Figure 1.

The simulation cycle was modeled from 610°CA to 860°CA, where the segment cyclic inlet boundary conditions were used for segment selections. Mesh movement is described with mesh rezoning procedure, compression, and expansion stroke, generated by the automatic masher. The liquid fuel properties greatly influence spray integration and evaporation [51]. Therefore, the injected liquid fuel used in the experiment Diesel EN590 B7 was defined with polynomial terms in FIRE™. The B7 in the name of fuel indicates around 7% biodiesel content, which indicates the utilization of biofuels in conventional diesel engines [52]. The injection rate timing has a direct influence on engine performance [53], for that reason, the inlet fuel velocity is calculated from the measured injection rate, which is shown in Figure 2. Figure 2 shows the injection curve rate is shown as a nondimensional parameter, where the area under the curve presents the total injected fuel mass in one operating cycle. The first introduced parcels that enter the domain are assumed to have the diameter same as the orifice diameter, 0.1 mm.

Table 1 Experimental engine and injection system properties.

Bore	85 mm	**Injector position**	(0, 0, -3.8) mm
Stroke	94 mm	Injector direction	(0, 0, 1)
Compression ratio	16	Spray angle	158°
Injected pressure	1200 – 1600 bar	Spray cone angle	15°
Fuel	Diesel EN590 B7	Number of nozzle holes	8
Fuel temperature	47°C	Nozzle hole diameter	100 µm
		Nozzle diameter at hole center position	4 mm
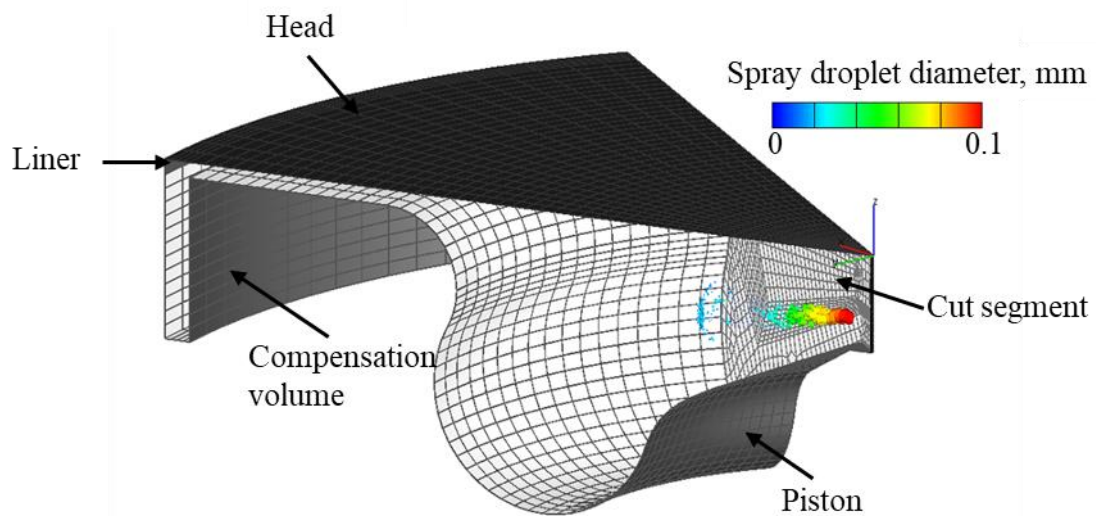
Figure 1   Computational engine mesh at the top dead center with the position of spray injector
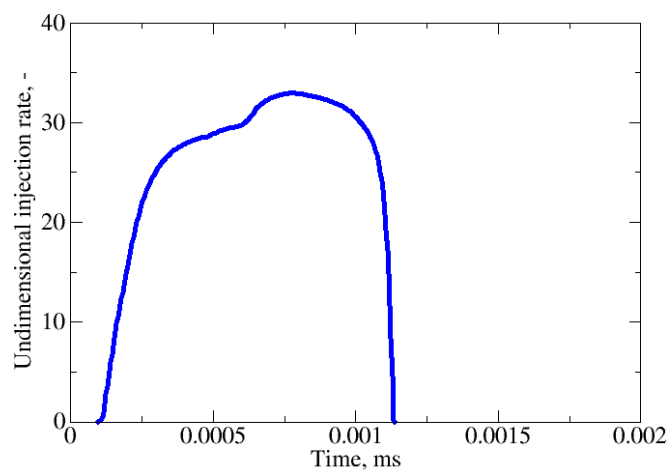
Figure 2   Injection rate profile of both observed operating points

In Table 2, boundary conditions for engine selections in Figure 1 are shown. Piston, liner, and headwall selections were modeled by an isothermal boundary condition, in which temperatures are obtained from the experimental analysis. For the compensation volume, an isolated boundary condition was assumed.

Table 2 Boundary conditions

Boundary condition	Type	Description
Head	Wall	Isothermal, 500 K
Liner	Mesh movement/Wall	Isothermal, 410 K
Compensation Volume	Mesh movement/Wall	Adiabatic
Cut segment	Inlet/Outlet	Periodic
Piston	Wall	Isothermal, 500 K

A mesh dependency study was performed to prove the validity of the generated mesh for simulations. Therefore, three hexahedral meshes with identical block cell structures were generated by varying the cell size. The total number of cells at the TDC position for the hexahedral generated meshes is shown in Table 3. All computational meshes are generated with a two-cell boundary layer to secure a correct calculation of the wall intensities. The simulations with the identical numerical setup were performed for the three meshes, and the mean pressure results were compared. Figure 3 shows the computed and measured mean in-cylinder pressure from 700 °CA, slightly before fuel injection, up to 750 °CA. The coarse mesh is selected for all the simulations presented in this paper based on the mesh dependency analysis. The three generated moving meshes consist of twenty deformable meshes alternately mapped with the crank angle rotation. The rezoning procedure was implemented to be called when the physical quantities are mapped to the next mesh. After the multiprocessing finish with a calculation for crank angle time where the rezoning procedure is needed, the new mesh division on each processor is performed. The transfer of radiation quantities at the nodes of the next mesh is inherited from the precedent mesh.

Table 3 Number of cells at TDC for the three generated meshes

Mesh	Cell number at the top dead center
Coarse	~24 000
Medium	~45 000
Fine	~63 000
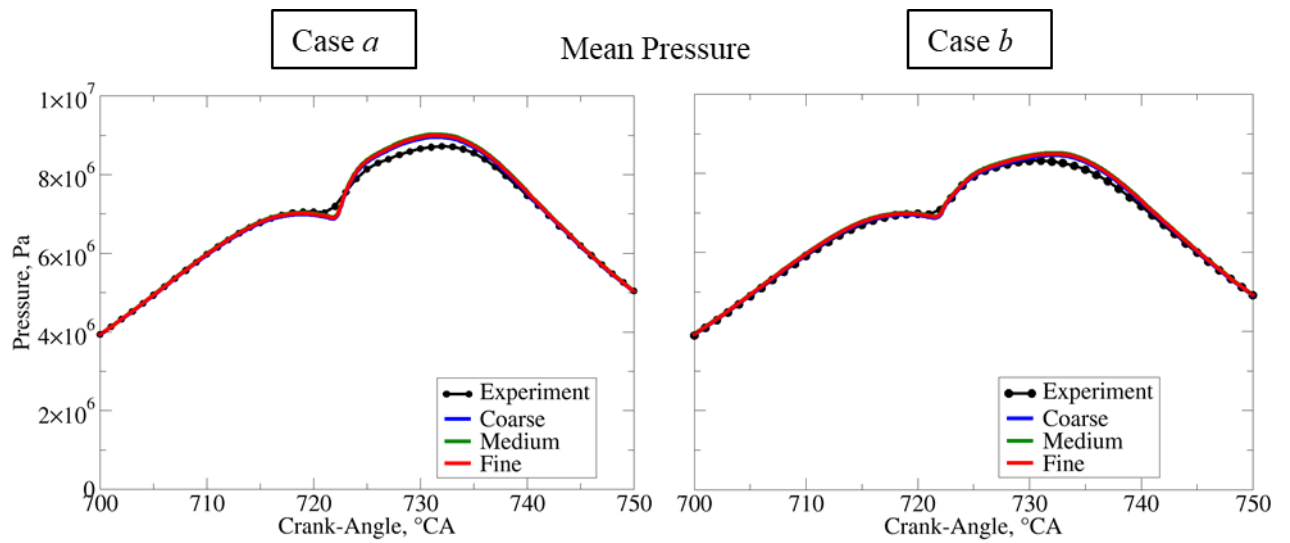
Figure 3   Mesh dependency results for three different meshes of the same block geometry

In this work, two operating points are observed, Case *a* and Case *b*. The initial conditions and gas-phase composition of fresh air and exhaust gas residuals (EGR) differ for these two cases and are given in Table 4. Case *a* and Case *b* differ slightly in initial temperature, pressure and gas composition, and swirl motion inside the combustion chamber, while the injected mass in a single injection was approximately the same. Additionally, the main difference between the two cases is that Case *a* features an earlier injection than Case *b*.

Table 4 Initial conditions and gas-phase composition

	Case *a*	Case *b*
Engine speed (rpm)	3000	3000
Number of injections	1	1
Injected mass (mg)	3.38	3.37
Pressure (Pa)	250000	235000
Temperature (K)	423	415
Swirl (1/min)	5403	5832
Start of injection (°CA)	712.5	713.5
End of injection (°CA)	735.4	734.8
Gas composition (kg/kg)		
O_2	0.2085	0.2030
N_2	0.7632	0.7620
CO_2	0.0196	0.0243
H_2O	0.0087	0.0117

For the combustion process modeling, the combustion parameters for autoignition and mixing of ECFM-3Z were used with default values, while for the Abramzon evaporation model, Lewis number was one.

In determining the radiative source term, each contribution of each control angle to radiative heat transfer needs to be accounted [54]. For the FVM model, the initial number of control angles is required, which affects the accuracy and computational demand of the calculations [55]. In this work, a selected number of control angles was eight after the control angle sensitivity analysis on temperature traces was performed. For the number of gray gases in the SLW model, calculations with ten gray gases were observed, while the model assumes the spectral dependent absorption coefficient of the participating species. In [56], the algorithm that calculates spatial discretization and control angles in this work is demonstrated. An emissivity value of unity was assumed for all wall boundaries. To save computational time, the radiative heat transfer solver was calculated for each 10th fluid flow iteration. This paper neglected the scattering due to the relatively small reflectivity of soot particles inside a chamber of IC engines, as was the case in [57].

For calculating the momentum differencing scheme, the central differencing scheme was used for the momentum equation and continuity equation, while the upwind scheme was used for radiative heat transfer, turbulence parameters, total energy, and scalar conservation equations. The convergence criteria were set to residual values below 10^{-4}. For the time discretization, a dynamic time step was employed, where each new time step was calculated from Courant–Friedrichs–Lewy (CFL) condition. The maximum CFL number was set to 1. The SIMPLE algorithm calculated the coupling between pressure and velocity for solving the pressure correction equation.

3.1. Validation of SLW model

The implemented absorption coefficient SLW model is validated on one-dimensional cases with an analytical solution. Two one-dimensional cases were selected for which the predefined temperature and mole fraction of CO_2 and H_2O are shown in**Error! Reference source not found.** [27]. A hexahedral mesh of cubic cells 3 x 3 x 300 was generated, where the profile is observed for the enclosed cell layer along the mesh axis.

Table 5 Specifications of the two validation cases [27]

	T, K	Y_{H2O}	Y_{CO2}	ϵ, -
1.	$1000 + 250 \cos(\tilde{x})$	0.1	0	1
2.	$1000 - 300 \cos(2\tilde{x})$	$0.5 - 0.5 \cos(\tilde{x})$	$0.5 + 0.5 \cos(\tilde{x})$	1

In**Error! Reference source not found.** the nondimensional coordinate $\tilde{x}$ is defined as:

$$\tilde{x} = \frac{\pi x}{L} \tag{19}$$

where x is the position in the coordinate system, and L is the total length. Figure 4**Error! Reference source not found.** shows the comparison of SLW against the analytical radiative source term for the first validation case in Table 5, where a good agreement is achieved for the trigonometric temperature profile with the SLW model. In Figure 5**Error! Reference source not found.**, the validation is shown for the second validation case in Table 5**Error! Reference source not found.**. Compared to the first validation case, the molar ratio of CO_2 and H_2O is also described with the trigonometric profile. The presented results in Figure 6 show that the simulation results insignificantly change when more control angles were applied to the numerical simulations. Based on the performed validation, it can be stated that the implemented SLW model is valid for describing the CO_2 and H_2O gas radiative properties.
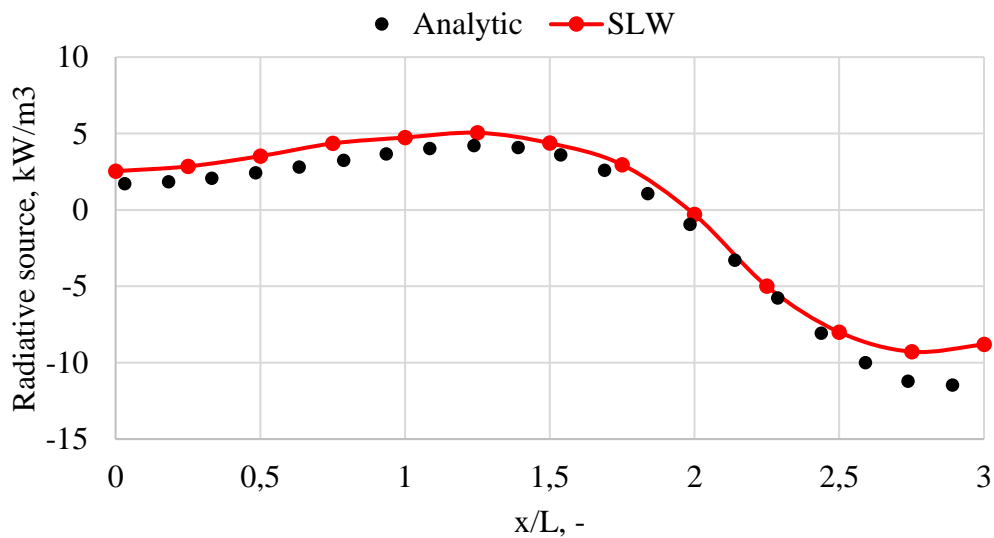
Figure 4   Radiative source profile results for the first validation case
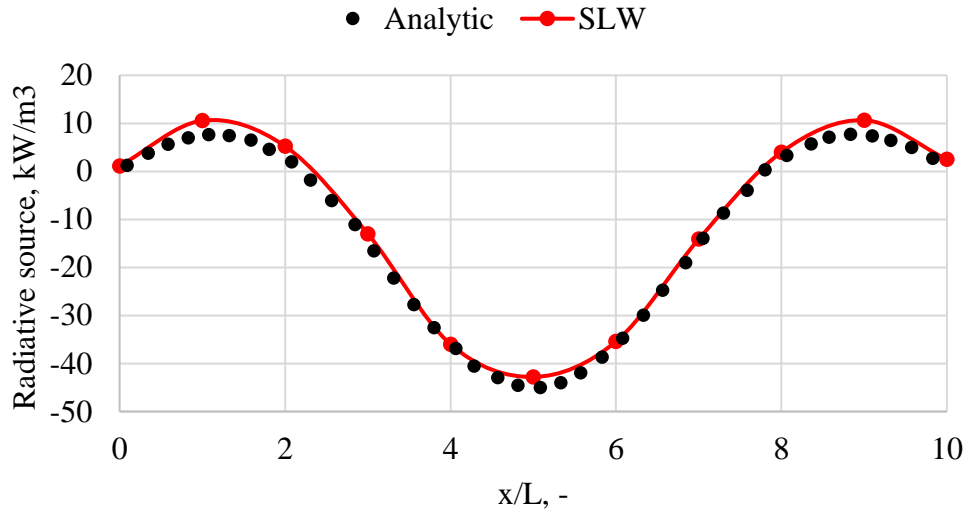
Figure 5   Radiative source profile results for the second validation case

4.   RESULTS AND DISCUSSION

This section discusses model validation, analysis of control angles, IC engine results, computational time, and specific conclusions and objectives of the paper.

4.1.   Results on compression ignition engine

Figure 6 compares temperature profiles for Case *a* and Case *b*. The orange curves show the numerical results calculated with eight control angles, the green curve shows sixteen control angles, and the violet curve for thirty-two control angles in the FVM radiation model. Experimental data are also presented as a reference, which indicates a better agreement of thirty-two control angles at the ignition phase of the combustion process. In comparison, the lower temperatures at eight control angles show a better matching in the developed combustion process. From the presented results in Figure 6, the simulation results insignificantly change when more control angles were applied to the numerical simulations. For that reason, all simulations in this work are computed with eight FVM control angles. A similar influence of control angle number on the simulation results is noticeable in both cases.

16
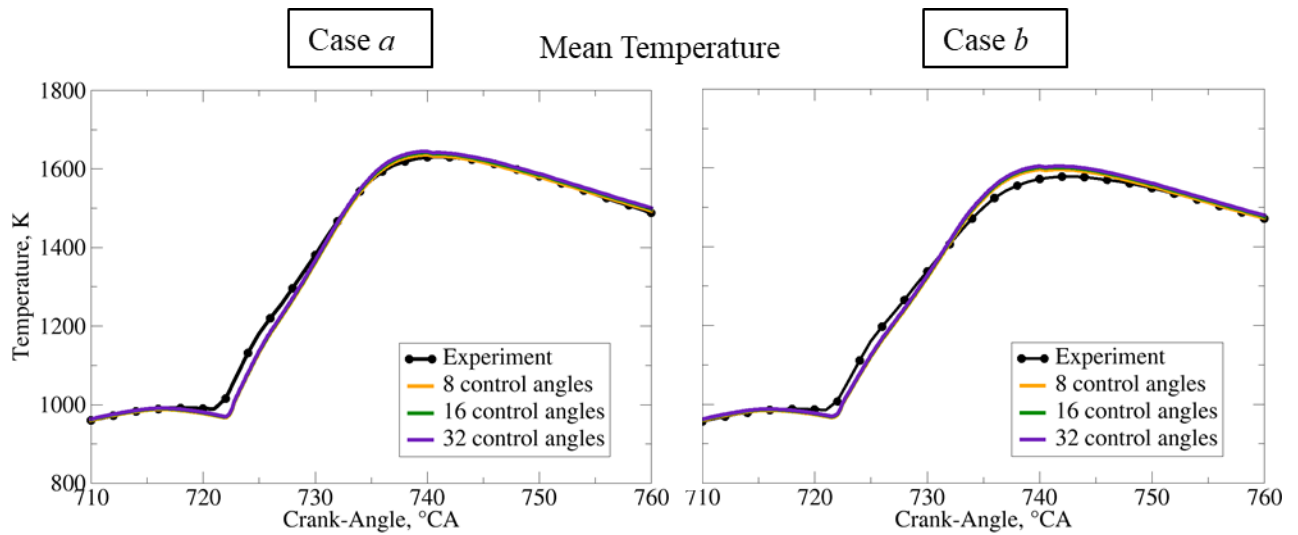
Figure 6   Mean temperature results for Case *a* and Case *b* with SLW model and different number of control angles in FVM radiation model

Figure 7 shows the mean pressure in the cylinder, mean temperature, and rate of heat release (RoHR) results for Case *a* and Case *b*. The RoHR results are shown for computational mesh, an eighth of an engine combustion chamber. The black lines with dots are experimental data, blue curves are results without considering radiation heat transport, and orange curves result from the implemented SLW model. For all results, a more significant discrepancy between SLW results and results without radiation is achieved for Case *a*, while for Case *b,* the later ignition time results in lower mean pressure, mean temperature, and RoHR results. The difference in the ignition delay between results with and without radiation is visible in Figure 7, associated with the different radiative absorption coefficient values. The radiative absorption energy of CO_2 and H_2O is approximately similar in Case *a* and Case *b*, which can be prescribed to their similar gas composition and thermodynamic conditions. Although the difference between the calculated impact of the radiation between Case *a* and Case *b* is visible in Figure 7. That is why the difference between results with SLW and without radiative heat transfer can be prescribed primarily to the absorption of soot particles, which have gray gas behavior. As expected, the radiative absorption of a large share of incident radiative flux is the largest in the regions of high temperatures. Overall, more accurate results and better agreement with experimental data were achieved with the SLW model, which considers the additional spectral phenomenon of radiative heat transport.
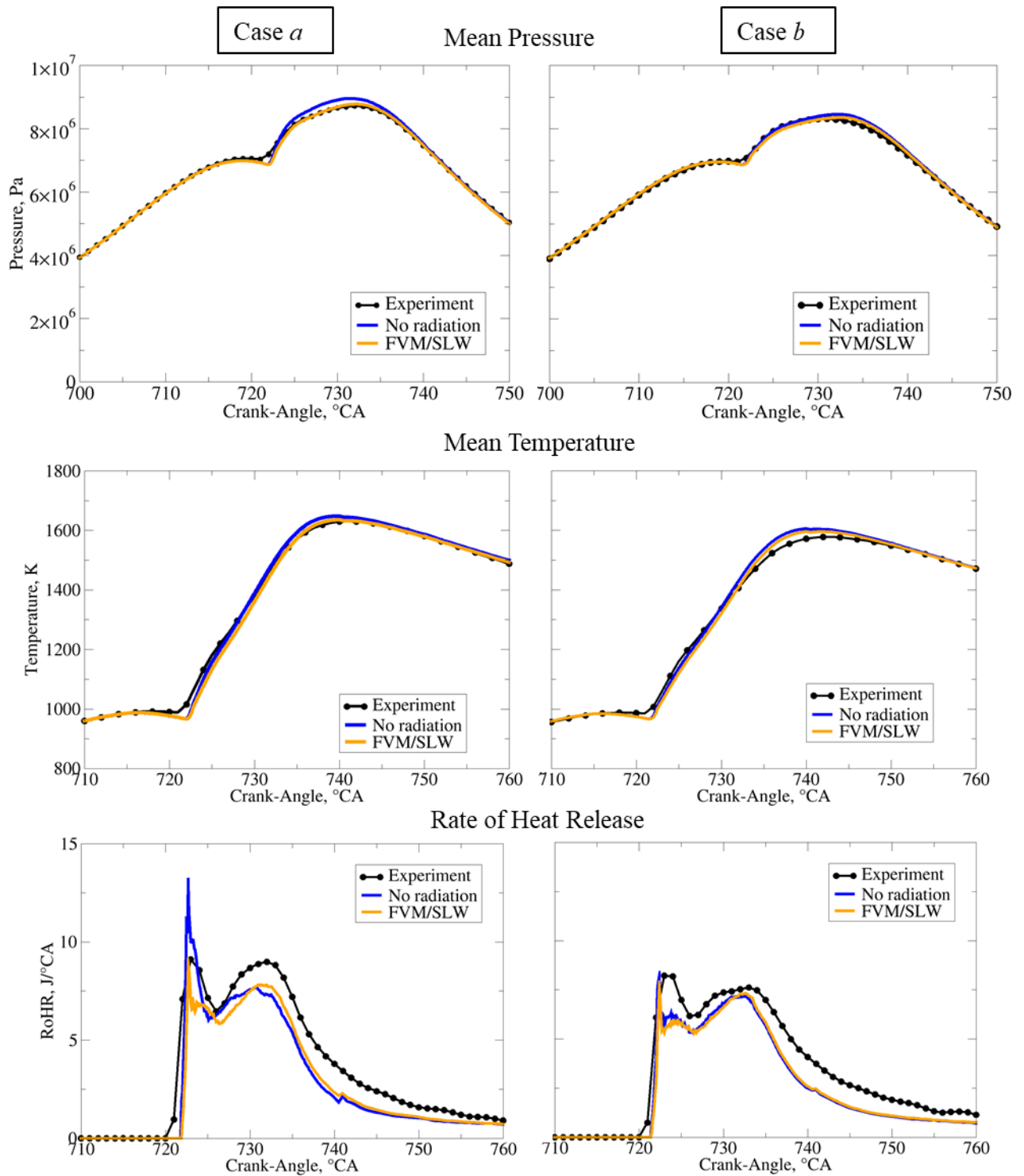
Figure 7   Mean in-cylinder pressure results, mean temperature, and RoHR results for
Case *a* (left) and Case *b* (right) with SLW model and without radiation against experimental
results

4.2. Emission results

Comparing experimental results and simulations with and without radiation is given in Table 6 for pollutant emissions at the crank angle position when the exhaust valve opens. The results show that the radiative heat transport improves the predictions, leading to a better agreement with the experimental data. Table 6 shows that the soot mass fraction increases when the radiative heat transport is included. This indicates that the lower temperatures in simulations with included radiative heat transfer result in a pronounced decrease in oxidation temperature versus the reduction in soot production. In contrast, the NO concentrations decrease, which are significantly generated by high-temperature regions. All predictions with the SLW accounting for radiation improve the prediction of NO emissions, which are of the same order of magnitude as the experimental data. It can be seen from Figure 7 that the tremendous difference between SLW and results without radiation is present in Case *a*, which can be mainly attributed to the gray gas soot assumption. The lower soot absorption indicates that the soot oxidation is pronounced in Case *a* since both cases have similar initial composition and the approximately same amount of injected fuel. The pronounced soot oxidation processes also correspond to higher calculated temperatures in Case *a*. For the last two columns in Table 6, the results with and without including TCI are compared. The exhaust pollutant molar mass

Table 6 Pollutant mass ratio in the exhaust system

	Experiment	No radiation	SLW
Case *a*			
Soot (ppm)	899	273	356
NO (ppm)	309	512	417
Case *b*			
Soot (ppm)	2462	512	985
NO (ppm)	196	217	205

Figure 8 shows calculated heat loss profiles for different crank angle positions for Case *b*. The heat losses are calculated through the wall boundary layer, where 9.5% of the total fuel energy is lost due to the convective losses. In comparison, the net radiative loss due to the higher emission than absorption of participating CO_2 and H_2O gasses is approximately 7-8% of convection heat loss. In Figure 9, the profiles of soot mass fraction for the simulation with and without including radiative heat transfer are shown, with the following Figure 10 shows temperature difference contour at the crank angle position with peak soot concentration, 732°CA. The interaction between soot concentrations and radiative heat transfer does not have

19

a simple influence as with NO formation. The soot for the obtained results is mainly influenced by the regions of lower temperatures computed by SLW simulations, which were dominant compared to the regions with lower temperatures, as shown in Figure 7. The higher temperature differences correlate to the fuel-rich regions along high-temperature regions. The area of highest difference is around the equivalence ratio values of 2-3, where the neighbor cells are already ignited and consumed their oxygen.
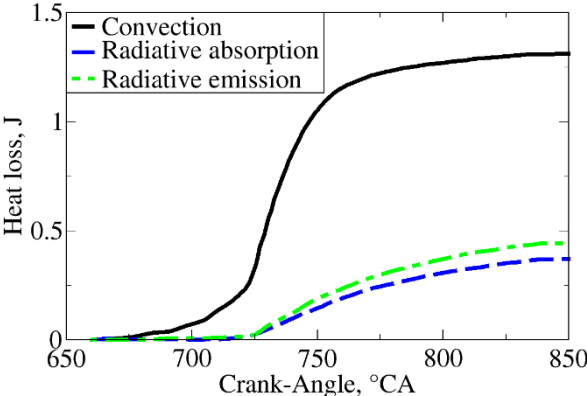
Figure 8   Convective, radiative absorption, and radiative emission heat losses for Case *b*
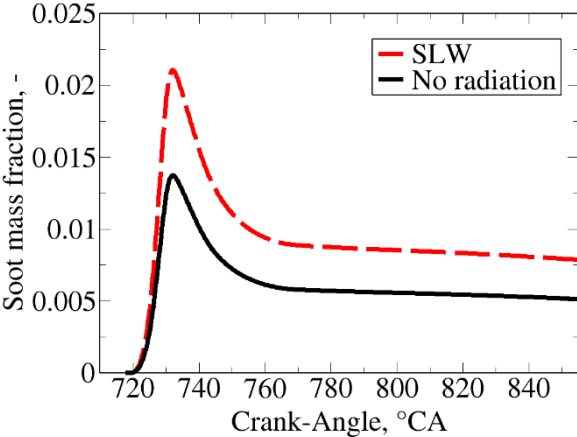
Figure 9   Soot mass fraction profile for Case *b*
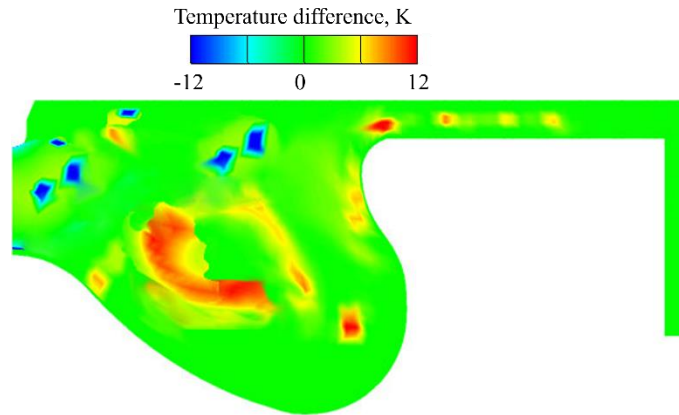
Figure 10   Temperature difference between results with SLW and without radiation at the crank-angle position with peak soot values (732°CA) for Case *b*

In Table 7, the difference in the computational requirements of the simulations is shown. The computational time increases around two times when thermal radiation is considered, which is related to the additional ten transport equations per control angle for each gray gas that needs to be solved in FVM/SLW.

Table 7 Computational time for Case *a* on 10 control processing units of Intel® Xeon® E5-2650 v4 at 2.20 GHz

Calculation time, min	No radiation	SLW
Case *a*	34	70
Case *b*	31	68

5.   CONCLUSION

The SLW model was coupled with FVM radiation solver and implemented by programable user routines in the CFD software AVL FIRE™. The implemented SLW model is based on correlations for unequal temperatures and mixtures of H_2O, CO_2, and soot, and the solver to radiative transfer equation was modified to account for the spectral gas properties with absorption cross-sections and associated weight of gray gases. The soot absorption was assumed as gray gas absorption, while the implementation of boundary conditions is performed for diffusely reflective walls, periodic inflow/outflow, and symmetry. The model was implemented for application to parallel computing, moving meshes, and rezoning processes to be suitable for calculating radiative heat transfer in IC engines. The implemented SLW model achieved a good matching with one-dimensional validation cases with the analytical radiative heat transfer solution. Additionally, this investigation in this work emphasizes the combined radiation heat transport and combustion characteristics in a compression ignition. The predicted

results of the in-cylinder pressure, temperature, and RoHR are significantly corresponding with the experiment data. As expected, the most decisive influence of the radiation transport in participating media is visible at crank positions with the highest pressures and temperatures, where the highest difference between simulations with SLW and with no radiation is obtained. The main difference between SLW and results without radiation arises at peak temperatures, where the gray gas soot assumption is its primary cause. The soot concentrations at the exhaust exit are increased with the SLW model, which could be prescribed to the lower temperatures that indicate a predominant decrease of soot oxidation versus the decrease in soot production. The higher temperature differences indicate that the soot regions are located in the fuel-rich regions along high-temperature regions. In contrast, the NO concentration emissions decrease with the inclusion of radiation in simulations, where the decrease is more pronounced with the more significant difference between the experiment and the simulation without radiation. The calculated heat convective losses through the wall boundary layer were 9.5% of the total fuel energy, while the net radiative loss due to the higher emission than absorption of participating CO_2 and H_2O gasses is 7-8% of convection heat loss. The soot production in both operating cases is approximately doubled, while the trend of soot production is achieved for simulations with included radiation and without radiation.

The computational time is around two times more demanding with the SLW model than in simulation without radiation, which is correlated to additional ten transport equations for each gray gas in the SLW model. Finally, it can be concluded that the presented method can serve as a solution for more physically correct predictions of the radiation heat transport in compression ignition engines. Although in the case of large IC engines, such as big trucks or large ships, the role of thermal radiation is expected to become relevant due to the larger cylinder volume. Future work is to investigate results in the operating cases with higher EGR values accounting for the turbulence radiation interaction.

REFERENCES

[1]   Krishnamoorthy G, Jimenez M. Non-gray modeling of radiative heat transfer in hydrogen

combustion scenarios. Int J Energy Res 2012;36:789–97. doi:10.1002/er.1836.

[2]   López Pérez S, Herrero López S, Ubieta Astigarraga E, del Hoyo Arce I, Gómez de Arteche Botas M, Iturralde Iñarga J, et al. Design of a Radiant Heat Capturing Device for Steel Mills. J Sustain Dev Energy, Water Environ Syst 2021;9:1–15. doi:10.13044/j.sdewes.d8.0365.

[3]   Paul C, Ferreyro Fernandez S, Haworth DC, Roy S, Modest MF. A detailed modeling study of radiative heat transfer in a heavy-duty diesel engine. Combust Flame 2019;200:325–41. doi:10.1016/j.combustflame.2018.11.032.

[4]   Dimitriadis A, Seljak T, Vihar R, Žvar Baškovič U, Dimaratos A, Bezergianni S, et al. Improving PM-NOx trade-off with paraffinic fuels: A study towards diesel engine optimization with HVO. Fuel 2020;265:116921. doi:10.1016/j.fuel.2019.116921.

[5]   Fujimori T, Hamano Y, Sato J. Radiative heat loss and NOx emission of turbulent jet flames in preheated air up to 1230 K. Proc Combust Inst 2000;28:455–61. doi:10.1016/S0082-0784(00)80243-X.

[6]   Lazaroiu G, Pană C, Mihaescu L, Cernat A, Negurescu N, Mocanu R, et al. Solutions for energy recovery of animal waste from leather industry. Energy Convers Manag 2017;149:1085–95. doi:10.1016/j.enconman.2017.06.042.

[7]   Mikulčić H, Cerinski D, Baleta J, Wang X. Improving Pulverized Coal and Biomass Co-Combustion in a Cement Rotary Kiln by Computational Fluid Dynamics. Chem Eng Technol 2019. doi:10.1002/ceat.201900086.

[8]   Józsa V, Hidegh G, Kun-Balog A, Ng J-H, Chong CT. Ultra-low emission combustion of diesel-coconut biodiesel fuels by a mixture temperature-controlled combustion mode. Energy Convers Manag 2020;214:112908. doi:10.1016/j.enconman.2020.112908.

[9]   Mikulčić H, Baleta J, Wang X, Wang J, Qi F, Wang F. Numerical simulation of ammonia/methane/air combustion using reduced chemical kinetics models. Int J Hydrogen Energy 2021;46:23548–63. doi:10.1016/j.ijhydene.2021.01.109.

[10] Paul C, Haworth DC, Modest MF. A simplified CFD model for spectral radiative heat transfer in high-pressure hydrocarbon–air combustion systems. Proc Combust Inst 2019;37:4617–24. doi:10.1016/j.proci.2018.08.024.

[11] Modest MF. Radiative Heat Transfer. 3rd ed. Elsevier; 2013. doi:10.1016/B978-0-12-503163-9.X5000-0.

[12] Coelho PJ. Radiative Transfer in Combustion Systems. Handb. Therm. Sci. Eng., Cham: Springer International Publishing; 2018, p. 1173–99. doi:10.1007/978-3-319-26695-4_61.

[13] Benajes J, Martin J, Garcia A, Villalta D, Warey A, Domenech V, et al. An Investigation of Radiation Heat Transfer in a Light-Duty Diesel Engine. SAE Int J Engines 2015;8. doi:10.4271/2015-24-2443.

[14] Jurić F, Petranović Z, Vujanović M, Duić N. Numerical assessment of radiative heat transfer impact on pollutant formation processes in a compression ignition engine. J Clean Prod 2020;275, 12308. doi:10.1016/j.jclepro.2020.123087.

[15] Yue Z, Reitz RD. Numerical investigation of radiative heat transfer in internal combustion engines. Appl Energy 2019;235:147–63. doi:10.1016/j.apenergy.2018.10.098.

[16] Juric F, Vujanovic M, Zivic M, Holik M, Wang X, Duic N. Assessment of radiative heat transfer impact on a temperature distribution inside a real industrial swirled furnace. Therm Sci 2020:285–285. doi:10.2298/TSCI200407285J.

[17] Mazzei L, Puggelli S, Bertini D, Pampaloni D, Andreini A. Modelling soot production and thermal radiation for turbulent diffusion flames. Energy Procedia 2017;126:826–33. doi:10.1016/j.egypro.2017.08.266.

[18] Mishra SC, Chugh P, Kumar P, Mitra K. Development and comparison of the DTM, the DOM and the FVM formulations for the short-pulse laser transport through a participating medium. Int J Heat Mass Transf 2006;49:1820–32. doi:10.1016/j.ijheatmasstransfer.2005.10.043.

[19] Coelho PJ. On the Convergence of the Discrete Ordinates and Finite Volume Methods for the Solution of the Radiative Transfer Equation. ASME Verif Valid Symp 2013.

[20] Ozen G, Ates C, Selçuk N, Kulah G. Assessment of SLW-1 model in the presence of gray and non-gray particles. Int J Therm Sci 2019;136:420–32. doi:10.1016/j.ijthermalsci.2018.10.038.

[21] Modest MF, Haworth DC. Radiative heat transfer in high-pressure combustion systems. SpringerBriefs Appl. Sci. Technol., Springer Verlag; 2016, p. 137–48. doi:10.1007/978-3-319-27291-7_7.

[22] Krishnamoorthy G. A new weighted-sum-of-gray-gases model for oxy-combustion scenarios. Int J Energy Res 2013;37:1752–63. doi:10.1002/er.2988.

[23] Guo J, Shen L, Wan J, Li P, Liu Z. A full spectrum k -distribution-based weighted-sum-of-gray-gases model for pressurized oxy-fuel combustion. Int J Energy Res 2021;45:3410–20. doi:10.1002/er.6010.

[24] Shan S, Zhou Z, Chen L, Wang Z, Cen K. New weighted-sum-of-gray-gases model for typical pressurized oxy-fuel conditions. Int J Energy Res 2017;41:2576–95.

doi:10.1002/er.3838.

[25] Denison MK, Webb BW. The Spectral Line-Based Weighted-Sum-of-Gray-Gases Model in Nonisothermal Nonhomogeneous Media. J Heat Transfer 1995;117:359–65. doi:10.1115/1.2822530.

[26] Ozen G, Selçuk N. SLW model for computational fluid dynamics modeling of combustion systems: Implementation and validation. Numer Heat Transf Part B Fundam 2016;70:47–55. doi:10.1080/10407790.2016.1173499.

[27] Garten B, Hunger F, Messig D, Stelzner B, Trimis D, Hasse C. Detailed radiation modeling of a partial-oxidation flame. Int J Therm Sci 2015;87:68–84. doi:10.1016/j.ijthermalsci.2014.07.022.

[28] Webb BW, Ma J, Pearson JT, Solovjov VP. SLW modeling of radiation transfer in comprehensive combustion predictions. Combust Sci Technol 2018;190:1392–408. doi:10.1080/00102202.2018.1452123.

[29] Ali HB, Askri F, Nasrallah S Ben. Comparative study of WSGG and SLW models coupled with control volume finite element method for non gray radiation prediction. Int J Therm Sci 2017;113:73–82. doi:10.1016/j.ijthermalsci.2016.11.009.

[30] Sun Y, Zhang X. Contributions of gray gases in SLW for non-gray radiation heat transfer and corresponding accuracies of FVM and P1 method. Int J Heat Mass Transf 2018;121:819–31. doi:10.1016/j.ijheatmasstransfer.2018.01.045.

[31] Yasar MS, Ozen G, Selçuk N, Kulah G. Assessment of improved banded model for spectral thermal radiation in presence of non-gray particles in fluidized bed combustors. Appl Therm Eng 2020;176:115322. doi:10.1016/j.applthermaleng.2020.115322.

[32] Payan S, Hosseini Sarvari SM, Behzadmehr A. Reconstruction of Temperature Distribution in the Combustion Region of a Non-Gray Medium. Numer Heat Transf Part A Appl 2015;68:908–24. doi:10.1080/10407782.2015.1023125.

[33] Klason T, Bai XS, Bahador M, Nilsson TK, Sundén B. Investigation of radiative heat transfer in fixed bed biomass furnaces. Fuel 2008;87:2141–53. doi:10.1016/j.fuel.2007.11.016.

[34] Ströhle J. Wide band correlated-k approaches for non-grey radiation modelling in oxy-fuel combustion with dry recycling. Fuel 2011;90:3007–13. doi:10.1016/j.fuel.2011.05.002.

[35] Liu F, Consalvi JL, Coelho PJ, Andre F, Gu M, Solovjov V, et al. The impact of radiative heat transfer in combustion processes and its modeling – with a focus on turbulent flames. Fuel 2020;281:118555. doi:10.1016/j.fuel.2020.118555.

[36] Webb BW, Solovjov VP, André F. The spectral line weighted-sum-of-gray-gases (SLW) model for prediction of radiative transfer in molecular gases, 2019, p. 207–98. doi:10.1016/bs.aiht.2019.08.003.

[37] Ozen G, Selçuk N. Sensitivity of Radiation Modeling to Property Estimation Techniques in the Freeboard of Lignite-Fired Bubbling Fluidized Bed Combustors (BFBCs). Combust Sci Technol 2014;186:684–97. doi:10.1080/00102202.2014.883848.

[38] Hanjalić K, Popovac M, Hadžiabdić M. A robust near-wall elliptic-relaxation eddy-viscosity turbulence model for CFD. Int J Heat Fluid Flow 2004;25:1047–51. doi:10.1016/j.ijheatfluidflow.2004.07.005.

[39] Pearson JT, Webb BW, Solovjov VP, Ma J. Efficient representation of the absorption line blackbody distribution function for H2O, CO2, and CO at variable temperature, mole fraction, and total pressure. J Quant Spectrosc Radiat Transf 2014;138:82–96. doi:10.1016/j.jqsrt.2014.01.019.

[40] Khalil EE, Truelove JS. Calculation of radiative heat transfer in a large gas fired furnace. Lett Heat Mass Transf 1977;4:353–65. doi:10.1016/0094-4548(77)90124-2.

[41] Jurić F, Stipić M, Samec N, Hriberšek M, Honus S, Vujanović M. Numerical investigation of multiphase reactive processes using flamelet generated manifold approach and extended coherent flame combustion model. Energy Convers Manag 2021;240:114261. doi:10.1016/j.enconman.2021.114261.

[42] Dhuchakallaya I, Watkins AP. Application of spray combustion simulation in DI diesel engine. Appl Energy 2010;87:1427–32. doi:10.1016/j.apenergy.2009.08.029.

[43] Abramzon B, Sirignano WA. Droplet vaporization model for spray combustion calculations. Int J Heat Mass Transf 1989;32:1605–18. doi:10.1016/0017-9310(89)90043-4.

[44] Bešenić T, Baleta J, Pachler K, Vujanović M. Numerical modelling of sulfur dioxide absorption for spray scrubbing. Energy Convers Manag 2020;217:112762. doi:10.1016/j.enconman.2020.112762.

[45] Bešenić T, Mikulčić H, Vujanović M, Duić N. Numerical modelling of emissions of nitrogen oxides in solid fuel combustion. J Environ Manage 2018;215:177–84. doi:10.1016/J.JENVMAN.2018.03.014.

[46] Cao H, Sun S, Liu Y, Wall TF. Computational Fluid Dynamics Modeling of NO x Reduction Mechanism in Oxy-Fuel Combustion †. Energy & Fuels 2010;24:131–5. doi:10.1021/ef900524b.

[47] Vujanović M, Duić N, Tatschl R. Validation of reduced mechanisms for nitrogen

chemistry in numerical simulation of a turbulent non-premixed flame. React Kinet Catal Lett 2009;96:125–38. doi:10.1007/s11144-009-5463-2.

[48] Karlsson A, Magnusson I, Balthasar M, Mauss F. Simulation of Soot Formation Under Diesel Engine Conditions Using a Detailed Kinetic Soot Model 1998. doi:10.4271/981022.

[49] Priesching P, Tatschl R, Mauss F, Saric F, Netzell K, Bauer W, et al. Soot Particle Size Distribution~A Joint Work for Kinetic Modelling and Experimental Investigations, 2005. doi:10.4271/2005-24-053.

[50] Petranović Z, Bešenić T, Vujanović M, Duić N. Modelling pollutant emissions in diesel engines, influence of biofuel on pollutant formation. J Environ Manage 2016:1–9. doi:10.1016/j.jenvman.2017.03.033.

[51] Csemány D, DarAli O, Rizvi SAH, Józsa V. Comparison of volatility characteristics and temperature-dependent density, surface tension, and kinematic viscosity of n-butanol-diesel and ABE-diesel fuel blends. Fuel 2022;312:122909. doi:10.1016/j.fuel.2021.122909.

[52] Stančin H, Mikulčić H, Wang X, Duić N. A review on alternative fuels in future energy system. Renew Sustain Energy Rev 2020;128:109927. doi:10.1016/j.rser.2020.109927.

[53] Sremec M, Taritaš I, Sjerić M, Kozarac D. Numerical Investigation of Injection Timing Influence on Fuel Slip and Influence of Compression Ratio on Knock Occurrence in Conventional Dual Fuel Engine. J Sustain Dev Energy, Water Environ Syst 2017;5:518–32. doi:10.13044/j.sdewes.d5.0163.

[54] Coelho PJ. Advances in the discrete ordinates and finite volume methods for the solution of radiative heat transfer problems in participating media. J Quant Spectrosc Radiat Transf 2014;145:121–46. doi:10.1016/j.jqsrt.2014.04.021.

[55] Mishra SC, Roy HK. Solving transient conduction and radiation heat transfer problems using the lattice Boltzmann method and the finite volume method 2007:89–107. doi:10.1016/j.jcp.2006.08.021.

[56] Chai JC, Parthasarathy G, Lee HS, Patankar S V. Finite volume radiative heat transfer procedure for irregular geometries. J Thermophys Heat Transf 1995;9:410–5. doi:10.2514/3.682.

[57] Fernandez SF, Paul C, Sircar A, Imren A, Haworth DC, Roy S, et al. Soot and spectral radiation modeling for high-pressure turbulent spray flames. Combust Flame 2018;190:402–15. doi:10.1016/j.combustflame.2017.12.016.

PAPER 7

Assessment of the Accuracy and Computational Efficiency of the SLW-1 Model in the Numerical Simulation of an Internal Combustion Engine

Filip Jurić[*]
Faculty of Mechanical Engineering and Naval Architecture
University of Zagreb, Zagreb, Croatia
e–mail: filip.juric@fsb.hr

Pedro J. Coelho
IDMEC, Instituto Superior Técnico
Universidade de Lisboa, Lisbon, Portugal

Peter Priesching
AVL List GmbH, Graz, Austria

Neven Duić
Faculty of Mechanical Engineering and Naval Architecture
University of Zagreb, Zagreb, Croatia

Milan Vujanović
Faculty of Mechanical Engineering and Naval Architecture
University of Zagreb, Zagreb, Croatia

ABSTRACT

Purpose – The spectral line weighted-sum-of-grey-gases (SLW) model and its minimal formulation consisting of a single grey gas and a clear one (SLW-1) are implemented in a computational fluid dynamics (CFD) code and applied in the simulation of an internal combustion engine (ICE). The SLW-1 model is firstly validated for one-dimensional radiative transfer problems without combustion and a non-premixed turbulent piloted methane-air jet flame (Sandia flame D). The accuracy and the efficiency of the SLW-1 and the influence of turbulence-radiation interaction (TRI) are then investigated in the simulation of an ICE and in the prediction of pollutant emissions.

Design/methodology/approach – The governing equations for the two-phase turbulent reactive flow in an ICE are numerically solved. The k-ζ-f model is used for turbulence closure, while the 3-zone extended coherent flame model is employed for combustion modelling. The finite volume method is used to solve the radiative transfer equation (RTE). Models for spray

---

[*] Corresponding author

and droplet break-up, evaporation and combustion of droplets, thermal NO formation and soot formation, and oxidation are also employed.

Findings - The SLW-1 model is computationally more efficient than the SLW model for ICE simulations, and the accuracy is quite satisfactory. In addition, the computational requirements are similar, and the predictions are more accurate compared to the classical weighted-sum-of-grey gases (WSGG) model. When radiative heat transfer is considered, and the nongrey radiative properties are calculated using the SLW-1 model, the accuracy of pollutant emission predictions is increased, being relatively close to the results obtained using SLW. The influence of TRI is small for the studied problem.

Originality – According to the authors' knowledge, the SLW-1 model accounting for TRI was never implemented in CFD calculations for complex geometries that feature a 3D moving mesh, such as ICEs.

KEYWORDS

Radiative heat transfer, participating media, SLW-1 model, internal combustion engines, pollutant emissions

NOMENCLATURE

Latin	Description	Unit
a	Grey gas weights	
c	Progress variable	
C_D	Drag coefficient	
C_P	Cunningham correction factor	
C_1	WAVE break-up model constant 1	
C_2	WAVE break-up model constant 2	
Ci	Absorption cross-section	
d	Droplet diameter	m
D	Effective diffusion coefficient	$m^2 \, s^{-1}$
E_a	Activation energy	$J \, kg^{-1}$
I	Radiation intensity	$W \, m^{-2} \, srad^{-1}$
f	Frequency	Hz
F_d	Drag force	N
gi	Cartesian component of the force vector	$m \, s^{-2}$
G	Incident radiaiton	$W \, m^{-2}$
h	Enthalpy	$kJ \, kg^{-1}$
H	Total enthalpy interfacial exchange term	$kJ \, kg^{-1}$
k	Turbulent kinetic energy	$m^2 \, s^{-2}$
l	Length of the nozzle	m
m	Mass	kg

2

$\dot{m}$	Mass flow	kg s^{-1}
M	Molar mass	kg kmol^{-1}
N	Number	
p	Pressure	Pa
q	Heat flux	W m^{-2}
q^t	Turbulent heat flux	W m^{-2}
r	Droplet radius	m
R	Ideal gas constant	J (mol K)$^{-1}$
S$_L$	Laminar flame speed	m s^{-1}
s	Control angle vector	
t	Time	s
T	Temperature	K
u,v	Velocity	m s^{-1}
V	Volume	m^3
w	Molecular weight of species k	kg kmol^{-1}
x	Cartesian coordinates	m
Y	Mass fraction	

Greek	Description	Unit
α	Volume fraction	
β	Coefficient in Arrhenius law	
γ	Half outer cone angle	rad
ζ	Velocity scale ratio	
ε	Turbulent dissipation rate	m^2 s^{-3}
Γ	Diffusion coefficient	
κ	Absorption coefficient	m^{-1}
λ_w	Wavelength	m
μ^t	Turbulent viscosity	Pa s
v	Eddy viscosity	
ρ	Density	kg m^{-3}
τ_a	Break-up time	s
τ	Autoignition delay time	s
ω	Reaction rate	
Ω	Control angle	sr

ABBREVIATIONS

ALBDF	Absorption Line Black Body Distribution Function
BC	Boundary Connection
BDC	Bottom Dead Centre
CA	Crank Angle
CFD	Computational Fluid Dynamics
CPU	Central Processing Unit

ECFM-3Z	Three-zone Extended Coherent flame model
FVM	Finite Volume Method
ICE	Internal Combustion Engine
RTE	Radiative Transfer Equation
SLW	Spectral line weighted-sum-of-grey-gases
SLW-1	Spectral line weighted-sum-of-grey-gases for one grey gas and transparent window
TRI	Turbulence Radiation Interaction
WSGG	Weighted-sum-of-grey gases
0D	Non-Dimensional
3D	Three-Dimensional

1. INTRODUCTION

The current increase in fossil fuel prices and the uncertainty of fuel supply have increased the pressure for the energy transition. Among the options available to implement this transition are the electrification of the transport sector and the development of new carbon-neutral fuels. Electrification requires additional investment and is more focused on passenger transport. At the same time, the development of new fuels is expected to allow for a faster energy transition in heavy-duty transport due to the possibility of being implemented in the current infrastructure. Carbon-neutral fuels are still not thoroughly investigated, and their implementation in the existing transportation system needs further research (Stančin et al., 2020). Computational fluid dynamics (CFD) is often used to investigate the combustion performance of such fuels.

The present work is concerned with the numerical simulation of a diesel engine, and particular attention is dedicated to the radiative transfer calculation. Indeed, Paul et al. (2019a) pointed out that accounting for radiative heat transfer in CFD simulations could improve predicting the temperature field and pollutant formation processes in ICEs. The solution of the Radiative Transfer Equation (RTE) adds an additional layer of complexity to the numerical simulations, increasing the accuracy of the calculated temperature at the expanse of higher computational demand (Viskanta, 2008). Detailed modelling of radiative heat transfer in diesel engine-like conditions was first reported by Mengüc et al., 1985. They used the method of spherical harmonics, P1 and P3 methods to solve the RTE in an axisymmetric, finite cylindrical geometry using temperature, soot, and fuel droplet distributions representative of a diesel engine during combustion. The importance of scattering from fuel droplets and of the spatial variation of the extinction coefficient was investigated. They found that scattering by fuel droplets can be neglected, but the spatial variation of the absorption coefficient needs to be taken into account. More recently, the influence of radiation on the operation of a diesel engine was investigated by Yoshikawa and Reitz (2009), who showed that the influence of radiative heat transfer on nitrogen oxides (NO_x) and soot emissions are not significant, with about a 3% difference in NO_x. In contrast, Benajes et al. (2015a) that the radiation emission from soot particles can be a significant component of the efficiency losses in modern direct-injection diesel engines. Benajes et al. (2015b) investigated the influence of different injection pressures. They found that an increase in the injection pressure caused an increase in the flame lift-off

length and a decrease in the soot volume fraction, spectral radiation intensity and radiative heat transfer. Chishty et al. (2016) reported that carbon dioxide (CO_2) and water vapour (H_2O) have a more important contribution than soot for the net radiative transfer in a liquid fuel-fired pressurised combustion chamber under typical ICE operating conditions. Similar conclusions were obtained by Yue and Reitz (2019) for an experimental diesel engine in Sandia Laboratory.

Different methods are available to solve the RTE and to calculate the radiative properties of the medium. Paul et al. (2019b) found that the solution of the RTE obtained using the P1 method along with a stepwise grey model with five bands for the calculation of the radiative properties of the medium predicted reabsorption with an error lower than 10% for different ICE operating conditions in comparison with the photon Monte Carlo/line-by-line methods. In contrast, the error of the P1/grey gas model was about 60%. The influence of radiative transfer on NO_x and soot formation in large marine engines was investigated in detail by Geringer (2021) using two different RTE solvers, namely the discrete ordinates method (DOM) and P1 method. The DOM, along with the WSGG model, was applied to an industrial engine by Jurić et al. (2020a). They found a decrease of about 20% in NO_x emissions and an increase in soot emissions compared with calculations without radiation. Increased accuracy was obtained by considering radiation at the expense of about 50% additional computational time. Mukut and Roy (2020) investigated soot and NO_x formation during combustion in a constant volume chamber under Engine Combustion Network spray A conditions. A multiphase photon Monte Carlo model was used for solving RTE in the gas phase and liquid spray droplets. The results showed that solving the RTE equation affects soot formation predictions insignificantly and causes a marginal decline in NO prediction.

The SLW model takes into account the detailed spectra of the absorbing species and provides a more theoretically sound approach to determine the radiative properties of the medium than the WSGG model. The SLW model has been widely applied to calculate radiative transfer in high-temperature media, such as rocket exhaust gases (Yadav et al., 2017) and industrial combustion systems, e.g., fluidized bed combustors (Doner and Selçuk, 2013) and glass furnaces (Galtier et al., 2022). It was recently applied to a one-cylinder ICE by Jurić, et al. (2022a), who showed that around 6% of the total heat loss was due to radiation losses from H_2O and CO_2. However, the computational time was approximately twice that without radiation.

A simplified version of SLW model, referred to as SLW-1 model (Solovjov et al., 2011a), also accounts for the spectral line structure of the real gas but consists of a single grey gas and a clear gas. It was shown that good accuracy is achieved in comparison with line-by-line benchmark results by the optimal choice of the grey gas absorption coefficient and its weight (Solovjov et al., 2011b). Both SLW and SLW-1 models are based on the absorption line black body distribution function, which is determined from a high-resolution spectral database, and replace the integration of radiative emission and absorption over the wavelength with integration over the absorption cross-section. The SLW-1 model was applied to a fluidized bed combustor by Ozen et al. (2019) and compared with the grey gas approximation. Although accurate results and lower computational demand were achieved using the SLW-1 model in comparison with SLW, the errors in the prediction of heat flux and radiative heat source increased in the presence of non-grey particles compared to those with grey particles. The first 3D implementation of SLW-1 for non-grey gas surrounded by non-grey walls was reported by

5

Yasar et al. (2020). The authors showed that the computational time is approximately 20-25 times lower than the SLW model while achieving reasonable accuracy for air and oxy-fired conditions.

Additional improvement in the accuracy of radiative transfer calculations in turbulent reactive flows is achieved by accounting for turbulence-radiation interaction (TRI), which is especially important in the case of Reynolds-averaged Navier–Stokes (RANS) equations. The TRI arises from the highly non-linear coupling between temperature fluctuations, species concentration and radiation intensity (Coelho, 2007). In most studies, TRI has not been considered, and the average quantities are used for the solution of the RTE, which in the case of turbulent combustion, can lead to errors in the range of 10% to 100% in the calculation of the mean radiation intensity (Coelho, 2012). The influence of TRI on pollutant formation for diesel engine conditions was investigated by Fernandez et al. (2018), who concluded that TRI influences radiative heat transfer for around 10% of net radiative heat transfer. At the high pressures found in ICEs, the TRI effects are small, leading to a few percent increase in radiative emission and absorption and less than a 5% increase in the radiation reaching the walls (Paul et al., 2019a).

According to the available literature, the SLW-1 and TRI have never been used to perform radiative transfer calculations in ICEs. Additionally, radiative heat transfer models have seldom been applied to complex 3D geometries with moving boundaries that require mesh rezoning, such as in ICEs, which are addressed in the present work.

Radiative heat transfer calculations require the input of temperature and absorbing species concentration distributions, which are obtained from the combustion model in reactive flows. The tabulation of chemistry properties for determining flamelet speed, autoignition, and enthalpy sources has recently attracted the attention of the combustion scientific society to the significantly reduced computational time during simulation processing and retention of all the effects of detailed chemistry (Kalbhor and Oijen, 2021). These tabulation methods require long pre-processing that is specific to the operating conditions.

The three-zone extended coherent flame model (ECFM3Z) developed by Colin and Benkenida (2004) is used in the present work. It has proved to be a robust and relatively accurate combustion model that uses pre-tabulated databases for an arbitrary fuel. The ECFM-3Z combustion model distinguishes all three main regimes present in diesel engines, namely auto-ignition, premixed flame and non-premixed flame (Mobasheri et al., 2012). The main disadvantage of this approach is the sensitivity of the premixed freely propagating flame reactors to high-temperature conditions, which often leads to unsuccessful calculations (Jurić et al., 2022b). Therefore, the laminar flame speed values at high temperatures must be extrapolated from successful reactors to have a fast, fully automated, and reliable procedure. The method developed by Jurić et al. (2022b) for the tabulation of laminar flame speed and auto-ignition for the ECFM-3Z model was used in this work.

The objective of the present work is to implement the SLW-1 model in combination with TRI for the calculation of radiative transfer in the AVL FIREm^{TM} code (AVL GmbH, 2022). According to the authors' knowledge, the SLW-1 model, and TRI were never implemented in the CFD framework for a complex geometry that features a 3D moving mesh and periodic

boundary conditions. The influence of radiative heat transfer and TRI on pollutant emissions in an ICE will be investigated.

2. MATHEMATICAL MODEL

2.1. Turbulence model

In this work, RANS CFD simulations are performed using the AVL FIREm™ software. The k-ζ-f model (Hanjalić et al., 2004) is employed for turbulence modelling. The k-ζ-f model is a suitable turbulence model commonly used in ICE combustion simulations that feature describing the spray injection. One advantage of the k-ζ-f model is its robustness for modelling strong swirling flows characteristic of ICE.

The k-ζ-f model aims to improve the numerical stability of the $\overline{v^2} - f$ model by solving the velocity scale ratio equation ($\zeta = \overline{v^2}/k$). The eddy viscosity, v, is obtained from:

$$v = C_\mu \zeta \frac{k^2}{\varepsilon}$$ (1)

where C_μ is a model constant, ζ is the velocity scale ratio, k is the turbulent kinetic energy, and ε is the rate of dissipation of turbulent kinetic energy. The transport equations of the turbulence model that are required to be solved are the following:

$$\rho \frac{Dk}{Dt} = \rho(P_k - \varepsilon) + \frac{\partial}{\partial x_j}\left[\left(\mu + \frac{\mu_t}{\sigma_k}\right)\frac{\partial k}{\partial x_j}\right]$$ (2)

$$\rho \frac{D\varepsilon}{Dt} = \rho \frac{(C_{\varepsilon 1}^* P_k - C_{\varepsilon 2}\varepsilon)}{T} + \frac{\partial}{\partial x_j}\left[\left(\mu + \frac{\mu_t}{\sigma_\varepsilon}\right)\frac{\partial \varepsilon}{\partial x_j}\right]$$ (3)

$$\rho \frac{D\zeta}{Dt} = \rho f - \rho \frac{\zeta}{k} P_k + \frac{\partial}{\partial x_j}\left[\left(\mu + \frac{\mu_t}{\sigma_\zeta}\right)\frac{\partial \zeta}{\partial x_j}\right]$$ (4)

where f is calculated from:

$$f - L^2 \frac{\partial^2 f}{\partial x_j \partial x_j} = \left(C_1 + C_2 \frac{P_k}{\varepsilon}\right)\frac{(2/3 - \zeta)}{T}$$ (5)

The turbulent time scale, T, and the length scale, L, are given by:

$$T = \max\left(\min\left(\frac{k}{\varepsilon}, \frac{a}{\sqrt{6}C_\mu |S|\zeta}\right), C_T \left(\frac{\upsilon}{\varepsilon}\right)^{1/2}\right)$$ (6)

$$L = C_L \max\left(\min\left(\frac{k^{3/2}}{\varepsilon}, \frac{k^{1/2}}{\sqrt{6}C_\mu |S|\zeta}\right), C_\eta \frac{\upsilon^{3/4}}{\varepsilon^{1/4}}\right)$$ (7)

where $C_{\varepsilon 1}^* = 1.4 \left(1 + \frac{0.012}{\zeta}\right)$, $C_{\varepsilon 2}$, σ_k, σ_ε, σ_ζ, C_1, C_2, a, C_T, C_η and C_L are constants of the model and S is the strain rate.

2.2. Spray model

It is known that the spray process influences air-fuel mixing, combustion, and pollutant formation processes (Gopinath et al., 2020). In this work, droplet disintegration of the spray

process is modelled as Euler Lagrangian spray. The momentum equation of Lagrangian parcels is described with Newton's second law, where the drag force is only considered to have an impact on the parcel momentum:

$$0.5\pi\, r^2 \rho C_D u_i{}^2 = m_p \frac{du_{pi}}{dt} \tag{8}$$

where the drag coefficient C_D is calculated from Schiller Neuman correlation formulation for a single sphere, based on Reynolds number (Re):

$$C_D = \begin{cases} \dfrac{24}{ReC_p}(1 + 0.15Re^{0.687}) & Re < 10^3 \\[2ex] \dfrac{0.44}{C_p} & Re \geq 10^3 \end{cases} \tag{9}$$

Reynolds number is defined as the combination of inertial forces for injected fuel parcels and viscous forces for the fluid viscosity.

$$Re = \frac{|\overline{u_p}|D_p}{\nu_g} \tag{10}$$

Cunningham correction factor C_p is based on Knudsen number (Cunningham, 1910):

$$C_p = 1 + Kn\left(2.492 + 0.84e^{\frac{-1.74}{Kn}}\right) \tag{11}$$

Knudsen number was defined as the ratio between the free path length of the gas phase and parcel diameter D_p.

$$Kn = \frac{1}{D_p}\frac{k_b T_g}{d_g \sqrt{2}\,\pi p_g} \tag{12}$$

Where mean molecule diameter in the gas phase, d_g=2.8·10^{-10} m. WAVE break-up model was employed for the growth of an initial perturbation on a liquid surface, where the radius reduction ratio of the parcels is defined as (Reitz and Diwakar, 1987):

$$\frac{dr}{dt} = -\frac{\Lambda\Omega(r - C_1 * \Lambda)}{3.726C_2 r} \tag{13}$$

The constant C_2 is used for tuning the break-up time equation to account for injector geometry. The droplet radius of parcels is defined with C_1 constant and the highest wave wavelength value on the surface of the parcel, where Λ is the wavelength and Ω is the growth rate of wave, which depends on the fluid properties in the cell. The size of droplet diameters ranges from 0.005 to 0.1 mm, and the radius of disintegrated droplets in each subsequent step is defined from C_1 constant that was set to model a default value of 0.61 (Liu et al., 1993). Different Weber number correlations were used for the droplet interaction with the wall based on the work of Jiro et al. (1994).

Abramzon model was employed for spray droplet evaporation, which accounts for transient heat and mass transfer of spherical droplets (Abramzon and Sazhin, 2006). In addition to the presence of liquid ligaments and the break-up of droplets, the evaporation process occurs simultaneously in the spray region. It occurs as a result of the reduction in droplet diameters as

8

they travel through the surrounding gas due to evaporation. This approach is based on the classical film theory, where the resistances to heat and mass transfer are represented by fictitious gas films of constant thickness, denoted as δ_T and δ_m. However, in the case of evaporating droplets, these film thickness values need to be adjusted using correction factors F_T and F_M. The evaporation of droplets is described by empirical Nusselt and Sherwood laws, which are derived from experiments conducted on single droplets under specific conditions. In Equation (14), the evaporation rate of droplets is defined (Abramzon and Sirignano, 1989).

$$\dot{m} = \pi \overline{\rho_g} D_d Sh \ln(1 + B_M) \tag{14}$$

$$\dot{m} = \pi \frac{\overline{k_g}}{\overline{c_{pF}}} D_d Nu \cdot \ln(1 + B_T) \tag{15}$$

where D_d is the droplet diameter, and $\overline{\rho_g}$, is average density, $\overline{\beta_g}$ is binary diffusion coefficient, and $\overline{k_g}$ is thermal conductivity of the gas mixture at reference conditions, $\overline{c_{pF}}$ is the average specific heat capacity of the vapour. The dimensionless quantity Nusselt and Sherwood numbers are calculated from unidimensional number non-evaporating droplet Sh_0 and Nu_0, and the corresponding correction factors for the film thickness F_M and F_T.

$$Sh = 2 + \frac{Sh_0 - 2}{F_M} \tag{16}$$

$$Sh_0 = 2 + 0.552\, Re^{\frac{1}{2}} Sc^{\frac{1}{3}} \tag{17}$$

$$Nu = 2 + \frac{Nu_0 - 2}{F_T} \tag{18}$$

$$Nu_0 = 2 + 0.552\, Re^{\frac{1}{2}} Pr^{\frac{1}{3}} \tag{19}$$

The mass and heat transfer numbers, B_M and B_T are then derived from the following equation.

$$B_M = \frac{Y_{Fs} - Y_\infty}{1 - Y_{Fs}} \tag{20}$$

$$B_T = \frac{\overline{c_{pF}}(T_\infty - T_s)}{L(T_s) + \frac{Q_L}{\dot{m}}} \tag{21}$$

In Equations (20) and (21), Y_{FS} represents the fuel mass fraction, and $L(T_s)$ represents the latent heat of vaporization at temperature T_s. The subscript s indicates the condition at the surface of the droplet, while the subscript ∞ represents the ambient condition. Q_L is the heat transferred to the droplet, and $\dot{m}$ is vaporisation rate.

2.3. Combustion modelling

The flamelet model ECFM-3Z was employed for combustion process modelling inside ICE, which has decoupled treatment of chemistry and turbulence. ECFM-3Z is based on an equation for flame surface density that incorporates the impact of turbulent eddies on the wrinkling of the flame front surface.

In the ECFM-3Z model, all computational cells are split into three regions to describe non-premixed combustion: unmixed fuel zone, mixed zone, and unmixed initial air zone (Colin and

Benkenida, 2004). In Figure 1, the scheme of 3 zones of ECFM-3Z is shown. The overall state influences each zone within the computational cell. If the fuel is introduced into the system and observed in a representative computational cell, initially only consisting of unburned and unmixed air, the fuel occupies a finite amount of cell space after evaporation. During this stage, it remains unmixed with the existing air, thereby creating two zones (unmixed and unburned air and unmixed and unburned fuel). Subsequently, the fuel and air begin to mix within the intermediate zone, giving rise to the third zone, which is mixed and unburned. At this point, the mixed zone is prepared for monitoring the ignition criterion. Once the ignition criterion is met, combustion initiates and propagates through the mixed zone, dividing it into two sub-zones: the burnt and unburned mixed zone.
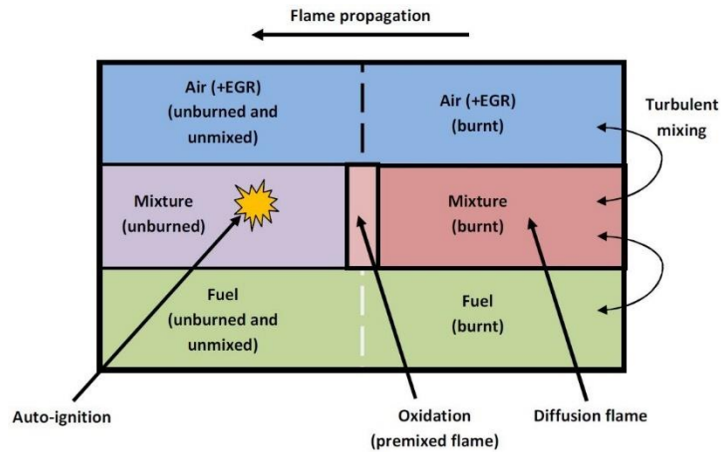

Figure 1 Mixing zones of ECFM-3Z model (Colin and Benkenida, 2004)

The representation of gas state determines the fundamental transport equations in the ECFM3Z modelhrough two properties: progress variable c and the mixture fraction Z. Additionally, transport equations for the following species are also solved (Colin et al., 2003): oxygen (O_2), nitrogen (N_2), nitrogen monoxide (NO), CO_2, carbon monoxide (CO), hydrogen (H_2), H_2O, hydrogen (H) and nitrogen (N) cation, oxygen (O), hydroxide (OH) anions.

$$\frac{\partial \bar{\rho}\tilde{Y}_X}{\partial t} + \frac{\partial \bar{\rho}\tilde{u}_i\tilde{Y}_X}{\partial x_i} = \frac{\partial}{\partial x_i}\left(\left(\frac{\mu}{Sc} + \frac{\mu_t}{Sc_t}\right)\frac{\partial \tilde{Y}_X}{\partial x_i}\right) + \bar{\rho}\tilde{\tilde{S}}_X \qquad (22)$$

t is the time variable, x_i is the space coordinate, μ is dynamic viscosity. Sc is Schmidt number, and t index indicates turbulent values. The turbulent Schmidt number is defined similarly, incorporating both the turbulent momentum transfer (eddy viscosity) and the turbulent mass transfer. $\tilde{\tilde{S}}_X$ is the mass-specified source term of chemical species X and $\tilde{Y}_X$ is its average mass fraction, which is defined as:

$$\tilde{Y}_X = \frac{\overline{m_x}}{\overline{m}} \qquad (23)$$

where $\overline{m_x}$ is the average mass of species X, and $\overline{m}$ is the total mass inside a cell. The previously defined general transport equation is divided to account for the burned and unburned subzones of the computational cell when considering the fuel species.

$$\frac{\partial \bar{\rho}\tilde{Y}_{uF}}{\partial t} + \frac{\partial \bar{\rho}\tilde{u}_i \tilde{Y}_{uF}}{\partial x_i} = \frac{\partial}{\partial x_i}\left(\left(\frac{\mu}{Sc} + \frac{\mu_t}{Sc_t}\right)\frac{\partial \tilde{Y}_{uF}}{\partial x_i}\right) + \bar{\rho}\tilde{S}_F \ c + \overline{\dot{\omega}_{uF}} - \overline{\dot{\omega}_{u\to b}} \qquad (24)$$

$$\frac{\partial \bar{\rho}\tilde{Y}_{bF}}{\partial t} + \frac{\partial \bar{\rho}\tilde{u}_i \tilde{Y}_{bF}}{\partial x_i} = \frac{\partial}{\partial x_i}\left(\left(\frac{\mu}{Sc} + \frac{\mu_t}{Sc_t}\right)\frac{\partial \tilde{Y}_{bF}}{\partial x_i}\right) + \bar{\rho}\tilde{S}_F \ (1-c) + \overline{\dot{\omega}_{bF}} + \overline{\dot{\omega}_{u\to b}} \qquad (25)$$

This partition of the fuel species into the unburned $\tilde{Y}_{uF}$, and burned $\tilde{Y}_{bF}$ is necessary to enable the influence of both propagating and diffusion flames. The rate of gaseous fuel production, resulting from phenomena such as the evaporation of liquid fuel droplets, is represented by the symbol $\tilde{S}_F$. This production rate is distributed between the burned and unburned sub-zones based on the progress variable $\tilde{c}$. Progress variable is calculated based on the assumption that the flame is an interface of infinitesimal thickness that separates the fresh gases from the burned gases and is given in Equation (26), where $\overline{\tilde{Y}_{TuF}}$ is the fuel mass fraction before the start of the combustion.

$$c = 1 - \frac{\overline{\tilde{Y}_{uF}}}{\overline{\tilde{Y}_{TuF}}} \qquad (26)$$

The reaction rate at which the unburned fuel is consumed in propagating flame is represented by the variable $\overline{\dot{\omega}_{uF}}$, and the rate on the opposite side represents the burned fuel oxidation in diffusive flame. The rates of fuel consumption are influenced by the local flame surface density and laminar flame velocity, and their calculations are outlined in the following section. In situations where the local equivalence ratio is rich, the unburned sub-zone lacks sufficient oxygen to completely consume all the unburned fuel. As a result, a portion of the unburned fuel represented with term $\overline{\dot{\omega}_{u\to b}}$ is transferred into the burned sub-zone through the source term. $\overline{\dot{\omega}_{u\to b}}$ is the source term due to the mixing process, which is defined as the turbulent properties and partial fuel density.

$$\overline{\dot{\omega}_{u\to b}} = \frac{\varepsilon}{k}\frac{\tilde{Y}_{Fu}}{\rho_{Fu}}\left(1 - \tilde{Y}_{Fu}\right) \qquad (27)$$

where k is turbulent kinetic energy and ε is the rate of turbulent energy dissipation from the turbulence model. Through the mixing turbulent time scale, turbulence interacts with the development of the combustion process.

In ECFM-3Z, the fuel combustion rate per unit volume is define as the product of flame surface density and the local fluid velocity of fuel/oxidizer mixture. The transport equation of flame surface density, Σ is defined as (Eder et al., 2018):

$$\frac{\partial \Sigma}{\partial t} + \frac{\partial \tilde{u}_i \Sigma}{\partial x_i} = \frac{\partial}{\partial x_i}\left(\frac{1}{\bar{\rho}}\left(\frac{\mu}{Sc} + \frac{\mu_t}{Sc_t}\right)\frac{\partial \Sigma}{\partial x_i}\right) + (P_1 + P_2 + P_3)\Sigma - D \qquad (28)$$

where source terms on the right-hand side are defined with the following equations:

$$P_1 = 1.6 \ K_t \qquad (29)$$

$$P_2 = \frac{2}{3}\frac{\partial \tilde{u}_i}{\partial x_i} \qquad (30)$$

$$P_3 = \frac{2}{3} S_L \frac{1-c}{c} \Sigma \tag{31}$$

$$D = S_L \frac{\Sigma^2}{1-c} \tag{32}$$

In Equation (29), K_t is intermittent turbulence net flame stretch defined by Hawkes and Chen (2005). S_L is laminar flame speed, which is in this work calculated from a pre-generated lookup database (later discussed).

Finally, $\overline{\dot{\omega}_{uF}}$ in Equation (24) is computed from the flame surface density and the laminar flame velocity:

$$\overline{\dot{\omega}_{uF}} = \bar{\rho} \tilde{Y}_{uF} \Sigma S_L \tag{33}$$

2.3.1. Ignition modelling

Within the ECFM-3Z combustion model, a straightforward methodology for ignition tracking is employed, drawing inspiration from the approach commonly utilized for predicting knocking in gasoline engines. This involves introducing a tracking intermediate species, denoted as I, which is entirely hypothetical and solely serves to determine the initiation time of ignition accurately. Initially, it was utilised exclusively to track the primary ignition. However, as da Cruz (2004) suggested, this principle can also be extended to account for low-temperature ignition, thereby incorporating the simulation of cool flame phenomena (Knop and Jay, 2006).

In the combustion model, the intermediate species undergo temporal evolution based on the following equation (da Cruz, 2004):

$$\frac{\partial \bar{\rho} \tilde{Y}_I}{\partial t} = \tilde{Y}_F \frac{\sqrt{\tau_d{}^2 + 4(1-\tau_d)\dfrac{\tilde{Y}_I}{\tilde{Y}_F}}}{\tau_d} \tag{34}$$

2.3.2. Autoignition and Laminar Flame Speed databases

For the calculation of input parameters, pre-calculated databases of autoignition and laminar flame speed are generated. The procedure for obtaining databases is founded on open-source Cantera chemistry solver reactors, where for autoignition, perfectly stirred non-dimensional reactors were used, while for the laminar flame speed, premixed one-dimensional (1D) reactors were used.

The general function featuring a lognormal distribution for equivalence ratio (φ), and exponential function for the pressure (p) direction was inherited from (Jurić, Ban, et al., 2022). Based on a chemical mechanism, the procedure calculates the permutation of all combinations in a prescribed grid with pressure, temperature, equivalence ratio and exhaust gas recirculation (EGR) points. The general function equation for the laminar flame speed takes the following term:

$$S_L(p,\varphi) = S_{L,ref} \left[\frac{1}{\varphi \sigma \sqrt{2\pi}} \exp\left(-\frac{(\ln \varphi - \mu)^2}{2\sigma^2} \right) \right] \left(\frac{p}{0.1 \text{MPa}} \right)^{\beta} \tag{35}$$

where μ and σ are parameters that are required to be calculated for each combination of the temperature and EGR. A solution for the best-fitting laminar flame speed is obtained with the employment of Levenberg-Marquardt algorithm, which is based on nonlinear regression. $S_{L,ref}$ is referent laminar flame speed at the selected calculated point, which was set at equivalence ratio 1, and pressure 0.1 MPa. The objective function for determining the best-fitting parameters is defined as:

$$f_{S_L} = \min \sum_{i=1}^{m} \left[S_{L_i} - S_L(p_i, \varphi_i) \right]^2 \tag{36}$$

where S_{L_i} is the calculated laminar flame speed from Cantera premixed solver, and m is the total number of points in pressure/equivalence ratio directions. The objective function is linearized for each iteration, where the φ is substituted with the $\varphi + \delta$. In order to determine δ, the following term is used:

$$f_{S_L} \approx S_L(p_i, \varphi_i + \delta) + \frac{\partial S_L(p_i, \varphi_i)}{\partial \varphi} \delta \tag{37}$$

The procedure of the developed method for generating the autoignition (τ) database is similar to the laminar flame speed database for the coherent flame models.

$$\tau(p, \varphi) = \tau_{ref} \left(\frac{p}{0.1\text{MPa}} \right)^\alpha (\varphi)^\beta \tag{38}$$

where α and β are two tuning parameters calculated for each combination of the temperature and EGR. The nonlinear least-squares method was employed with the calculation of α and β parameters that have the lowest disagreement with the raw data. The nonlinear least-squares method was employed also with the Levenberg-Marquardt algorithm.

2.4. NO formation modelling

In general, the most significant NO source in ICEs is thermal NO, while prompt NO and fuel NO are negligible. One of the most widely used models to describe NO formation at high temperatures is the extended Zeldovich mechanism:

$$N_2 + O \overset{k_1}{\leftrightarrow} N + NO \tag{39}$$

$$N + O_2 \overset{k_2}{\leftrightarrow} O + NO \tag{40}$$

$$N + OH \overset{k_3}{\leftrightarrow} H + NO \tag{41}$$

where k_1, k_2, k_3 are the reaction rates of elementary reactions (18) to (20), respectively. It is worth noting that all three reactions exhibit a strong temperature dependency. The rate change of NO concentration is given by:

$$\frac{dc_{NO}}{dt} = k_{1f}c_O c_{N_2} + k_{2f}c_N c_{O_2} + k_{3f}c_N c_{OH} - k_{1b}c_{NO}c_N - k_{2b}c_{NO}c_O \\ - k_{3b}c_{NO}c_H \tag{42}$$

where c denotes the concentration of a chemical species, while subscripts b and f denote backward and forward reactions, respectively.

2.4.1. Temperature fluctuation model

Combustion processes commonly occur in turbulent environments, necessitating special considerations for predicting NO (nitric oxide) concentrations. Significant discrepancies can arise in NO profiles when using mean values of temperature and density compared to incorporating the fluctuating values of these properties caused by turbulence. Therefore, it is crucial to account for the effects of turbulent fluctuations on the NO formation process. To address this, a presumed Probability Density Function (PDF) approach is employed to consider the impact of turbulent fluctuations on the kinetic rates of NO. The NO rate is integrated with respect to the fluctuation temperature like:

$$\bar{S}_{Y_{NO}} = \int_0^1 P(T) S_{Y_{NO}}(T)\, dT \tag{43}$$

where P(T) is PDF of the normalized temperature $\bar{T}$, and $S_{Y_{NO}}$ is instantaneous NO source. The PDF is assumed to be a second-moment beta function and is defined as:

$$P(T) = \frac{1}{B(\alpha,\beta)} T^{\alpha-1}(1-T)^{\beta-1} \tag{44}$$

$$B(\alpha,\beta) = \frac{\Gamma(\alpha)\Gamma(\beta)}{\Gamma(\alpha+\beta)} \tag{45}$$

Where Γ is gamma function and α and β are parameters that depend on the mean temperature $\bar{T}$ value and its variance T".

$$\alpha = \frac{1}{B(\alpha,\beta)} T^{\alpha-1}(1-T)^{\beta-1} \tag{46}$$

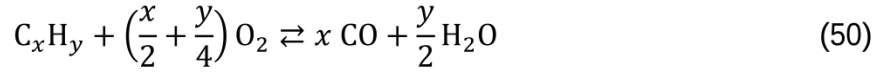$$B(\alpha,\beta) = \frac{\Gamma(\alpha)\Gamma(\beta)}{\Gamma(\alpha+\beta)} \tag{47}$$

$$\alpha = \bar{T}\left(\frac{\bar{T}(1-\bar{T})}{T"} - 1\right) \tag{48}$$

$$\beta = (1-\bar{T})\left(\frac{\bar{T}(1-\bar{T})}{T"} - 1\right) \tag{49}$$

The lower limit of T" is 0.002.

2.4.2. Soot formation and oxidation modelling

The soot formation and oxidation are modelled with kinetic soot model, that is available in AVL FIREm™ software (Priesching et al., 2005). The kinetic soot model is a reduced mechanism of the detailed mechanism proposed by Karlsson et al., (1998) that consists of seven gas phase reactions in the combustion model, with only one additional species for the soot for which an additional transport equation is being solved. The reduced mechanism applied in this work is described with the following chemical reactions:

$$C_xH_y + \left(\frac{x}{2} + \frac{y}{4}\right)O_2 \rightleftarrows x\,CO + \frac{y}{2}H_2O \tag{50}$$

$$2H_2 + O_2 \rightleftarrows 2H_2O \tag{51}$$

$$2CO + O_2 \rightleftarrows 2CO_2 \tag{52}$$

$$CO + H_2O \rightleftarrows CO_2 + H_2 \tag{53}$$

$$C_xH_y + C_xH_y \rightleftarrows 2x\,C + y\,H_2 \tag{54}$$

$$2C + O_2 \rightleftarrows 2CO \tag{55}$$

$$C + H_2O \rightleftarrows CO + H_2 \tag{56}$$

where the chemical species denoted by C represents the soot. In this work, C_xH_y is modelled for diesel fuel combustion as $C_{12}H_{26}$.

2.5. Radiative transfer model

In this work, the finite volume method (FVM) is used for the solution of the RTE, where only absorption and emission are considered. When Reynolds averaging is applied to the RTE and the SLW method is used to determine the radiative properties of the medium, the following equation is obtained:

$$\frac{d\bar{I}_{l,j}}{ds_l} = \overline{a_j \kappa_j I_b} - \bar{\kappa}_j \bar{I}_{l,j} \tag{57}$$

where $\bar{I}_{l,j}$ is the mean radiation intensity in the control angle l and for grey gas j, s_l is the spatial coordinate along the direction of propagation of the radiation intensity, κ_j is the absorption coefficient of the grey gas j, a_j is the respective emission weighting factor, and I_b is the blackbody radiation intensity. The transient term in RTE is neglected since the scale of radiation intensity change with time is negligible. The mean absorption coefficient is calculated based on the PDF in NO turbulence fluctuation model:

$$\bar{\kappa}_j = \int_0^1 \kappa_j(T)\,P(T)dT \tag{58}$$

The emission term in Equation (57) is calculated as well from the PDF:

$$\overline{a_j \kappa_j I_b} = \int_0^1 a_j(T)\kappa_j(T)I_b(T)\,P(T)dT \tag{59}$$

The radiation intensity wall boundary condition for grey, diffuse and opaque walls is given by:

$$\bar{I}_{w,l,j} = \epsilon_w a_j \frac{\sigma T_w^{\,4}}{\pi} + (1 - \epsilon_w) \sum_{D_{cl} < 0} I_{l,j}\,|D_{cl}| \tag{60}$$

where ϵ_w is the wall emissivity, σ is the Stefan-Boltzmann constant, T_w is the temperature of the wall, and D_{cl} is an auxiliary term that represents the integral over the control angle l of the cosine of the angle between the direction of propagation of radiation and the normal to wall.

In the ICE studied here, only a sector of the cylinder with a single injector is simulated, and periodic boundary conditions are implemented at symmetry planes. The radiation propagating into the computational domain at a boundary point where periodic boundary conditions are applied is related to the radiation leaving the computational domain at a rotationally periodic point and direction called boundary connection. An example is shown in Figure 1, which

illustrates how the boundary connection is implemented for defining the radiation intensity values at periodic boundary faces.

The radiation intensity represented by a green vector at the left boundary of the domain, $I_{w,1}$, is equal to the radiation intensity represented by a purple vector in the opposite direction, $\bar{I}_{wBC,l_{BC,3}}$, on the right-hand side boundary, while the radiation intensity represented by the orange vector at the left boundary is equal to that represented by the orange vector at the right boundary. Equation (61) describes this procedure, where the subscript BC in $\bar{I}_{wBC,l_{BC},j}$ denotes boundary connection values. The radiation intensity boundary connection is calculated and updated at the start of each time step.
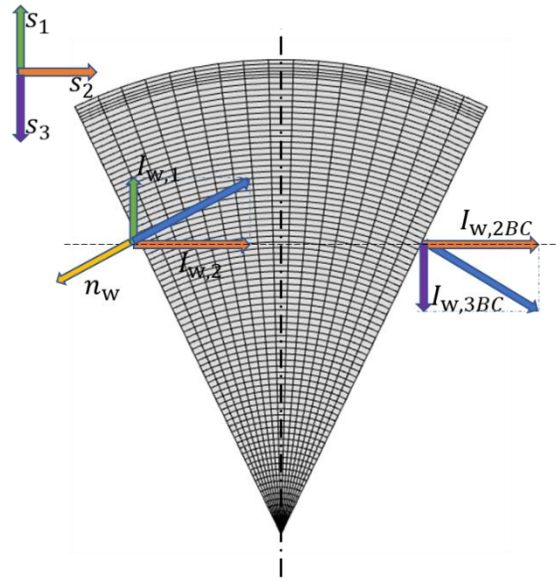

Figure 2 Boundary connection for periodic boundary conditions

$$\bar{I}_{w,l,j}(l) = \begin{cases} \bar{I}_{wBC,l_{BC},j}(l_{BC}), & (s_l \cdot n_w) < 0 \\ \bar{I}_{w,l,j}(l), & (s_l \cdot n_w) \geq 0 \end{cases} \tag{61}$$

The total intensity of radiation is the sum of grey gas intensities for CO_2 and H_2O:

$$I_l = \sum_{i=0}^{N_{CO2}} \sum_{j=0}^{N_{H2O}} I_{l,i,j} \tag{62}$$

The total incident radiation at a control volume is computed from the summation of all control angles:

$$G = \sum_{l=1}^{N_\Omega} I_l \Delta\Omega_l \tag{63}$$

The radiative source term of the energy equation is defined as the sum extended over all grey gases of the difference between the radiative emission and the radiative absorption, and is calculated by the following equation (Webb et al., 2019):

$$\nabla q = \sum_{j=0}^{N_g} \left(4\pi \overline{a_j \kappa_j I_b} - \overline{\kappa_j} \sum_{l=1}^{N_\Omega} \overline{I_{l,j}} \Delta \Omega_l \right)$$ (64)

2.5.1. SLW-1 model

In this work, the SLW-1 model is implemented by means of user function routines in the AVL FIREm™ CFD software. The results were compared with the grey gas WSGG model and SLW model that were previously implemented in AVL FIREm™ CFD software (Jurić, Coelho, et al., 2022; Jurić et al., 2020). WSGG coefficients in this work are based on HITEMP2010 correlations by Dorigon et al. (2013), and SLW model spectroscopic properties are calculated by HITEMP2010 correlation for absorption line blackbody distribution function (ALBDF) (Pearson et al., 2014). The SLW-1 model is a simplified formulation of the SLW model, where only one grey gas and a transparent window are considered. When the SLW-1 model is applied to the RTE, the two following equations are obtained, where the first one is for the transparent window, and the second one is for the single participating grey gas (Solovjov et al., 2011a):

$$\frac{d\bar{I}_{l,0}}{ds_l} = 0$$ (65)

$$\frac{d\bar{I}_{l,1}}{ds_l} = \overline{a_1 \kappa_1 I_b} - \overline{\kappa_1} \bar{I}_{l,1}$$ (66)

The parameters of the clear gas in SLW-1 are determined as follows:

$$a_0 = 1 - a_1$$ (67)
$$\kappa_0 = 0$$ (68)

The parameters of the single participating grey gas a_1 and κ_1 are unknown. To solve them, firstly, the double integration procedure from SLW model also is employed for SLW-1 model and is applied to CO_2 and H_2O mixture as a single gas with the following equations for two emissivities in the arbitrary band of the spectrum.

$$\varepsilon_{mix,j,L_2} = \sum_{i=0}^{N_{CO2}} \sum_{j=0}^{N_{H2O}} a_{w,i} a_{c,j} \left(1 - e^{-N(Y_w C_{w,i} + Y_c C_{c,j})L_1} \right)$$ (69)

$$\varepsilon_{mix,j,L_1} = \sum_{i=0}^{N_{CO2}} \sum_{j=0}^{N_{H2O}} a_{w,i} a_{c,j} \left(1 - e^{-N(Y_w C_{w,i} + Y_c C_{c,j})L_2} \right)$$ (70)

Where grey gas weights $a_{w,i}$ and $a_{c,j}$ are calculated using ALBDF:

$$a_{w,i} = F_w\big(\widetilde{C}_l, T_g, Y_w\big) - F_w\big(\widetilde{C}_l, T_g, Y_w\big)$$ (71)
$$a_{c,j} = F_c\big(\widetilde{C}_j, T_g, Y_c\big) - F_w\big(\widetilde{C}_j, T_g, Y_c\big)$$ (72)

Solovjov et al., (2011a) proposed several implementation methods for single-participating grey gas a_1 and κ_1 with the uncertainty analysis, from which $\varepsilon_1 - \varepsilon_2$ method is applied in this work, which fits the total emissivity calculated for two different pathlengths L_1, and L_2. Total emissivities are calculated by SLW model.

$$\varepsilon_{mix,1} = a_1\big(1 - e^{-\kappa_1 L_1}\big)$$ (73)
$$\varepsilon_{mix,2} = a_1\big(1 - e^{-\kappa_1 L_2}\big)$$ (74)

17

From algebraic Equations (73) and (74), a_1 and κ_1 are obtained for $L_1 = 2L_2$. Furthermore, the clear gas spectral parameter a_0 is obtained from Equation (67), and the cross section C_0 is obtained from ALBDF multiplication approach of the mixture by bisection approach:

$$a_0 = F_{mix}(C_0, T, Y_c, Y_w) \tag{75}$$

Finally, the reference grey gas absorption cross-section is calculated from the following term:

$$C_1 = \frac{\kappa_1}{N} \tag{76}$$

The in-cell grey gas absorption coefficient is then defined as:

$$\kappa_{loc} = \kappa_1 + \kappa_s \tag{77}$$

where κ_s is grey gas absorption soot coefficient. The soot absorption coefficient is considered to be independent of the wavenumber and can be determined by an emission-based average along the spectrum (Cassol et al., 2015):

$$\kappa_s = bf_v(c_0 + c_1 T + c_2 T) \tag{78}$$

In the previous equation, f_v is the dimensionless volumetric fraction of the soot agglomerate, and b is a dimensionless constant that depends on the fuel. In this work, b was 4.1 for methane combustion and 6.3 for diesel combustion based on research by Cassol et al. (2015). In the brackets is a polynomial approximation based on the constant coefficient published by Cassol et al. (2015).

3. NUMERICAL SETUP

3.1. Validation tests

Validation was first performed for radiative transfer between two parallel walls. In this configuration, there is no combustion. The temperature, uniform CO_2, and H_2O mole fractions are prescribed according to as summarized in Table I. Details about Case a and Case b can be found in the work of Solovjov et al. (2010).

Table I   Definition of two validation cases

Case	T, K	Y_{H2O}	Y_{CO2}	ϵ_w	L, m
a	1000+500 cos($\tilde{x}$)	0.5-0.5 cos($\tilde{x}$)	0.5+0.5 cos($\tilde{x}$)	1	10
b	700-300 cos($\tilde{x}$)	0.2-0.15 cos($\tilde{x}$)	2/3 Y_{H2O}	1	3

The non-dimensional coordinate $\tilde{x}$ in Table I is defined as follows:

$$\tilde{x} = \frac{\pi x}{L} \tag{79}$$

where x is the distance normal to the left wall (x=0) and L is the distance between the walls. The calculations were performed using a mesh with 300 grid nodes.

Flame D from Sandia National Laboratories was simulated in the second test case (Barlow et al., 2005). A mixture of 25% methane and 75% air (volume basis) at 294 K was injected through a central tube with an inner diameter of 5 mm at Re number 22400. A mixture of C_2H_2, H_2, air, CO, and N_2 is injected through an annular tube with inner and outer diameters of 7.7 mm and 18.2 mm, respectively, with the same enthalpy and equilibrium composition as methane/air at 0.77 equivalence ratio and at 1880 K. Experimental data for the temperature and

species concentrations are available in (Mahmoud et al., 2018). The axisymmetric computational domain is 400 mm long and 96.5 mm wide. The simulations were performed using a mesh with approximately 77,000 control volumes. The chemical mechanism from TU Vienna was used for the generation of the methane laminar flame speed and autoignition databases (Schuh and Winter, 2020). The Sandia Flame D was also used for the validation of TRI.

3.2. Numerical setup for ICE simulations

A passenger car ICE (Volvo I5D) was investigated in this work. The most relevant engine and injection system characteristics are given in Table II. The fuel is EN590 B7 diesel, which is injected at a temperature of $44^{\circ}C$.

Table II Engine and injection system specifications

Type	direct injection engine
Bore	81 mm
Stroke	93 mm
Compression ratio	16.5
Number of nozzle holes	7
Spray Angle	16°
Nozzle hole diameter	125 μm

The fuel inlet velocities were determined from the experimentally measured injection rate shown in Appendix 1. Company AVL GmbH conducted all the experimental research through their in-house experimental setup, which was provided for numerical validation in several publications (Jurić et al., 2020, 2021; Petranovic et al., 2017; Tvrdojevic et al., 2019). All the experimental temperature profiles obtained during operating cycles are mean values of repeated a hundred operating 4-stroke operating cycles and are available for $0.1^{\circ}CA$ increment. The numerical simulations of the 4-stroke ICE were performed for only stroke periods from when the intake valves close at $585^{\circ}C$ until the exhaust valves open at $855^{\circ}CA$. At the beginning of the simulation, the combustion chamber was initialized with a uniform mixture and EGR ratio. The temperatures of the head, cylinder and piston walls were known from the experimental data. The emissivity of the walls was assumed to be equal to 1. The influence of the wall emissivity values on the results is illustrated in Appendix 2. Due to the symmetry, the computational domain corresponds to a single injection nozzle. Meshes ranging from approximately 55,000 control volumes at the Top Dead Centre (TDC) to approximately 113,000 cells at the Bottom Dead Centre (BDC) were generated using the AVL FIREm™ mesh tools. The mesh at TDC and BDC is shown in Appendix 3. The piston movement is described with 35 different meshes from BDC to TDC that include a 2-cell layer next to the piston wall to improve the flow modelling in the boundary layer. An isolated compensation volume is included at the piston wall to account for shape irregularities and gas leakage. A remeshing procedure to transfer radiative values between different meshes was implemented in order to have automated simulations for moving meshes. A remeshing procedure is inherited from existing fluid flow and combustion field remeshing procedures. All field arrays are reallocated

at each remeshing, where the field arrays from the calculating mesh are transferred to the new mesh. The generated ICE mesh is shown in Figure 3, where the boundary connection is defined at the two periodic boundaries. In Appendix 2, a mesh independence study is briefly described. Additionally, the code is adapted for multiple processing calculations, where the mesh is decomposed into region meshes with a buffer layer for each Central Processing Unit (CPU). The buffer layer consists of a 2-cell layer of the neighbouring mesh region for updating the intersection values. The computational time loss is sourced mainly from updating intersection values, performed when all CPUs are finished with an iteration. The parallelisation efficiency of the implemented model is around 50-55% for ICE simulations that feature moving mesh and around 70% for single mesh. The parallelisation efficiency of ICE simulation has additional loss in remeshing, where the mesh decomposition is called multiple times.
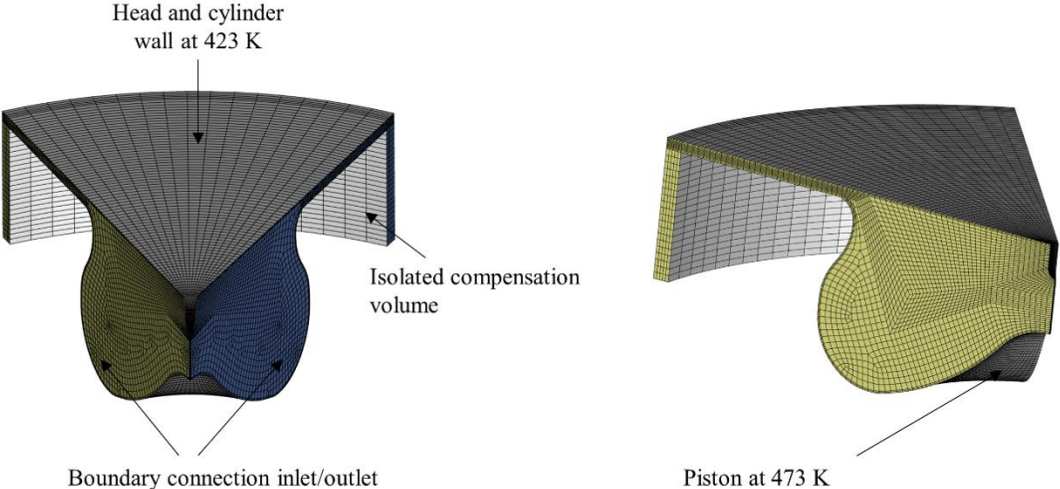

Figure 3 ICE mesh with the boundary conditions

The central differencing scheme was used with AMG linear solver for the calculation of the continuity equation. The convective terms of the momentum were discretized using the MINMOD scheme, while the energy and combustion transport equation upwind scheme was used for the turbulence. The normalized sum of absolute residual values is used as the convergence criterion for all variables and was 10^{-5} in this work. The marching algorithm is employed for the calculation of FVM. A maximum number of twenty iterations is used for the RTE solver, which is called every 10th-time step of the fluid flow solver.

From the conducted analysis in Appendix 4, a control volumes analysis was performed. The angular discretization of the RTE comprised 64 control angles for the solid angle of 4π. In the SLW model, twenty grey gases were employed. Table III and Table III provide information about the generation of the laminar flame speed and autoignition databases. A chemical mechanism for a diesel fuel surrogate (Pei et al., 2015) was selected for generating the values of the database.

Table III Values used for the generation of the laminar flame speed database

Laminar flame speed	Conditions

Temperature, K	300, 500, 750, 1000, 1250
Pressure, MPa	0.1, 0.2, 0.5, 1, 2, 5, 10, 15, 20, 25, 30
Equivalence ratio, -	0.2, 0.4, 0.6, 0.8, 0.9, 1, 1.1, 1.2, 1.4, 1.6, 1.8, 2, 3, 4, 5
EGR, -	$0 - 0.6$ (increment 0.2)

Table IV Values used for the generation of the autoignition delay database

Autoignition	Conditions
Temperature, K	$600 - 760$ (increment 20), 780, $800 - 1440$ (increment 40), 1500
Pressure, MPa	0.1, 0.2, 0.5, 1, 2, 5, 10, 15, 20, 25, 30
Equivalence ratio, -	0.2, 0.4, 0.6, 0.8, 0.9, 1, 1.1, 1.2, 1.4, 1.6, 1.8, 2, 3, 4, 5
EGR, -	$0 - 0.8$ (increment 0.1)

Four operating ICE points are observed in this work: two with single and two with multi-injection strategies. Multi-injection strategy significantly influences decreasing peak temperatures and NO emissions. The initial condition of operating points and details about the number of injections and the total injected mass are shown in Table V. Based on the experimental research, and the initial velocity field was set as the swirl of 4740 rounds per minute over the cylinder axis in all cases. All four operating cycles rotate at the constant rotation velocity of 2000 rounds per minute and have approximately equal total injected fuel. Selected operating cases have similar initial values, where only EGR was introduced to the cylinder and is variated for single injection in Case #2 and multi-injection in Case #4. The initial temperatures of Case #2 and Case #4 are also slightly increased compared to Cases without EGR.

Table V Initial conditions of ICE operating points

Operating point	Case #1	Case #2	Case #3	Case #4
Number of injections	1	1	3	3
Total injected mass (mg)	4.1	4.1	4.0	4.0
Pressure (MPa)	0.21	0.21	0.22	0.22
Temperature (K)	365	418	389	427

Table VI Initial gas composition of ICE operating points

Mass fraction, -	Case #1	Case #2	Case #3	Case #4
O_2	0.2278	0.1846	0.2092	0.1830
N_2	0.7672	0.7583	0.7634	0.7560
CO_2	0.0034	0.0389	0.0187	0.0402
H_2O	0.0016	0.0182	0.0087	0.0188

4. RESULTS AND DISCUSSION

In this section, firstly, the validation of SLW-1 model and verification with the other radiative absorption coefficient models is given on the simple 1D case without combustion process, 2D Sandia flame D benchmark case, and complex 3D ICE case.

4.1. Validation and verification of SLW-1 model

The implemented radiative absorption coefficient model SLW-1 is validated on 1D cases with a benchmark solution that is calculated by line-by-line method (LBL) (Solovjov et al., 2010). Figure 2 shows the validation of implemented SLW-1 model in the FVM framework against the benchmark results of the radiative heat source for Case a in Table I. A total number of control angles was 64 for all absorption coefficient model calculations, and the number of grey gasses in SLW model was 20. The highest disagreement along the axis with the benchmark is achieved with WSGG model. Contrary to WSGG, SLW and SLW-1 achieve overprediction. A good trend in the sinusoid curve is achieved for all models. Additionally, a significantly better agreement with SLW and SLW-1 is achieved at the boundaries.

Case b validation is shown in Figure 5. In case b, a similar discrepancy from the benchmark results is achieved for all models. The overprediction of WSGG at the low radiative source term values is reached again in case b. However, the most significant discrepancy is at 3m, where the SLW-1 has a pronounced disagreement with SLW and WSGG models. The more accurate results are obtained with the SLW-1 and SLW models than with WSGG in both cases, which indicates that the consideration of spectral line properties leads to a better agreement of the results with the LBL benchmark solution. From the conducted 1D validation, it can be stated that the implemented SLW-1 model is suitable for describing the radiative gas properties.
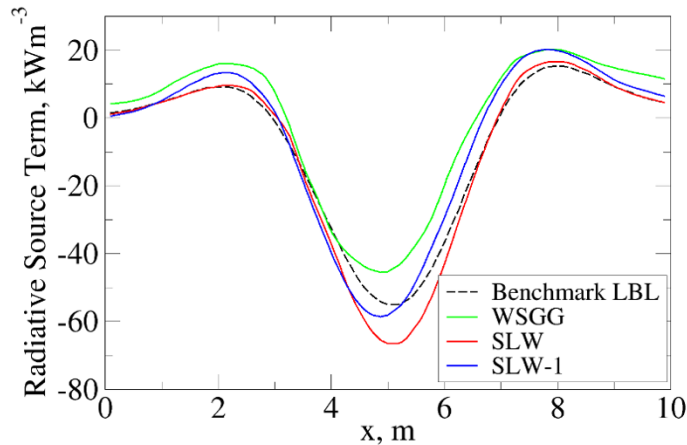

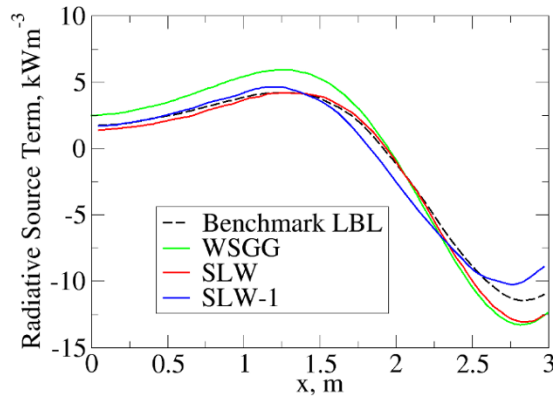Figure 4   The 1D validation case a: radiative source term along the observed axis

22

Figure 5   The 1D validation case b: radiative source term along the observed axis

Temperature profiles at the different axial locations (x=15D and x=30D) are compared in Figure 6 for the 2D validation case of Sandia flame D. WSGG, SLW and SLW-1 are calculated together with the FVM radiation model and ECFM-3Z combustion model. The same as in the 1D validation case, the total number of control angles was 64 for all absorption coefficient model calculations, and the number of grey gasses in SLW was 20. The best agreement between all radiative absorption coefficient models is achieved at the radial position of tube diameter D. A higher discrepancy is achieved at the axis for the position x=30D, in which the SLW model achieves more accurate results than the WSGG and SLW-1 models. Although the trend of WSGG is well predicted at x=15D, it is significantly changed near the axis at x=15D compared to SLW and SLW-1 models. That indicates that the flame temperature could be better described within the SLW-1 model compared to the WSGG. The best agreement was achieved with the SLW model. The SLW-1 model achieves a similar trend to the SLW model. Temperature profiles of the SLW and SLW-1 model with TRI influence are shown in Figure 7.
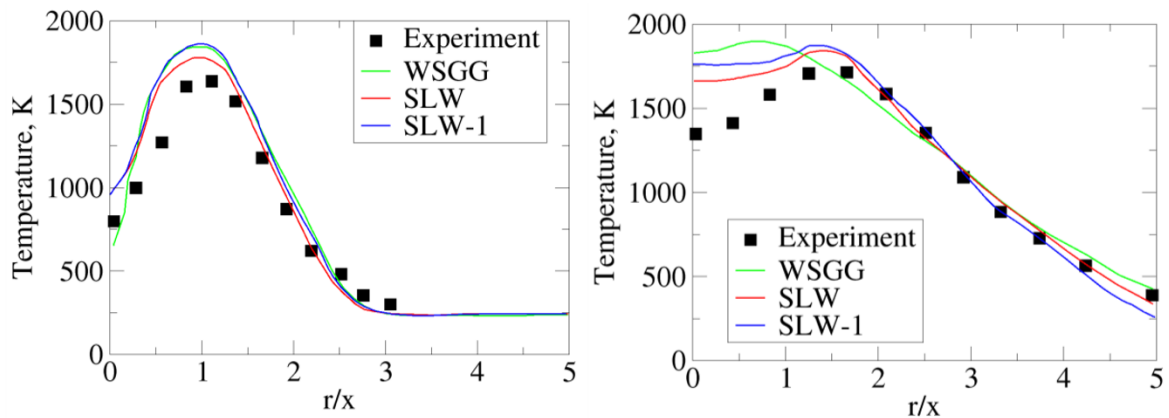

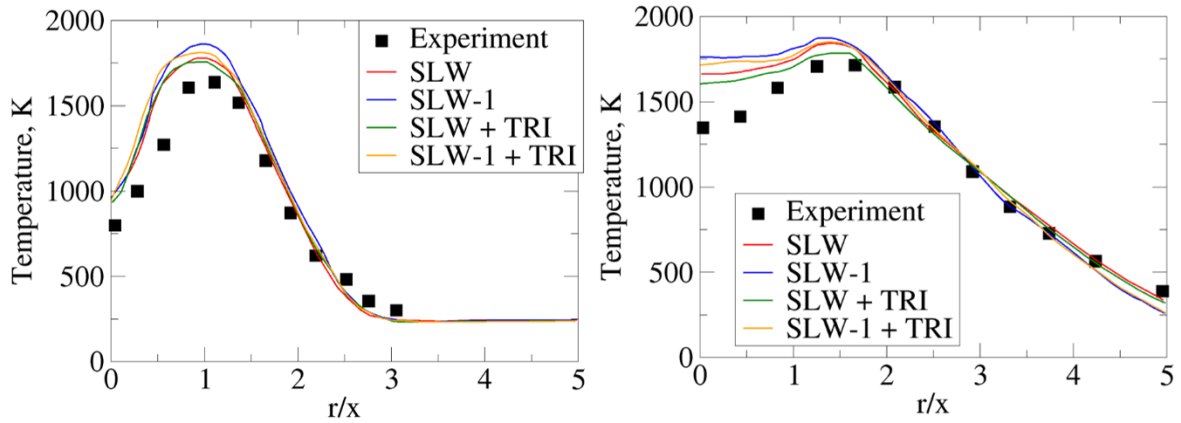Figure 6 Temperature profiles for two different axial positions of benchmark case Sandia flame D: x=15D, and x=30D

23

Figure 7 Temperature profiles with TRI for two different axial positions of benchmark case Sandia flame D: x=30D, and x=15D

4.2. ICE results

This section confirms results from 3D CFD calculations on ICE operating cycles against the experimental ICE in-cylinder data.

Figure 8 shows the mean in-cylinder temperature for four observing operating ICE cases, including TRI for SLW and SLW-1 models. All models achieved a good trend for the single injection Case #1 and Case #2. The temperature difference between radiative absorption models was within 10 K for Case #1 and 20K for Case #2, which has a greater initial EGR ratio and temperature. The higher temperature difference between models in Case #2 is due to the higher mole fraction of participating gases CO_2 and H_2O in the cylinder. The best agreement with experimental results is achieved with the SLW results, while the lowest agreement is achieved with the WSGG model for all four operating cases. The highest discrepancy with experimental data is achieved around the peak temperature and during the cylinder expansion, where the combustion products CO2 and H2O are also increasing. For the multi-injection Case #3 and Case #4, a correct trend for autoignition detection of separated injections is achieved, which is visible in temperature inflexion points, where the temperature gradient arises. A higher discrepancy is achieved for the multi-injection cases, especially in Case #4, which has a higher EGR mass fraction. The model discrepancy goes up to approximately 27 K, with the highest difference achieved in expansion, similar to the single injection cases. The SLW-1 results for all operating cases are in good agreement with the SLW model and are notably better than the results obtained with WSGG. SLW-1 represent the compromise between WSGG and SLW models. SLW-1 considers spectral line gas properties for a single grey gas and transparent window but without solving additional time-consuming transport equations for the grey gases.
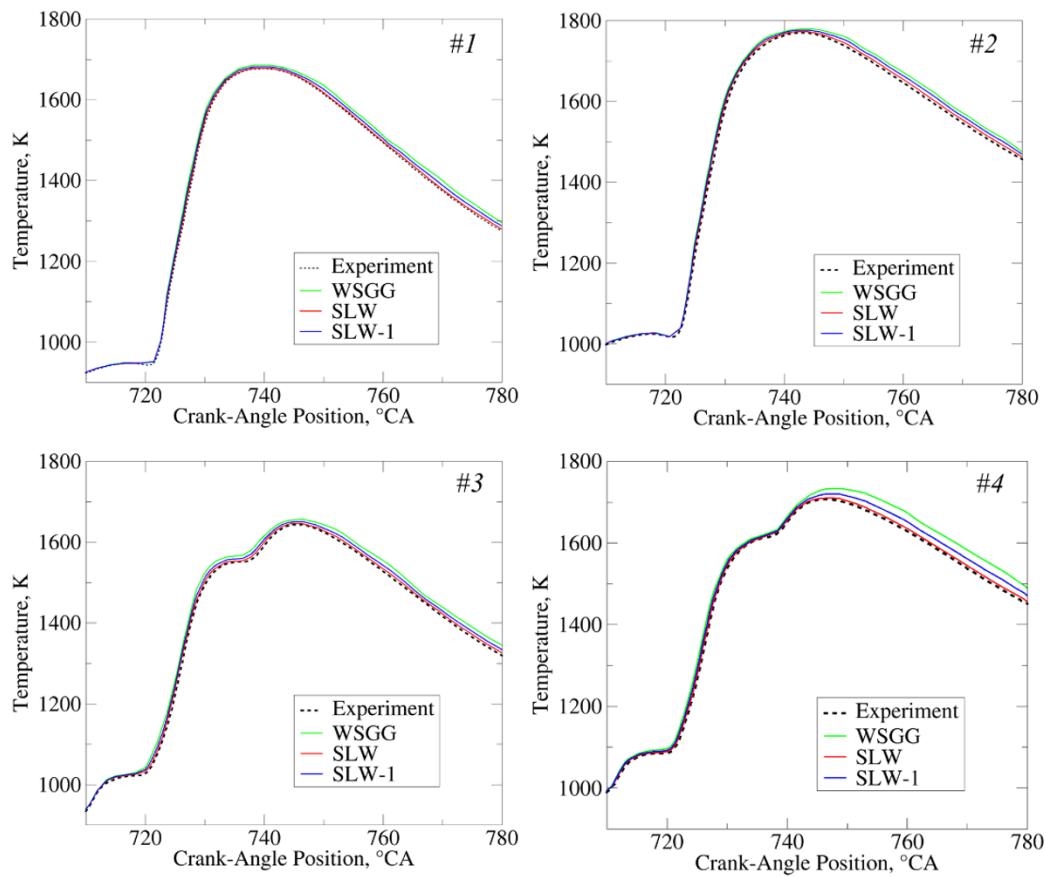
Figure 8   Mean temperature results for all observing ICE operating points, and radiative absorption coefficient models: WSGG, SLW, and SLW-1

The comparison between SLW-1 results with and without TRI for Case #1 and Case #2 is shown in Figure 9. A higher disagreement between simulation and experimental data with and without TRI is more pronounced for Case #2, which has a higher mean in-cylinder temperature and EGR ratio. The maximal mean temperature difference is approximately 8 K, while for Case #1, significantly lower. As expected, a more significant TRI influence is observed at higher temperatures. The temperature decrease for simulation with included TRI was also observed in the results obtained for Sanda Flame D simulation, shown in Figure 7.
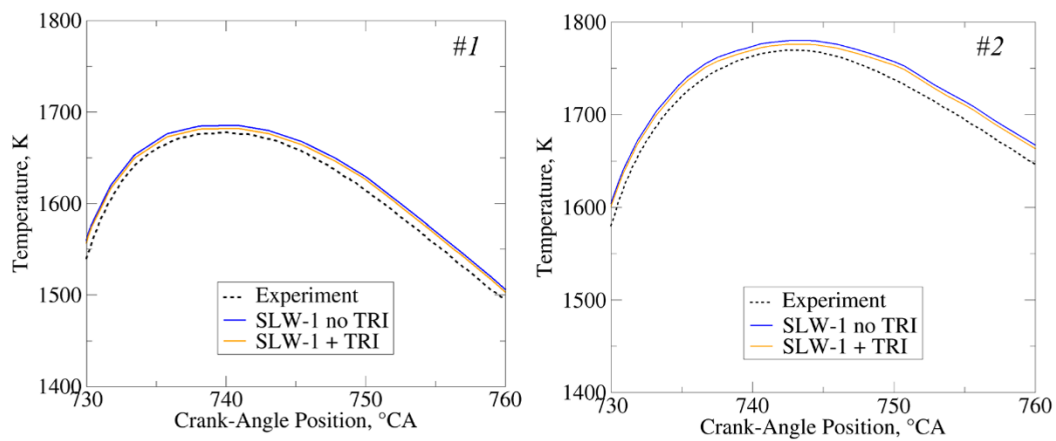
Figure 9   Mean temperature results of SLW-1 model with/without TRI for operating Case #1 and Case #2

Figure 10 shows 3D profiles at 15 °CA after TDC for Case #2: The mean temperature, the temperature difference between simulation with and without TRI, radiative participating gases CO_2 and H_2O, and pollutant emissions for NO and soot. At 15 °CA after TDC, fuel injection is finished, and temperature distribution is developed, where the peak temperatures are achieved at the cylinder bowl. The peak NO mass fraction can also be observed in the same region. H_2O distribution significantly correlates to the temperature field. The CO_2 distribution shows the regions of the completed combustion where the area closer to the injector is still not fully combusted. The low-temperature part of the cylinder bowl is due to the cooling from injected fuel. Those regions are also the highest soot formation regions, primarily associated with lower temperatures and evaporated fuel-rich regions. Temperature difference distribution between simulations with and without radiation correlates to the right-hand diagram in Figure 9. The highest differences are in the regions of the highest temperature gradients.
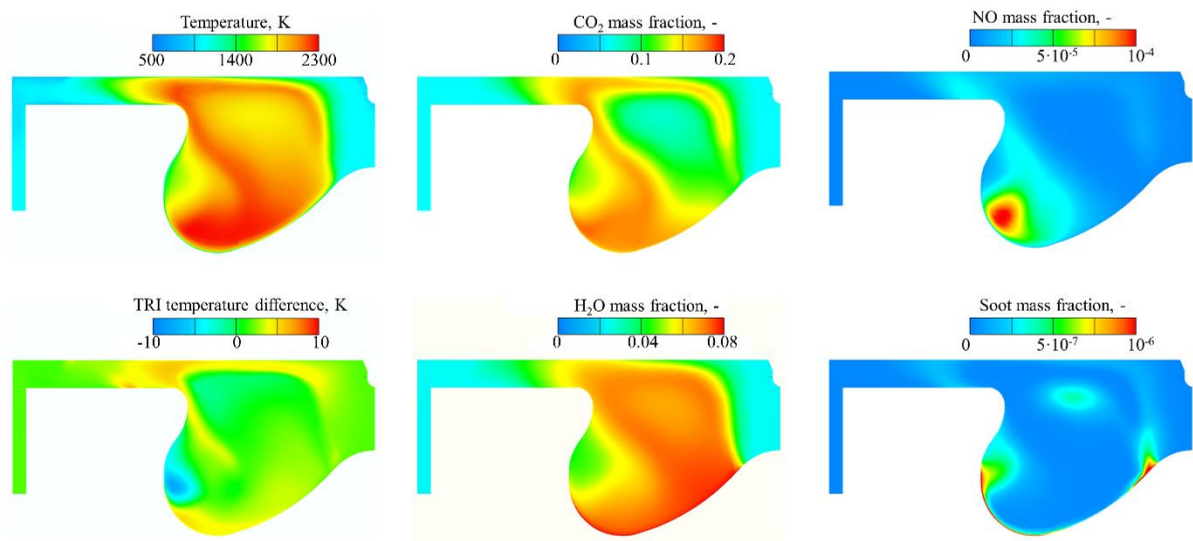
Figure 10   Different 3D profiles of Case #2 at 15 °CA after TDC (735 °CA)

Figure 11 shows the calculated boundary values of incident radiation for implemented periodic boundary connection boundary condition. The right segment has a slightly higher incident radiation value than the left segment due to the initial fluid flow swirling inside the cylinder. All radiative intensity that goes outside from a segment is transferred as input on its boundary connection segment.
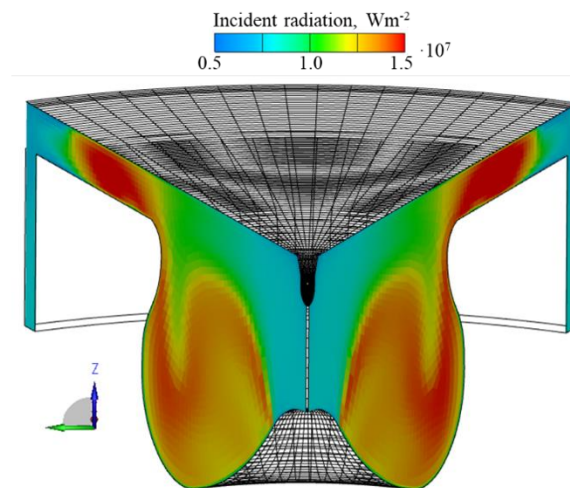

Figure 11   Incident radiation results at the boundary connection walls for Case #2 at 15 °CA after TDC

4.2.1. Pollutant emission results

Figure 12 shows NO formation described with the extended Zeldovich model for the operating Case #1 and Case #2. Despite the increased temperature, the initial EGR strongly reduces the mean NO emissions in the operating cycle. The NO emission results when exhaust

27

values start to open are given in Figure 13 for all operating points and compared with available experimental data. The overprediction of NO emissions compared to the experimental data is achieved for both operating single injection cases. The overpredicted NO emissions also correlate to the higher mean temperatures in Figure 8 results. SLW-1 achieved an accuracy in-between WSGG and SLW models same as for the temperature results.

The temperature is the primary generator of NO emissions in the extended Zeldovich model, due to that NO results from CFD simulations exceed the experimental NO concentrations in all four operating ICE cases. The temperature and NO emissions results are increased for all radiative absorption models. Additionally, TRI interaction on the final emissions is of minor importance compared to the differences in the radiative absorption models.
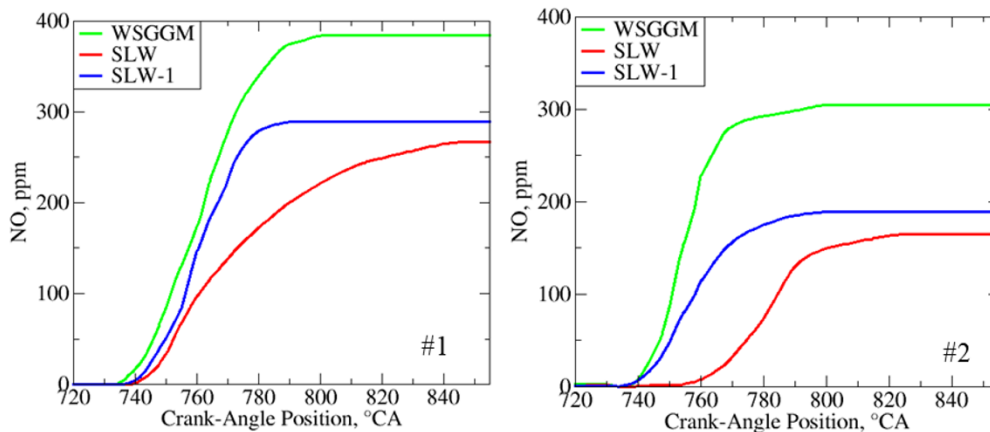

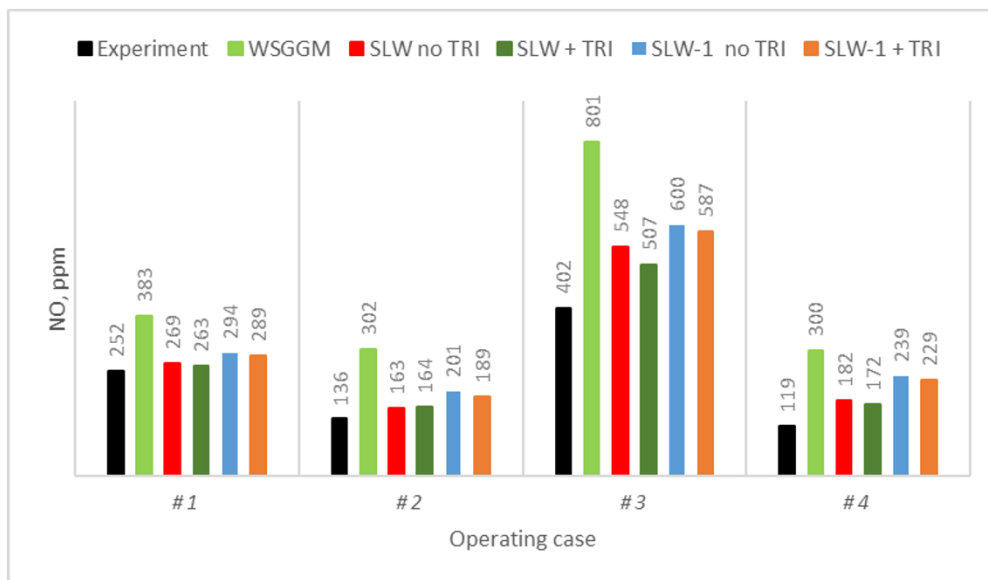Figure 12   NO profile formation for concentration different

Figure 13   NO results at the exhaust system for ICE cases

Figure 14 shows soot results at the end of all operating cycles. The overall low concentrations of soot are achieved for Case #1 and Case #3, which feature a low initial EGR ratio. That is one of the reasons why radiative absorption of CO_2 and H_2O dominates soot

absorption in Case #1 and Case #3. A higher difference between predicted soot emissions is achieved for the operating points with the higher initial EGR values. The impact of radiative heat transfer and TRI is also lower on exhaust soot results than on NO results, as seen in Figure 14.
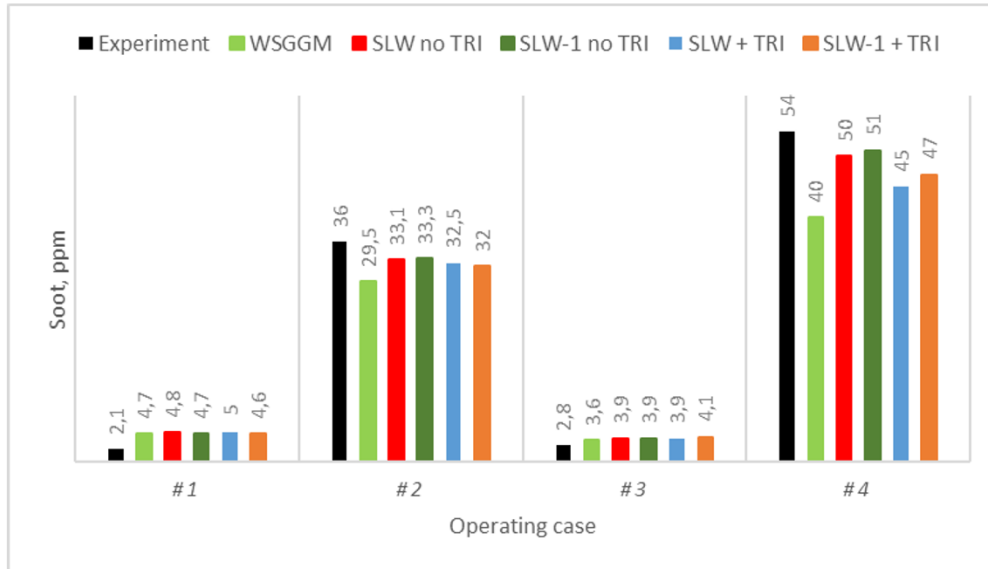

Figure 14   Soot results at the exhaust system for ICE cases

Table VII shows the average computational CPU time of each simulation. A simulation without RTE solver FVM is given as a reference. It can be concluded that the SLW model is computationally too demanding for the ICE simulations at the expense of not providing significantly more accurate results than the SLW-1 model. Additionally, SLW-1 features a similar computational time as WSGG but gives additional accuracy with the consideration of spectral line properties. Although it does not add significantly increased accuracy in ICE, TRI is recommended for inclusion due to the non-significant increase in computational time.

Table VII   Average CPU time in seconds

Without radiation	WSGG	SLW no TRI	SLW-1 no TRI	SLW + TRI	SLW-1 + TRI
25064	42157	69012	45129	70213	47001

5. CONCLUSION

An integrated simulation approach for more efficient estimation of pollutant formation in industrial multiphase reactive applications is presented in this work, which couples radiative heat transfer and pregenerated laminar flame speed and autoignition databases. The spectral-line formulation using only a single grey gas and one transparent gas, called SLW-1 model, is implemented in AVL FIREm™ CFD code via user routines, for modelling radiative gas properties. SLW-1 is implemented in the FVM for the calculation of RTE. The periodic

29

boundary conditions, connection with remeshing in moving mesh, and multi-thread calculation are additionally implemented for ICE calculations. TRI calculation is inherited from the existing NO turbulence fluctuation model. A good agreement with 1D validation cases without combustion and for the 2D Sandia flame D case is achieved. Additionally, the SLW-1 model, in combination with TRI, is applied to complex 3D ICE cases with single and multi-injection strategies and different EGR initialisation. The verification with other radiative absorption coefficient models, WSGG and SLW, was also performed in each validation case. It can be stated that the radiative heat transfer shows a higher difference between absorption coefficient models and the experimental data for operating cases loaded with higher values of EGR ratio. Additionally, NO_x results from CFD simulations exceed the experimental NO_x concentrations in all four operating ICE cases due to the overpredicting mean temperature in all observed cases. It was observed that the participation of CO_2 and H_2O has a higher impact on the overall radiative heat transfer than soot. The influence of radiative heat transfer and the TRI model on exhaust soot results is less significant than their impact on NO results.

The computational demands of the SLW model outweigh its insignificant benefits in terms of accuracy compared to the SLW-1 model in ICE simulations. On the other hand, the SLW-1 model demonstrates comparable computational efficiency to the WSGG model while offering improved accuracy by considering spectral line properties. Incorporating radiative heat transfer and utilizing the SLW-1 model for calculating nongrey radiative properties significantly enhances the accuracy of pollutant emission predictions in ICE, approaching the level achieved by the SLW model. Although the TRI model does not yield a substantial increase in accuracy for ICE simulations, the inclusion of the TRI model is recommended due to its negligible impact on computational time. Future work is to adapt the implemented SLW-1 for calculating methane participation in radiative heat transfer for dual-fuel combustion.

ACKNOWLEDGMENT

REFERENCES

Abramzon, B. and Sazhin, S. (2006), "Convective vaporization of a fuel droplet with thermal radiation absorption", Fuel, Vol. 85 No. 1, pp. 32–46, doi: 10.1016/j.fuel.2005.02.027.

Abramzon, B. and Sirignano, W.A. (1989), "Droplet vaporization model for spray combustion calculations", International Journal of Heat and Mass Transfer, Vol. 32 No. 9, pp. 1605–1618, doi: 10.1016/0017-9310(89)90043-4.

AVL GmbH. (2022), "avl.com", available at: https://www.avl.com/fire-m (accessed 22 November 2022).

Barlow, R., Frank, J., Karpetis, A. and Chen, J. (2005), "Piloted methane/air jet flames: Transport effects and aspects of scalar structure", Combustion and Flame, Vol. 143 No. 4, pp. 433–449, doi: 10.1016/j.combustflame.2005.08.017.

Benajes, J., Martín, J., García, A., Villalta, D. and Warey, A. (2015), "In-cylinder soot radiation heat transfer in direct-injection diesel engines", Energy Conversion and Management, Pergamon, Vol. 106, pp. 414–427, doi: 10.1016/J.ENCONMAN.2015.09.059.

Benajes, J., Martin, J., Garcia, A., Villalta, D., Warey, A., Domenech, V. and Vassallo, A. (2015), "An Investigation of Radiation Heat Transfer in a Light-Duty Diesel Engine", SAE International Journal of Engines, SAE International, Vol. 8 No. 5, doi: 10.4271/2015-24-2443.

Cassol, F., Brittes, R., Centeno, F.R., da Silva, C.V. and França, F.H.R. (2015), "Evaluation of the gray gas model to compute radiative transfer in non-isothermal, non-homogeneous participating medium containing CO_2, H_2O and soot", Journal of the Brazilian Society of Mechanical Sciences and Engineering, Vol. 37 No. 1, pp. 163–172, doi: 10.1007/s40430-014-0168-5.

Chishty, M.A., Bolla, M., Hawkes, E., Pei, Y. and Kook, S. (2016), "Assessing the Importance of Radiative Heat Transfer for ECN Spray A Using the Transported PDF Method", SAE International Journal of Fuels and Lubricants, SAE International, Vol. 9 No. 1, pp. 100–107, doi: 10.4271/2016-01-0857.

Coelho, P.J. (2007), "Numerical simulation of the interaction between turbulence and radiation in reactive flows", Progress in Energy and Combustion Science, August, doi: 10.1016/j.pecs.2006.11.002.

Coelho, P.J. (2012), "Turbulence-radiation interaction: From theory to application in numerical simulations", Journal of Heat Transfer, Vol. 134 No. 3, doi: 10.1115/1.4005130.

Colin, O. and Benkenida, A. (2004), "The 3-Zones Extended Coherent Flame Model \(Ecfm3z\) for Computing Premixed/Diffusion Combustion; The 3-Zones Extended Coherent Flame Model \(Ecfm3z\) for Computing Premixed/Diffusion Combustion", doi: 10.2516/ogst:2004043ï.

Colin, O., Benkenida, A. and Angelberger, C. (2003), 3D Modeling of Mixing, Ignition and Combustion Phenomena in Highly Stratified Gasoline Engines, Oil & Gas Science and Technology-Rev. IFP, Vol. 58.

da Cruz, A.P. (2004), "THREE-DIMENSIONAL MODELING OF SELF-IGNITION IN HCCI AND CONVENTIONAL DIESEL ENGINES", Combustion Science and Technology, Vol. 176 No. 5–6, pp. 867–887, doi: 10.1080/00102200490428503.

Cunningham, E. (1910), "On the velocity of steady fall of spherical particles through fluid medium", Proceedings of the Royal Society of London. Series A, Containing Papers of a Mathematical and Physical Character, Vol. 83 No. 563, pp. 357–365, doi: 10.1098/rspa.1910.0024.

Doner, N. and Selçuk, N. (2013), "An application of Spectral line-based weighted sum of grey gases (SLW) model with geometric optics approximation for radiative heat transfer in 3-D participating media", Applied Thermal Engineering, Vol. 50 No. 1, pp. 89–93, doi: 10.1016/j.applthermaleng.2012.05.035.

Dorigon, L.J., Duciak, G., Brittes, R., Cassol, F., Galarça, M. and França, F.H.R. (2013), "WSGG correlations based on HITEMP2010 for computation of thermal radiation in non-isothermal, non-homogeneous H_2O/CO_2 mixtures", International Journal of Heat and Mass Transfer, Vol. 64, pp. 863–873, doi: 10.1016/j.ijheatmasstransfer.2013.05.010.

Eder, L., Ban, M., Pirker, G., Vujanovic, M., Priesching, P. and Wimmer, A. (2018), "Development and validation of 3D-CFD injection and combustion models for dual fuel combustion in diesel ignited large gas engines", Energies, MDPI AG, Vol. 11 No. 3, doi: 10.3390/en11030643.

Fernandez, S.F., Paul, C., Sircar, A., Imren, A., Haworth, D.C., Roy, S. and Modest, M.F. (2018), "Soot and spectral radiation modeling for high-pressure turbulent spray flames", Combustion and Flame, Vol. 190, pp. 402–415, doi: 10.1016/j.combustflame.2017.12.016.

Galtier, M., Woelffel, W., André, F., Solovjov, V.P., Webb, B.W. and Roy, S. (2022), "Assessment of narrow-band and full spectrum gas radiation methods in a real industrial glass furnace configuration", Applied Thermal Engineering, Vol. 216, p. 119020, doi: 10.1016/j.applthermaleng.2022.119020.

Geringer, S. (2021), Influence of Radiative Heat Transfer on NOx and Soot Formation in Large Two-Stroke Marine Diesel Engines, 16 June, doi: 10.3929/ETHZ-B-000489745.

Gopinath, S., Devan, P.K., Sabarish, V., Sabharish Babu, B. v., Sakthivel, S. and Vignesh, P. (2020), "Effect of spray characteristics influences combustion in DI diesel engine – A review", Materials Today: Proceedings, Elsevier, Vol. 33, pp. 52–65, doi: 10.1016/J.MATPR.2020.03.130.

Hanjalić, K., Popovac, M. and Hadžiabdić, M. (2004), "A robust near-wall elliptic-relaxation eddy-viscosity turbulence model for CFD", International Journal of Heat and Fluid Flow, Vol. 25 No. 6, pp. 1047–1051, doi: 10.1016/j.ijheatfluidflow.2004.07.005.

Hawkes, E.R. and Chen, J.H. (2005), "Evaluation of models for flame stretch due to curvature in the thin reaction zones regime", Proceedings of the Combustion Institute, Vol. 30 No. 1, pp. 647–655, doi: 10.1016/j.proci.2004.08.106.

Jiro, S., Kobayashi, M., Iwashita, S. and Fujimoto, H. (1994), "Modeling of Diesel Spray Impingement on a Flat Wall", doi: 10.4271/941894.

Jurić, F., Ban, M., Priesching, P., Schmalhorst, C., Duić, N. and Vujanović, M. (2022), "Numerical modeling of laminar flame speed and autoignition delay using general fuel-independent function", Fuel, Elsevier, Vol. 323, p. 124432, doi: 10.1016/j.fuel.2022.124432.

Jurić, F., Coelho, P.J., Priesching, P., Duić, N., Honus, S. and Vujanović, M. (2022), "Implementation of the spectral line-based weighted-sum-of-gray-gases model in the finite volume method for radiation modeling in internal combustion engines", International Journal of Energy Research, John Wiley & Sons, Ltd, doi: 10.1002/er.8177.

Jurić, F., Petranović, Z., Vujanović, M. and Duić, N. (2020), "Numerical assessment of radiative heat transfer impact on pollutant formation processes in a compression ignition engine", Journal of Cleaner Production, Vol. 275, doi: 10.1016/j.jclepro.2020.123087.

Jurić, F., Stipić, M., Samec, N., Hriberšek, M., Honus, S. and Vujanović, M. (2021), "Numerical investigation of multiphase reactive processes using flamelet generated manifold approach and extended coherent flame combustion model", Energy Conversion and Management, Vol. 240, doi: 10.1016/j.enconman.2021.114261.

Kalbhor, A. and Oijen, J. van. (2021), "An assessment of the sectional soot model and FGM tabulated chemistry coupling in laminar flame simulations", Combustion and Flame, Vol. 229, p. 111381, doi: 10.1016/j.combustflame.2021.02.027.

Karlsson, A., Magnusson, I., Balthasar, M. and Mauss, F. (1998), "Simulation of Soot Formation Under Diesel Engine Conditions Using a Detailed Kinetic Soot Model", doi: 10.4271/981022.

Knop, V. and Jay, S. (2006), "Latest Developments in Gasoline Auto-Ignition Modelling Applied to an Optical CAI (Tm) Engine", Oil & Gas Science and Technology, Vol. 61 No. 1, pp. 121–137, doi: 10.2516/ogst:2006008x.

Liu, A.B., Mather, D. and Reitz, R.D. (1993), "Modeling the Effects of Drop Drag and Breakup on Fuel Sprays", doi: 10.4271/930072.

Mahmoud, R., Jangi, M., Fiorina, B., Pfitzner, M. and Sadiki, A. (2018), "Numerical Investigation of an OxyfuelNon-Premixed CombustionUsing a Hybrid Eulerian Stochastic Field/Flamelet Progress Variable Approach: Effects of H2/CO2Enrichment and Reynolds Number", Energies, Vol. 11 No. 11, p. 3158, doi: 10.3390/en11113158.

Mengüc, M.P., Viskanta, R. and Ferguson, C.R. (1985), "Multidimensional Modeling of Radiative Heat Transfer in Diesel Engines", doi: 10.4271/850503.

Mobasheri, R., Peng, Z. and Mirsalim, S.M. (2012), "Analysis the effect of advanced injection strategies on engine performance and pollutant emissions in a heavy duty DI-diesel engine by CFD modeling", International Journal of Heat and Fluid Flow, Vol. 33 No. 1, pp. 59–69, doi: 10.1016/j.ijheatfluidflow.2011.10.004.

Mukut, K.M. and Roy, S.P. (2020), "Effect of O2 concentration in ambient mixture and multiphase radiation on pollutant formation in ECN spray-A", Combustion Theory and Modelling, Taylor and Francis Ltd., Vol. 24 No. 3, pp. 549–572, doi: 10.1080/13647830.2020.1721561.

Ozen, G., Ates, C., Selçuk, N. and Kulah, G. (2019), "Assessment of SLW-1 model in the presence of gray and non-gray particles", International Journal of Thermal Sciences, Elsevier, Vol. 136 No. June 2018, pp. 420–432, doi: 10.1016/j.ijthermalsci.2018.10.038.

Paul, C., Ferreyro Fernandez, S., Haworth, D.C., Roy, S. and Modest, M.F. (2019), "A detailed modeling study of radiative heat transfer in a heavy-duty diesel engine", Combustion and Flame, Elsevier, Vol. 200, pp. 325–341, doi: 10.1016/j.combustflame.2018.11.032.

Paul, C., Haworth, D.C. and Modest, M.F. (2019), "A simplified CFD model for spectral radiative heat transfer in high-pressure hydrocarbon–air combustion systems", Proceedings of the Combustion Institute, Vol. 37 No. 4, pp. 4617–4624, doi: 10.1016/j.proci.2018.08.024.

Pearson, J.T., Webb, B.W., Solovjov, V.P. and Ma, J. (2014), "Efficient representation of the absorption line blackbody distribution function for H2O, CO2, and CO at variable temperature, mole fraction, and total pressure", Journal of Quantitative Spectroscopy and Radiative Transfer, Vol. 138, pp. 82–96, doi: 10.1016/j.jqsrt.2014.01.019.

Pei, Y., Mehl, M., Liu, W., Lu, T., Pitz, W.J. and Som, S. (2015), "A Multicomponent Blend as a Diesel Fuel Surrogate for Compression Ignition Engine Applications", Journal of Engineering for Gas Turbines and Power, Vol. 137 No. 11, doi: 10.1115/1.4030416.

Petranovic, Z., Edelbauer, W., Vujanović, M., Priesching, P., Tatschl, R. and Duić, N. (2017), "Modeling of Reactive Spray Processes in DI Diesel Engines", doi: 10.4271/2017-01-0547.

Priesching, P., Tatschl, R., Bauer, W., Schmid, M., Leipertz, A., Merola, S.S. and Vaglieco, B.M. (2005), Soot Particle Size Distribution-a Joint Work for Kinetic Modeling and Experimental Investigations.

Reitz, R.D. and Diwakar, R. (1987), "Structure of High-Pressure Fuel Sprays", doi: 10.4271/870598.

Schuh, S. and Winter, F. (2020), "Dual Fuel Reaction Mechanism 2.0 including NOx Formation and Laminar Flame Speed Calculations Using Methane/Propane/n-Heptane Fuel Blends", Energies, Vol. 13 No. 4, p. 778, doi: 10.3390/en13040778.

Solovjov, V.P., Lemonnier, D. and Webb, B.W. (2010), "SLW-1 Modelling of Radiative Heat Transfer in Non-Isothermal Non-Homogeneous Gas Mixtures With Soot", Proceedings of the 14th International Heat Transfer Conference IHTC14, Proceedings of the 14th International Heat Transfer Conference IHTC14, Vol. IHTC14-22299.

Solovjov, V.P., Lemonnier, D. and Webb, B.W. (2011a), "The SLW-1 model for efficient prediction of radiative transfer in high temperature gases", Journal of Quantitative Spectroscopy and Radiative Transfer, Vol. 112 No. 7, pp. 1205–1212, doi: 10.1016/j.jqsrt.2010.08.009.

Solovjov, V.P., Lemonnier, D. and Webb, B.W. (2011b), "SLW-1 modeling of radiative heat transfer in nonisothermal nonhomogeneous gas mixtures with soot", Journal of Heat Transfer, Vol. 133 No. 10, doi: 10.1115/1.4003903.

Stančin, H., Mikulčić, H., Wang, X. and Duić, N. (2020), "A review on alternative fuels in future energy system", Renewable and Sustainable Energy Reviews, Vol. 128, p. 109927, doi: 10.1016/j.rser.2020.109927.

Tvrdojevic, M., Vujanovic, M., Priesching, P., Tap, F.A., Starikov, A., Goryntsev, D. and Gavaises, M. (2019), "Implementation of the Semi Empirical Kinetic Soot Model Within Chemistry Tabulation Framework for Efficient Emissions Predictions in Diesel Engines", Open Physics, Vol. 17 No. 1, pp. 905–915, doi: 10.1515/phys-2019-0096.

Viskanta, R. (2008), "Computation of radiative transfer in combustion systems", International Journal of Numerical Methods for Heat and Fluid Flow, Emerald Group Publishing Limited, Vol. 18 No. 3–4, pp. 415–442, doi: 10.1108/09615530810853664/FULL/PDF.

Webb, B.W., Solovjov, V.P. and André, F. (2019), "The spectral line weighted-sum-of-gray-gases (SLW) model for prediction of radiative transfer in molecular gases", pp. 207–298, doi: 10.1016/bs.aiht.2019.08.003.

Yadav, R., Balaji, C. and Venkateshan, S.P. (2017), "Implementation of SLW model in the radiative heat transfer problems with particles and high temperature gradients", International Journal of Numerical Methods for Heat and Fluid Flow, Emerald Group Publishing Ltd., Vol. 27 No. 5, pp. 1128–1141, doi: 10.1108/HFF-03-2016-0095/FULL/PDF.

Yasar, M.S., Ozen, G., Selçuk, N. and Kulah, G. (2020), "Performance of banded SLW-1 in presence of non-gray walls and particles in fluidized bed combustors", Journal of

Quantitative Spectroscopy and Radiative Transfer, Vol. 257, p. 107370, doi: 10.1016/j.jqsrt.2020.107370.

Yoshikawa, T. and Reitz, R.D. (2009), "Effect of radiation on diesel engine combustion and heat transfer", Journal of Thermal Science and Technology, Vol. 4 No. 1, pp. 86–97, doi: 10.1299/jtst.4.86.

Yue, Z. and Reitz, R.D. (2019), "Numerical investigation of radiative heat transfer in internal combustion engines", Applied Energy, Vol. 235, pp. 147–163, doi: 10.1016/j.apenergy.2018.10.098.